Growth and characterization of ZnS nanowires : highlights of polytypism

Sumit Kumar

THÈSE DE DOCTORAT

NNT : 2022UPAST039

Croissance et caractérisation des nanofils ZnS : étude du polytypisme

Growth and characterization of ZnS nanowires: highlights of polytypism

Thèse de doctorat de l'université Paris-Saclay

École doctorale n° 573, Interfaces : matériaux, systèmes, usages (INTERFACES)
Spécialité de doctorat : Physique
Graduate School : Sciences de l'ingénierie et des systèmes
Référent : Université de Versailles Saint-Quentin-en-Yvelines

Thèse préparée dans l'unité de recherche GEMaC (Université Paris-Saclay, UVSQ, CNRS) sous la direction de **Vincent SALLET**, Chargé de recherche, CNRS-UVSQ

Thèse soutenue à Versailles, le 08 mars 2022, par

Sumit KUMAR

Composition du Jury

Jean-Pierre HERMIER Professeur des Universités, GEMaC, CNRS-UVSQ, Université Paris-Saclay	Président
Edith BELLET-AMALRIC Ingénieur CEA, PHELIQS, CEA et Université Grenoble Alpes	Rapporteur et examinatrice
Jean-Luc MAURICE Directeur de recherche, LPICM, CNRS, Ecole Polytechnique et Institut Polytechnique de Paris	Rapporteur et examinateur
Vincent CONSONNI Chargé de recherche, LMGP, CNRS, Grenoble INP, Université Grenoble Alpes	Examinateur
Laetitia VINCENT Chargée de recherche, C2N, CNRS, Université Paris-Saclay	Examinatrice
Vincent SALLET Chargé de recherche, GEMaC, CNRS-UVSQ, Université Paris-Saclay	Directeur de thèse

Titre : Croissance et caractérisation des nanofils ZnS : étude du polytypisme

Mots clés : ZnS, polytypisme, croissance MOCVD, nanofils, microscopie électronique en transmission

Résumé : Les nanofils (NFs) à base de semiconducteurs II-VI constituent une nouvelle classe de matériaux à l'échelle nanométrique, et présentent un potentiel exceptionnel comme nanocomposants à intégrer dans les futurs dispositifs et systèmes électroniques et optoélectroniques. Les progrès futurs de ces dispositifs dépendront de la fabrication des nanofils avec un contrôle précis de leur morphologie, de leur structure cristalline, de leur composition, de leur dopage, et de leur efficacité quantique. La méthode la plus prometteuse pour la croissance des nanofils II-VI est probablement le dépôt chimique en phase vapeur par décomposition d'organométalliques (MOCVD, technique industrielle), qui utilise des nanoparticules d'Au pour stimuler la croissance des nanofils via le mécanisme vapeur-liquide-solide (VLS) ou vapeur-solide-solide (VSS). Ce procédé de fabrication permet de varier et d'optimiser plusieurs paramètres de croissance, notamment la température de croissance, et les débits des précurseurs du groupe II et du groupe VI, et leur rapport VI/II. Néanmoins, avant d'intégrer les NFs dans de nouveaux dispositifs, de nombreux problèmes d'élaboration doivent être résolus. Il s'agit notamment des directions de croissance irrégulières, de l'effilement des NFs, de la recombinaison non-radiative au niveau des surfaces latérales, et des défauts cristallographiques tels que les macles, les défauts d'empilement, et le mélange de phases cristallines entre structures blende de zinc (cubique, 3C) et wurtzite (hexagonale, 2H). De manière intéressante, le mode de croissance particulier des NFs catalysés permet la réalisation de phases originales, 4H ou 6H. C'est ce nomme "polytypisme dans les nanofils semiconducteurs".

Cette thèse explore les mécanismes de croissance et les propriétés structurales des NFs de sulfure de zinc (ZnS). Le ZnS présente des différences d'énergie de cohésion très faibles entre les phases cristallographiques 3C, 4H, 6H, 15R et 2H. Par conséquent, un changement modeste des conditions de croissance serait suffisant pour obtenir des polytypes différents.

Nous avons ainsi appliqué deux approches de croissance distinctes des nanofils de ZnS : VLS assistée par un catalyseur liquide et VSS assistée par un catalyseur solide. A l'aide de la microscopie électronique en transmission, nous avons montré que les nanofils obtenus par VSS présentent de grands segments hexagonaux et de petits segments cubiques. En revanche, les nanofils catalysés par une gouttelette d'alliage Au-Ga à l'état liquide révèlent une phase cristalline 15R inattendue.

Nous avons développé un modèle de nucléation pour expliquer la formation de ces polytypes originaux (4H, 6H, 15R) dans les NFs semiconducteurs. Nous avons combiné la théorie classique de la nucléation, le modèle ANNNI (Ising), et les calculs de probabilité pour modéliser et expliquer l'apparition des polytypes dans les nanofils de ZnS. Ce modèle systématique nous permet de comprendre le mécanisme de croissance des NFs, et en conséquence, nous avons confirmé la validité de notre modèle théorique par des démonstrations expérimentales.

Enfin, nous avons étudié les hétérostructures axiales ZnS/ZnSe et coeur/coquille ZnS/ZnMgS. Nous avons relevé différents défis inhérents à ces hétérostructure axiales/latérales. Les propriétés optiques des NFs ont été étudiées par photoluminescence et cathodoluminescence. Les mesures de CL à température cryogénique ont permis de mieux comprendre les qualités optiques essentielles et la luminescence des hétérostructures 1D.

En conclusion, nous avons eu pour ambition de contribuer à la croissance de NWs de ZnS de haute qualité, ainsi que d'hétérostructures 1D à base de semiconducteurs à grande bande interdite. Nous avons révélé un phénomène de polytypisme inattendu et singulier dans le développement de nos matériaux à l'échelle nanométrique. Cette étude peut ouvrir la voie au contrôle de la phase cristalline et à la compréhension des polytypes dans les nanofils semi-conducteurs.

université PARIS-SACLAY | ÉCOLE DOCTORALE Interfaces: matériaux, systèmes, usages

Title : Growth and characterization of ZnS nanowires : highlights of polytypism

Keywords : ZnS, polytypism, MOCVD growth, nanowires, transmission electron microscopy

Abstract : II-VI semiconductor nanowires (NWs) are a novel class of nanoscale materials that exhibit exceptional potential as nanocomponents in future electronic and optoelectronic devices. The advancement of II-VI NW-based systems is contingent upon fabricating NWs with precise control over their morphology, crystal structure, composition, doping, and quantum efficiency. Possibly the most promising method for growing II-VI NWs on an industrial scale is metalorganic chemical vapor deposition (MOCVD), which utilizes Au nanoparticles to drive NW growth via the vapor-liquid-solid (VLS) or vapor-solid-solid (VSS) mechanism. This fabrication process allows optimizing several growth parameters, including the growth temperature, the input VI/II ratio, and the absolute flow rates of group II and group VI precursor species. Nonetheless, before II-VI NWs could be integrated in device applications, many growth issues must be addressed. These include kinking and irregular growth directions, tapering of NWs, non-radiative recombinations at lateral surfaces, and crystallographic defects such as twins, stacking faults, and phase mixing between zinc-blende (cubic, 3C) and wurtzite (hexagonal, 2H) structures. But interestingly, the particular growth mode of catalysed nanowires opens opportunities to produce original crystal phases such as 4H or 6H. This is known as "polytypism in semiconductor nanowires".

This thesis explores the growth mechanisms and structural properties of zinc sulfide (ZnS) semiconductor NWs. ZnS has slight differences in cohesive energy between the 3C, 4H, 6H, 15R, and 2H crystallographic phases. Therefore, a modest change in the growth conditions would be sufficient to attain polytypes.

Thus, we applied two different ZnS nanowire growth approaches, namely "VLS assisted" by a liquid catalyst, and "VSS assisted" by a solid catalyst. Transmission electron microscopy analysis revealed that the VSS-grown nanowires exhibit large hexagonal segments with small cubic segments. In contrast, the nanowires catalyzed by an Au-Ga alloyed droplet in the liquid state exhibit an unexpected 15R crystal phase.

We developed a detailed nucleation model to explain the formation of these high order polytypes (4H, 6H, 15R) in semiconductor NWs. We employed a combination of classical nucleation theory, ANNNI model (Ising), and probability calculations to simulate and explain the occurrence of polytypes in ZnS nanowires. This systematic model allowed us to understand the NWs growth mechanism, and as a consequence, we confirmed the validity of our theoretical model with experimental demonstrations.

Finally, we have studied the axial ZnS/ZnSe and core/shell ZnS/ZnMgS heterostructures. We have tackled different challenges inherent to these axial/lateral NW heterostructures. The optical properties of 1D heterostructures were studied using photoluminescence and cathodoluminescence. CL measurements at cryogenic temperature provided insights into vital optical qualities and luminescence from NW heterostructures.

In conclusion, this work aimed to contribute to the achievement of high-quality ZnS NWs and wide bandgap 1D heterostructures. It revealed intriguing polytypic behavior in the development of nanoscale materials. This study can help to control the crystal phase and understand the phenomenon of polytypism in semiconductor NWs.

Dedicated to my grandfather
Sub Maj. Sh. Sri Chand Yadav
1945-2021
Fulfilling his last wish!

&

Dedicated to my best friend
Dr. Yogendra Singh
1992-2022
Left us too early

A special thanks to Dr. Frank Glas, Directeur de recherche, C2N, CNRS, Université Paris-Saclay, for being part of the defense as Invited jury member.

Don’t be afraid of committing mistakes; mistakes lead to great scientific discoveries.[i]

~Vincent SALLET

[i] Quoted every time I made a mistake. Indeed, we found something unexpected from mistakes and a deep thinking helped us to open new opportunity and ideas. This is an excellent example of how chance can drive science.

Acknowledgement

The best part of the thesis is writing acknowledgement and thanking all the people who helped me during my doctorate. First, it is a great pleasure to express my deep sense of thanks and gratitude to my thesis supervisor Dr. Vincent Sallet. His expertise on MOCVD is commendable and his humble attitude allowed me to learn and use freely the MOCVD available at GEMaC. It was never easy to move to a foreign country with all the complicated administration processes, but he has made it so easy for me. He has always been the first person that I can go to in case of any problem (scientific or non-scientific). His timely advice, meticulous scrutiny, scholarly advice, and scientific approach have helped me to a very great extent to accomplish this task.

I would like to thank all the jury members for agreeing to evaluate this work. The reviewers Dr. Jean Luc Maurice and Dr. Edith Bellet-Amalric for agreeing to review this work and for their kind words, encouragement, and suggestions. Likewise, the examinators Dr. Laetitia Vincent and Dr. Vincent Consonni, the president of the jury Professor Jean-Pierre Hermier, and the invited member Dr. Frank Glas. I am very delighted and honored to have you all as a part of this jury.

I would also like to thank my colleagues and collaborators for sharing their scientific experience and expertise that helped me enormously to learn new experimental techniques and their analysis. A special thanks to Dr. Gaelle Amiri, who helped me to operate MOCVD and SEM. We had long interactions via sports (running and badminton), festival celebrations (Christmas, Holi), and cultural discussions. It's now time to thank our rockstar Dr. Frederic Fossard, our collaborator at LEM laboratory. His cheerful nature and expertise in TEM allowed me to learn the concepts of TEM, different imaging techniques, and its deep technical analysis. This thesis work is mostly focused and dependent on the TEM measurements carried out by him. Without him, the discovery of '15R' was not possible. Professor J.M. Chauveau joined our team during my final year of the thesis. His new ideas and eagerness to understand this work helped me to design a new set of experiments that ultimately verified our theoretical modeling results. A big thanks to him for helping us with TEM measurements and the long discussions we had. Dr. Julien Barjon, Dr. Christophe Arnold (diamond team), and Dr. Alain Lusson shared their expertise in optical measurements with me. They helped with cathodoluminescence and photoluminescence experiments and analysis. For the theoretical modeling part, our collaborator Dr. Frank Glas at the C2N laboratory invited us many times for the long discussions and helped us with nanowire modeling. Thanks to my all GEMaC colleagues for helping me out in one or another way.

I would also like to thank the administration and friends at GEMaC. Karen Bremond, Laurence Turpin, and Amel Bach were so kind to help me with all the administration work. Thank you very much Houcem Fourati for helping me with the python coding. Thanks to my friends and office fellows Yogendra Singh, Nour Belmouri, Mamadou Ndiaye, Ismail Madaci, and Mohammed Bouras for the lively discussions, and encouragement, and I was able to learn a lot from all of you.

Thank you Dr. Yogendra Singh for being there for me since 2014. You left too early (died in an unfortunate event on 18th May 2022); Now, I just have your precious memories to live with. You always made my life easier in India and followed it even here in France. I am crying while writing this line, Yogi you will always stay alive in my heart. You left me alone

in this world, it is not the same without you. I love you my brother and miss you every single second. You deserve every single word written in this thesis.

Coming to my lifeline in Paris, I am at a loss of words to thank you all. The lockdown was never easy but I always felt at home with your presence. A special thanks to Mahima Chaudhary for helping me out immensely during my thesis as well as when I suffered from COVID. I can't even express here your efforts and help during the critical period of my thesis. I made numerous close friends and discussed a variety of topics including conferences, politics, and communications. Thanks to Ayush, Ankush, Saurabh, Mihir, Sanket, Amulya, Pragya, Shalu, Saurav, Pranav, Pranjal, Amrut, Abhijit, Irene, Kartik, Shweta, Thea, Sagar, Harsh, Gaurav, Nripesh, Monika, Monica, Maha, Jaya…

The hardest part is to express gratitude for my family and their immense and unaccountable sacrifices. It was not possible to achieve this milestone without your love, blessings, and support at each step. Thanks to my grandparents for believing in the role of education in society and my parents for all the support, dedication, and sacrifices they have made to make me achieve this milestone. To my brother for the amazing childhood memories and for showing me the path to follow and for always believing in me. Thanks to my big extended family Chacha Ji, Chachi Ji, and my cousins for supporting me. Last, but most importantly, my fiancée and best friend Dr. Komalika Rani. She was always there for me since 2010. She witnessed and pursued the same hard work. We grew, flew, and fall together in the last 12 years but stayed motivated because the goal was clear, to get a Ph.D. in Physics. Thanks to her for immense support, love, motivation, and being there on my side. We started our thesis together and wrote it together, yes, we struggled but, in the end, we did it! Now we started working together in the same company. NEVER-ENDING PARTNERSHIP!

Introduction

"There's Plenty of Room at the Bottom"
An invitation letter to enter a new field of Physics
December 29, 1959

In a visionary lecture 62 years ago [1], Richard P. Feynman with his famous classic talk at the California Institute of Technology, foresaw the capability of manipulating matter at the atomic level. With the ability to construct small objects upwards, we will be able to design them more accurately and regulate their behavior and properties. As a result, nanotechnology was born, and it also served as a catalyst for its continued expansion. With the advent of nanoscience and technology around the turn of the century, this prediction came true, and the rest, as they say, is history.

This led to the advancement of nanotechnology as well as its acceleration. Since then, nanoscience and nanotechnology have been the focus of intense research and development on a global scale, both in academic institutions and the corporate sector. Nanotechnology strives to develop structures, devices, and systems with novel and superior characteristics by controlling size and form at the nanoscale scale (10^{-9} m, atomic and molecular scale).

Nanotechnology is concerned with the design of structures, devices, and systems, as well as their characterization, manufacture, and application. The most essential feature of nanotechnology-derived materials is that they have a higher surface-to-volume ratio, which is helpful for a wide range of applications. Another critical component of nanotechnology is the ability to manufacture materials in one dimension (nanowires), two dimensions (nanosheets), or all three dimensions (nanoparticles). This is especially beneficial in goods meant for industrial uses. Various materials have been made and examined in nano-scale structures, and researchers working in this field have uncovered a host of novel properties in the nanomaterials they have discovered.

Very small structures are constructed by etching/milling and reducing the size of the material to µm- or mm using "top-down" methods. They can also be constructed from the ground up, atom by atom or molecule by molecule, utilizing "bottom-up" methods. Semiconductors are incredibly essential due to the vast array of applications they have for human life, and as a result, their nanostructures are of great interest to a significant number of researchers (like us) worldwide.

Semiconducting nanowires (SC NWs) are quasi-one-dimensional nanostructures, having a diameter typically less than 100 nm and an unconstrained length. Due to their quasi-one-dimensional (1D) shape and a large surface-to-volume ratio enable tailoring the material, quantum confinement properties, and photonics applications. For instance, a quantum dot embedded in a nanowire allows the confinement of carriers (electrons and holes) which can be used as a photon emitter for quantum optics. The advancement of SC NW based devices is depending upon the ability to fabricate NWs nanowires with precise control over their shape, orientation, crystal structure, doping, composition, optical properties, and quantum efficiency. In particular, II-VI SC NWs have shown as promising candidates to serve as building blocks in electronic and optoelectronic nanodevices.

Challenges and overview of the thesis

In this thesis, we are interested to explore growth, structural, and optical properties of ZnS nanowires. ZnS is one of the first discovered compound semiconductor and has been widely used in several optoelectronic applications. Most importantly for this study, ZnS offers a very wide range of possible polymorphs (or polytypes). As the electronic structure varies with crystal structure; the achievement of new phases in semiconductors pave the way to novel physics and original applications. Indeed, similar to the case of III-V nanowires, we expect that new ZnS polymorphs would be useful for designing crystal phase heterostructures, bandgap engineering, enhanced thermal and mechanical properties, and direct intersubband optical transitions.

Interestingly, in the case of 1D nanostructures, polytypism can arise due to the particular growth mode below a catalyst droplet, that may induce different stacking sequences along the length of nanowire. Thus, in the light of variety of ZnS polytypes available in the bulk form, the occurrence of different crystal structures is high expected in ZnS nanowires with tuning the growth parameters.

ZnS NWs have been synthesized by various techniques but most of these techniques result in randomly aligned nanoribbons or nanotubes growth. For integrated photonic devices generally straight, vertical nanowires epitaxial with the substrate are typically required. Thus, we aim to carry out experimental studies to grow vertical arrays of ZnS nanowires with controlled morphology, crystal structure, and defects. Indeed, we predict twins and stacking faults (SFs) to easily occur due to a low SF formation energy. For comparison, the experimental intrinsic SF energy in zinc blende is less than 6 mJ/m^2, and 45 mJ/m^2 in GaAs. This gives us the opportunity to exclusively study these SF to identify possible new crystal phases.

Finally, as a wide bandgap semiconductor (3.7-3.8 eV), ZnS offers impressive potential in optoelectronics, and hence its optical properties are of great importance. Especially, it is important to minimize the non-radiative recombination surface effects which adversely affect the optical properties of nanowires.

The biggest challenge is to grow ZnS nanowires with well-controlled orientation, morphology (radial growth and tapering), and a defect-free crystal phase. In this work, we employ the metalorganic chemical vapor deposition (MOCVD) technique using an Au catalyst for ZnS nanowire growth. It offers varying numerous growth conditions, including growth temperature, VI/II ratio, nanowire growth flux, and catalyst composition. This thesis examines these parameters to control nanowire growth and tailor their crystal phases to fabricate suitable ZnS nanowires for electronic and photonic applications. 1D II-VI heterostructures will be targeted.

Keeping the above goals and challenges in mind, this thesis work is presented in seven chapters.

- Chapter 1 aims at introducing the readers to the context, basic concepts, and fundamentals necessary to comprehend the findings of this thesis. First, we provide details of the SC NWs properties, polytypism phenomenon, and nanowire growth mechanisms. In the second part, we focus on the state of the art of II-VI NWs with particular attention given to ZnS material, polytypism, and in-situ TEM studies.
- Chapter 2 provides an overview on the theoretical aspects and experimental techniques employed in this thesis. The first part is devoted to summarizing nucleation theory and the ANNNI model. In the second part, we focus on the description of MOCVD growth and the main characterization techniques.

- Chapter 3 presents the MOCVD growth of ZnS thin films and nanowires. We first grow ZnS layers to understand the MOCVD growth regimes and kinetics. Then, we use various characterization tools (XRD, SEM, and AFM) to assess the layer's structural and morphological qualities. Subsequently, we investigate Au droplet formation on different substrates. Finally, we carefully study the growth parameters leading to the best quality of ZnS NWs in terms of vertical alignment and uniformity.
- Chapter 4 is dedicated to investigating two different ZnS nanowire growth approaches, namely vapor-liquid-solid (VLS) assisted by a liquid catalyst and vapor solid-solid (VSS) assisted by a solid catalyst. We compare the differences in structural properties induced by the two growth modes. Remarkably, VLS grown ZnS nanowires exhibit a 15R crystal phase; highlighted for the first time in nanowires. Finally, the involved mechanisms in VLS as well as VSS cases are carefully discussed on the basis of the knowledge related to III-V and II-VI nanowires.
- Chapter 5 presents a theoretical model based on previously developed nanowire growth models which combine two contributions: i) classical nucleation theory-based nanowire growth dynamics, and ii) probabilistic polytype calculation. At first, we will present and apply Johansson's approach for calculating the probability of formation of the 3C, 4H, 6H, and 2H polytypes in GaAs, and further introduce 15R as another potential crystal phase. In the second part of the chapter, we will extend this model to better describe the surface energies of the developing nucleus at the TPL. The extended model will be applied to GaAs as well as ZnS nanowires.
- Chapter 6 implements our model findings to achieve pure phases (wurtzite, zinc blende, and 15R) in ZnS nanowires. First, we pursue the idea that supersaturation in the catalyst droplet plays a significant role in controlling crystal phases in nanowires. We varied the supersaturation through variation in Zn and S partial pressures and studied the impact on the structural properties of ZnS NWs. In a second part, we emphasize how the composition of the catalyst particle may change the growth mechanism and consequently the crystal phase of the growing nanowire.
- Chapter 7 provides optical studies of our grown materials using photoluminescence and cathodoluminescence. We start with thin films, ZnS, $Zn_xMg_{1-x}S$, as well as ZnSe (zinc selenide), which is the chosen material to investigate the growth of heterostructures. Subsequently, we carry out CL on single ZnS nanowires. The benefit of coating the NW with a $Zn_xMg_{1-x}S$ shell is emphasized. Finally, ZnS/ZnSe axial heterostructures are investigated. This latter case will correspond to preliminary studies since we faced difficulties in the preparation of the samples

Finally, we conclude this thesis with general conclusions and prospects.

Table of contents

Chapter 1

Basic concepts and state of the art

Contents

This chapter aims to provide a general introduction to the topic of semiconductor nanowires (NWs) and applications. First, we detailed the particularities of II-VI semiconductors, phenomenon of polytypism, and NW growth mechanisms. In the second part, we provide detailed state of the art focusing on II-VI NWs, with particular attention given to ZnS material.

1.1 Semiconductor nanowires

The topic of NW growth has been around since 1964, when Wagner and Ellis first employed the vapor-liquid-solid (VLS) mechanism to interpret the growth of gold-catalyzed Si whiskers [2]. Givargizov [3] pioneered the theoretical foundations for VLS growth in 1975, when he recognized the essential principles of whisker growth. However, it wasn't until the mid-1990s that Prof. K. Hiruma's group at Hitachi in Japan created the first III-V nanowhiskers [4,5] with a p-n junction [6]. At the end of the decade, Lieber et al. [7] emphasized that the NW geometry and the VLS provide a unique environment to elemental and compound semiconductor growth. As a result, the fundamental properties of these materials were different from traditional thin film or bulk crystal growth techniques. Nanowires are a beautiful example of nanotechnology, and they were termed "nanowires" due to the reduction in their diameter throughout the years. In the past two decades (2000-2020), enormous development and maturity have been witnessed in this research. A historical timeline of the milestones and breakthroughs in the NW field is given in Figure 1.1, adapted from the reference [8].

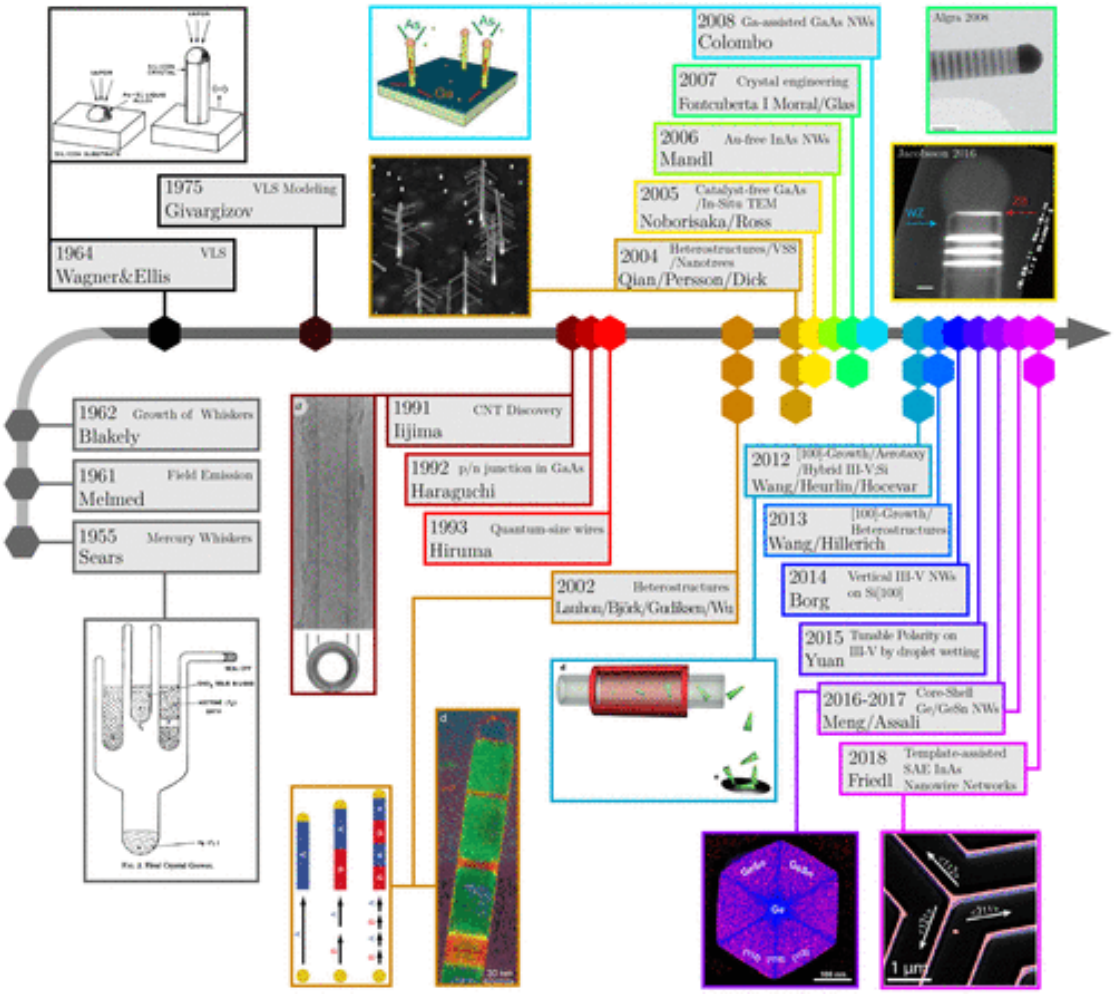

Figure 1.1: Historical timeline of breakthroughs in the NW field. Adapted from ref [8].

The distinct shape of NWs provides substantial advantages over traditional planar systems. If the diameter of the nanowire is small enough, smaller than the Bohr radius, their quantum mechanical properties tend to emerge and demonstrate quantum confinement in two dimensions. The high surface-to-volume ratio of nanowires makes them exceedingly sensitive to charges surrounding the wire surface, influencing the optoelectrical properties and making

them suitable for a wide range of applications, notably sensing applications. Furthermore, NW materials have been grown with different crystal structures and superior properties with respect to the bulk [9–11]. These superior properties of semiconductors inspired research on the synthesis of nanowires in many different materials systems [12]: there is an extensive range of compounds from single elemental semiconductors such as Si [7,13] and Ge [14,15], III−Vs [11,16–21], II−VIs [22–26], IV-IVs [27,28], IV-Vs [29] and II-Vs [30,31].

Semiconductor nanowires have enormous potential as critical components of future technologies and platforms. These nanostructures are promising nano-building blocks because they have low dimensionality, excellent material properties, and the capacity to be assembled from the bottom up. A plethora of nanowire-based electronic and photonic devices have already been developed, including nanowire solar cells [32,33], light-emitting diodes [34–36], quantum dot single-photon sources [37–40], lasers [41,42], Majorana physics [43,44], photodetectors [45,46], highly sensitive biological and chemical sensors [47,48], etc.

The semiconductor industry has had tremendous success due to the application of bandgap engineering. When the chemical composition or crystal structure of the layers in a layer stack is regulated on a spatial scale, the electrical properties of a layer/heterostructure stack can be precisely controlled. Furthermore, nanowires can be tailored to produce different axial and radial heterostructures, greatly expanding the spectrum of device applications that can be realized with these materials. Aligning materials of different bandgaps forming heterostructures results in internal fields that can localize, store, separate, and displace carriers. The particular and attractive novelty with the nanowire geometry is that heterostructure formation can occur in two dimensions, illustrated in Figure 1.2 and 1.3. In this specific morphology, the strain can relax more effectively, providing the setting for novel heterostructures. Strain relaxation is more effective for axial than radial structures [49]. In addition, systems of lower dimensionality (0-D or 1-D) such as quantum wells and quantum dots can be embedded in the nanowire geometry to increase the functionality (see Figure 1.2 and 1.3).

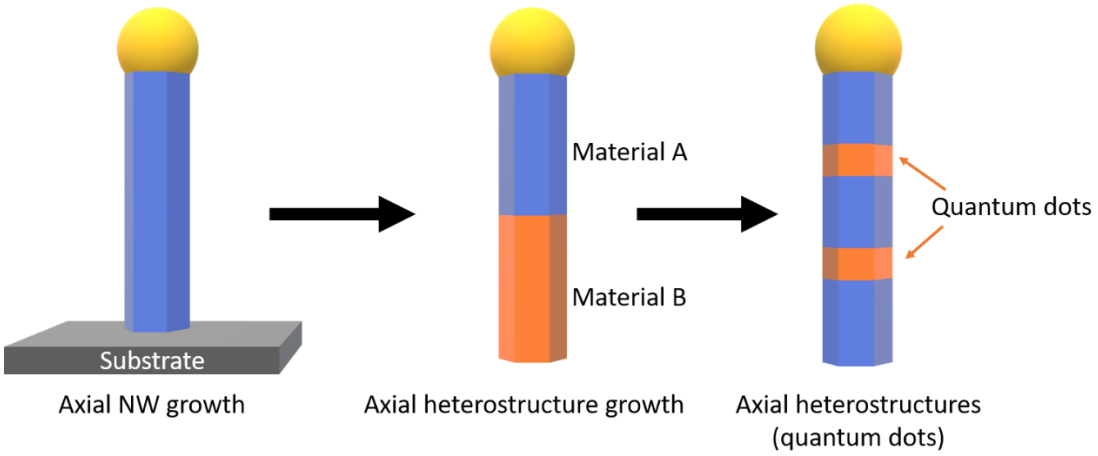

Figure 1.2: Schematic diagrams of axial heterostructure and quantum dots embedded in a nanowire geometry.

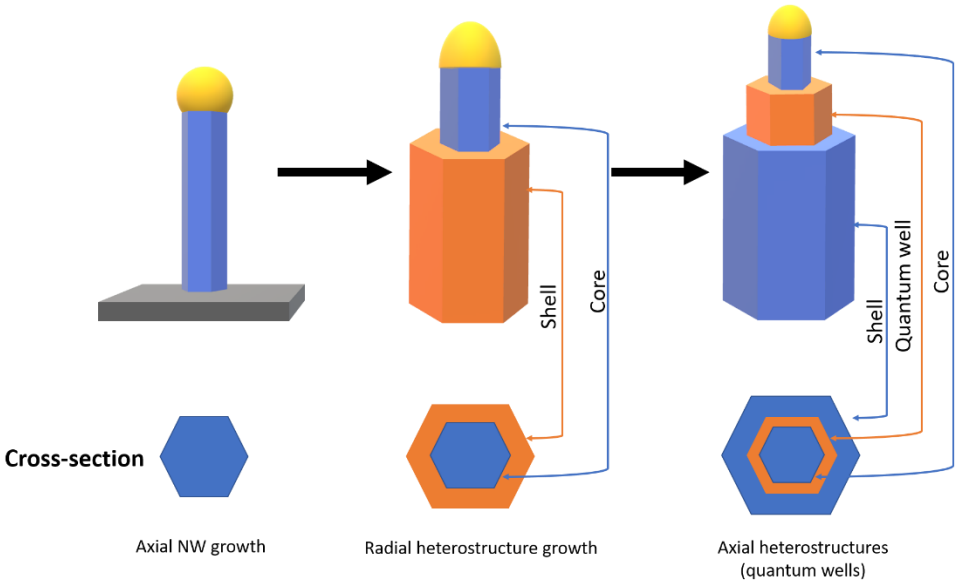

Figure 1.3: Schematic diagrams of radial heterostructure and quantum well embedded in a nanowire geometry.

The crystal phase engineering of NWs opened up a new area of research [21,50]. Interestingly, semiconductor NWs adopt remarkably different stable crystal phases in contrast to their bulk form (except for highly ionic crystals such as SiC, ZnO, GaN, or when using heavy doping [51–56]). As an example, GaAs NWs are found both in zinc-blende (bulk phase) and wurtzite structure [11]; more recently, Si and Ge NWs have been synthesized in the hexagonal form [57–60]. The hexagonal or wurtzite structure results from modifying the stacking sequence along the [111] or [0001] direction. The stacking modification can be engineered to form intermediate polytypes and twining superlattices, opening possibilities for controlled crystal phase quantum dots [17,21,61].

1.2 II-VI semiconductors

II-VI semiconductors refer to compounds of a metal from either group 2 (IIA) or 12 (IIB) (II = Zn, Cd, Hg, or Mg) of the periodic table, and a nonmetal from group 16 (the chalcogens, VIB = O, S, Se or Te). Group II elements have two valence electrons in the outermost s shell, while group VI elements have six valence electrons in total, two in the *s* shell and four in the *p* shell. Group-II elements donate their two electrons to group-VI elements (anion) to generate II-VI semiconductor materials via sp^3 hybridization of molecular orbitals. Interaction between these orbitals results in a periodic crystal structure that is typically either zinc-blende (ZB) or wurtzite (WZ) phase.

ZnS, ZnSe, ZnTe, CdTe, and other alloys such as CdZnTe, CdMnTe, and ZnMgTe all have a stable zinc-blende crystal structure in bulk. This structure is composed of two face-centered cubic lattices, one of which is composed of element II atoms and the other of which is composed of element VI atoms, separated by 1/4 of the distance along the <111> direction. However, II-VI compounds can also crystallize in the metastable WZ phase when grown in particular conditions.

The stacking sequences for the ZB [111] and WZ [0001] directions are depicted in Figure 1.4. The main difference between them is a difference of $\pi/3$ rotations in their tetrahedrons. The ZB atomic layer sequence is ABCABCABC (with the C plane rotated by $\pi/3$ relative to the A plane), whereas the WZ is composed of tetrahedral atoms stacked in the

ABABAB sequence. According to the convention, the surface with the II-element on top is designated as (111)A, while the surface with the VI-element on top is defined as (111)B. The same convention is followed for III-V materials. For example, GaAs (111)A surface ends with Ga atoms and GaAs(111)B with As atoms.

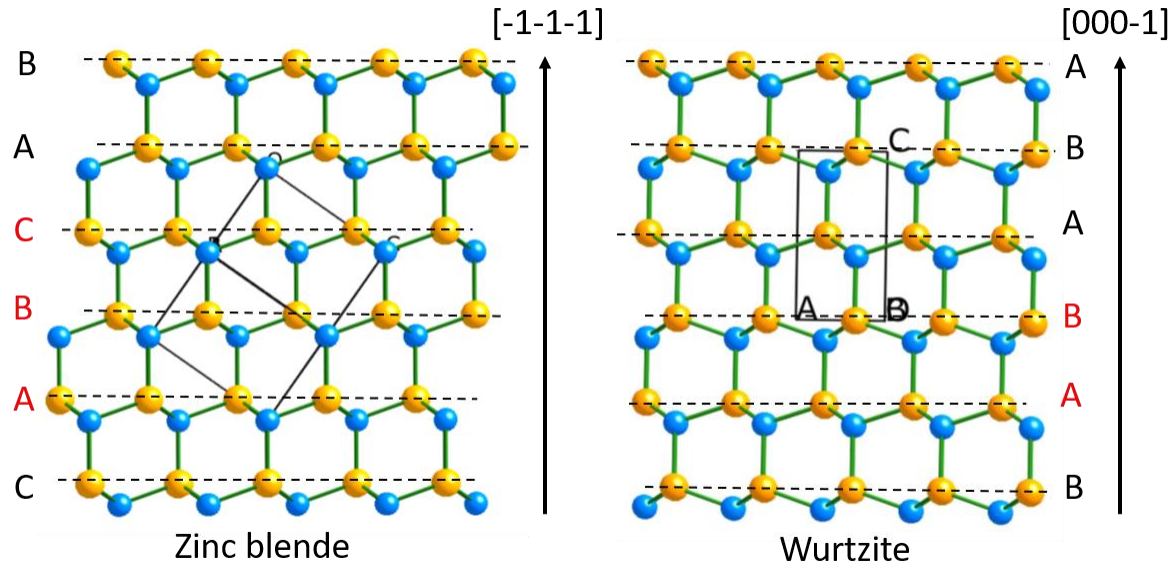

Figure 1.4: Zinc blende (ZB) (zone axis [-110]] and wurtzite (WZ) (zone axis [-110]) stacking sequences along the {111} and {0001} direction.

Understanding and controlling the crystal phase in NWs is a topic of interest in the scientific community since the electronic band structure of the materials depends on their crystal phase. Remarkably, the co-existence of these phases (polytypism) is frequently observed in NWs, and it would pave the way to original crystal phase engineering in NWs.

As we underlined in the introduction to the synthesis, research on II-VI semiconductors remains very intense due to the variety of materials available and their applications. The diagram representing the lattice parameter as a function of the bandgap energy clearly illustrates the potentialities in optoelectronics (see Figure 1.5). The wavelength range covered by II-VI is very wide, from infra-red (with CdHgTe, HgTe even being a semimetal) to UV (ZnS at 3.8 eV) passing by the visible (CdTe at 1.6 eV used in commercial solar cells, ZnSe for emission in the blue-green). By adjusting the composition of the alloys, for example, in the (Zn, Mg, S, Se) system, it is possible to play on the lattice parameter of the heterostructures epitaxially grown on GaAs, and to reduce the stresses. Most of the II-VI semiconductors have a direct bandgap. The energy of the exciton is often high (ZnS 36 meV, ZnSe 21 meV, ZnO 60 meV), opening possibilities of excitonic transitions to the ambient.

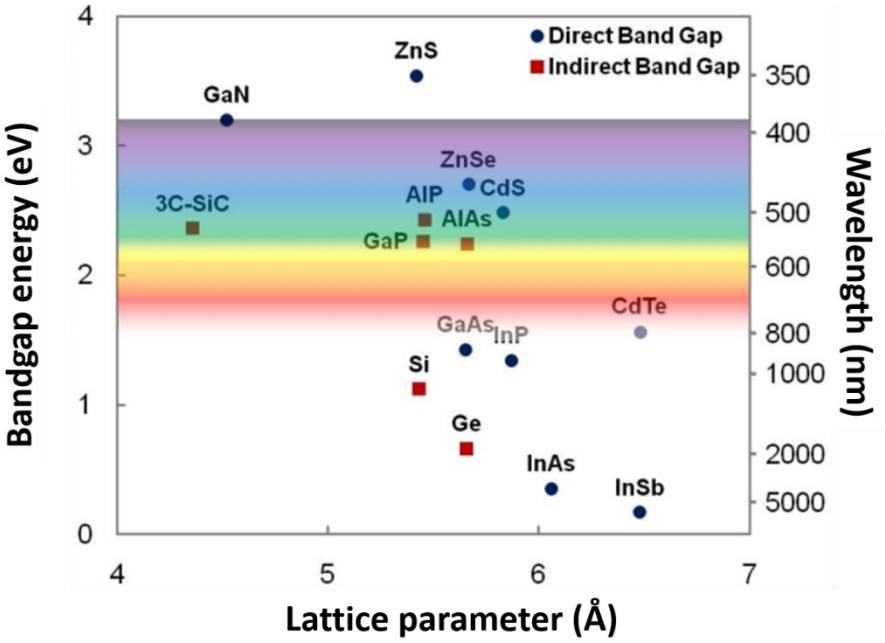

Figure 1.5: Band gap energy at T = 4K as a function of the lattice parameter for different II-VI, III-V, IV-IV semiconductors. Adapted from [62].

Bulk crystals and thin films based on II-VI materials have in the past given rise to numerous devices, some commercialized, for the detection and emission of light, old cathode ray screens, laser windows, etc. Regarding fundamentals, studies have primarily concerned semi-magnetic semiconductors such as CdMnTe or ZnMnTe [63], with the downside of a shallow Curie temperature (of the order of some Kelvin for CdMnTe). In the form of nanostructures, we will mention the CdSe nanoparticles (Qdots), sold commercially and widely used for single-photon emission and quantum cryptography studies. Concerning II-VI nanowires, there is relatively little work given the potentialities offered, apart from the ZnO nanowires. In the field of II-VI nanostructures, ZnO is a bit like "the tree hiding the forest".

1.3 Polytypism in semiconductors

1.3.1 What are polytypes?

Polytypes are simply different stacking sequences of identical layers. Considering the structure of semiconductors, they can be thought of as layers stacked parallel to the [111] direction. Each layer can adopt one of two orientations (see Figure 1.7), irrespective of its neighbors, while maintaining the tetrahedral coordination of each atom. Thus, n layers can be stacked in 2^{n-1} different ways, forming 2^{n-1} different polytypes. Because each layer has just two orientations, a layer can be expressed by a + or – sign (pseudo spin, explained later in the thesis), and then sequences such as + + – – + + – – written out [64].

There is a clear need for a concise notation to facilitate the discussion of such structures, and two of them are discussed here. The first, due to Ramsdell [65], describes the number of layers before a stacking sequence repeats, and then the symmetry of the crystal — cubic, hexagonal, or rhombohedral. In this notation, the above structure (+ + – – + + – –) would be called ‘4H’. The repeat period of four is apparent, and the hexagonal symmetry arises from consideration of this particular lattice. A more precise notation is Zhdanov [66], which describes the number of layers before the orientation is reversed. In the above example, with two layers stacked one way, then two the other, the symbol ‘<22>’ or simply ‘<2>’ would be

used. Table 1.1 names the most common polytypes. The difference in the apparent repeated distances between the Zhdanov and Ramsdell symbols arises because the Ramsdell symbol describes the repeat distance along the c axis, whereas the Zhdanov symbol represents it in layers. Thus, in the case of <23>, or 15R, after one unit, that is five layers, there is a shift in the [1-10] direction for another two units, giving rise to 15 layers (3 units×5, more on this in Chapter 4) [67].

The ZB and WZ structures are the most common crystal forms of semiconductor compounds. Several binary semiconductors such as SiC, ZnS, CdS, and CdSe can be grown in either state. To repeat, the crystal construction can be thought of as a series of stacked levels, with each layer having a choice of two possible orientations (see Figure 1.6). Thus, there is an infinite number of structures (see Figure 1.7), or stacking sequences, in which SiC and ZnS could form, and each of these is called a polytype [68,69].

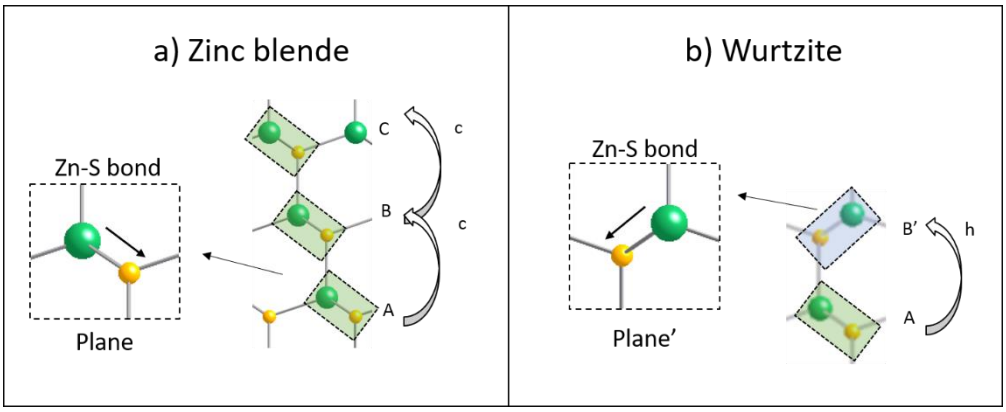

Figure 1.6: The two possible orientations of Zn-S bonds in a) Zinc blende (*c* represents cubic stacking, b) Wurtzite (*h* represents hexagonal stacking).

WZ-ZB polytypism is a well-known phenomenon that shows minimal structural differences and slight differences in the inter energies (about 20 meV/atom) of the atoms [70]. Despite these structural similarities, the spectroscopic properties of WZ and ZB can be quite different: for example, the band gaps of SiC in the WZ and ZB forms are 3.33 and 2.42 eV, respectively, and their phonon frequencies exhibit significant systematic fluctuation [71].

Polytype stacking	Ramsdell symbol	Zhandov notation	Other names
..+ + +.. (..ABC..)	3C	< ∞ >	Cubic, Zinc blende
+ + – – (ABCB)	4H	< 2 >	
+ + + – – – (ABCACB)	6H	< 3 >	
+ + – – – (ABCBA)	15R	< 23 >	
+ – (AB)	2H	< 1 >	Hexagonal, Wurtzite

Table 1.1: The notation used for different crystal structures and stacking sequences.

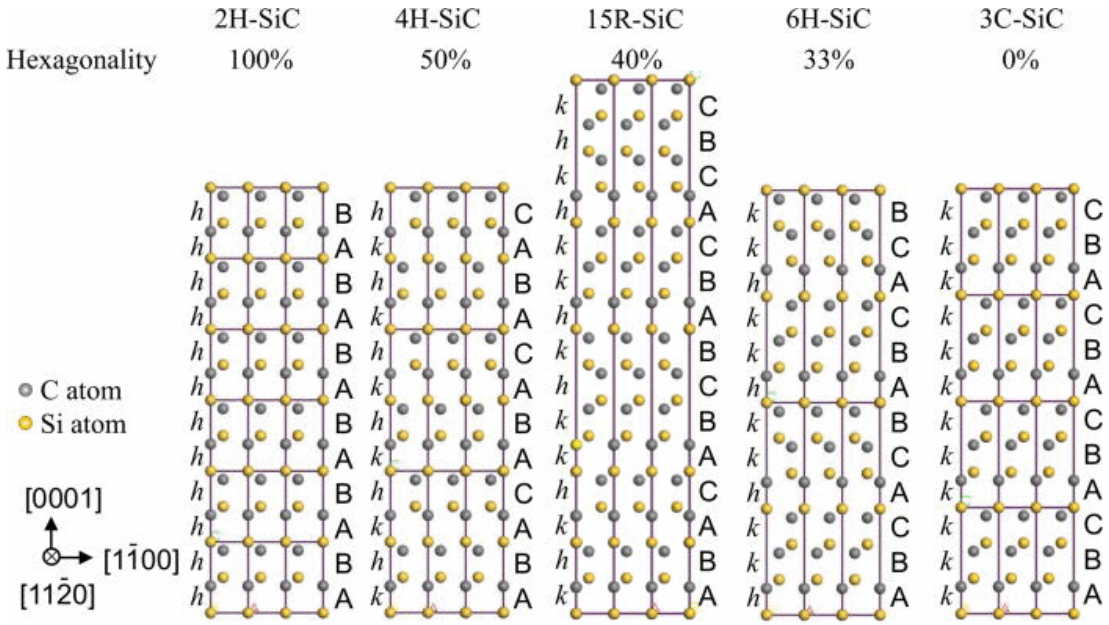

Figure 1.7 Crystal structure of 2H, 3C, 4H, 6H, and 15R SiC. The stacking sequences are described in *hk* notation [72] and ABC notation. Adapted from [73].

Even though various polytypes have been discovered experimentally, it is still unclear whether they represent thermodynamically stable phases under the conditions of their fabrication, or whether they are simply growth processes in their early stages of development. In addition, impurities may also be important in stabilizing certain polytypes. Because the nearest–neighbor environment of each atom is independent of the polytype, the physical properties of the polytypes would be expected to be very similar. This is indeed the case for densities and bulk moduli [64]. However, electrical characteristics are highly dependent on crystal symmetry and vary significantly amongst polytypes [71]. Some proposed mechanisms such as dislocations [74], phonon stabilization [75], and "frozen in" surface effects [76] might assist the formation of polytypes.

1.3.2 Polytypes in semiconductor nanowires

Remarkably, in the case of 1D nanostructures, polytypism can arise due to the particular growth mode below a catalyst droplet that may induce different stacking sequences along the nanowire. In semiconducting NWs, a high density of randomly distributed twin defects and stacking faults has commonly been observed [17,24], as well as random mixtures of cubic and hexagonal phases [77]. However, the stacking faults can be correlated [78] and form ordered arrays until giving rise to new phases (polytypes) with distinct properties [79]. Hence, 4H, 6H, 8H, and 10H (so-called high order polytypes) have been observed in Ge, Si, GaAs, InAs, and ZnS nanowires [80–83].

1.4 Growth mechanism of semiconductor NWs

The formation of NWs can be achieved in two fundamental ways: top-down and bottom-up approaches. First, the top-down technique requires a high-quality bulk material from which it is possible to selectively etch the material and shape the final structure. To make this technique viable, the material must be transformed into a 1-D structure recycling the wasted part. Also, the impact of etching on exposed surfaces must be managed, otherwise it can damage the

intrinsic material quality. The top-down method has been utilized successfully to construct NW structures that improve device performance [84,85] and show additional capabilities [86]. However, this technology is limited in that it can only be utilized with materials and material combinations that already exist in bulk form.

The bottom-up technique starts with a disordered starting material assembled or grown under the appropriate circumstances, such as reactants, temperature, and pressure. Bottom-up synthesis of semiconductor NWs has created new opportunities for nanofabrication and the design and realization of various devices. Crystal growth means the evolution of a solid from vapor, liquid, or solid phase resulting in nucleation and subsequently resulting in the formation of a crystal. A primary reason for fabricating NWs is the inherent advantages of self-assembly, which enables the NWs to develop without any top-down method, resulting in potentially ideal, unaffected surface and material properties. The most often utilized methods for NW synthesis can be classified as: i) seed particle aided (where the seed is frequently liquid or solid), also known as vapor-liquid-solid (VLS) and vapor-solid-solid (VSS) growth, or ii) selective area growth, which utilizes growth rate variations between distinct crystal facets. Seed-driven growth is a technique that uses a metallic nanoparticle (catalyst) to promote the growth of NWs along with the specific crystal orientation of the semiconductor material.

1.4.1 Vapor-liquid-solid (VLS)

The use of a metal seed to form an elongated semiconductor crystal dates back to the 1960s (almost 60 years back, Wagner and Ellis at Bell laboratories first demonstrated that adding gold particles to a silicon wafer with its surface orientated in [111]-direction may generate silicon rods [2]. With increasing temperature and a silicon-containing precursor gas, a gold-silicon eutectic alloy was formed on the wafer surface. The supersaturation of the alloy caused extra silicon to be deposited at the interface between the Au-Si droplet and the substrate, forming a monolithic silicon rod perpendicular to the wafer surface. This growth mode is called vapor-liquid-solid (VLS).

Figure 1.8 shows a schematic of NW growth assisted by a metal seeded VLS mechanism. The seed particle can first react with the substrate or semiconductor above the eutectic temperature to form a liquid metal-semiconductor alloy. For example, the eutectic temperature for Si NW growth with Au-Si alloy as catalyst occurs at about 360° C. As species from the gas phase diffuse into the Au alloy nanoparticle, this latter becomes supersaturated, and crystal nucleation occurs at the liquid alloy/substrate contact. The crystal gets elongated beneath the particle, creating a nanowire as reactants are supplied. The direction of nanowire depends on total system free energy and particle/substrate interface free energy. Chapter 2 will describe the nanowire growth dynamics using the classical nucleation theory.

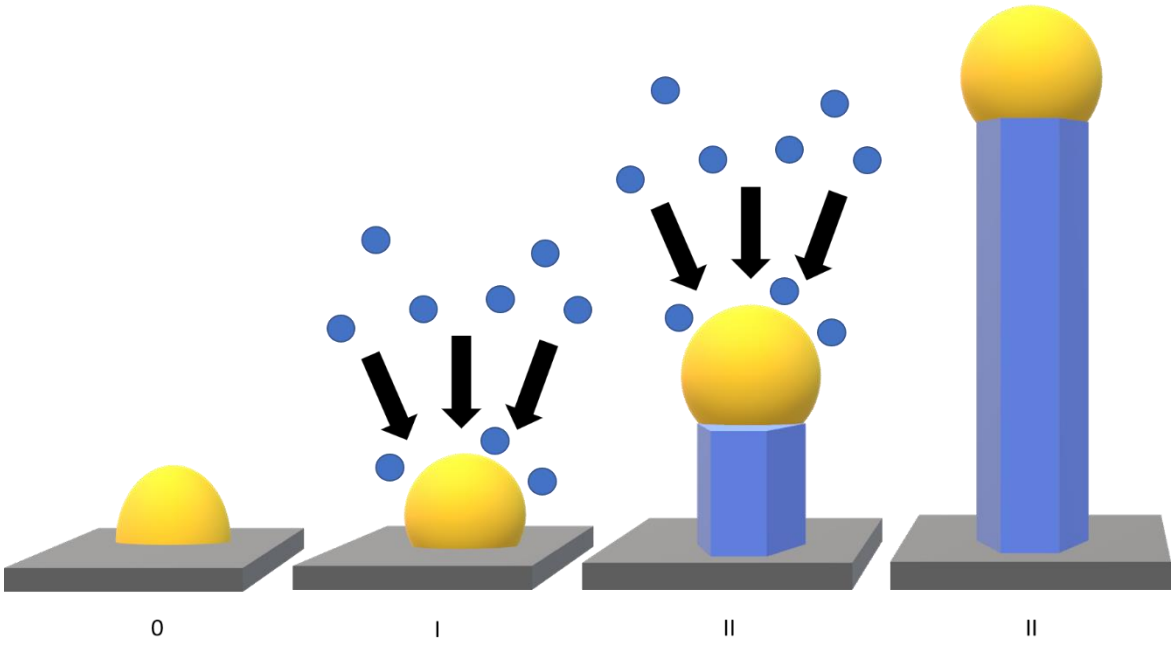

Figure 1.8 Schematic of VLS NW growth. The growth starts with the formation of a gold seed on the substrate (0), followed by liquid seed-semiconductor alloy (I), and progresses toward the desired NW (II and III).

Gold is the most employed metal in VLS as it does not oxidize, and it facilitates the decomposition and gathering of many precursors. However, gold is incompatible with CMOS technology. Gold leads to deep traps in silicon, causing damages in the electronic properties even at very low concentrations [87]. In the absence of Au in Si technology, what makes a metal a suitable catalyst for VLS or VSS growth? The following factors should be considered when selecting a catalyst: (i) precursor solubility in metal, (ii) catalyst solubility in the material to be grown, and (iii) catalyst surface tension. The thermodynamic phase diagram of the two (metal-semiconductor) will determine the temperature range at which VLS and/or VSS can occur. The thermodynamic phase diagram also provides information on the solubility of the supplied elements.

Other foreign metals such as Cu [88], Ag [89], Sn [90], Al [91], and Ni [92] have also been used in the growth of semiconductor NWs. Alternatively, with VLS self-assisted growth, one can utilize an element composed of the grown material. For example, Ga assisted GaAs and GaP NW growth. Unlike Au seeded growth, no contaminants are expected to be incorporated from the self-assisted catalyst, and the catalyst can be consumed to change growth mode from axial to radial [93].

The droplet and its reservoir effect provide a significant barrier to the development of precisely abrupt surfaces (or memory effect). Assume we grow a NW of material A and wish to switch to material B to create a heterostructure. If material A is accumulated in the droplet at the time of the switch and the wire continues to grow, a compositional gradient zone will form. How quickly material A is purged from the droplet determines the thickness of this zone and thus the junction abruptness. One can think about using a solid catalyst to suppress this reservoir effect.

1.4.2 Vapor-solid-solid (VSS)

A slight variation to the VLS method consists of the VSS method [91,94–98]. The mechanism is primarily identical to VLS, the only difference being that the metal droplet stays solid during the whole process. For example, if the metal-semiconductor eutectic temperature is greater than the NW growth temperature, the seed will remain crystalline during the growth process. In general, for a given substance, its solubility in a solid is much lower than that in a liquid. The low diffusivity of the impinging species results in a bit slower nanowire growth. The main advantage of VSS is the possibility of obtaining sharper heterostructures, potentially down to the monolayer accuracy.

In the in-situ growth experiment by Wen et al. [95], sharp interfaces (~1 nm for a NW diameter of 17 nm) were obtained for Si-Ge nanowires. Finally, Rueda-Fonseca et al. investigated the VSS growth mode for II-VI semiconductors by putting a buffer layer of the same material on the substrate to prevent the Au-seed from interacting with the substrate, forcing the seed to be solid [26].

1.4.3 Nanowire side-facets

Figure 1.9 illustrates the possible NW side-facets, reproduced from [99]. In hexagon form, WZ NWs have either six {11-20} side-facets, or six {1-100} side-facets. The {11-20} and {1-100} surfaces are non-polar, and the NW cross-section is hexagonal with six faces of equal length (Figure 1.9a-b). ZB NWs can exhibit a wider range of morphologies. ZB NWs can be composed of truncated octahedral segments, each with three {1-1-1}A and three {-111}B side-facets. Each octahedral segment is bounded by a twin plane above and a twin plane below, such that each octahedral segment has a crystal structure rotated $\pi/3$ around the [-1-1-1] growth axis compared to the adjacent segments. This structure is illustrated in Figure 1.9c. Like WZ nanowires, ZB nanowires can have hexagonal cross-sections with either six {1-10} or six {11-2} side-facets, as shown in Figure 1.9a-b. Note that the {1-10} ZB and {11-20} WZ families are crystallographically parallel, as well as the {11-2} ZB and {1-100} WZ families.

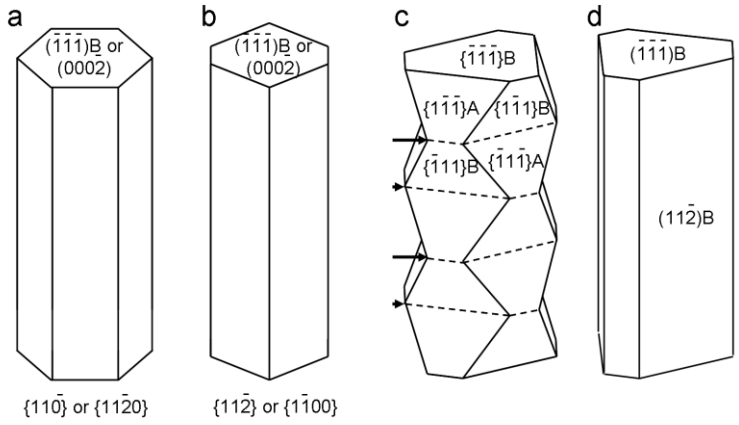

Figure 1.9 Schematics illustration of possible nanowire side-facets, a) hexagonal cross-section with six six {1-10}/{11-20} side-facets, (b) hexagonal cross-section with six {11-2}/{1-100} side-facets, (c) Octahedral segments with {111}A and B faces, the dotted lines with arrows indicate twin planes, (d) near triangular cross-section with three dominant {11-2}B facets and three smaller {-1-12}A facets. Adapted from [99].

1.5 Review and state of the art

This section will review the recent advances in II-VI semiconductor NWs. Additionally, each chapter may contain complementary information on state of the art in this thesis.

1.5.1 Overview of II-VI nanowires

Since the discovery of phosphorescence in ZnS crystals in 1866, II-VI semiconductors have been the subject of extensive research starting from the 1920s and continuing to the present. As a result of the continued success and rapid development of NWs over the past two decades, II-VI compound nanowires have received considerable attention to developing novel optoelectronic devices. This has been attributed to their excellent optical and electric properties, superior to their bulk counterparts [100–105]. However, II-VI NWs are still not as well developed as III-V NWs except in the case of ZnO.

The unusual optical properties of vertically aligned nanowires (NWs), including efficient light absorption, wavelength selectivity, light confinement phenomena, and spectral responses over a wide range of wavelengths, are crucial for photonics applications. Here, we will focus on the recent studies of vertical aligned VLS and VSS growth of II-VI NWs. Figure 1.10 gathers the VLS and VSS growth of ZnTe, ZnO, CdTe, and ZnSe NWs.

ZnTe NWs

Hajer et al., in their recent study, combined selective area and VLS growth of ZnTe NWs on GaAs (111)B substrates using molecular beam epitaxy (MBE) [106]. They have reported a pure ZB crystal phase for their NWs (see Figure 1.10i). Interestingly, their EDS mapping shows a significant Zn inside the catalyst droplet and is nearly free of Te. Rueda et al. introduced a ZnTe buffer layer on GaAs substrate to grow ZnTe NWs with a VSS growth mode (see Figure 1.10ii) [26]. Their NWs reported two geometries of NWs: i) cylindrical-shaped WZ NWs, and ii) cone-shaped ZB NWs. The NWs follow the (111)B polarity, i.e., Te-terminated. Interestingly, they have found Te-rich condition favors NW growth (specially ZB), while Zn-rich suppresses it.

ZnO NWs

Coming to the case of ZnO, Sallet et al. reported opposite crystal polarities for VLS (O-polar) and spontaneous (Zn-polar) growth of ZnO NWs [107]. In their case, they have also reported a better vertical yield in O-rich conditions (see Figure 1.10iii). Subannajui et al. reported the ZnO NW growth based on VS mechanism on GaN substrate [108]. Like most ZnO NWs, their VS grown NW adopt a WZ (c-orientation) structure (see Figure 1.10iv), but they have observed a non-polar a-oriented growth for NWs grown with ionic liquid assisted growth technique. The change in orientations results in the improved defect density observed through photoluminescence (PL).

CdTe NWs

Au catalyzed growth of CdTe NWs using MOVPE has been reported by the group of Lovergine [109]. They have deposited a thick (2 μm) CdTe buffer layer on GaAs (111)B substrates followed by Au nanoparticles. First, they supplied Te to reach a eutectic temperature for the Au-Te system (447 °C), then Cd atoms entered the liquid Au-Te droplet to grow CdTe NWs by the VLS mechanism. However, they have considered the possibility of a high Cd concentration inside the droplet that can increase the melting point of the ternary alloy, resulting in a VSS growth or combined VLS and VSS.

ZnSe NWs

Bellet-Amalric et al. reported the growth of ZnSe NWs using a solid Au catalyst (see Figure 1.10vi) [110]. They have observed the presence of two monolayers (MLs) high steps at the Au/NW interface, and recently their group presented the in-situ study following a two MLs step during the VSS growth [111]. Furthermore, they have reported an abrupt interface (less than 1nm thick) between the ZnSe and the CdSe quantum dot, allowing high confinement of the excitons. Zannier et al. reported VLS growth of ZnSe NWs on GaAs (111)B substrates [112]. Interestingly, their NWs follow the VLS growth mode using an Au-Ga alloyed catalyst under Zn rich conditions, while Se rich conditions switch the growth mode to VSS (see Figure 1.10vii). The two growth mechanisms highly impact the morphology and crystal quality.

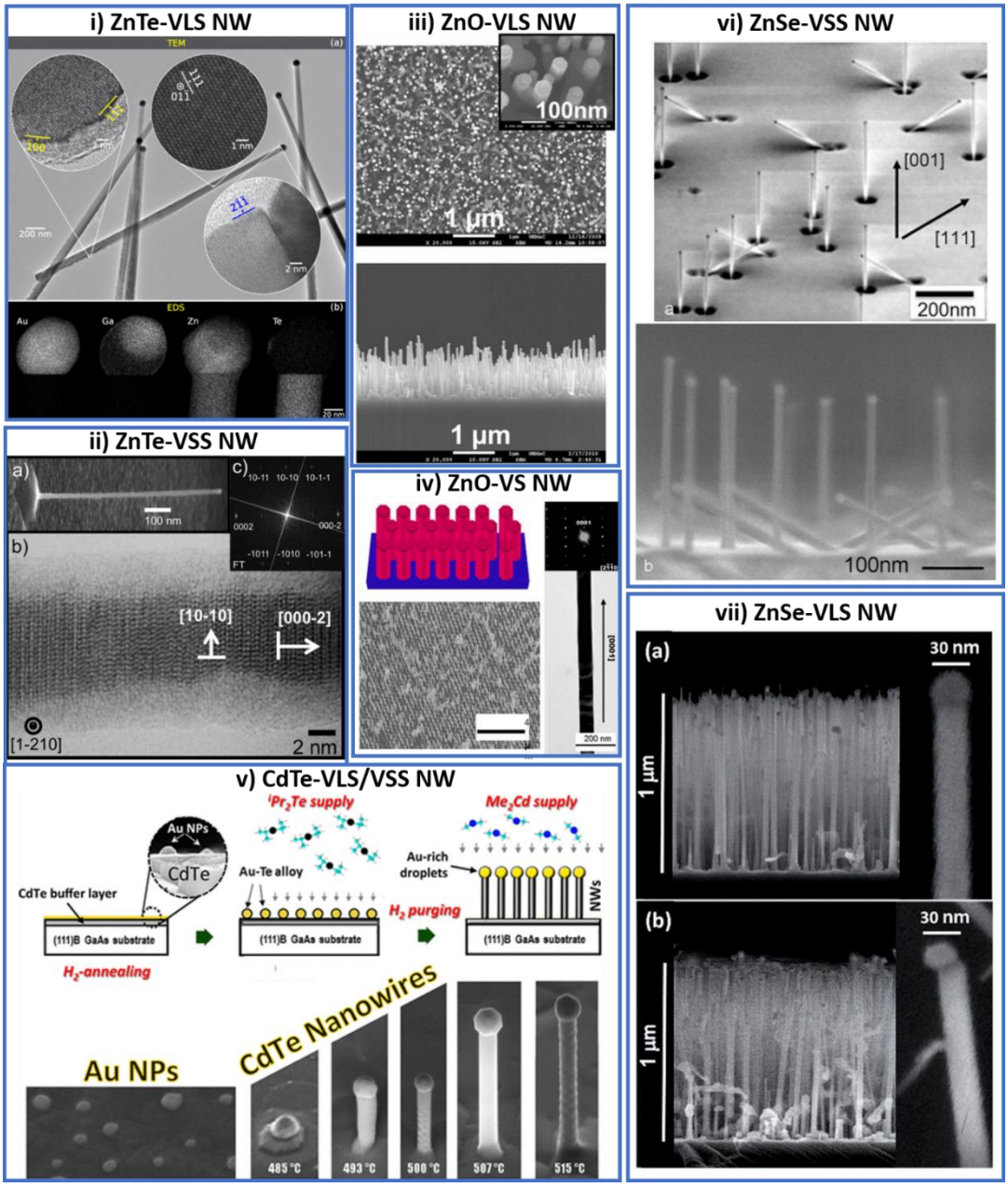

Figure 1.10: The vertical aligned NWs of II-VI semiconductors, i) ZnTe-VLS NW growth [106], ii) ZnTe-VSS NW growth [26], iii) ZnO-VLS NW growth [107], iv) ZnO-VS growth [108], v) CdTe-VLS/VSS growth [109], vi) ZnSe-VSS NW growth [110], and vii) ZnSe-VLS NW growth [112].

To conclude, we have provided some examples of the VLS and VSS growth for different II-VI compound NWs. We tried looking for vertical aligned CdS and CdSe NWs grown with VLS or VSS growth mode, and to the best of our knowledge, we didn't find conclusive articles reporting the straight homogenous vertical growth of NWs for these two compounds. However, catalyst free van der Waal epitaxial growth of vertically CdS and CdSe nanowire has been reported [113].

1.5.2 The particular case of ZnS NWs

This thesis focuses on the particular case of ZnS NWs growth. There have been a variety of techniques used to synthesize ZnS NWs, including the solvothermal approach [114], molecular beam epitaxy (MBE) [115], solid-state reaction [116], hydrothermal route [117], and MOCVD [82,118,119]. A lot of ZnS NWs were grown by using vapor phase transport (VPT) in a tube/furnace (often horizontal) with ZnS powder source [24,120]. However, most of these techniques result in the growth of uncontrolled randomly aligned nanowires, nanoribbons, and nanotubes. Even though ZnS has outstanding optical responses, this constitutes a significant hurdle to its use in the intended application. And even if substantial progress has been made in the controlled synthesis of semiconductor NWs due to multiple research efforts, the ability to control the growth direction, diameter, length, and crystal phase of ZnS NWs has not been fully developed. As shown in Table 1.2, we gathered references that reported the VLS development of ZnS NWs employing a variety of catalysts, growth methods, substrates, and preferred crystal structure preferences. Many research groups have attempted to develop ZnS NWs on Si substrates using an Au catalyst to explore the optical characteristics of the materials. It is worth noting that the WZ phase has been more often observed for ZnS NWs than ZB. In particular, the MOCVD development of ZnS NWs on GaAs (111)B substrates demonstrates a promising potential for increasing the vertical yield of the NWs [121,122].

Growth Method	**Catalyst/Substrate**	**Diameter**	**Crystal Structure**	**Ref**	**Verticall y aligned**
Thermal Evaporation	Au/Si wafers	30-60 nm	WZ	[120]	No
Thermal Evaporation	Au/Si wafers	100 nm	WZ/Heavily faulted	[123]	No
Thermal Evaporation	Au/Si	10-20 nm	ZB	[116]	No
MOCVD	Au/SiO2-Si	20 nm	ZB	[117]	No
Laser ablation	Au/Si	30 nm	8H/10H/Heavil y faulted	[124]	No
Thermal Evaporation	Au/Sapphire (0001)	>100 nm	WZ	[118]	No
Tube furnace	Au/ZnS wafer	50-100 nm	WZ	[125]	Yes
Thermal Evaporation	Au/Si	80-100 nm	WZ	[119]	No
Pulsed laser vaporization	Au/Quartz/Si	50-200 nm	WZ	[126]	No
A simple vapor deposition	Au/Si (111)	50-100 nm	(ZnS/Eu^{2+})/WZ	[127]	Yes
Horizontal tube furnace	Au/Si (100)	60-100 nm	Periodic twinning/ WZ	[128]	No

Horizontal tube furnace	Sn/Alumina Plate	20-100 nm	WZ	[129]	No
MOCVD	Ag-Au/GaAs (100, 110, 311A, 111B)	30-80 nm	WZ/Heavily faulted	[121]	Yes
MOCVD	Ga/GaAs (111)B	80-200 nm	ZB/stacking faults	[122]	Yes
Vapor Phase transport	Au/Sapphire	20-100 nm	WZ	[130]	No
MOCVD	Ag2S/Si	30-80 nm	WZ	[131]	No
Horizontal tube furnace	Au/p-Si	150 nm	WZ	[132]	No
CVD	Ag	150-300 nm	WZ/stacking faults	[133]	No
Horizontal tube furnace	Au, Sn, Mn/Si	20-60 nm	--	[134]	No

Table 1.2: A comprehensive summary of ZnS NWs grown on different substrates and with different catalysts.

Again, we focus our detailed literature study on the straight and homogenous aligned VLS assisted NWs. Most of the results reporting controlled VLS growth of ZnS NWs are gathered in Figure 1.11.

Lu et al. reported aligned ZnS NWs on silicon using a horizontal quartz tube [135]. The NWs were 60 nm in diameter, and they had no catalyst on the top. In an original way, the authors wetted the substrate surface with a solution of zinc-acetate before introduction in the tube, helping to trigger the NW growth. The SAED pattern confirms a WZ structure of the NWs (see Figure 1.11i). Further, they showed the broad photoluminescence centered at ~440 nm and discussed the growth mechanism of these ZnS NWs.

Liang et al. used Ga as a catalyst to grow VLS assisted ZnS NWs on GaAs (111)B using MOCVD [122]. The NWs were straight and well-aligned, as shown in Figure 1.11ii. They demonstrated the control of diameter and density of NWs with substrate annealing duration. Their NWs adopted a ZB crystal phase with a high density of stacking faults. In ZnS NWs, it seems challenging to obtain a ZB blende structure and using Ga as a catalyst provides insight to achieve ZB NWs without stacking faults. In the thesis, we will come back later on that result. Furthermore, the NWs were assembled into a photodetector device, showing fast UV detection.

Wang et al. employed a unique method to grow ZnS NWs on ZnS columns [125]. First, they have prepared a few μm thick ZnS columns on the ZnS wafer; then, these columns were coated with Au films at different temperatures. The Au particle density was controlled, and the ZnS NW density (0.33 to 3.04 wires/μm^2) using a VLS process. Without a doubt, the grown ZnS NWs were highly aligned and straight with a WZ structure, as shown in Figure 1.11iii.

Liang et al., in another study, employed Au and Ag catalysts to grow VLS assisted ZnS NWs on GaAs (111)B substrates [121]. They have reported a structural transformation from WZ to ZB with increasing NW diameter (see Figure 1.11iv). They have suggested a range of diameters, namely 30-70 nm, for which a high density of stacking faults was found. But below and above that range, ZnS NWs crystallize in the WZ and ZB structures, respectively.

Hao et al. reported exciting results using vapor phase transport to grow Au-catalyzed ZnS NWs. They have observed periodically twinning in their NWs (refer to Figure 1.11v) and suggested a growth model [128]. According to this model, the periodic twinning originated from periodical fluctuation between the diffusion rate inside the catalytic droplet and the

growth rate on the liquid-solid interface. They explained that when growth conditions (mainly high growth temperature) lead to the situation that the diffusion of species in the liquid catalyst is slower than the crystal growth at the L–S interface, periodic depletion of Zn and S results in a modulation of the droplet contact angle, due to a change in the wettability. Thus, very early in 2006, they emphasized that contact angle might be an essential parameter for the growth of semiconductor NWs.

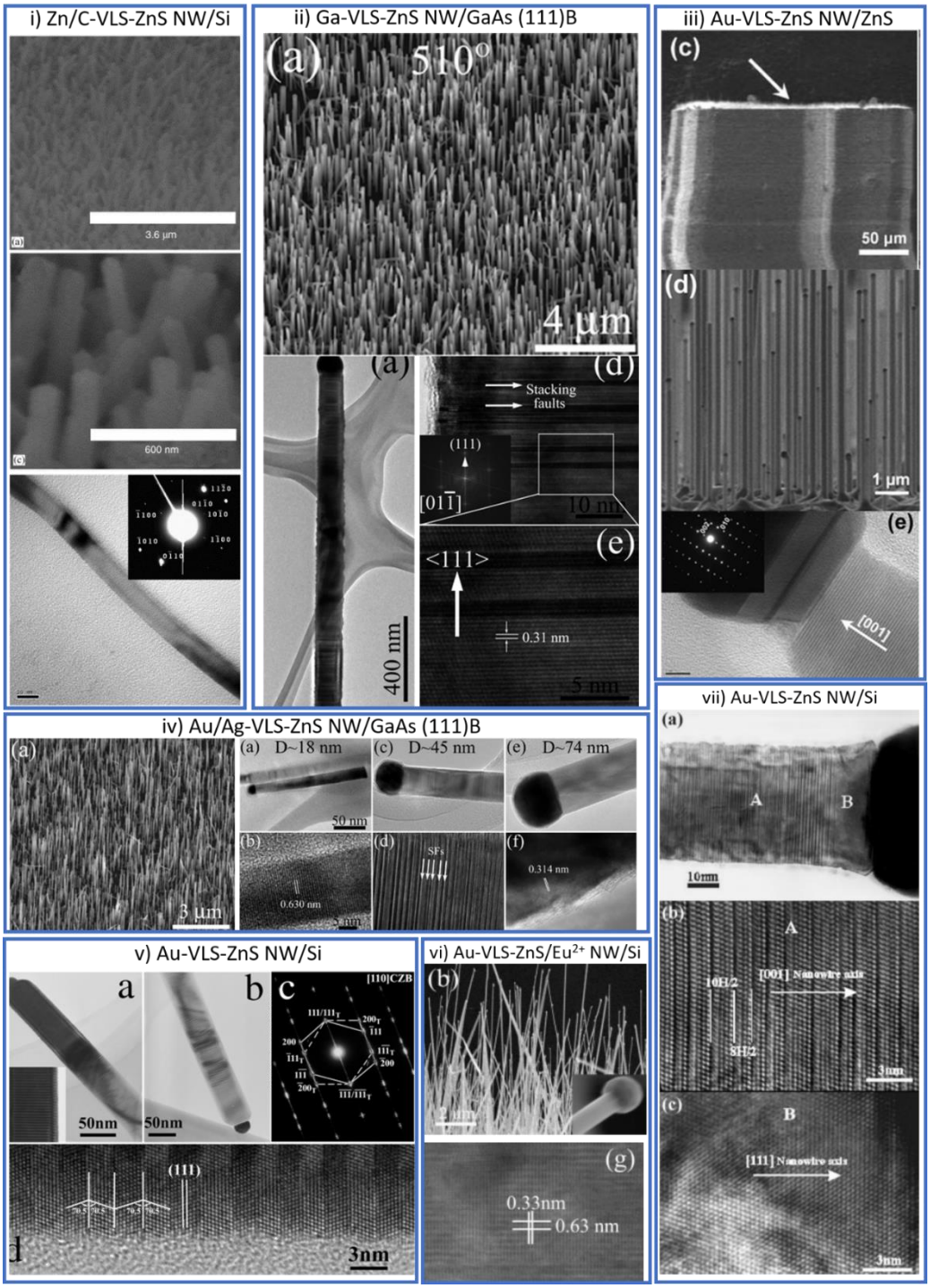

Figure 1.11: The vertical aligned VLS grown ZnS NWs, i) Zn acetate-VLS-ZnS NW/Si [135], ii) Ga-VLS-ZnS NW/GaAs (111)B [122], iii) Au-VLS-ZnS NW/ZnS [125], iv) Au/Ag-VLS-ZnS NW/GaAs (111)B [121], v) Au-VLS-ZnS NW/Si [24], vi) Au-VLS-ZnS/Eu^{2+} NW/Si [127], and vii) Au-VLS-ZnS NW/Si [124].

Cheng et al. reported Eu^{2+} doped WZ ZnS NWs on Au-coated Si (111) wafers using a vapor deposition method under a weakly reducing atmosphere [135]. The doping resulted in a modulated composition and crystal structure, which led to a high density of defects in ZnS NWs, as shown in Figure 1.11vi. The ion doping causes intense fluorescence and persistent phosphorescence in ZnS nanowires.

At last, Jiang et al. obtained WZ polytype modulated structure via intermittent laser ablation-catalytic growth of ZnS NWs [124]. They have analyzed the stacking sequence from the HRTEM image, shown in Figure 1.11vii, composed of WZ variant half cells of 8H and 10H appearing along the entire wire length in turns. Such modulated structure was reported for the first and only time for ZnS NWs. Furthermore, they have reported a broad room temperature photoluminescence centered at 3.66 eV.

We now underline the main conclusions from this state of the art:

1) Using GaAs (111)B or ZnS (homoepitaxial) substrate (irrespective of catalyst Au, Ag, or Ga) aids to achieve straight vertical aligned ZnS NWs compared to other choices of substrates.
2) The diameter and density of the NWs can be controlled by controlling the size and density of the Au droplets on the substrate.
3) A range of NW diameters (30-70 nm) predicts a structural transformation from WZ to ZB.
4) There is the possibility of using Ga as a catalyst to achieve the ZB phase in ZnS NWs.
5) The effect of contact angle was discussed by Hao [128], who showed it could impact the liquid-solid interface.
6) ZnS compound is known for its polytypic behavior having more than 200 different structural polytypes [68]. Similar to Jiang [124], we can expect the formation of such modulated structure with variation in the growth conditions (VLS, VSS, VI/II ratio, etc.).
7) Interestingly, the VSS growth of ZnS nanowire has never been studied before. However, the growth of ZnS NWs on the ZnS column might be assisted by VSS, but the authors suggested a VLS growth mode [125].

Thus, we will grab this opportunity to explore what treasures do VSS method holds for ZnS semiconductor NWs and keep the above points in mind to control the VLS growth of ZnS NWs.

1.5.2 ZnS material: structural and optical properties

ZnS is one of the first discovered compound semiconductors and has been widely used in flat panel displays, UV sensors, electroluminescent devices, and infrared windows [136,137]. ZnS has two common crystal structures: one with a ZB structure and the other with a WZ structure. At atmospheric pressure, cubic phase ZnS is more stable at low temperatures and transforms to wurtzite ZnS at temperatures higher than 1000 °C [70].

The lattice parameters of ZB are a = b = c = 5.41 Å, Z = 4 (space group F4-3 m), and for WZ, a = b = 3.82 Å, c = 6.26 Å, Z = 2 (space group = P63mc). ZnS nanostructures offer fascinating properties such as direct wide bandgap (3.72 eV for cubic and 3.77 eV for hexagonal), presence of polar surfaces, high electronic mobility, and thermal stability [138]. From theoretical calculations, a slight difference in atomic arrangements of ZB and WZ might lead to a significant difference in band gaps, electronic structure, and properties of ZnS material [70].

The optical spectra are linked to band structure and inter-band transitions probabilities. The optical characteristics of the ZnS ZB and WZ phases have been demonstrated experimentally to be unique. To better understand these distinctions, the electronic band structure of various phases have been extensively studied [139–141]. The band dispersions for the ZnS ZB and WZ phases calculated using density functional theory (DFT) are shown in Figure 1.12. It can be seen that the conduction-band minima are much more dispersive than the valence band maxima for both phases. Additionally, the authors state that electron mobility in these materials is greater than in holes [141]. Also, *p*-electrons forming the topmost valence band states tightly bind to sulfur and make the valence band holes less mobile. Hence, the contribution of the holes to the conductivity is expected to be smaller. The valence band comprises three regions: a lower region consists of the *s* bands of Zn and S, a higher-lying region contains well-localized Zn *3d* bands, and a top broader band originating from the *s*–*p* states hybridized with Zn *3d* states [136].

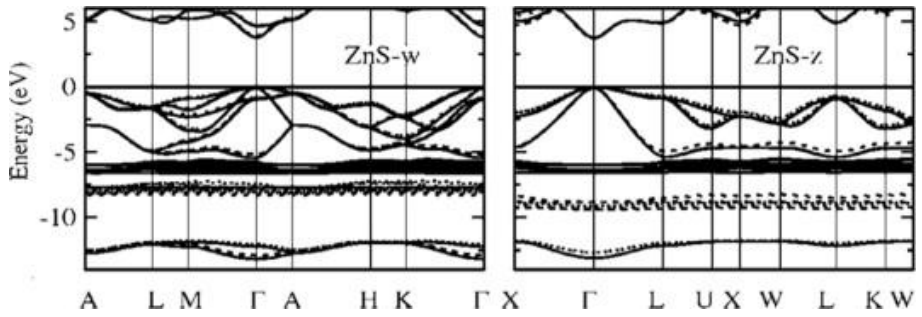

Figure 1.12: Band dispersion for WZ and ZB ZnS calculated according to LDA (solid lines) and LDA+U (dotted lines). The Fermi level is set to zero energy. Adapted from [141].

Using empirical calculations, Akiyama and coworkers demonstrated that reducing ZnS nanostructures to a few nanometers stabilizes the high-temperature WZ structure [142]. They calculated cohesive energies for NWs with ZB and WZ structures and demonstrated that the stability of a crystal structure depends on the NW diameter. Figure 1.13 shows the plot of energy differences between 6H and ZB structures (ΔE_{6H-ZB}), 4H and ZB structures (ΔE_{4H-ZB}), and WZ and ZB structures (ΔE_{WZ-ZB}) of ZnS NWs as a function of their diameter.

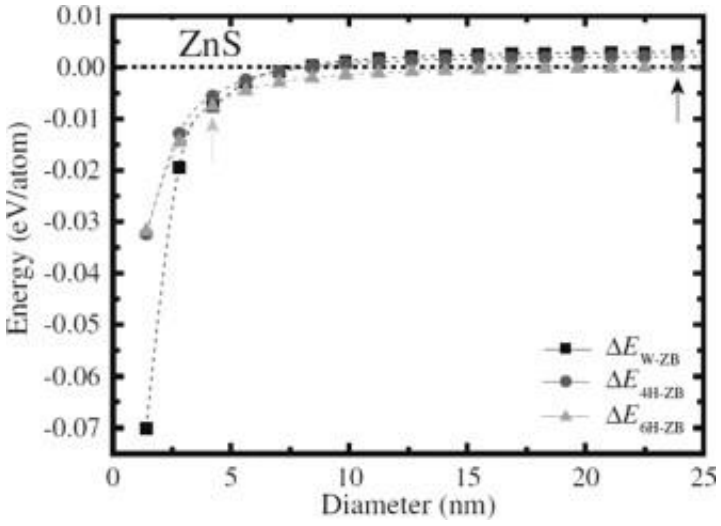

Figure 1.13: Plot of energy differences between WZ and ZB structures ΔE_{WZ-ZB} (squares), 6H and ZB structures ΔE_{6H-ZB} (triangles), 4H and ZB structures ΔE_{4H-ZB} (circles), for a ZnS nanowire as a function of its diameter. Adapted from [142].

As shown in the plot, the energy differences converge towards the bulk phase with increasing diameter, indicating the appearance of bulk features. The WZ structure is preferred for diameters under 4 nm. But the ZB structure, the most stable in bulk, is favored for diameters over 24 nm. The authors explained this behavior based on two- and three-coordinated surface atoms on nanowire facets. Unlike in bulk (fourfold coordination), the Zn and S atoms at the side surfaces of WZ-ZnS NWs are all threefold coordinated with one unsaturated bond. In the case of the ZB-ZnS NWs, in addition to the threefold coordinated atoms, there are also certain twofold coordinated atoms located at the edges of the NWs facets. This makes the surface energy of ZB-ZnS nanowires larger than that of WZ-ZnS NWs, which results in lower stability. Therefore, when the nanostructure has a small volume to surface ratio, it favors the WZ phase with fewer dangling bonds.

Most importantly for this study, ZnS offers an extensive range of possible polymorphs, all currently identified and listed in Ref. [68], with several layers in the elementary stacking sequence up to 64. Similar to SiC, the standard 4H, 6H, 8H, and 10H phases were observed in ZnS, as well as the 15R phase [124,143].

1.5.3 Polytypism and in-situ TEM studies

Understanding the crystal phase selection is essential for NW applications because a mixed crystal phase has a significant impact on the electronic properties of NWs [144]. Since the crystal structure affects the electronic structure, controlling the crystal structure opens the door to new ideas. For example, WZ GaAs has a slightly higher bandgap than ZB, making the two form a type II band alignment [145], and it was shown in a GaAs crystal phase heterostructure [146]. If a material has an indirect bandgap in ZB form, it could become material with a direct bandgap in WZ form, like GaP, Ge, and SiGe [60,147].

Glas et al. introduced a nucleation-based model to explain why the WZ phase is found in NWs instead of ZB that usually occurs in bulk [11]. In past years, it was predicted that the growth proceeds on a layer-by-layer basis limited by nucleation, and the position of the nucleus plays a significant role in defining the phase. This determines the orientation of each layer concerning the previous layer.

The implementation of an epitaxial technique in an operational transmission electron microscope leads to a unique instrument: you can now see crystals growing right in front of your eyes! The resolution is so high that you can see down to the atomic level. This kind of experiment has made a big difference in understanding the NW growth process because it shows images of the process right away [18,148]. Recently, the groups of Harmand [148] and Ross [18] verified the layer-by-layer growth (or monolayer regime) using in-situ TEM studies. The recent exciting findings in NW polytypism are gathered in Figure 1.14.

The triple-phase line (TPL) significance in the nucleation of each new bilayer is critical and well established at this point. In-situ TEM study verified that for a flat liquid-solid interface, growth starts from a corner at TPL and spreads outward from there [148]. However, the nucleation point of a new layer for a truncated liquid−solid interface is less clear. This is partly because the new layer forms so rapidly that current microscope systems cannot capture the initial stages. Each new bilayer is formed with an instantaneous disappearance of the truncation. It could be the formation of a new bilayer as well. Thus, nucleation might still occur at the TPL [18,149].

The contact-angle role has been considered a vital parameter for the crystal phase selection in NWs. Various studies have predicted and demonstrated it in the past 15 years [11,18,128]. The contact angle engineering of the liquid phase in VLS supports the control on

the crystalline growth direction and even polarity [150,151]. In a recent in-situ TEM study, Panciera et al. have demonstrated the crystal phase switching between the ZB and WZ structure using the sole parameter, the droplet contact angle for self-catalyzed GaAs NWs. The droplet angle can be finely tuned by changing the group III and V fluxes. The ZB phase forms at small (<100°) and large (>125°) contact angles, whereas the pure WZ phase is observed for intermediate contact angles, as shown in Figure 1.15.

Consequently, new strategies could be developed to create perfect superlattices and perfectly reproducible quantum heterostructures. One possibility could be the control of the liquid supersaturation down to the atomic scale. This would require growth at a meager rate and achieving liquid catalysts of the same size in an array. The next breakthroughs are around the corner when high-speed cameras record growth times below milliseconds.

The followed significant developments in NWs are beneficial to studying ZnS, a polytype superstar.

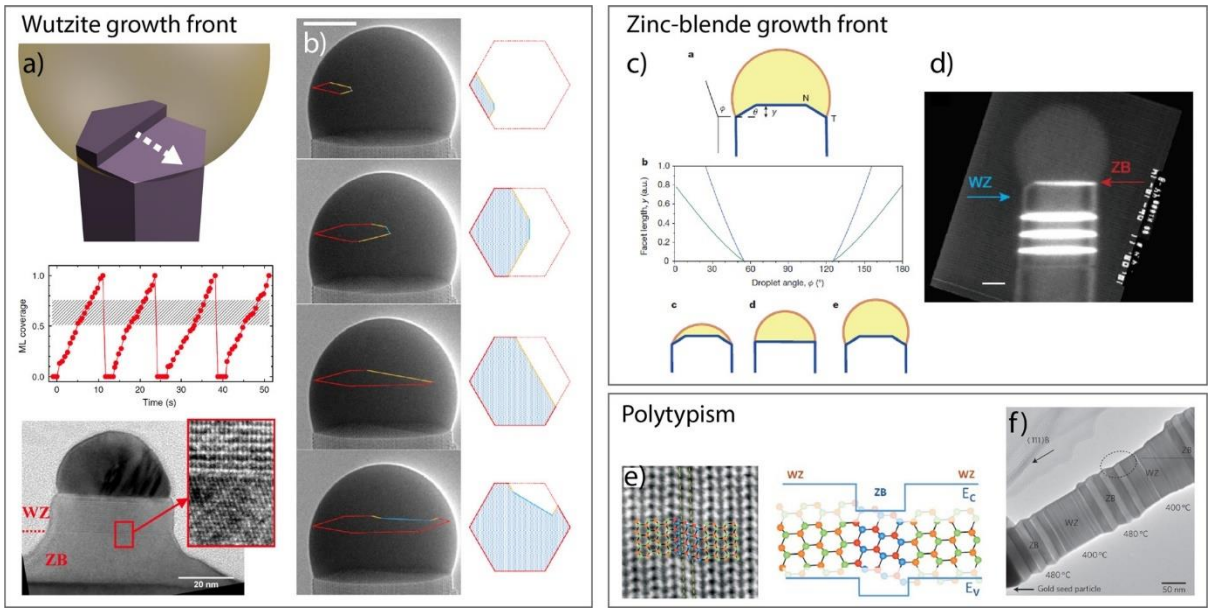

Figure 1.14: Scheme showing several breakthroughs in in-situ measurements of the TPL for GaAs nanowires. (a,b) Studies by Harmand, Glas et al. on WZ growth front [11,148], (c,d) Details of the discoveries by Jacobsson et al. on ZB growth front [18], (e) The effect of polytypisms on the energy bands [146], and (f) on the morphology of GaAs nanowires [17] Adapted from [8].

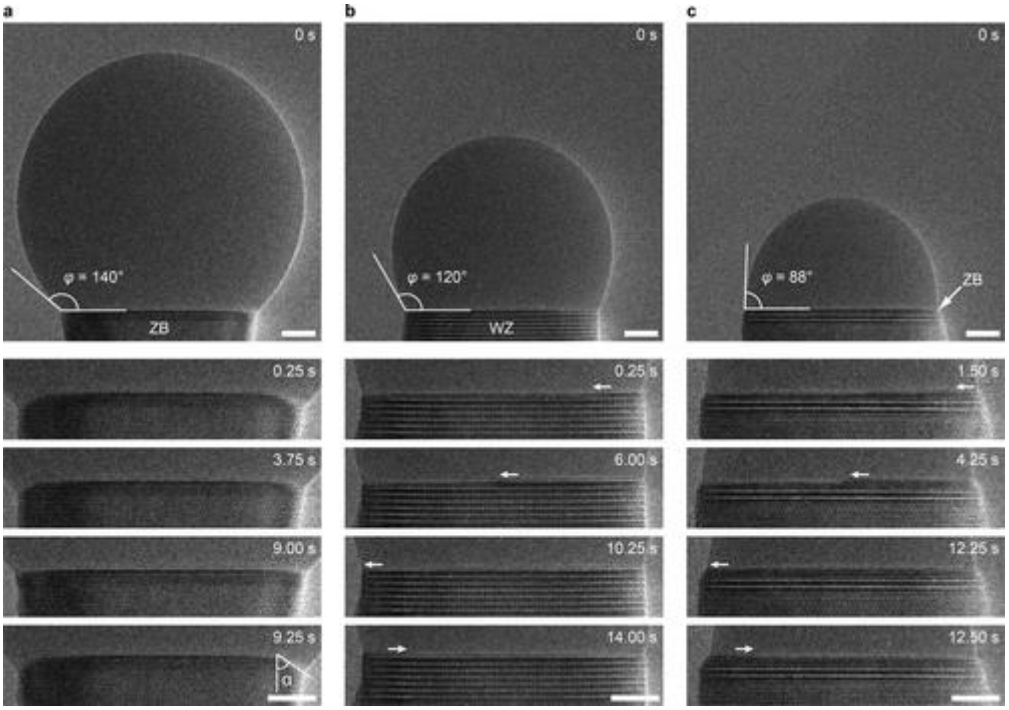

Figure 1.15 shows the growth mode and phase selection at different contact angles for self-catalyzed GaAs NWs. Adapted from [149].

After such introduction and presentation of the subject and context, let us repeat here the objectives of the thesis.

This work mainly focuses on the MOCVD epitaxial growth of 1-D nanostructures termed as "nanowires" based on ZnS material. The goal is to investigate various growth modes and study the induced structural modifications in ZnS NWs. From the literature review, we are aware of polytypic behavior of ZnS and the challenges to optimize vertical growth and subsequently, achieve pure and controlled crystal phases. For that purpose, we first want to study different growth strategies such as varying the effect of growth temperature, precursor fluxes, VI/II ratio to optimize the NW homogenous growth, and using buffered substrates to impose a solid catalyst. As a second part, we investigate the structural properties and induced polytypic behavior in ZnS NWs. We perform deep analysis using TEM and theoretical modeling to study and explore polytypism in ZnS, on the light of the GaAs case, i.e. with the aid of the impressive theoretical and experimental work already reported on the topic. Then, we design and carry out new experiments with the objective of proving our theoretical findings. Because optoelectronic and photonic applications are targeted, in the last step we aim to study the optical properties of ZnS NWs and provides insights on the axial growth of NW heterostructures based on wide bandgap ZnS semiconductor.

Chapter 2

Elements of theory and experimental techniques

Contents

This chapter will overview the theoretical aspects and the experimental tools employed in this work. It aims to introduce the essential concepts needed to understand the results presented in this thesis. The first part is devoted to summarizing nucleation theory and the ANNNI model. In the second part, we focus on the description of MOCVD growth and the main characterization techniques used in this work.

Unit conversions: 1J = 1e+7 erg = 6.24e+18 eV

2.1 Elements of theory

2.1.1 Nanowire nucleation theory

Here, we consider the vapor-liquid-solid (VLS) epitaxial growth of nanowires on a substrate. Hence, the system consists of a liquid catalyst, growth species in vapor, and solid wire (or substrate). The NW diameter is mainly determined by the size of the catalyst present on the substrate before growth. The nucleation model considers that the NW growth proceeds layer by layer, starting with forming a critical-sized nucleus at the solid-liquid interface, and this nucleus spreads out rapidly to cover the whole interface. In this nucleation model, it is presumed that the position/orientation of the nucleus with respect to the previous layer defines the crystal structure of the entire layer (either WZ or ZB).

To explain factors that affect the rate at which nuclei form, we need a nucleation theory. We present specific formulas from fundamental nucleation theory that will be used in this work.

2.1.1.1 The nucleus and its formation energy, ΔG

The change in enthalpy (or energy barrier) for the formation of a nucleus at the liquid-solid (LS) interface involves the contribution from the nucleus surfaces and edges (it costs energy), minus the thermodynamic solidification of $\Delta\mu$ (it brings energy). It is expressed as:

$$\Delta G = -Ah\Delta\mu + Ph\Gamma + A\sigma \qquad (2.1)$$

Where A and P are the area and perimeter of the nucleus, respectively, $\Delta\mu$ is the chemical potential difference (supersaturation) of reacting species in the droplet, h is the height of a single bilayer of II-VI pairs, Γ is the step energy that includes the edge energies of the nucleus, and σ is the interface energy between the nanowire and nucleus.

The sum of these volume and surface terms results in ΔG to be a concave function of l (l being the size of the nucleus) with a maximum ΔG^* for some l^*, known as the critical size of the nucleus (Figure 2.1a). Nuclei with a size smaller than the critical one will dissolve, and nuclei bigger than the critical size will grow indefinitely.

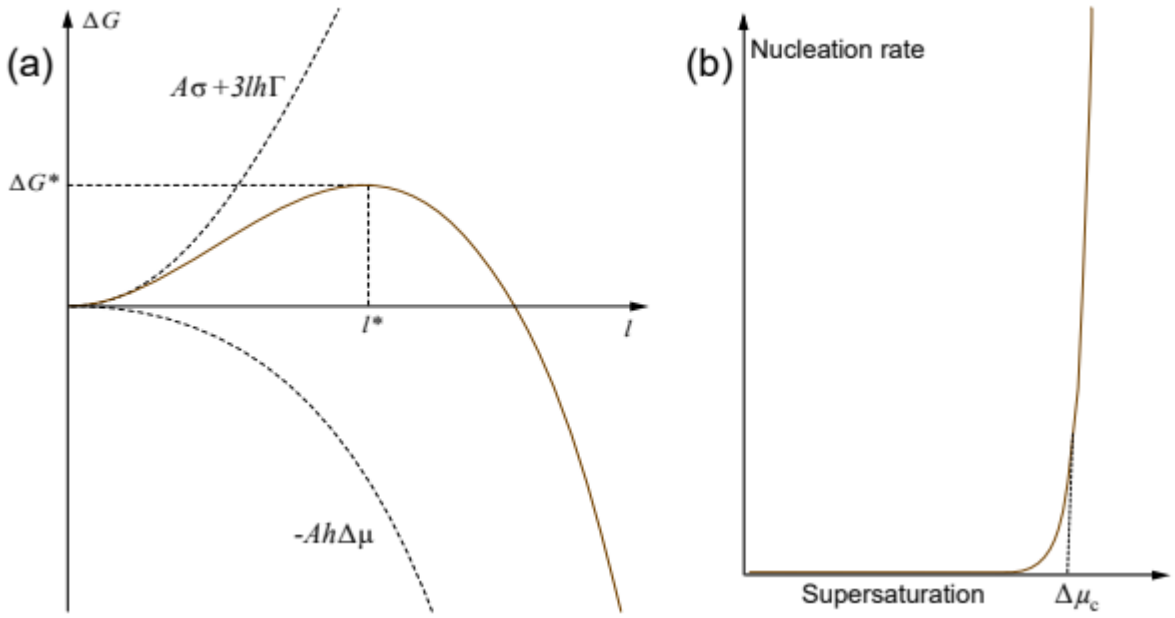

Figure 2.1: a) Free energy change ΔG as a function of the nucleus size l (continuous line), which is the sum of the volume and surface terms (dashed lines). B) Qualitative dependence of the nucleation rate as a function of the supersaturation $\Delta\mu$: the nucleation rate is practically zero until a critical value of supersaturation $\Delta\mu_c$ is reached, increasing steeply afterward. Adapted from [152].

2.1.1.2 Nucleation at the triple-phase line (TPL)

The relative orientation of the new layer with respect to the preceding one will be determined by the orientation of the nucleus (ZB or WZ). Therefore, to obtain a pure ZB or WZ phase, all nuclei must form in either ZB or WZ position (orientation) with respect to the previous one.

We assign a surface energy γ_F to the interface energy (σ). Let us consider the case in which nucleation occurs away from the triple-phase line (TPL) (Figure 2.2a). The interface energy of the solid-nucleus will be zero for nucleation in the ZB position and will be some $\gamma_F > 0$ (i.e., the cost of creating a stacking fault) for nucleation in the WZ position. Therefore, the difference in free energy change (Eq. 2.1) between the two cases is $\Delta G_{WZ} - \Delta G_{ZB} = A\gamma_F > 0$, and nucleation away from the TPL always favors ZB nucleation. On the other hand, the nucleation at TPL could be WZ or ZB (Figure 2.2b), depending upon the contact angle and the surface energies of WZ and ZB planes. WZ nucleation can only occur at TPL if the supersaturation conditions are favorable (discussed in chapter 5) [11].

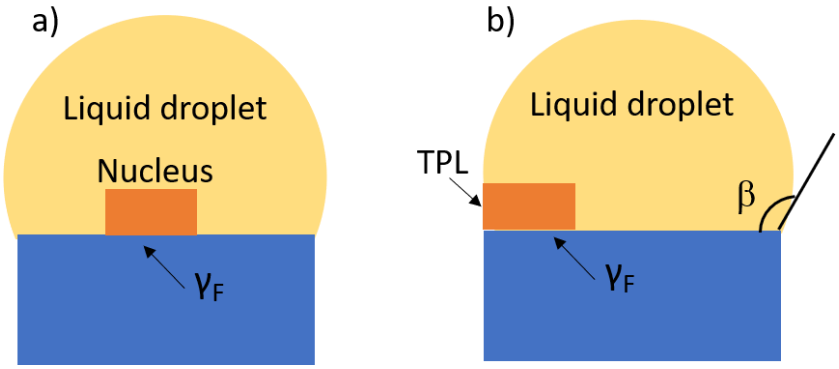

Figure 2.2 a) Nucleation inside the droplet, b) Nucleation at TPL.

2.1.1.3 Nucleus geometry

It has been observed from in-situ TEM experiments that nucleation starting from a hexagonal corner has a high probability [148]. Thus, here we consider the nucleation is triggered at TPL and more likely from one of the corners of the hexagonal interface. However, the critical nucleus was never seen, and the first island observed was a rhomboid with sides of different lengths. Thus, the shape of the nucleus can be considered as a triangle or rhombus [11,153]. The two nucleus geometries are shown in Figure 2.3.

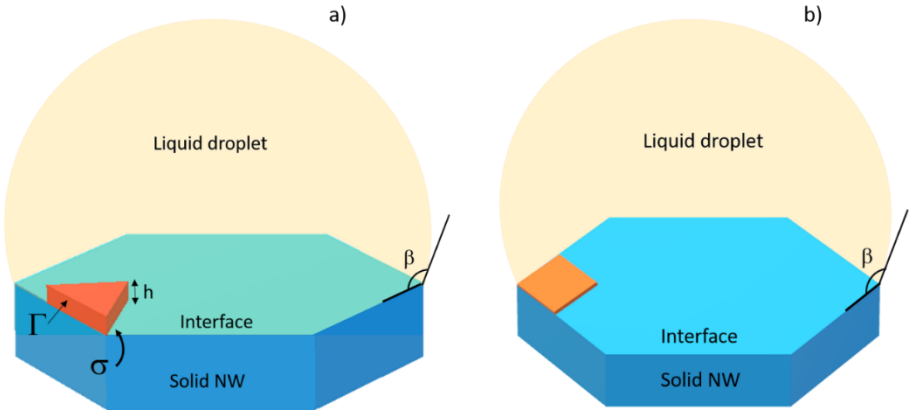

Figure 2.3 The nucleation event at the droplet-NW interface. The two possible geometries of the nucleus are: a) triangular, or b) rhombus

Triangular nucleus

We consider that the nucleus has the shape of a triangle of side length *l*.

Here, the area and perimeter of the triangular nucleus are $A = \frac{\sqrt{3}l^2}{4}$ and $P = 3l$, respectively.

The nucleation formation energy is modified as,

$$\Delta G = -\frac{\sqrt{3}l^2}{4}h\Delta\mu + 3lh\Gamma + \frac{\sqrt{3}l^2}{4}\sigma \qquad (2.2)$$

The maximum is calculated by,

$$\frac{\partial \Delta G}{\partial l} = 0$$

$$\frac{\partial \Delta G}{\partial l} = -\frac{\sqrt{3}}{2}lh\Delta\mu + 3h\Gamma + \frac{\sqrt{3}}{2}l\sigma$$

$$= 0 \qquad (2.3)$$

$$l^* = 2\sqrt{3}\frac{\Gamma}{(\Delta\mu - \sigma/h)}$$

Where l^* is the critical side length of the nucleus, and hence the corresponding critical energy ΔG^* is given by,

$$\Delta G^* = \Delta G|_{l^*} = 3\sqrt{3}\frac{h\Gamma^2}{(\Delta\mu - \sigma/h)} \quad (2.4)$$

Rhombus nucleus

We consider that the nucleus has the shape of a rhombus of side length *l*.

Here, the area and perimeter of the rhombus nucleus are $A = \frac{\sqrt{3}l^2}{2}$ and $P = 4l$, respectively.

The nucleation formation energy is modified as,

$$\Delta G = -\frac{\sqrt{3}l^2}{2}h\Delta\mu + 4lh\Gamma + \frac{\sqrt{3}l^2}{2}\sigma \quad (2.5)$$

The maximum is calculated by,

$$\frac{\partial \Delta G}{\partial l} = 0$$

$$\frac{\partial \Delta G}{\partial l} = -\sqrt{3}lh\Delta\mu + 4h\Gamma + \sqrt{3}l\sigma$$

$$= 0 \quad (2.6)$$

$$l^* = \frac{4\sqrt{3}}{3}\frac{\Gamma}{(\Delta\mu - \sigma/h)}$$

The corresponding critical energy ΔG^* is,

$$\Delta G^* = \Delta G|_{l^*} = \frac{8\sqrt{3}}{3}\frac{h\Gamma^2}{(\Delta\mu - \sigma/h)} \quad (2.7)$$

2.1.1.4 Nucleation rate

The classical nucleation rate mainly depends on the exponential of critical barrier energy (ΔG^*). The nucleation rate can be expressed as [154]:

$$N = AZ\exp\left(\frac{-\Delta G^*}{k_B T}\right) \quad (2.8)$$

Where *A* is a function of attachment frequency of III-V pairs to the critical radius and their concentration in the droplet, k_B is the Boltzmann's constant, *Z* is the Zeldovich factor, and *T* is the growth temperature in kelvin.

The Zeldovich factor is given by:

$$Z = \sqrt{\frac{\Delta G^*}{3\pi k_B T i^{*2}}} \quad (2.9)$$

Where i^* is the number of atoms in the critical nucleus. Z is the probability that a nucleus of critical size (at the maximum of the energy barrier) will continue to grow and not dissolve by statistical fluctuations.

The consequence of expression 2.8 is remarkable and reflects a characteristic feature of nucleation: when the supersaturation $\Delta\mu$ is lower than some critical $\Delta\mu_c$, pretty much nothing happens (Figure 2.1b). As we approach $\Delta\mu_c$, the nucleation rate increases abruptly by many orders of magnitude.

2.1.2 The ANNNI model

In chapter 1, we described what polytypism is in materials. Here we wish to comment on how it has previously been studied by extending the atomic plane interactions beyond the nearest neighbor. This modeling approach is called ANNNI (axial nearest-neighbor Ising), in which pseudo spins are allocated to previously stacked layers depending on the bond orientations of molecular tetrahedra. The ANNNI model considers the pair interactions between the newly stacked layer and the preceding layers via the interaction energy coefficients J_i. As a result, this model provides an excellent and efficient method for examining the long-range structural correlation that is thought to be root cause for polytype formation. Other than 3C (cubic, zinc blende) and 2H (hexagonal, wurtzite), polytypes with a higher order are referred to as high order polytypes (HOP). For example, in Figure 2.4, polytypes 4H, 6H, and 15R all replicate the principal structure after 4, 6, and 15 stacked layers, respectively, and so their development could be a result of a long-range interaction. The ANNNI model was introduced in 1961 but did not receive its current designation until 1980 [155,156]. In 1988, the ANNNI model was utilized to investigate and explain the polytypism observed in bulk ZnS and SiC materials [157,158]. Researchers have recently used this method to better understand the polytypism and long-range structural correlations in III-V nanowires (NWs) [159–161]. The nanowire growth dynamics have been formulated within the framework of classical nucleation theory to account for the polytypism of two typical phases, 3C and 2H [162–164]. However, the high order polytypes existence in semiconducting nanowires has only been reported by a few studies [160,161,165–167].

Reference [157] provides an excellent overview of the ANNNI model and its application to the study of polytypism in SiC. A stacking sequence of planes is considered as a sequence of distinct pseudo spins. These pseudo spins $s_i = \pm 1$ are assigned to each i^{th} ML depending on the orientation of the bonds (see chapter 1, Figure 1.7): $s_i = s_{i-1}$ if *i* ML is of type *c* (cubic stacking, bond parallel to that of preceding ML) and $s_i = -s_{i-1}$ if *i* ML is of type *h* (hexagonal stacking, bond not parallel) [67].

Table 2.1 describes 3C, 4H, 6H, 15R, and 2H polytypes in terms of *h*-*c* notation and their spin assignment. Here, we consider the first spin arbitrarily as +1 for reference.

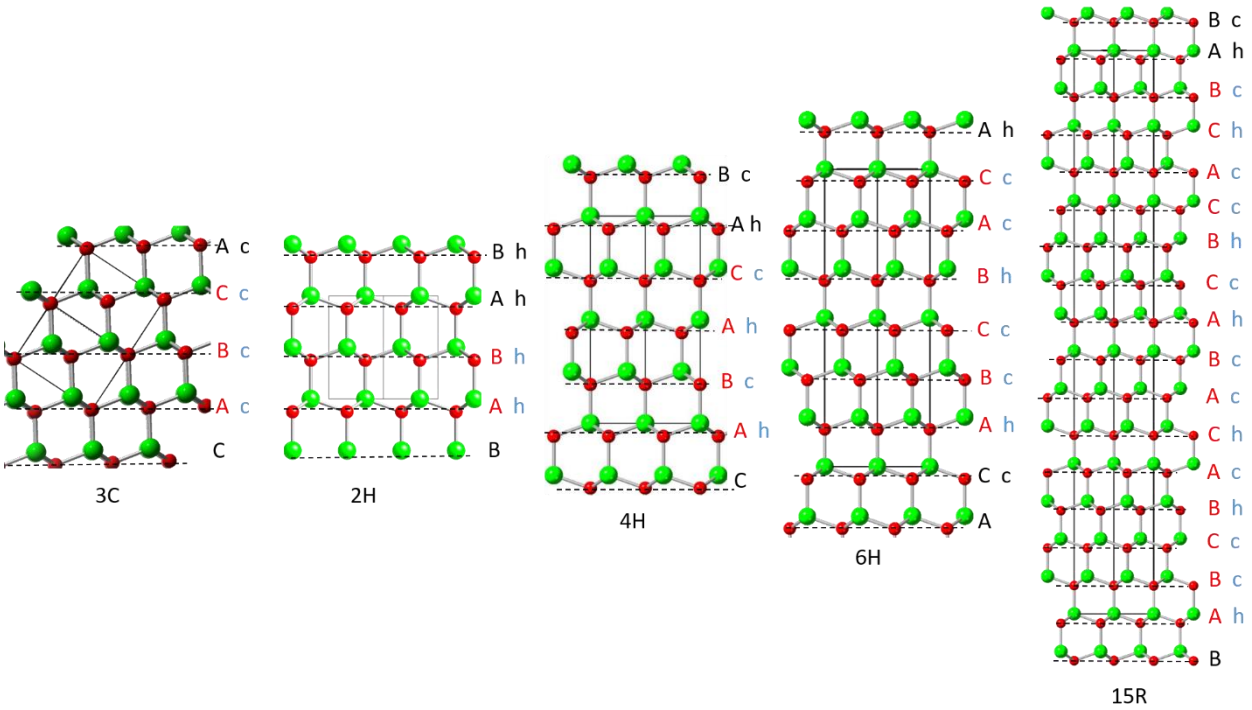

Figure 2.4: The stacking sequence of two common polytypes, 3C (ABC) and 2H (AB), and high order polytypes 4H (ABAC), 6H (ABCBAC), and 15R (ABCBACABACBCACB) with their *h-c* notations.

Polytype	Stacking sequence	h-c notation	Spin
3C	ABC	ccc	↑|↑↑↑ or 1|111
4H	ABCB	hchc	↑|↓↓↑↑ or 1|$\bar{1}\bar{1}11$
6H	ABCACB	hcchcc	↑|↓↓↓↑↑↑ or 1|$\bar{1}\bar{1}\bar{1}111$
15R	ABCBA-CABAC-BCACB	hcchc-hcchc-hcchc	↑|↓↓↓↑↑-↓↓↓↑↑-↓↓↓↑↑ or 1|$\bar{1}\bar{1}\bar{1}11-\bar{1}\bar{1}\bar{1}11-\bar{1}\bar{1}\bar{1}11$
2H	AB	hh	↑|↓↑ or 1|$\bar{1}1$

Table 2.1: This table gathers the stacking sequences of several polytypes with their h-c notation and corresponding spin assignment. We should consider an arbitrary spin reference (taken as ↑ (+1) here) to assign spins.

We take pair interactions into account down to the 3rd ML underneath the nucleus (i = 0 for the nucleus), via interaction parameters Ji, i = 1 to 3 (refer to Figure 2.5), such that the total interaction energy for a system of N layers is given as:

$$NE = NE_{\circ} - s_{\circ}\sum_{i=1}^{3} J_i s_i \qquad (2.10)$$

$E_{\circ}$ is the reference energy.

According to above equation 2.10, the energies of polytypes are:

$$
\begin{aligned}
E_{2H} &= E_{\circ} + J_1 - J_2 + J_3 \\
E_{3C} &= E_{\circ} - J_1 - J_2 - J_3 \\
E_{4H} &= E_{\circ} + J_2 \\
E_{6H} &= E_{\circ} - \frac{1}{3} J_1 + \frac{1}{3} J_2 + J_3 \\
E_{15R} &= E_{\circ} - \frac{1}{5} J_1 + \frac{3}{5} J_2 + \frac{3}{5} J_3
\end{aligned}
\qquad (2.11)
$$

Further, we can calculate the energy difference of each polytype with respect to the 3C.

$$
\begin{aligned}
\Delta E_{2H} &= 2J_1 + 2J_3 \\
\Delta E_{4H} &= J_1 + 2J_2 + J_3 \\
\Delta E_{6H} &= \frac{2}{3} J_1 + \frac{4}{3} J_2 + 2J_3 \\
\Delta E_{15R} &= \frac{4}{5} J_1 + \frac{8}{5} J_2 + \frac{8}{5} J_3
\end{aligned}
\qquad (2.12)
$$

Hence, the interaction parameters, J_1, J_2, and J_3 can be expressed in terms of ΔE_{2H}, ΔE_{4H}, ΔE_{6H}, ΔE_{15R} and further calculated within the density functional theory (DFT) [168].

To sum up, different polytypes correspond to distinct sequences of generalized spins, resulting in particular total interaction energy expressions that can be applied to interface energies within the framework of nucleation theory, as illustrated in Figure 2.5. This will be done in chapter 5.

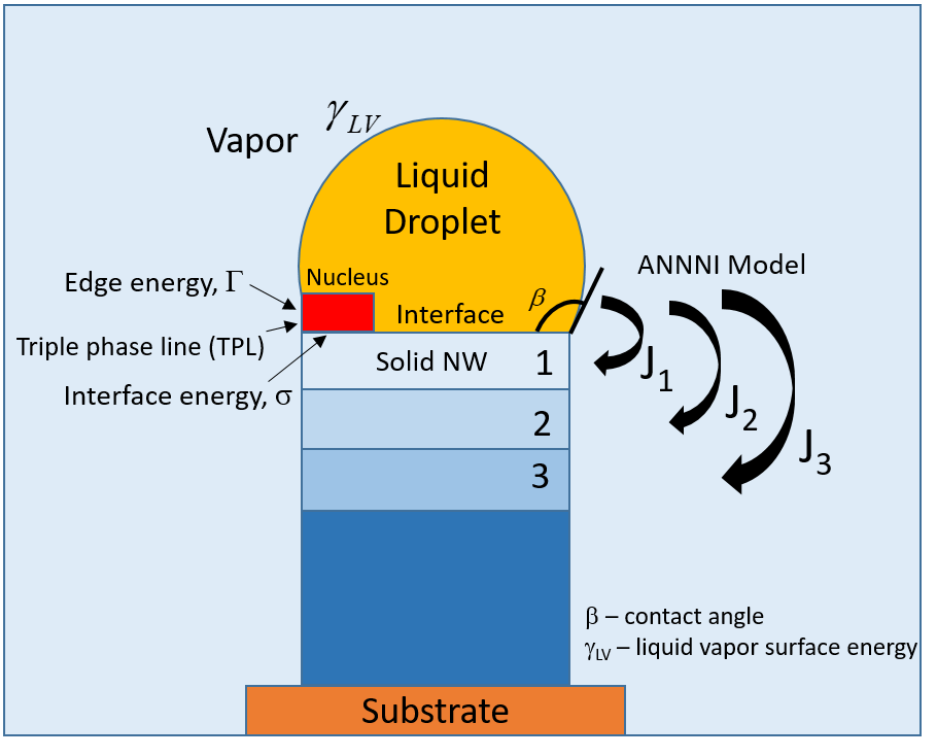

Figure 2.5: The nanowire nucleation model with interface and edge energies defined to form a new nucleus at the triple-phase line (TPL, nucleus in red). J_1, J_2, and J_3 are the pair interaction parameters considering the interaction of nucleus (j) with previously stacked layers.

2.2 Experimental techniques

2.2.1 Metal organic chemical vapor deposition (MOCVD)

2.2.1.1 Fundamentals

Metalorganic chemical vapor deposition (MOCVD) is a vapor phase technique in which at least one of the precursors is an organometallic compound. Each gaseous precursor is transported independently to the reactor using a carrier gas flow. This process is done to prevent the precursors from reacting chemically with each other before reaching the reactor. Ideally, the flow of the carrier gas and the reactor design must comply with the laminar regime conditions.

Once the precursors are injected inside the reactor, a series of physical and chemical processes take place and depend on the dynamics of transport of the precursors to the substrate and the interactions of these precursors in the gas phase and on the crystalline surface.

The different stages of MOCVD growth are listed below according to the order in which they occur and depicted in Figure 2.6 (illustration of GaN growth using TMGa and NH_3) :

1. Diffusion of the MO species through the boundary layer; note that gas-phase reactions often occur at this stage and even before, giving rise to MO adducts.
2. Adsorption of the species onto the substrate surface.
3. Surface processes: decomposition of precursors and/or adducts, chemical reactions, diffusion of species on the surface, incorporation of atoms into the crystal lattice.
4. Desorption of residual products (alkyls).
5. Transfer of residual products to carrier gas and evacuation of the waste products from the reactor

Because the above processes occur sequentially, the material deposition rate will be limited by the slowest process in the series. Keeping this in mind, it is possible to distinguish between various growth regimes according to the nature of the limiting process. When the growth rate is limited by the species diffusion and transfer to the substrate, a "mass-transport regime" is defined. If the growth rate is limited by any of the processes occurring at the surface, growth is said to be kinetically limited ("kinetic regime"). A third regime is defined for high temperatures, where a noticeable decrease of the growth rate occurs due to the desorption of precursors from the substrate surface or the evaporation of already deposited material.

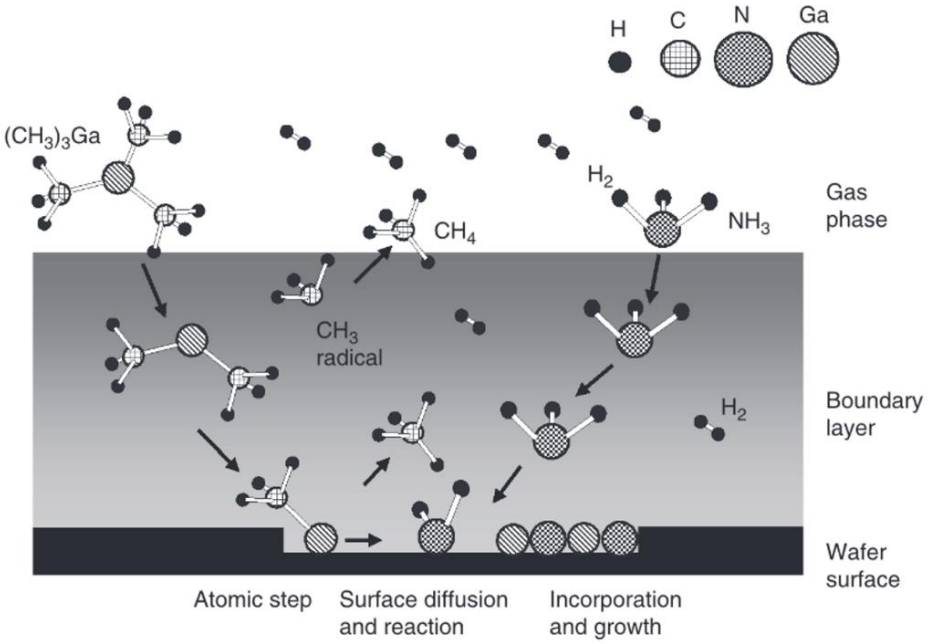

Figure 2.6: Simplified MOCVD growth mechanism for GaN. Adapted from [169].

Decomposition kinetics of precursors play an essential role. In this thesis, ZnS material will be grown using diethyl-zinc and ditertiarybutyl-sulfide as MOs. We will come back to the precursor presentation in the next section, but we want to mention here information regarding their decomposition. In the past, the group studied the thermal decomposition of the diethyl-Zn organometallic molecule, by using a quadrupole mass spectrometer coupled with an isothermal reactor. Experimental details and results are reported in reference [170]. Under a hydrogen atmosphere, DEZn starts to decompose at 300°C, following a two-step homolytic fission.

$(C_2H_5)_2Zn \Rightarrow C_2H_5{*}Zn + C_2H_5{*}$

$C_2H_5{*}Zn \Rightarrow Zn + C_2H_5{*}$

$2C_2H_5{*} \Rightarrow C_4H_{10}$ or $2C_2H_5{*} \Rightarrow C_2H_6 + C_2H_4$

The complete decomposition is achieved at 360°C. The activation energy is calculated at around 51 kcal/mol. The recombination of ethyl radicals gives the hydrocarbons by-products, ethylene, and ethane, which are further eliminated. In the same way, the thermal decomposition of ditertiarybutyl-sulfide (C_4H_9-S-C_4H_9) had been preliminary investigated [171]. We found that DTBS alone decomposes between 500°C (onset) and 550°C (end). In the presence of a Zn-organometallic, due to the co-pyrolysis effect, the decomposition is shifted toward low temperatures, between 350 and 400°C.

2.2.1.2 MOCVD at GEMaC

In this work, all the samples were grown using a vertical flow MOCVD reactor available at GEMaC (see Figure 2.7a-b). This MOCVD system is optimized for the growth of II-VI semiconductors. It comprises different components to achieve the growth of thin-film semiconductors. The different parts constituting the MOCVD frame are as follows:

• Two gas panels: two stainless steel gas lines reach the reactor inlet. The first line supplies MO flows from the bubblers containing the zinc, magnesium, and gallium precursors. The second is from the bubblers containing the sulfur, selenium, and oxygen precursors.

• The vertical growth reactor.

• Sources of organometallic (OM) precursors.

Figure 2.7: These images depict all the lines and equipment (valves, mass flow meters, connection lines, bubblers…), ensuring the transport of active gases toward the reactor and get growth. The gas lines are stainless steel tubes electropolished on the inside with low roughness to limit the memory effect. The components are connected to the lines by means of metal gaskets serving as fittings, ensuring a good seal. The substrates are placed on the susceptor before introduction in the reactor.

The MOCVD system uses a carrier gas to transport the organometallic compounds to the reactor. The carrier gas can be, for example, hydrogen (H_2), nitrogen (N_2), or helium (He). Hydrogen is purified through a palladium membrane heated to 265 °C. Hydrogen is a gas that participates in chemical reactions. At high temperatures, materials like ZnO are not stable under H_2. Therefore, we tend to use hydrogen at low temperatures (below 600 °C). In contrast, nitrogen and helium are neutral gases and can be used at higher temperatures.

An explanatory diagram of the gas panel can be seen in Figure 2.8. The carrier gas arrives through the inlet of the gas panel and sweeps the lines and the reactor. After bubbling the MOs, the carrier gas brings the precursors to the part called “Manifold”, which comprises a set of pneumatic valves and allows the MOs to be switched either to the vent line (exhaust to the outlet installations) or to the reactor. Before the growth begins, all the active species are directed towards the vent line for a few minutes to stabilize the flows. Then, the valves corresponding to the necessary precursor lines close on the vent side and open on the reactor side. The manifold should be located near the reactor so that the gases take as little time as possible to reach it. The system is computer-controlled to ensure the correct sequence in the procedure of a growth stage.

It is essential to collect and secure the exhaust gas flow. To that end, a trap system consisting of bubblers is placed at the outlet of the MOCVD system in its lower part. This trap contains an empty bottle to prevent the liquid from returning to the lines and another bottle

containing a sodium hydroxide solution to neutralize possible hydrides formed during reactions.

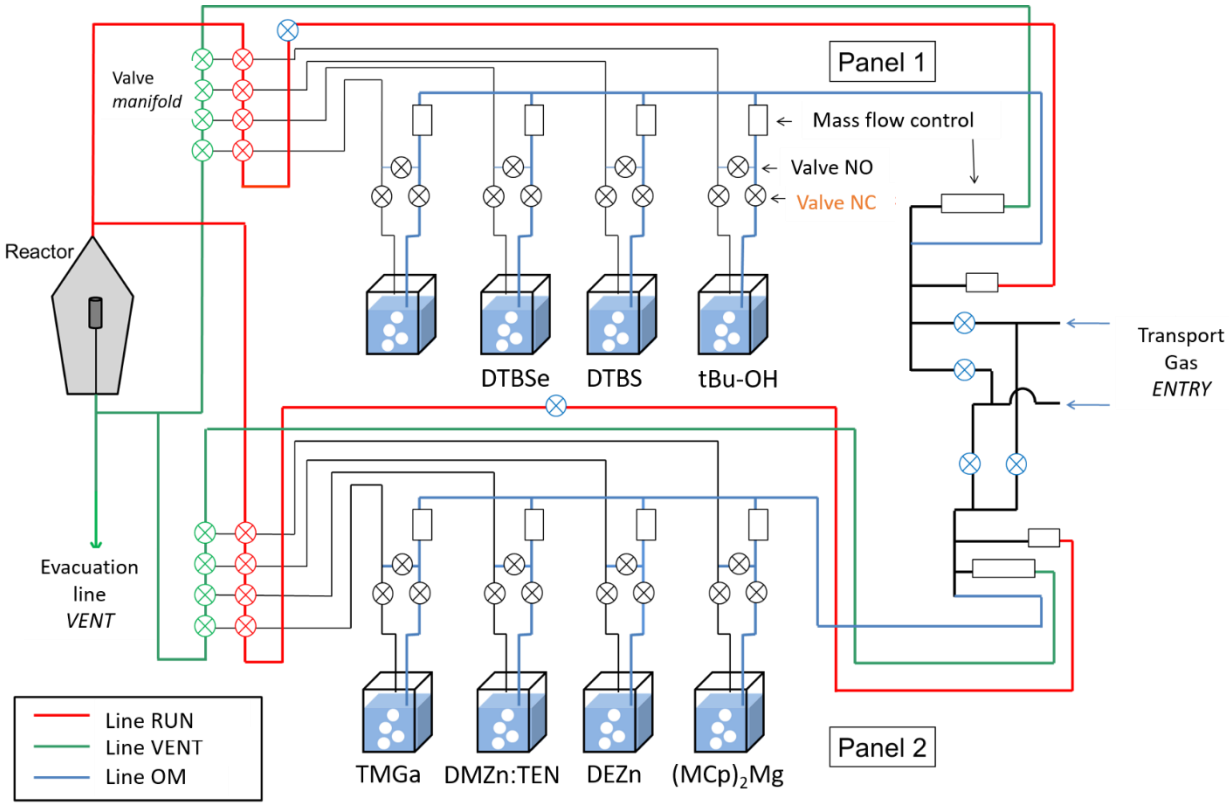

Figure 2.8: Schematic diagram of our MOCVD system.

The growth reactor, an essential part of the system, is vertical, water-cooled, and made of quartz. In the growth zone, the internal diameter is equal to 40 mm. The active gases enter the reactor through its upper part. The substrate is placed on a graphite susceptor coated with SiC and located at the center of the reactor. The susceptor surface can be flat (perpendicular to the flow) or inclined at 45°. The susceptor is heated by induction provided by a coil surrounding the quartz tube and powered by a RF generator. The lower part of the susceptor has a cavity into which we introduce a Chromel-Alumel thermocouple connected to the temperature regulator. Overheating of the reactor walls can lead to parasitic reactions. To limit this phenomenon, the envelope of the reactor is cooled by a circulating water system maintained at 20 ° C.

By definition, an organometallic, or metalorganic, is a chemical molecule made up of one or more metal atoms linked to alkyl groups with covalent bonds. Most metals are available as MO compounds. The sources of elements II and VI used for the growth of ZnS, ZnSe, $Zn_xMg_{1-x}S$ are diethyl-zinc (DEZn), ditertiarybutyl-sulfide (DTBS), ditertiarybutyl-selenium (DTBSe), and bis(methylcyclopentadienyl)-magnesium $(MCp)_2Mg$. Indeed,

i) they are pyrophoric chemicals.

ii) most are liquid, except $(MCp)_2Mg$, which is solid, and all are stored in an individual stainless-steel bubbler maintained at a fixed temperature in a thermostatic bath. Dip tubes conduct carrier gases which "bubble" in the liquid. On leaving the bubblers, the carrier gases are saturated with MOs (Figure 2.7c).

iii) they have a sufficiently high vapor pressure to be transported in large quantities in the vapor phase; the bath temperature controls the vapor pressure.

iv) there decomposition temperatures enable growths from 300 °C, and even less.

MOs are commercial products, and suppliers provide some physicochemical and safety properties, including vapor pressures that are given in Table 2.2.

The variation as a function of temperature is given by the Clapeyron formula:

$$\log P_v = A - \frac{B}{T} \qquad (2.14)$$

Where P_v is the vapor pressure (in mmHg), T is the temperature of the thermostatic bath (in K), and A, B are the vapor pressure constants.

Hence the MO flux leaving the bubbler and injected into the growth reactor depends on the vapor pressure. In the MOCVD reactor, the partial pressure of species is calculated using the formula below:

$$P_A = \frac{P_V \times D_A}{D} \qquad (2.15)$$

Where P_A is the partial vapor pressure of species A, P_v is the vapor pressure (in Pa), D_A is the flow of species A, and D is the total flow in the reactor.

	A	B	T (K)	P_v (Pa)
DEZn	8.28	2109	290	1356
DTBS	8.010	2152	290	518
DTBSe	7.870	2040	290	911
$(MCp)_2Mg$	10	3372	308	35

Table 2.2: Parameters and calculated vapor pressures for the different MO precursors.

Using the partial pressure calculation for Zn and S, we can calculate the VI/II ratio, given as:

$$R_{VI/II} = \frac{P_S}{P_{Zn}}$$

Where P_S and P_{Zn} are the partial vapor pressures of DTBS and DEZn.

2.2.2 Electron microscopy techniques

An electron microscope uses a beam of electrons to illuminate a specimen and create a highly magnified image. Electron microscopes can achieve atomic resolution and thus have much better resolution than optical microscopes, which are limited to resolutions of approximately 200 nm.

2.2.2.1 Scanning electron microscopy

SEM is a microscopy technique based on the interaction of focalized electron beam and the surface of a sample. We used a Jeol JSM 7001F microscope operating at 5-15 kV (resolution 3 nm) with a typical beam current of 5 nA and a working distance of 10 mm.

When the electron beam irradiates the sample, the electron loses energy by scattering and being absorbed in a volume that looks like a tear. This is shown in Figure 2.9. This volume is called interaction volume, and how far from the surface it goes depends on the energy of the electron beam, atomic number, and the density of the sample. The interaction results in the reflection of electrons by elastic scattering, emission of secondary electrons through inelastic scattering, and emission of radiations like X-rays and cathodoluminescence. The instrument has several detectors that can measure and detect the electrons and radiations that come from these different processes.

Our system implements an Everhart-Thornley detector to characterize the samples and detect the secondary emitted electrons. We used SEM to assess the size and density of NWs, Au nanoparticles and get detailed information on the morphology of samples. Additionally, the contrast of the image generated with secondary electrons is linked to the topography of the surface and is also linked to significant changes in the chemical composition. For example, large changes in atomic number Z can produce a chemical contrast between the ZnS NWs and the Au catalyst on top of them (Z_{Zn} = 30, Z_S = 16, and Z_{Au} = 79). The SEM images were taken from the top or the side of the sample (tilted at 45° or 90°).

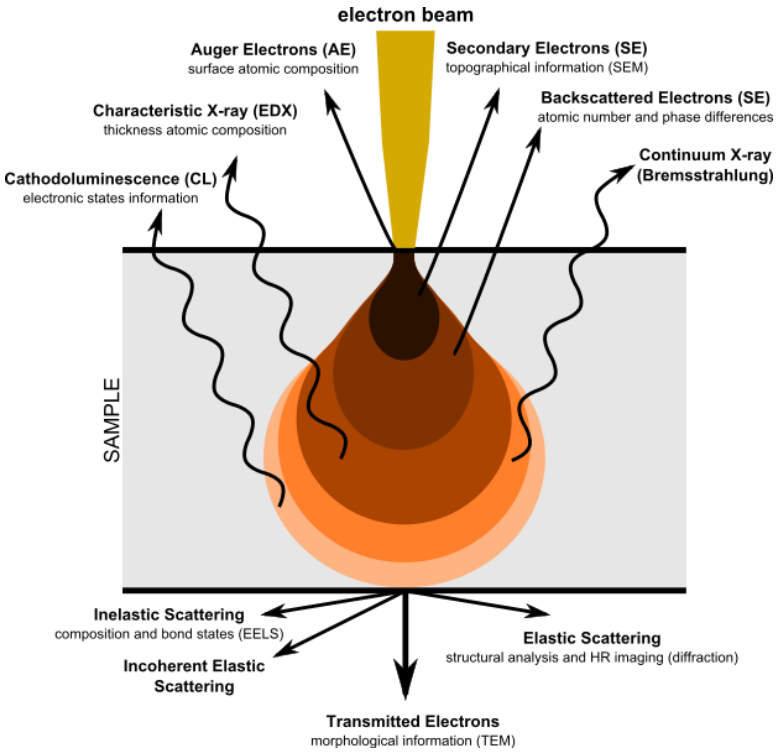

Figure 2.9: Electron interaction with matter

(Adapted from https://commons.wikimedia.org/wiki/File:Electron_Interaction_with_Matter.svg)

2.2.3.2 Transmission electron microscopy

TEM is a well-known technique to study the crystallinity and microstructure of the materials. In contrast to SEM, where the image is formed using the secondary electrons, TEM utilizes a high-energy electron beam (200-300 kV) and a very thin specimen (up to a few hundred nm thick) so that the electron beam can pass through the specimen. Since NWs are inherently thin, thus we don't need special preparation for TEM measurements. In this manuscript, we used

diffraction and various imaging mode such as bright-field (BF), dark-field (DF), high-resolution (HR) TEM, and Scanning TEM (STEM).

Most of the TEM experiments were carried out by Dr. Frédéric Fossard (at LEM) and partly by Prof. J-M Chauveau.

Note: The image interpretation of TEM images is much more complicated and trickier than for SEM.

TEM imaging and diffraction

I. High-resolution image formation (HRTEM mode):

The HRTEM imaging mode relies on the interference of electrons passing through the crystal resulting in phase contrast. The targeted crystal is irradiated with electrons having paths parallel to each other. Ideally, the electrons arriving at the surface of the sample form a monochromatic plane wave. By interacting with the atomic potential of the crystal V (~ r) (the crystal field), the wave function of the electrons Ψt (~ r) is expressed at the output of the crystal as a superimposition of plane waves in reciprocal space, which can be described from the resolution of a time-dependent Schrödinger equation where time plays the role of the direction of propagation of the incident beam in the sample. Determining the phase and intensity of this output wave helps to trace the atomic structure of the sample. In practice, the coherence of the source is not perfect, and the microscope has a transfer function that alters the image. Therefore, it is necessary to acquire focal series (images acquired for different focal lengths of the objective lens) and image simulations to interpret the contrasts observed in high resolution.

II. Diffraction:

The arrangement of atoms in a crystal is periodic. More particularly, certain planes are denser and constitute a diffraction source for the electrons. A description reasonably representing the observed behavior considers that these planes reflect the incident electrons elastically. In order for the electrons thus reflected to remain in phase, it is necessary for the path difference between two beams diffracted by two adjacent planes of the same family to be equal to an integer number of times the wavelength. Thus, if the interplanar distance of a family of planes is denoted d, and the angle of incidence and reflection of the electrons is denoted θ, the path difference between the two beams is then $2d\sin\theta$. We, therefore, find Bragg's law: $n\lambda = 2d\sin\theta$. This expression highlights the reciprocal relationship between the measured diffraction angle and the interplanar distance of the considered family of planes. In TEM, this crystallographic information can be directly accessed by acquiring diffraction patterns. This diagram is, in first approximation, a plane section of the reciprocal lattice of the crystal perpendicular to the trajectory of the electrons. The diffraction spots correspond to the families of planes satisfying the Bragg conditions. These planes have their normal perpendicular to the electron path, and the crystallographic direction common to all planes under diffraction conditions is called the zone axis.

The image formation is carried out using various constituent optics of the microscope column. Here we are particularly interested in the Zeiss Libra 200 MC, which is the machine with which the LEM is equipped. At the top of the column is the electron gun, which allows the generation of the electron beam. This source is equipped with a monochromator. A first set of electromagnetic lenses is there to form the virtual source. The electrons are then accelerated by anodes to achieve the desired energy (typically 200 kV).

The second set of lenses, the condenser part, enables the beam to be prepared to configure it as a converging beam (see Figure 2.10) or a parallel beam. At this point, we can introduce a diaphragm (condenser) to keep only the electrons close to the optical axis and limit aberrations to the detriment of brightness. The electrons then pass through the sample and converge at the rear focal plane of the objective lens where the crystal diffraction pattern is located. You can insert an objective diaphragm (or contrast diaphragm) to select the electrons that will be used to reconstruct the image. By selecting electrons that have not undergone elastic interactions close to the optical axis, a bright-field image is obtained. The most scattering/diffracting areas, therefore, appear in dark contrast (diffraction contrast) on a light background. It is also possible to choose to select a particular diffraction spot/scattering angle to obtain a dark field image. Areas of the sample whose orientation allows this diffraction light up while the rest of the image remains black. Since the intensity of the diffraction spots is very sensitive to the Bragg angle deviation, this second technique is particularly suitable for imaging crystal defects. The first image of the output wave function, which provides a projected image of the sample, is formed in the image plane of the objective lens. In the image plane, an selected area diaphragm can be introduced, making it possible to select an area of the sample for which the diffraction pattern is to be obtained. Then there are the projector lenses that allow the magnification of the image or diffraction pattern depending on the mode selected. Finally, the electrons are converted for the observation and acquisition of signals. For microscope settings and direct observation, a fluorescent screen is used. The areas irradiated by the electrons emit light in the visible. To acquire the signals, the electrons are collected by a CCD (Charge-Coupled Device) camera.

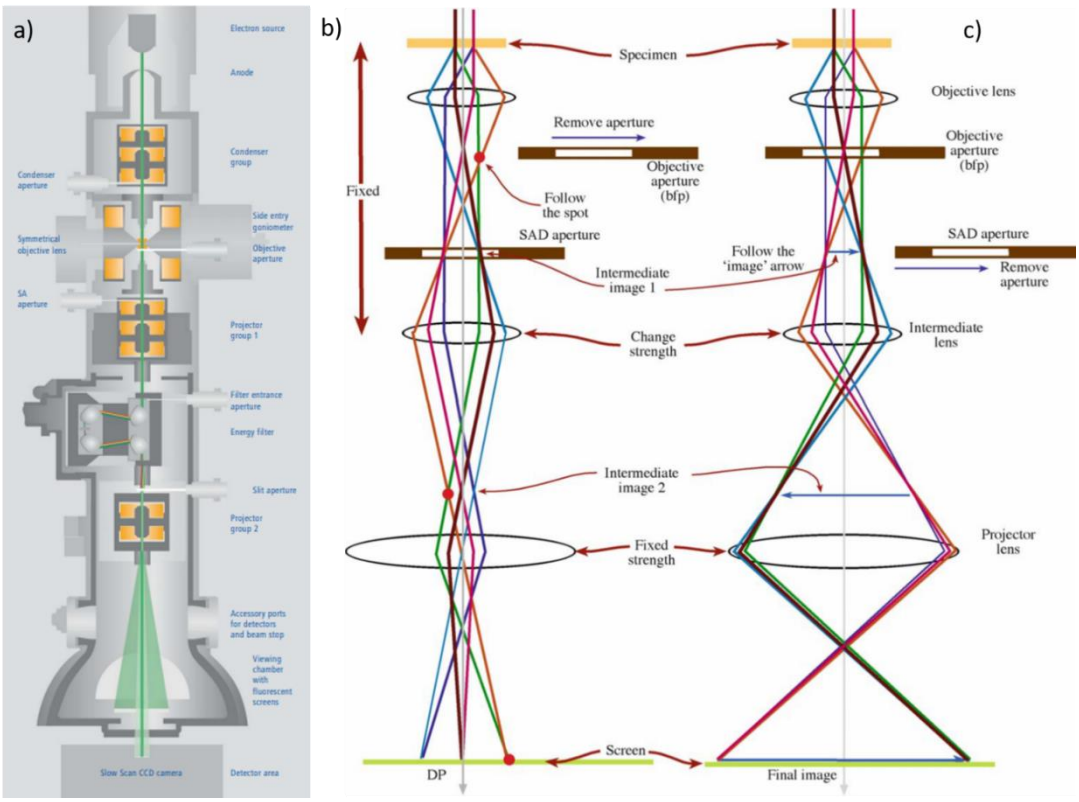

Figure 2.10: a) Column diagram of the Zeiss Libra 200 TEM. Ray diagram of a TEM for b) imaging mode, where the image is projected onto the viewing screen, and c) diffraction mode, where the diffraction pattern is projected onto the viewing screen. In each case, the intermediate lens selects either the image plane or the back focal plane of the objective lens as its object. Adapted from [172].

III. Scanning transmission electron microscopy (STEM):

With the development of aberration correctors, the electron probe can be focused at the nanometer scale, and another mode of operation of microscopes is called: scanning transmission electron microscopy (STEM). The irradiation is then done by a converging beam that sweeps the surface of the sample. Figure 2.11 shows the primary detectors of electrons transmitted through the sample. Just like for conventional microscopy, it is possible to obtain images whose contrast depends on the crystallography of the sample and to acquire the image in a bright field ("Bright Field" detector, BF) or dark field ("Annular Dark Field" detector, ADF). The difference is in the way the electrons are collected and analyzed. While in TEM, these two imaging modes give images directly, in STEM, the image is reconstructed by relating the position of the electron beam to the intensity measured by the various annular detectors.

Thanks to the STEM mode, we can also access a particularly interesting signal by collecting the electrons scattered at large angles using the "High-Angle Annular Dark Field" (HAADF) detector. These are electrons that have interacted with the nuclei of atoms according to Rutherford scattering rules. The intensity of this signal is proportional to Z^{α}, with α between 1.5 and 2, and Z the average atomic number encountered by the probe across the sample. Since the nature of the scattering is incoherent, these Z contrast images are therefore much simpler to interpret than HRTEM images which take into account dynamical effects.

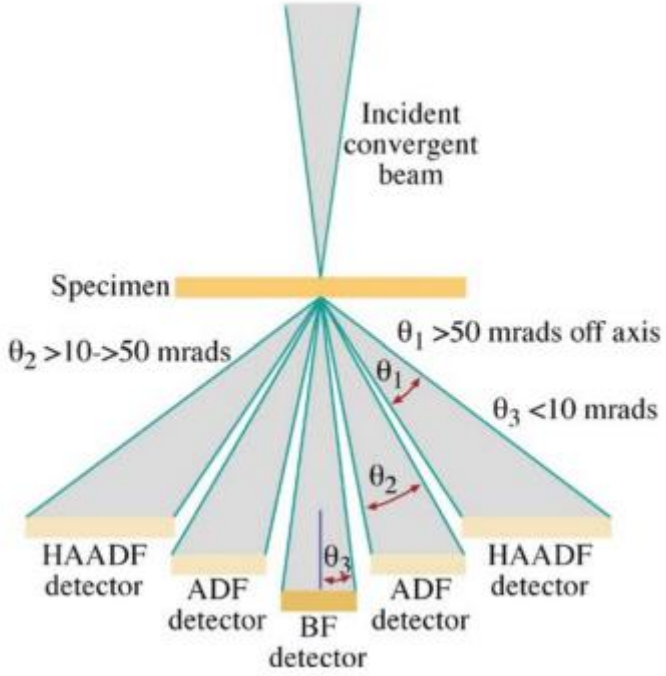

Figure 2.11: Diagram of the detectors available in STEM and the characteristic electron scattering angles collected by these detectors. Adapted from [172].

IV. Energy dispersive X-ray spectroscopy (EDS)

As represented earlier in Figure 2.12, X-rays are produced by electron-sample interaction. X-rays are due to the inelastic scattering of electrons and can be triggered in two ways, the Bremsstrahlung (continuum) or the characteristic x-ray emission. Bremsstrahlung X-rays result from electrons that lose energy due to the deceleration when they interact with an atom (Figure 2.12a). Characteristic X-rays are the X-ray emission caused by the transition of an electron

from an outer shell towards the inner/deeper shell. This transition occurs due to the hole created in the first place by a high-energy incident electron from the beam (Figure 2.12b). The X-ray emission energy is equivalent to the energy level difference between the outer and inner shell electron involved in the transition. Hence, the characteristic X-ray emissions are seen as sharper peaks in the spectra with the wavelength or energy equal to the transition concerned. This can be translated into determining the nature of the atom and inner shell involved in the process.

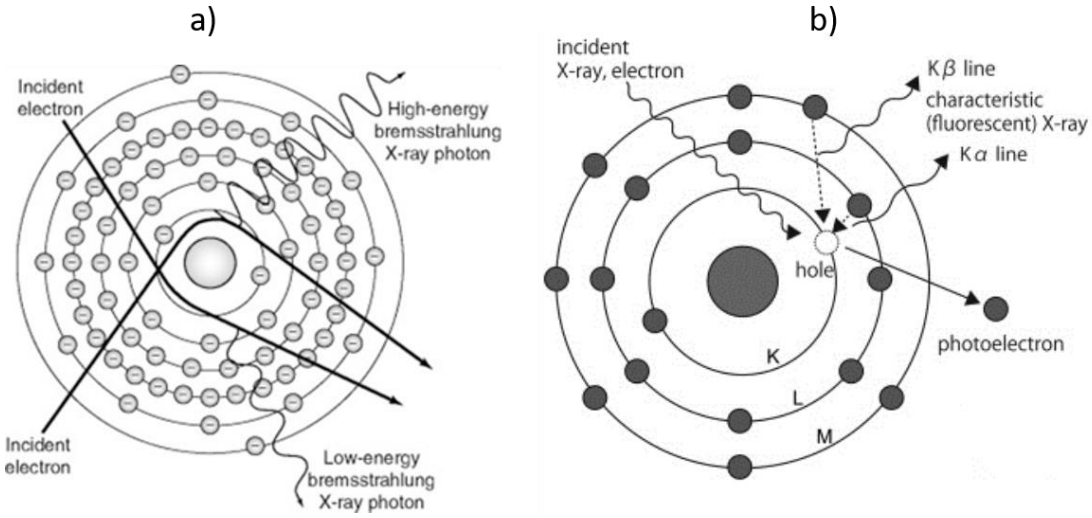

Figure 2.12: The process of a) Bremsstrahlung and b) characteristic x-rays emission.

At LEM, we used a Zeiss Libra 200 MC which has a FEG-Schottky electron source coupled with a monochromator. This makes it possible to gain spatial resolution (which is at best 1.2 Å at 200 kV). It can operate for acceleration voltages of 40, 60, 80, and 200 kV, which allows a compromise between resolution and degradation of the material. It is equipped with an UltraScan 1000 CCD camera (Gatan). High angle annular dark-field (HAADF) images and energy dispersive spectroscopy (EDS) was performed in Scanning TEM (STEM) mode with a nanometric probe.

V. TEM analysis

The TEM micrographs were evaluated using Digital Micrograph 1.8. The Fast Fourier Filtered (FFT) patterns were obtained from the HRTEM micrographs. All of the information in a given HRTEM micrograph can be found in the FFT of that image, but it is only in a frequency-based domain. If there is any periodic pattern in the original image, it will correspond to spots in the FFT. This is how the inverse FFT (IFFT) is made: Apply a bandpass mask to the FFT pattern of an HRTEM micrograph with a specific frequency range. In this way, all spatial frequencies outside the mask are filtered out, and the IFFT calculation shows only the information you want from reciprocal space in real space.

2.2.3 Optical characterization

2.2.3.1 Photoluminescence

In bulk materials and semiconductor nanostructures, photoluminescence (PL) spectroscopy is a convenient, contact-free, and non-destructive technique to study the optical properties and determine the electronic impurity states of the material. In PL spectroscopy, photons with higher energies than the semiconductor bandgap are used to excite electrons from the valence

band to the conduction band, creating electron-hole pairs. These carriers then relax by either recombining non-radiatively, emitting phonons or transferring the energy to other particles, or recombining radiatively to emit photons. This process is called photoluminescence. In PL spectroscopy, the emitted photons are detected, from which information about the electron energy levels and carrier lifetimes can be extracted.

The interband transitions are intrinsic transitions with greater energy than the bandgap. The second type of transition is extrinsic, which involves defects or impurities in the gap. A band diagram with several extrinsic transitions is shown schematically in Figure 2.13. Gilliland's review provides an in-depth discussion of PL spectroscopy [173].

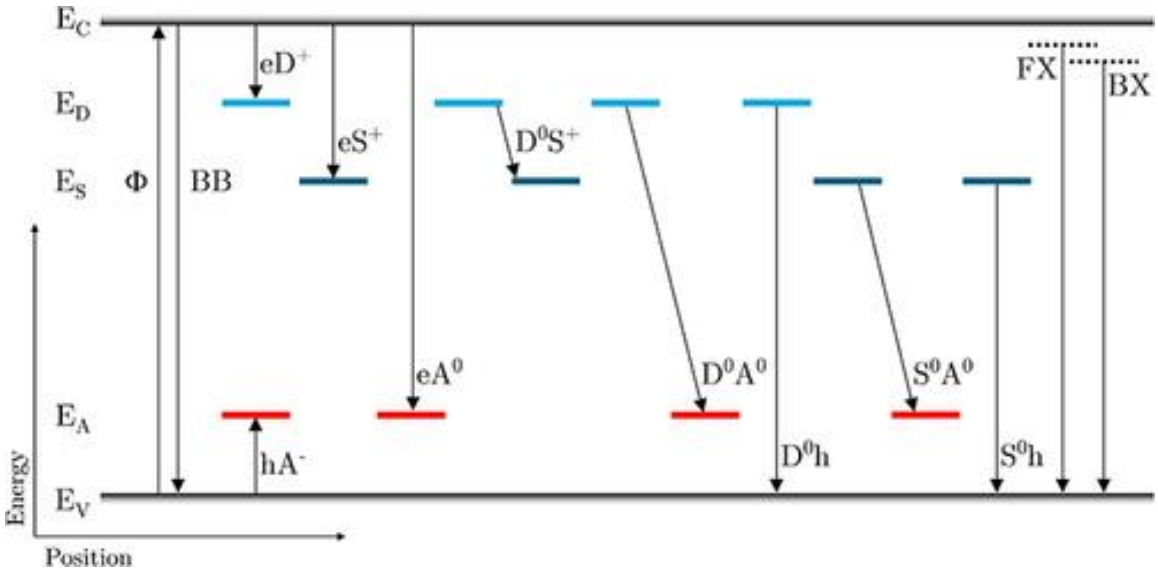

Figure 2.13: Band diagram of transitions in a semiconductor with a shallow donor level at E_D, a shallow acceptor level at E_A, and a deep donor-like level at E_S. Free (FX) and bound (BX) exciton transitions are given with reference to the band-to-band (BB) transition. The conduction band minimum is labeled with E_C and the valence band maximum with E_V. Adapted from [174].

At GEMAC, PL experiments were conducted by Dr. Alain Lusson. The experimental setup for photoluminescence measurements is represented in Figure 2.14.

This assembly is composed of the following elements:

1. An excitation source produced by a He-Cd laser, most photoluminescence measurements were performed with an excitation power of 10 mW and a wavelength emitting in UV ($\lambda = 325$).
2. A sample holder immersed in a cryostat in a bath of helium (4 K) and nitrogen shield (77 K). The latter thus makes it possible to maintain the samples at a very low temperature (2 K) to better observe the exciton lines in the photoluminescence spectra. Also, this cryostat is coupled to a heating system which varies the temperature up to 300 K.
3. A device of mirrors, lens, and diaphragms to collect photoluminescence. Indeed, the incident beam is directed towards the sample using mirrors tilted 45°. Diaphragms are placed on the path of the beam to attenuate the lines plasma from the laser. The power density after focusing is approximately 100 W/cm^2 on the sample. The

photoluminescence signal emitted by the sample is collected by one lens and focused by another achromatic lens on the slit of the monochromator in order to be analyzed.

4. A monochromator for analyzing the photoluminescence spectrum. It is the determining component of the PL assembly seen that the choice of the network that it contains, the opening width of the entry and exit slits, as well as its focal length, make it possible to obtain with precision the separation of the different lengths of wave-making up the PL spectrum emitted by the sample. Our system is equipped with a Jobin Yvon TRIAX 550 monochromator which contains two gratings of 600 or 1800 lines / mm with a focal length of 0.55 m and a minimum slit width of 20 µm. Its resolution is around 0.2 meV.
5. A detection system consisting of a CCD camera cooled with liquid nitrogen (77 K) with a resolution of 1024 × 256 pixels of 25 µm in diameter each. This system detects the photoluminescence signal and converts it into an electrical signal. In high-resolution PL measurements (U1000 dual monochromator), a photomultiplier is used to avoid the resolution limit by the pixel size of a CCD camera.

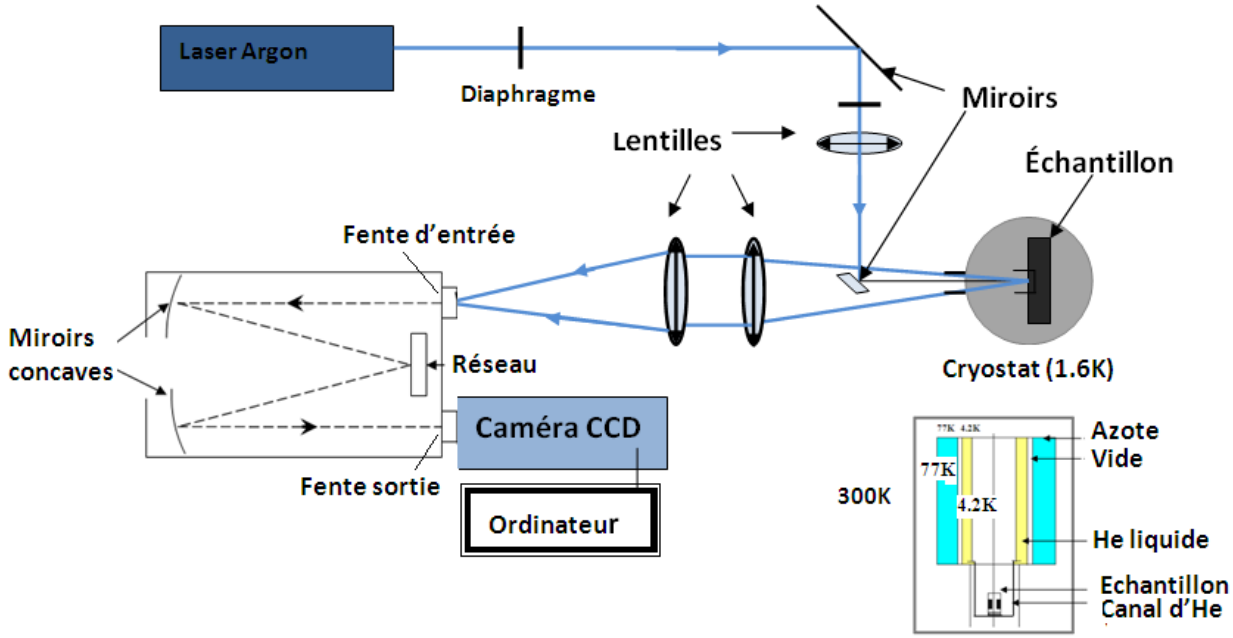

Figure 2.14: PL setup available at GEMAC

2.2.3.2 Cathodoluminescence

As mentioned above, cathodoluminescence (CL) is a luminescence signal generated by the de-excitation of a material subjected to electronic excitation. This technique is generally used in a SEM, making it possible to take huge advantage of a much more local excitation than in photoluminescence. Moreover, due to the absence of a continuous laser emitting in UV-C (280-100 nm), the CL is particularly well suited to the study of wide bandgap semiconductors.

CL measurements were carried by Dr. Christophe Arnold and Sumit Kumar. Figure 2.15 presents the experimental setup for cathodoluminescence used in this thesis. The electron excitation is performed in a MEB Jeol 7001F operating between 1kV to 15 kV for a current of up to 200 nA. An Everhart and Thornley detector collect secondary electrons. It is used in imaging as well as in CL experiments. The ultimate resolution of this microscope is 1.2 nm

obtained at 30 kV, low current (<1 nA), and short working distance ("working distance", WD ≈ 5 mm).

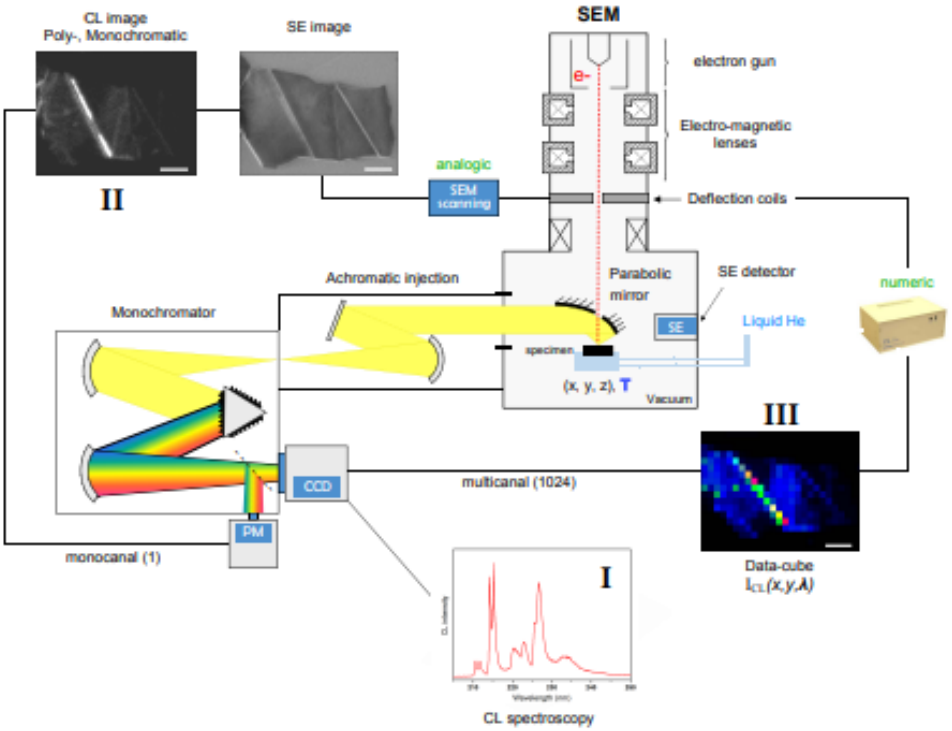

Figure 2.15: Cathodoluminescence setup installed at GEMaC. The different acquisition modes are represented: I) Classical one-point spectroscopy. II) Image of luminescence at a given wavelength. III) Hyperspectral imagery: Each pixel of the image contains a spectrum. Adapted from [175].

CL experiments require collecting the photons emitted by the crystal. This is done using a retractable parabolic mirror (RPM2000, Horiba Jobin Yvon (HJY)). It is inserted between the end of the electronic column and the sample and imposes a working distance of 12mm. For analysis conditions of 15 kV and 5 nA, the resolution is 3 nm (SE imaging).

The system also includes a cryostat (CF302 - Gatan), allowing the temperature of the crystal to be regulated between 5 and 300 K. The cryogenic system is based on a removable door which contains a sample holder and allows liquid helium to circulate around it, and in a finger cooling the sample. The temperature is measured at the level of this cold finger.

The sample can be moved in all three directions of space using micrometer motors. In-plane movement allows the exploration of different areas of the sample while vertical movement is used to focus. The source of photons (coming from the sample) is placed at the focus of this mirror to collimate the emitted light and send it to the detection chain.

The photons are then headed to the monochromator's injection box, which focuses the photons on the entry slit. The various optical elements are mirrors (aluminum coated with an MgF2 deposit to limit absorption in the UV) which eliminates the chromatic aberrations specific to the lenses. This allows the acquisition of spectra over a wide range between 190 and 1000 nm without changing the optical alignment. The spectrometer (TRIAX550, HJY) has three networks of 150, 600, and 1800 lines/mm blazed at 500, 300, and 250 nm, respectively, making it suitable for infrared to ultraviolet studies. The ultimate spectral resolution for the

1800 lines / mm grating is 0.02 nm for a 10 µm entry slit. The scattered light can be transmitted to a silicon CCD camera 1024 × 256 pixels (25µm per pixel) (Symphony, HJY) cooled with liquid nitrogen, or a photomultiplier (Hamamatsu, HJY) cooled by Peltier effect to -30 °C depending on the desired acquisition mode.

With this system, it is possible to acquire data in different ways, as shown in Fig.2.15. Mode I is the classical spectroscopy mode. The position of the electron beam is fixed on the region of interest for obtaining a local spectrum. Mode II is the CL imaging mode. Here the electron beam scans the region of interest. Photons are collected with the photomultiplier (PM). The intensity measured by the PM at any time is related to the position of the electron beam to construct a luminescence image at the selected wavelength. This acquisition mode works in parallel with the acquisition of SEI images, which makes it possible to relate a luminescence signal with the topography of the sample. Acquisition mode III is mapping mode (hyperspectral images). It allows the acquisition of spectra at different points of the sample along a line or on a surface. The position of the electron beam is controlled by a box (CL Link, HJY). Data acquisition and processing is performed with LabSpec software (HJY). This method allows access to all the spectral information of the sample over the defined area.

2.2.4 Other techniques

2.2.4.1 Atomic force microscopy (AFM)

We used a Bruker Dimension ICON atomic force microscope equipped with automatic imaging optimization (ScanAsyst) in PeakForce tapping mode. Atomic Force Microscopy is based on detecting the forces of interactions between a tip and the surface of a conductive or insulating sample. The displacement of the tip above the sample (lateral and vertical) is ensured by a piezoelectric tube. AFM allows the characterization of the surface state (roughness) and metrological measurements at the nanometric scale.

2.2.4.2 X-Ray diffraction (XRD)

The structural quality of ZnS layers has been assessed by high-resolution x-ray diffraction HRXRD measurements using a SEIFERT XRD 3000 diffractometer (Cu-Kα radiation, $\lambda_{Cu\text{-}K\alpha}$ = 0.15406 nm) with a Gobël mirror prior to the Ge220 two-bounce monochromator and soller slits in front of the detector. Experiments were conducted by Dr. Gaëlle Amiri and Sumit Kumar.

2.2.4.3 Edwards evaporator

We have used Edwards Auto 306 evaporator to deposit Au films on our substrates. We utilized pure Au wire as a source, which first wets a tungsten filament. Then, a shutter is open, and Au atoms are evaporated toward the sample. The deposition was done under a high vacuum (10^{-6} mbar) and at room temperature. The minimum thickness that can be reached is around 0.1 nm, given by the precision of the quartz crystal microbalance.

Figure 2.16 Edwards Auto 306 evaporator

Chapter 3

MOCVD growth of ZnS nanowires

Contents

This chapter is devoted to the MOCVD growth of ZnS thin films and nanowires. We will first study ZnS layers to understand the MOCVD growth regimes and kinetics. We will then use various characterization tools (XRD, SEM, and AFM) to assess the layer's structural and morphological qualities. Subsequently, we will investigate Au droplet formation on different substrates. Finally, we will carefully study the growth parameters leading to the best quality of ZnS NWs in terms of vertical alignment and uniformity.

3.1 Introduction

As discussed in the introduction chapter, the unusual optical properties of vertically aligned NWs open new opportunities for photonics applications. It is possible to create significant confinement and absorption of incident light using nanowire arrays by manipulating their physical characteristics such as diameter, height, and crystal phase. In a bottom-up approach, accurate control of the nanowire growth is therefore crucial to achieving the desired design.

Figure 3.1 shows examples of VLS assisted ZnS NWs using the CVD technique, taken from the literature [122,176]. In Figure 3.1a, ZnS NWs were grown on Si substrate with Au catalyst; the NWs are highly dense and randomly oriented. ZnS NWs grown with Ga catalyst on GaAs (111)B (see Figure 3.1) are uniformly aligned and vertically oriented. Hence, the first goal of this thesis is to achieve vertically oriented NWs with controlled morphology. We give a comprehensive investigation into the formation of ZnS NWs on various substrates (GaAs, GaP, ZnS buffer) utilizing Au as a catalyst.

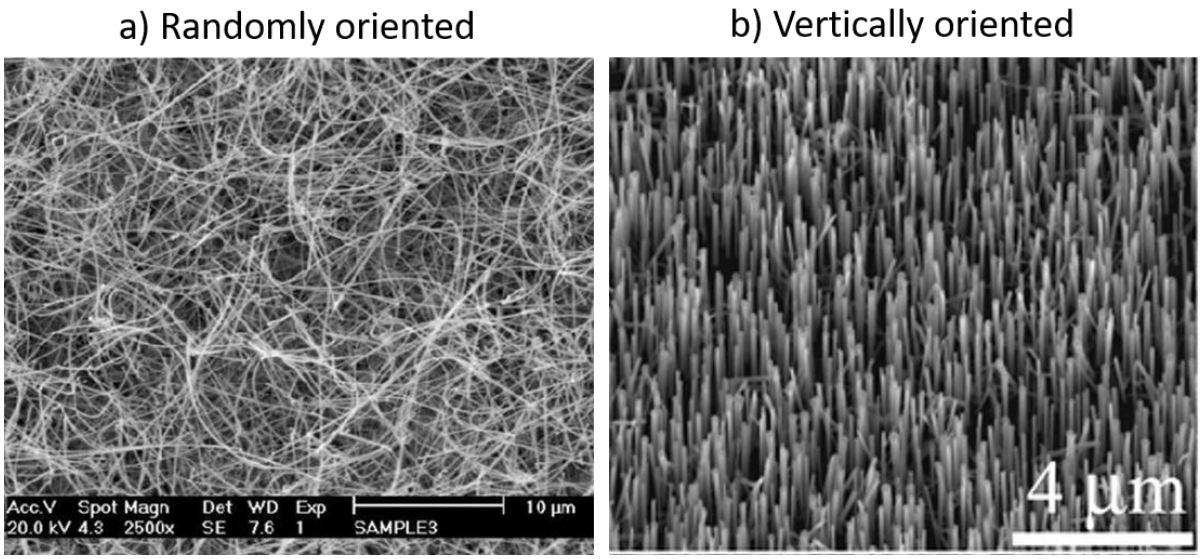

Figure 3.1: The example of ZnS nanowire growth a) random oriented on Si [176] and b) vertically oriented on GaAs (111)B [122].

3.2 ZnS thin films: MOCVD basic studies

We started our growth journey by studying the classical MOCVD growth parameters. We optimized the growth parameters such as temperature and precursor fluxes with ZnS thin film growth. Since thermodynamics, reaction kinetics, and mass transport play essential roles, a thorough investigation of MOCVD dynamics is required to provide insights into material development.

3.2.1 MOCVD growth regimes

For basic growth studies, we used standard GaAs (100) substrates. First, after introduction in the reactor, substrates are deoxidized at 550 °C for 10 min under a flow of H_2 gas. This is a typical process used in MOVPE. However, there is no in situ tool like RHEED to control the removal of the oxide on the surface. Deoxidation at a temperature higher than 550 °C damages the GaAs substrate (will be discussed in Chapter 6). Two series of samples were made: i)

varying growth temperatures in the range 320 - 570°C while maintaining constant DEZn and DTBS fluxes at a fixed ratio $R_{VI/II} = 2$, and ii) varying VI/II ratio between 0.6 and 3.2, keeping growth temperature at 450°C. All these samples underwent a 45-minute growing period.

From the decomposition kinetics of the organometallics detailed in chapter 2, we expect the optimum growth temperature conditions for the MOCVD growth of ZnS to be in the range 400°-500°C. A first series was made at various growth between 320°C and 570°C (samples TF1-TF9, see table 3.1). In Figure 3.2a, the growth rate is plotted as a function of the substrate temperature. We can identify three distinct growth regimes for MOCVD [177]: a) a kinetically limited regime between 320°C and 390°C, governed by surface reactions; b) a mass transport regime in the range 400-510°C, where species diffuse through the boundary layer just above the substrate; c) a re-evaporation regime, where adatoms desorb from the surface. The mass transport growth is characterized by high growth rates and a weak dependence on the substrate temperature. For semiconductor thins films, most MOCVD growth processes will likely occur in such a regime, where it is easier to control the growth rate. In the case of ZnS, 400-500°C appears as a suitable range, in agreement with the decomposition studies of DEZn and DTBS.

Type	Study	Reference	Tg (°C)	P_{DEZn} (Pa)	P_{DTBS} (Pa)	VI/II ratio	Substrate
Thin films	Temperature	TF1	320	7.8	15.6	2	GaAs (100)
		TF2	360				
		TF3	390				
		TF4	420				
		TF5	450				
		TF6	480				
		TF7	510				
		TF8	540				
		TF9	570				
	VI/II ratio	TF10	450	7.8	5.1	0.65	
		TF11	450		7.8	1	
		TF12	450		11.7	1.5	
		TF13	450		15.6	2	
		TF14	450		24.96	3.2	

Table 3.1: Sample list (thin films), indicating growth conditions.

The second series of ZnS thin films was fabricated to identify the regimes for various precursor fluxes, similar to the temperature investigation. During the experiment, the sulfur partial pressure was changed between 5.1 and 24.5 Pa while the zinc partial pressure and temperature remained constant at 7.8 Pa and 450 °C, respectively. Figure 3.2b depicts two growth regimes that emphasize the influence of sulfur precursor on the growth rate. In a first regime (low sulfur flows in the range between 5.1 and 12 Pa), the growth rate increases linearly with the sulfur flow, meaning that the growth proceeds under zinc-rich conditions. The growth rate starts to saturate when the sulfur flux supply rises over 12 Pa ($R_{VI/II} = 1.5$), and this is referred to as a sulfur-rich regime where the zinc supply now regulates the growth rate.

Interestingly, it is noteworthy that the transition between Zn-rich and S-rich regimes does not correspond to a precursor ratio of 1. This indeed may depend on the decomposition rate of each organometallic source at a given temperature. For the subsequent development of ZnS NWs (1D growth), it is important to have identified such sulfur- and zinc-rich regimes.

In conclusion, fundamental studies on ZnS thin films growth enabled us to identify mass-transport regime and zinc- (sulfur-) rich conditions. It also allows determining the optimized growth conditions for the ZnS buffer layer to be deposited on GaAs substrate, i.e., 450°C with $R_{VI/II} = 2$.

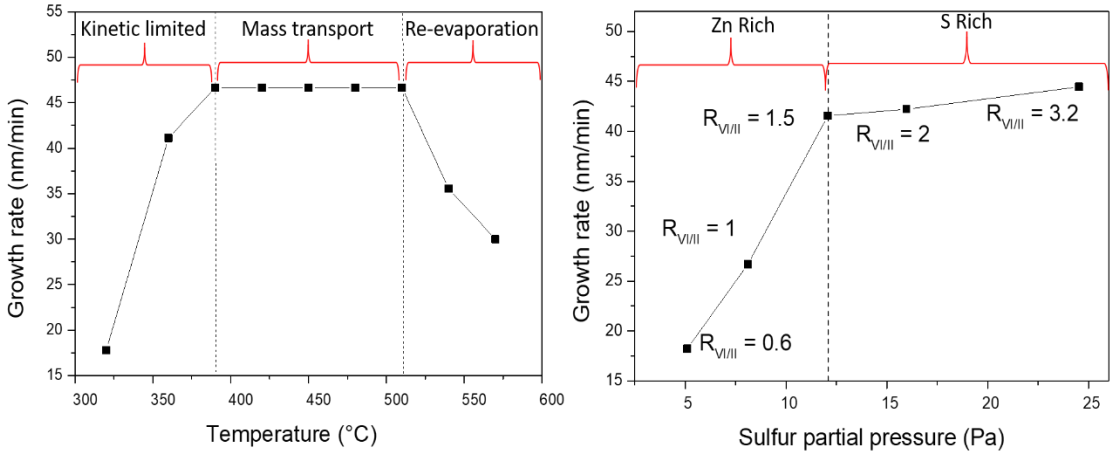

Figure 3.2. The growth rate of ZnS thin films as a function of a) substrate temperature, three growth regimes are identified for MOCVD, and b) DTBS partial pressure, Zn rich and S rich growth regimes are identified for our MOCVD system.

3.2.2 Choice of substrates

As discussed earlier, the vertical yield of ZnS NWs is significantly dependent on the substrate and its orientation. ZnS NWs growth on GaAs substrates yields homogenous vertical arrays [121], however, GaP substrate would be worth considering since the lattice mismatch is minimal with ZnS. The lattice mismatch of a substrate with the semiconductor compound can be calculated by the following expression:

$$\text{Mismatch} = \frac{a_{substrate} - a_{ZnS}}{a_{substrate}}$$

Where a is the lattice constant.

Semiconductor compound	Lattice parameter a (Å)
ZnS	5.42
ZnSe	5.66
GaAs	5.65
GaP	5.45
Si	5.43

Table 3.2: Semiconductor compounds with the lattice parameter values.

For ZnS, this calculates a mismatch of 4 % with GaAs and 0.5% with GaP. These substrates are commercially available, even if GaP substrates are expensive! To favor the emergence of ZnS NWs on a lattice-matched surface, we can also prepare a ZnS layer (called buffer layer) on the III-V substrates.

Hence, we employed a variety of substrates to gain a comprehensive understanding of the influence of substrates on the morphology and structural properties of NWs. In this study, we used the following substrates for NW growth:

1) GaAs – (100), (111)A, and (111)B
2) GaP (111)
3) ZnS buffer/GaAs or /GaP for homoepitaxial growth

In the following sections, we will discuss the crystalline properties of ZnS thin films using XRD and SEM.

3.3 Characterization of ZnS buffer layer

The crystalline properties of ZnS thin films were studied to assess and optimize the quality of the ZnS buffer layer on which the gold catalyst droplet will lay and hence will trigger the NW growth.

3.3.1 Structural analysis using XRD

Figure 3.3a gathers XRD measurements (θ-2θ scans) of ZnS layers grown on GaAs (100) at different temperatures between 320 and 570 °C. The GaAs substrate diffraction peaks are seen in all spectra, namely (002) and (004), at 2θ = 31.6° and 66°. For the lowest growth temperatures (from 320 to 390 °C), a rather broad peak observed at 2θ = 28.4° is attributed to ZnS (111) plane diffraction. It is clear that increasing the growth temperature above 400°C changes the film orientation, which turns to the (001) plane. The intensity of the (002) diffraction at 2θ = 33° increases with increasing the temperature up to 480 °C. In Figure 3.3b, the variation of the full width half maximum (FWHM) of ZnS (002) diffraction peak is plotted as a function of the growth temperature. We find a minimum FWHM around 480 °C. Thus, XRD measurements indicate an improvement in crystallization up to 500°C. Above 510°C, due to re-evaporation of the adsorbed species, the thickness strongly decreases, and the comparison of crystal quality is not relevant.

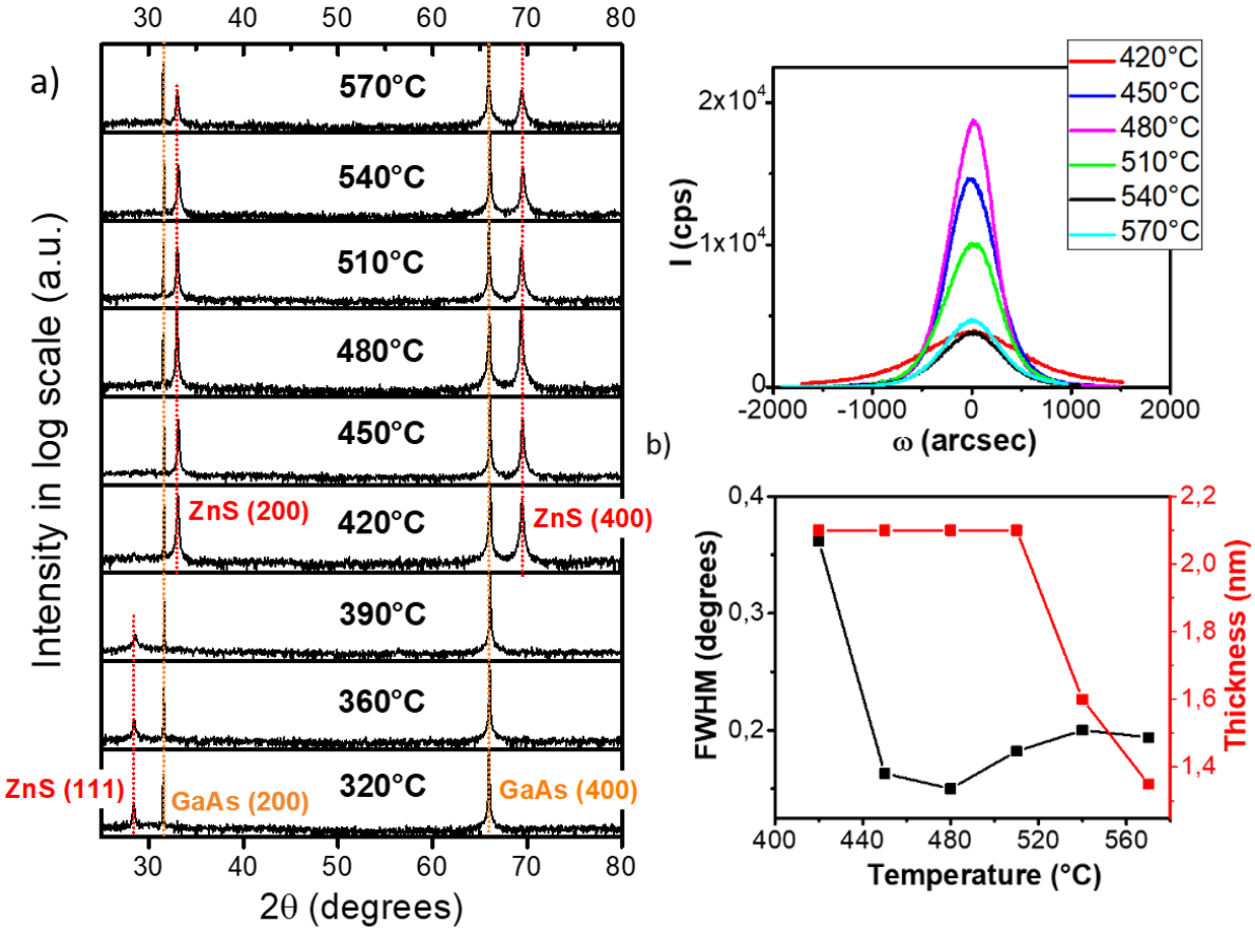

Figure 3.3: X-ray diffraction analysis of ZnS layers grown at various temperatures, from 320°C to 570°C: a) θ-2θ scans, and b) ω-2θ rocking curves and full widths at half-maximum.

In the same way, we performed XRD measurements of the ZnS thin films grown at 450 °C different sulfur partial pressure, or VI/II ratios (between 0.6 and 3.2). Figure 3.4a gathers the θ–2θ scans, confirming that the grown films are crystalline. In all spectra, GaAs substrate diffraction peaks are still observed at 2θ = 31.6° and 66°, as well as the ZnS (002) and (004) peaks at 2θ = 33° and 2θ = 69.5°. ω-2θ scans (rocking-curves) were also performed, and the variation of FWHM of ZnS (002) diffraction peak are plotted in Figure 3.4b as a function of sulfur flux. It was found that the ZnS (002) peak sharpens when the film thickness reaches 2 µm. This is a logical behavior since the material is highly dislocated close to its interface with the hetero-substrate. Hence the crystal quality improves with thickness. We found a minimum value of FWHM for a VI/II ratio of 2. Above that value, sulfur-rich conditions do not improve the crystalline quality of the film.

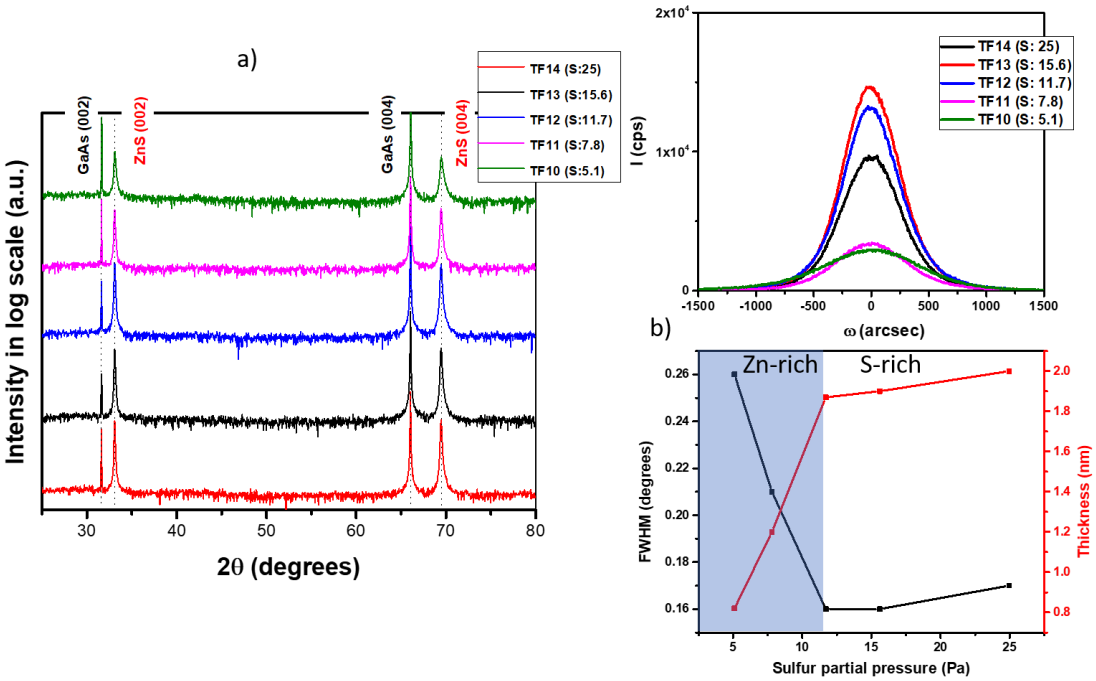

Figure 3.4: X-ray diffraction analysis of ZnS layers grown at different sulfur partial pressures and 450°C (TF10-TF14): a) θ-2θ scans, and b) ω-2θ rocking curves and full widths at half-maximum.

3.3.2 Morphological analysis using SEM

SEM images for samples with temperature variation are gathered in Figure 3.5. We observe a rough and polycrystalline-like surface with faceted grains at low temperatures 320-390°C. This is consistent with the low crystal quality of the samples and the change of film orientation from [001] to [111]. While at temperature 450 °C, the surface looks relatively smooth. At high growth temperature (540°C onwards), the surface is degraded as roughness increases and the presence of pin-holes is noticed.

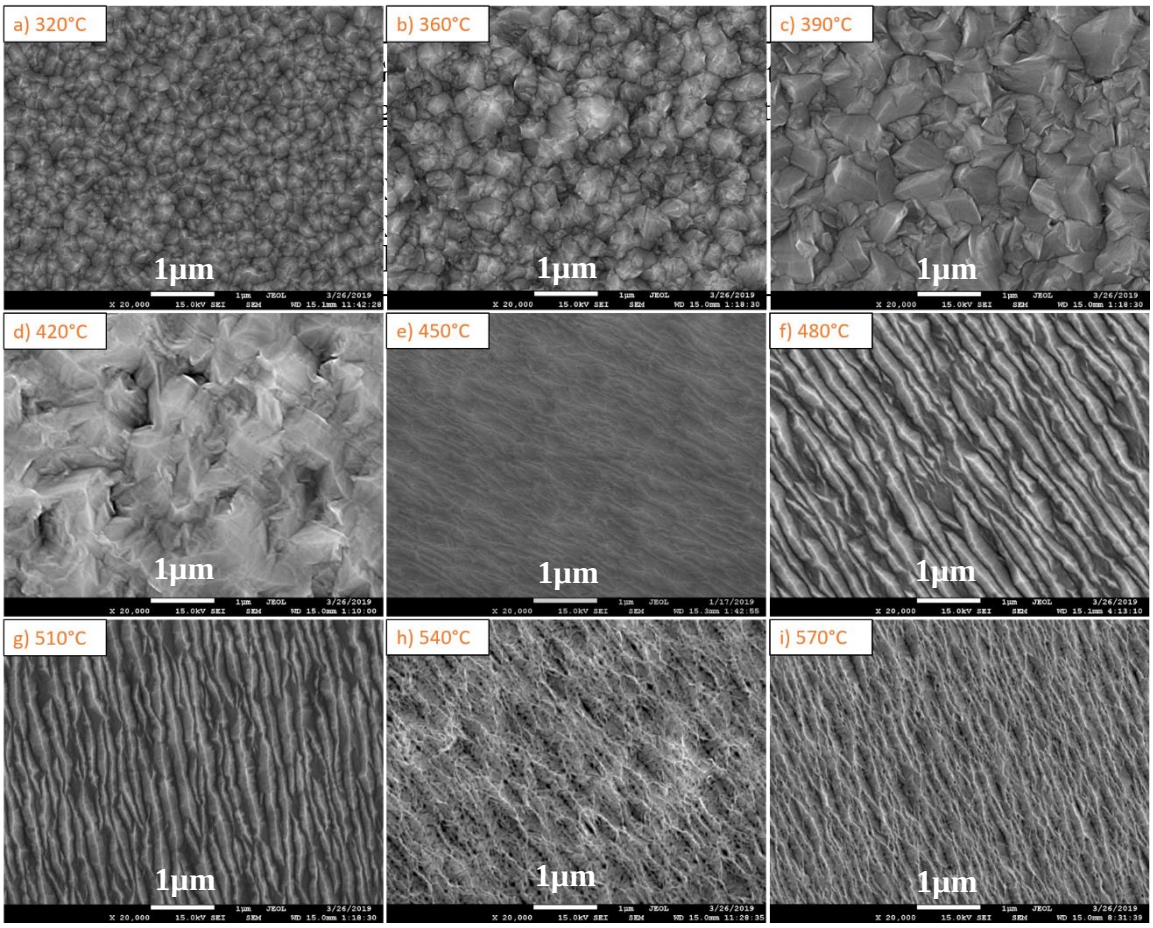

Figure 3.5: SEM images of ZnS layers grown on GaAs (100) with different temperature: a) 320°C, b) 360°C, c) 390°C, d) 420°C, e) 450°C, f) 480°C, g) 510°C, h) 540°C, and i) 570°C. At temperature 450 °C, the surface appears smooth and flat. Scale bar 1µm.

The SEM images of ZnS thin films grown with different VI/II ratios are presented in Figure 3.6. The films grown at a low VI/II ratio (0.6 and 1) show faceted surfaces, elongated pyramids, and pinholes. The surface appears smoother with a ratio of 1.5 and 2. At the highest ratio (3.2), the surface exhibits flat areas and shows faceted cavities with holes at the bottom. Such pin-holes may arise from threading dislocations.

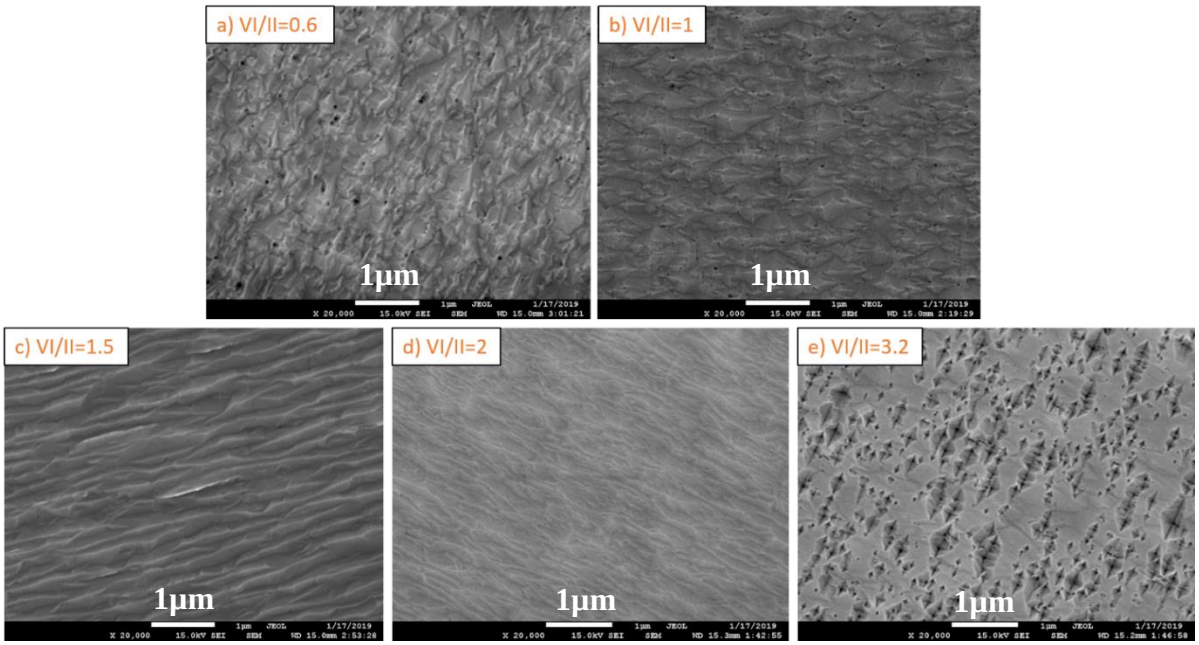

Figure 3.6: SEM images of ZnS layers grown on GaAs (100) with different VI/II ratio: a) 0.6, b) 1, c) 1.5, d) 2, and e) 3.2. The layer grown with a ratio of 2 is smoother and flat. Scale bar 1µm.

In conclusion, the above analysis led to an optimized VI/II ratio of around 2, i.e., sulfur-rich regime. Therefore, we will set $R_{VI/II} = 2$ and growth temperature at 450°C for the deposition of the ZnS buffer on different orientations of GaAs and GaP substrates.

3.3.3 Characteristics of ZnS buffer layer on GaAs (111)A and (111)B substrate

The growth of ZnS thin films was also performed on GaAs (111)A and (111)B. This was done using optimized conditions, i.e., temperature 450 °C and VI/II = 2 (S: 15.6 Pa, and Zn: 7.8 Pa).

XRD patterns of two ZnS thin films grown on GaAs (111)A and (111)B samples are shown in Figure 3.7. GaAs (111) and (222) diffraction peaks are seen at $2\theta = 27.3°$ and 56.4°, respectively. We observe that ZnS films crystallize in (111) orientation, thus following the same orientation as GaAs substrate. ZnS (111) is measured at $2\theta = 28.5°$ and ZnS (222) at $2\theta = 59.2°$.

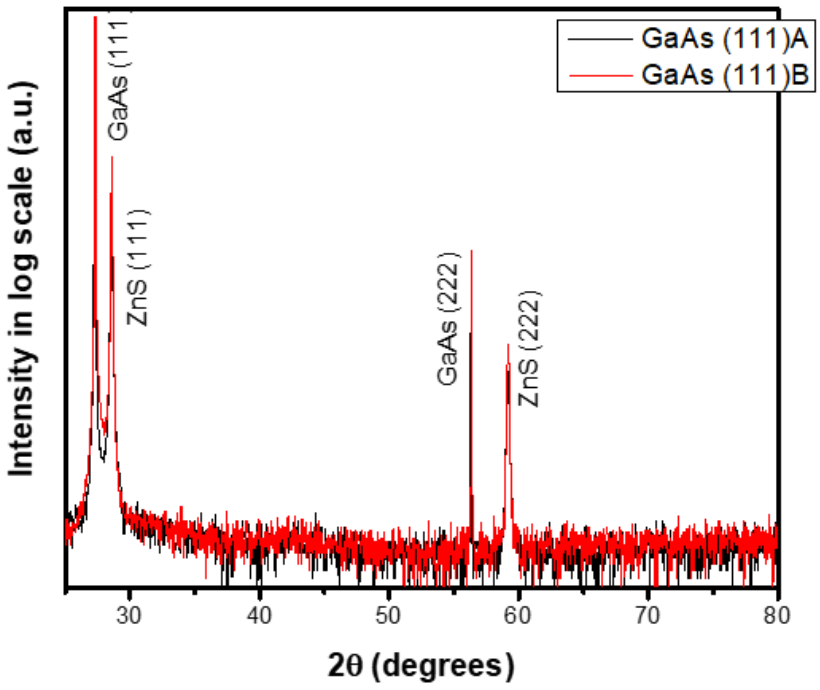

Figure 3.7: XRD plot of ZnS thin films grown on GaAs (111)A and (111)B under optimized conditions.

The SEM images of ZnS films on substrate GaAs (111)A and (111)B are shown in Figure 3.8. ZnS film on GaAs (111)A exhibits huge pyramids on the surface, while film on (111)B substrate looks relatively smooth and flat. However, the surface is still faceted and composed of pyramids, but smaller for this latter case.

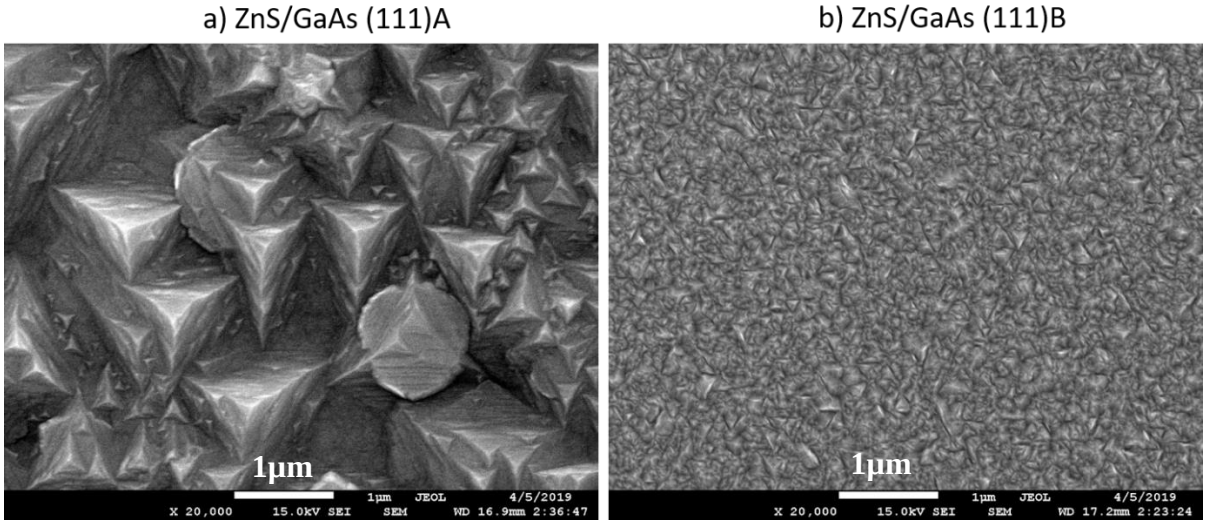

Figure 3.8: SEM images of ZnS layers grown on a) GaAs (111)A and b) GaAs (111)B. Formation of pyramids has been observed on GaAs (111)A, and films grown on GaAs (111)B are smoother. Scale bar 1μm.

The AFM images of ZnS films are shown in Figure 3.9. The morphology is consistent with the one observed by SEM. The RMS (root mean square) roughness of the ZnS films grown

on GaAs (111)A (Figure 3.9a) is 43nm. On the other hand, ZnS films grown on GaAs (111)B are smoother with a RMS roughness of 1.95 nm (Figure 3.9b).

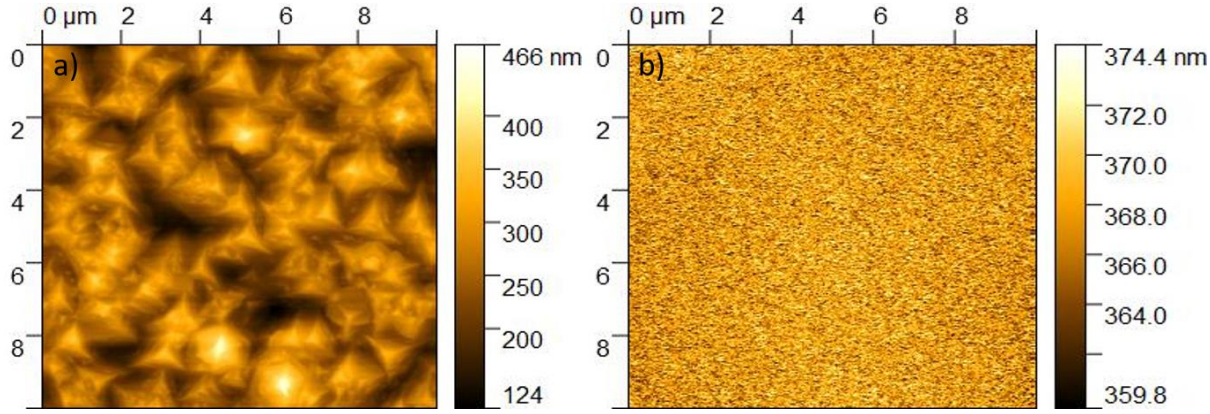

Figure 3.9: AFM images of ZnS layers grown on a) GaAs (111)A has a RMS roughness of 43 nm, b) GaAs (111)B has low roughness of 1.95 nm (right).

3.4 Au dewetting on different surfaces

The VLS and VSS processes involve catalyst droplets on the substrate or pseudo-substrate surface. In the following section, we investigate the formation of gold nanoparticles on GaAs (100), GaAs (111)B, and ZnS/GaAs (111)B.

A thin Au layer (typically a few nm thick) can be deposited on the substrates using the thermal evaporator Edwards Auto306 available at GEMAC. Subsequently, a dewetting process (annealing at high temperature) produces the Au nanoparticles. The dewetting of an Au film initiates the formation of nanoparticles favored by Ostwald ripening and island coalescence [178]. The dependence on the film thickness, annealing duration, and annealing temperature on the size of the nanoparticles has been well studied in the past on different substrates [179,180]. The size of gold nanoparticles is directly proportional to the thickness, annealing duration, and temperature, while the density is inversely proportional. However, the Au droplet statistics on the ZnS buffer are still to be drawn. Herein, the size distribution and the density of Au nanoparticles on different substrates were estimated after analyzing SEM images and using ImageJ software.

3.4.1 Au dewetting on GaAs (100)

We have studied the dependence of dewetting duration, Au film thickness, and dewetting temperature on the nanoparticle's size and density. This was done on GaAs (100) substrates since they are much cheaper than the (111)B oriented ones, and we expect the same proportionality behavior for all the substrates. Keeping in mind that the diameter of the growing nanowire may follow one of the Au droplets, we aim to have a clear insight into the size and density of nanoparticles before initiating the catalyzed growth and possibly optimize such characteristics according to the requirement for the NW growth. Figure 3.10a shows a SEM image of gold droplets formed after dewetting a 3 nm thick Au layer at 500°C for 30 min. This image allowed us to calculate the nanoparticle diameter and density statistics, presented in Figure 3.10b. The average diameter is 24 nm with a density of ~570 particles/µm^2. The full width at half maximum (FWHM) is calculated as 11.2 ± 0.5 nm from the Gaussian curve.

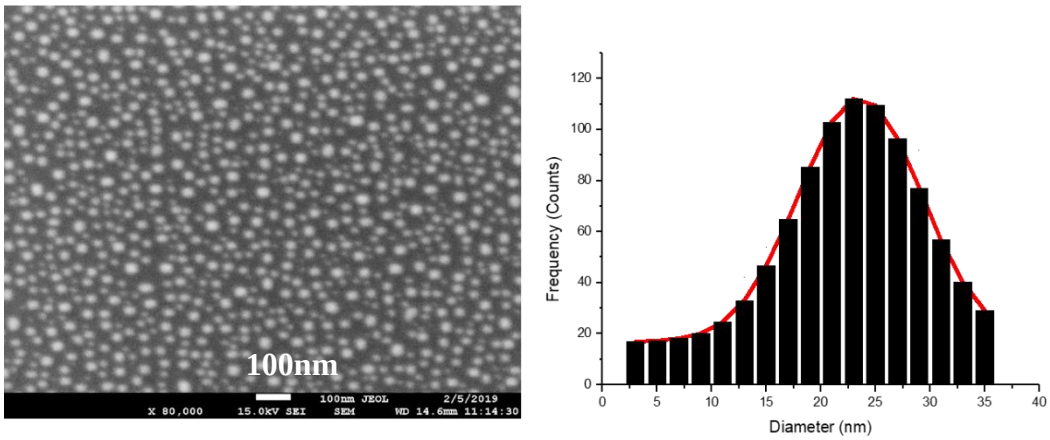

Figure 3.10: a) SEM image of gold droplet formation on GaAs (100) substrate, b) statistical analysis of droplets from SEM image. Au thickness = 3 nm and dewetting at 500 °C for 30 min. Scale bar 100 nm.

3.4.1.1 Effect of dewetting time

The effect of dewetting time on the average size and density of nanoparticles is represented in Figure 3.11. The dewetting time varied from 10 min to 120 min for a 3 nm thick Au film dewetted at 500 °C. The size of nanoparticles directly relates to dewetting duration (see Figure 3.11a), i.e., increases with time, while the density shows the opposite tendency. This is expected because the overall volume of Au remains constant on the substrate surface; if the size of gold droplets increases, then droplet volume increases, thus the density of the droplets on the surface will decrease (see expression below, the droplet density and volume of the droplet has an inverse relationship).

$$\text{droplet density} \times \frac{4}{3}\pi\left(\frac{diameter}{2}\right)^3 = \text{constant}$$

The density of Au nanoparticles decreases from 810 to 400 particles/μm^2 with dewetting temperature, whereas the average size increases from 21 to 27 nm.

The FWHM is calculated for each Gaussian distribution and plotted in Figure 3.11b as a function of dewetting time. The FWHM values increase from 11.2 to 15 nm with an error of 0.5 nm. A low FWHM value signifies a lower Au particles size distribution from the average value. Thus, shorter dewetting time favors a more homogenous distribution of Au droplets.

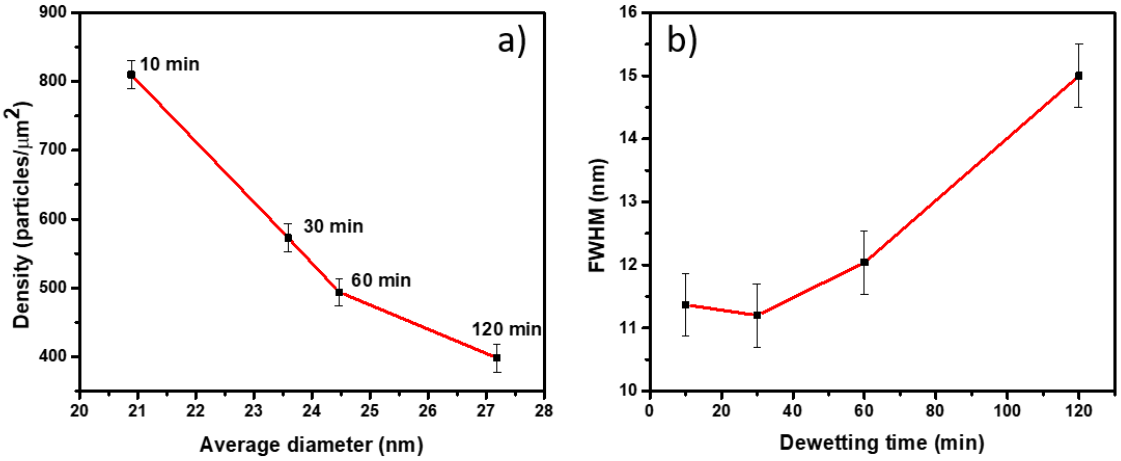

Figure 3.11: a) The plot of nanoparticle density as a function of average size (error bar, 50 particles), b) the full width half maxima (FWHM) calculated from the gaussian distribution of Au nanoparticles plotted as a function of dewetting time (error bar, 0.5 nm). More homogenous distribution of Au nanoparticles is achieved at a shorter dewetting duration.

3.4.1.2 Effect of Au film thickness

Next, we developed the nanoparticles statistics to study the effect of Au film thickness. We varied the Au thickness between 1 and 5 nm. The dewetting was performed at 500°C for 120 min. The density of Au nanoparticles decreases from 480 to 200 particles/μm^2, whereas the average size increases from 22 to 40 nm. The FWHM values increase from 7 to 24 nm. Thus, lower Au thickness favors a homogenous distribution of Au droplets.

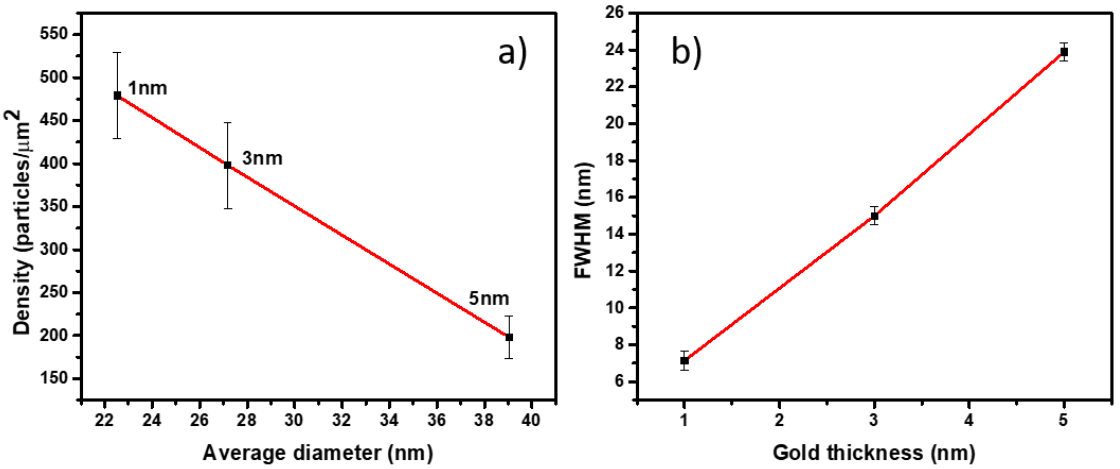

Figure 3.12: a) The plot of nanoparticle density as a function of average size for different Au thickness (error bar, 50 particles), b) the full width half maxima (FWHM) calculated from the gaussian distribution of Au nanoparticles plotted as a function of Au thickness (error bar, 0.5 nm). Homogenous distribution of Au nanoparticles is achieved at lower thickness.

3.4.1.3 Effect of dewetting temperature

We continued the nanoparticles statistics by studying the dewetting temperature effect. We varied temperature between 400 and 550°C. The dewetting was performed for 3 nm thick samples for 120 min. The density of Au nanoparticles decreases from 640 to 290 particles/μm^2, whereas the average size increases from 11 to 43 nm. We have noticed a significant difference in the average size of nanoparticles dewetted at a lower temperature (400°C). This might be due to a lower diffusion of gallium inside the Au nanoparticles originating from GaAs substrate (more detailed in Chapter 4). The FWHM values increase from 9 to 17 nm. Thus, lower temperature favors a homogenous distribution of Au droplets.

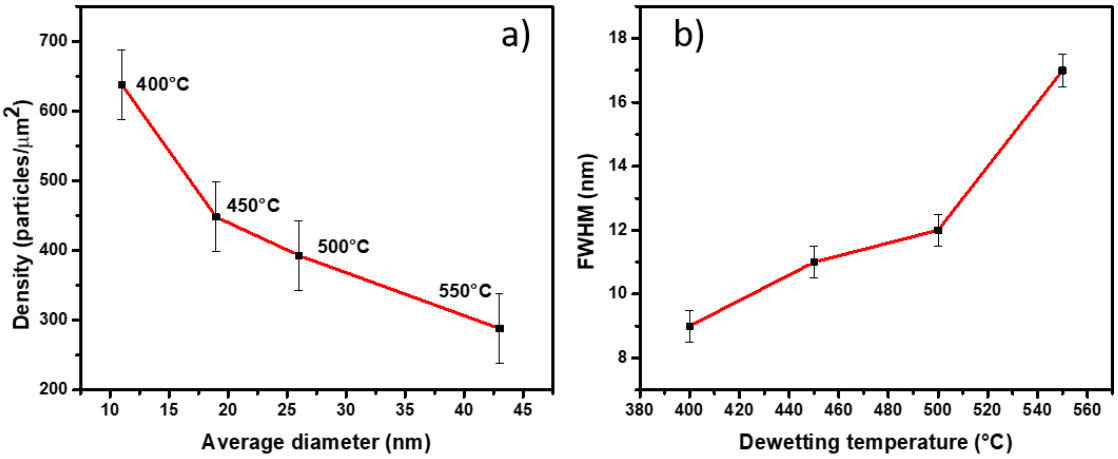

Figure 3.13: a) The plot of nanoparticle density as a function of average size for different dewetting temperatures (error bar, 50 particles), b) the full width half maxima (FWHM) calculated from the gaussian distribution of Au nanoparticles plotted as a function of dewetting temperature (error bar, 0.5 nm).

In conclusion, we have studied the Au nanoparticles distribution over GaAs (100) surface and plotted the tendencies of dewetting temperature, time, and Au thickness. We have found that the average size, density, and uniform distribution of nanoparticles could be better controlled with these parameters. The optimized conditions for Au dewetting frequently used in this thesis are 1 nm Au thickness, 500°C dewetting temperature, and 10 min dewetting duration. However, we keep in mind that, after the dewetting process, the sample has to reach the growth temperature of NWs (typically in 1-3 minutes), which can be above 500°C, possibly involving further evolution of the droplet.

3.4.2 Comparison of Au dewetting on GaAs (100), (111)B and ZnS buffer/GaAs (111)B

A thin Au layer of 1 nm is first deposited on the substrates. SEM images and distribution statistics of the Au nanoparticles are presented in Figure 3.14. For GaAs (100), the nanoparticle diameter expands from 3 to 48 nm with an average of 25 nm, and a density of 350 particles/µm2 is calculated. On GaAs (111)B, the density is lower, 240 particles/µm2, and the nanoparticle size range is broader, between 3 and 62 nm, but the average remains around 25 nm. The dewetting process on the ZnS buffer layers leads to quite different statistics. The size

distribution is measured between 3 – 32 nm (average 13 nm, i.e., half of the value on GaAs surface) with a higher density of 600 particles/µm2. Consequently, the mean size of nanoparticles on bare GaAs is larger than the one on the ZnS surface. This is due to the interaction between the gold film and the substrate. Such interaction leads to the interdiffusion of Ga atoms from the substrate to the Au nanoparticles and produces Au-Ga alloyed nanoparticles [181]. The phase of the alloyed catalyst is dependent on the composition of Ga present in the catalyst. Different metallic compounds have been identified and reported in the past, such as hexagonal β' Au_7Ga_2 and orthorhombic AuGa or Au_2Ga [181,182].

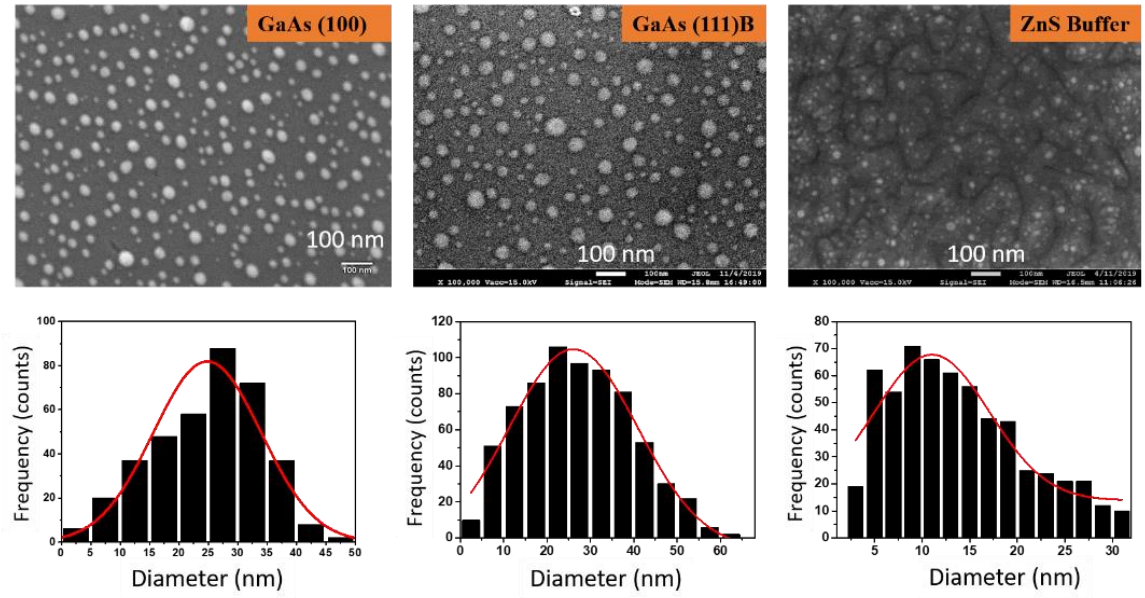

Figure 3.14: SEM images and statistics of gold droplets deposited and dewetted on GaAs (100), GaAs (111)B, and ZnS/GaAs (111)B substrates.

3.5 ZnS nanowires growth

Substrate temperature, flux ratio, supersaturation, or buffer layer, are critical parameters regarding the growth of III-Vs and II-VIs NWs [26,183]. Figure 3.15 illustrates the emergence of a catalyzed nanowire due to the competition between 2D growth on the substrate, 1D (axial) growth below the droplet (pure Au or Au_x-Ga_y alloy), and radial growth on the side of the NW. As mentioned in the state of the art, few papers deal with Au-assisted ZnS NWs growth by MOCVD. Hereafter, we take this opportunity to investigate the role of growth parameters carefully.

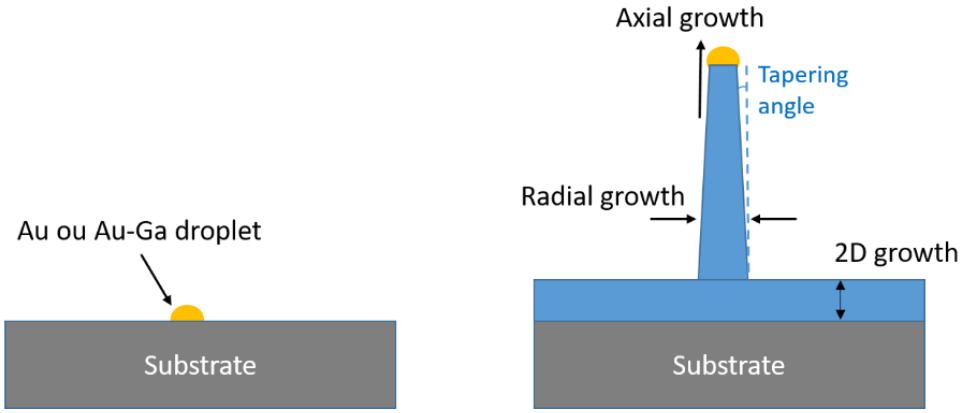

Figure 3.15. Schematic of NW growth, distinguishing axial, radial, and 2D growths.

3.5.1 Growth parameter studies

The list of nanowire samples prepared for temperature, VI/II ratio, and substrate study is gathered with detailed growth conditions in Table 3.3.

Table 3.3: Sample list (nanowires), indicating growth conditions.

Type	Study	Reference	Tg (°C)	P_{DEZn} (Pa)	P_{DTBS} (Pa)	VI/II ratio	Substrate
Nanowires	Temperature	NW1	450	7.8	15.6	2	GaAs (111)B and ZnS buffer
		NW2	500				
		NW3	525				
		NW4	550				
		NW5	575				
	VI/II ratio	NW6	550	7.8	5.1	0.65	
		NW7	550		7.8	1	
		NW8	550		11.7	1.5	
		NW9	550		24.96	3.2	
	Substrate orientation	NW10	550	7.8	15.6	2	GaAs 100 and ZnS buffer
		NW11	550	7.8	15.6	2	GaAs (111)A and ZnS buffer
		NW12	550	7.8	15.6	2	GaP (111) and ZnS buffer

3.5.1.1 Effect of temperature

The first step was to study the effect of temperature on the growth of ZnS NWs, and a series of experiments were performed, increasing the substrate temperature from 450 to 575 °C. The

growth duration was 3 minutes for all samples (S partial pressure: 15.6 Pa, Zn flow: 7.8 Pa and ratio $R_{VI/II}$ = 2, samples NW1 to NW5, see table 3.3). At the lowest temperature, 450 °C, the growth produced a rough ZnS layer which entirely covered the catalyst, and hence no NWs were observed (not shown here). Figure 3.16 gathers 45°-tilted SEM images of samples prepared on GaAs (111)B at different temperatures: a) 500 °C, b) 525 °C, c) 550 °C and d) 575 °C. It appears that the growth of NWs initiates at 500 °C but still forms a rough layer with 3D objects on the surface. The increase of the temperature at 525 °C and 550 °C reinforces the growth of vertical and more homogeneous NWs. The maximum length is around 2 µm, and the diameter is in the range ~10-50 nm, even if it is challenging to measure from SEM image accurately. TEM experiments will provide more information on droplet and NW diameters in the next chapter. However, some NWs are inclined, and 3D objects are still present on the surface. Further increase in the temperature, at 575 °C, yields er long but disordered NWs, and the density is lower.

Interestingly, if one refers to Figure 3.2 presenting the three growth regimes for ZnS films, the emergence of ZnS NWs occurs in the re-evaporation regime. In the mass-transport regime, the droplet is buried in the growing layer. This could be due to equivalent axial and 2D growth rates. In the re-evaporation regime, zinc and/or sulfur atoms desorb from the substrate surface, decreasing the 2D rate strongly. Then we can assume that, on the contrary, the diffusion of species in the catalyst-droplet is enhanced by the temperature, and this is why the axial growth rate increases. In previous work on ZnO NWs growth, the group has demonstrated the strong effect of the gold droplets, which efficiently catalyze the adsorption of the zinc precursor (DEZn) to initiate the growth of nanostructures [107]. Here we expect the same behavior for ZnS NWs; i.e. preferential adsorption and diffusion of the precursor species at the catalyst particle (Au or Au-Ga alloy) instead of their re-evaporation. Therefore, in such temperature conditions, the ratio axial $\frac{axial\ V_g}{2D\ V_g}$ is favorable for NW fabrication.

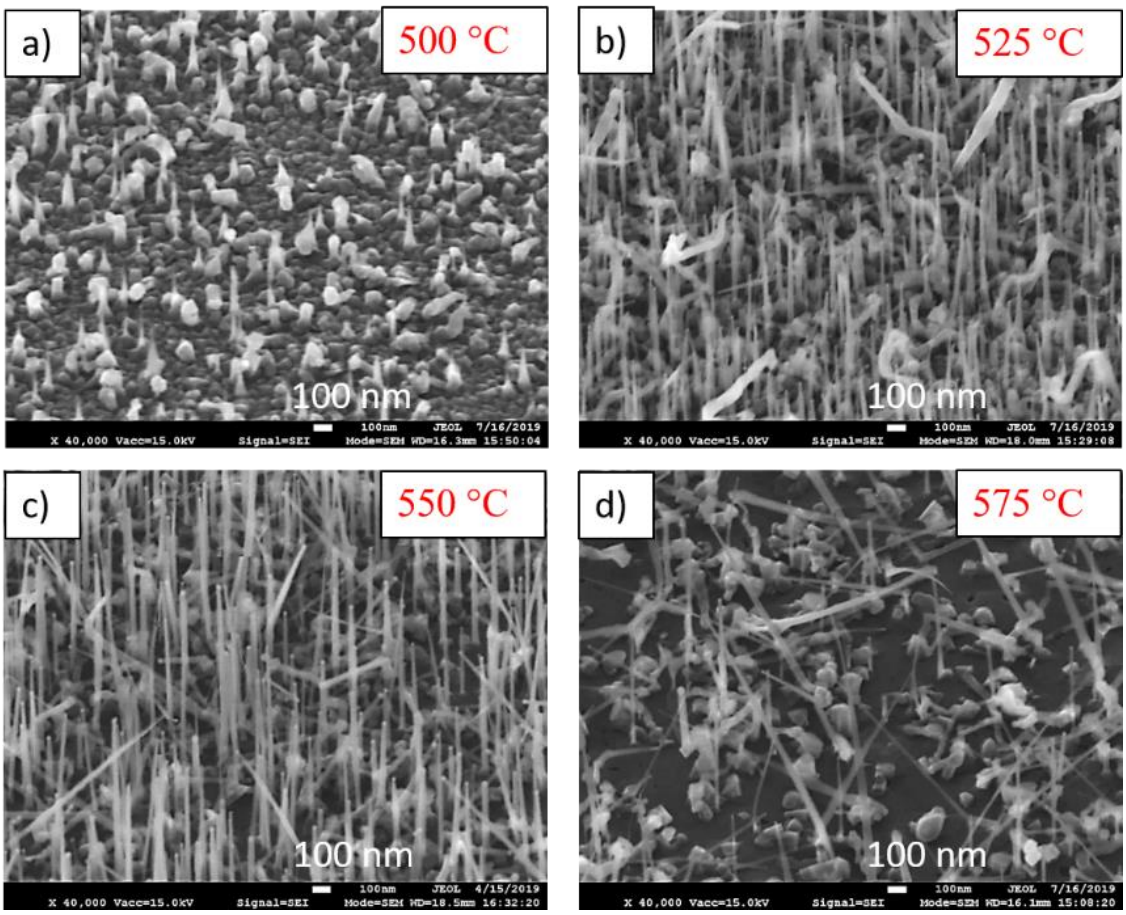

Figure 3.16. 45°-tilted SEM images of samples prepared on GaAs (111)B sustaining $R_{VI/II}$ = 2 at different temperatures: a) 500 °C, b) 525 °C, c) 550 °C and d) 575 °C.

3.5.1.2 Effect of VI/II ratio

We continued with the study of the VI/II ratio ($R_{VI/II}$). Another series of samples were prepared to vary the precursor partial pressure ratio at 550°C, as this temperature was considered as the optimized one (see table 3.3, samples NW6 to NW9). The SEM images of the NWs grown on GaAs (111)B varying $R_{VI/II}$ are shown in Figure 3.17. Taking into account the preliminary study of ZnS layers in section 3.1, we remind that VI/II ratios of 0.6 and 1 correspond to zinc-rich conditions, 1.5 is the equilibrium point, and 2 and 3.2 correspond to sulfur-rich growth. It is clear from the SEM images that the zinc-rich regime ($R_{VI/II}$ = 0.6 and 1, Figure 3.17a and 3.17b) does not enable the growth of NWs, but rather leads to dots and 3D objects on the surface. An increase of the sulfur partial pressure initiates the 1D growth ($R_{VI/II}$ = 1.5 in Figure 3.17c), as short NWs are observed, with lengths up to a few hundreds of nanometers. Setting $R_{VI/II}$ = 2 (Figure 3.17d) produces the best ZnS NWs. They are 1-2 µm long, and most are vertically aligned. Further increase in the sulfur flow ($R_{VI/II}$ = 3.2, Figure 3.17e) leads to longer NWs, above 2 µm, but appears to disturb the vertical orientation. These results show that zinc-rich conditions (refer to Figure 3.2) suppress the growth of NWs whereas sulfur-rich conditions yield long and vertical NWs, with an optimized VI/II ratio of around 2. A similar influence of precursor ratios was observed for ZnTe NWs [26] , and ZnSe NWS [184] grown by MBE, i.e. excess of group VI element is required. We have no explanation for that, especially since another group found opposite behavior in ZnSe NWs [112], i.e. worm-like and kinked in selenium-rich conditions, but straight in zinc-rich.

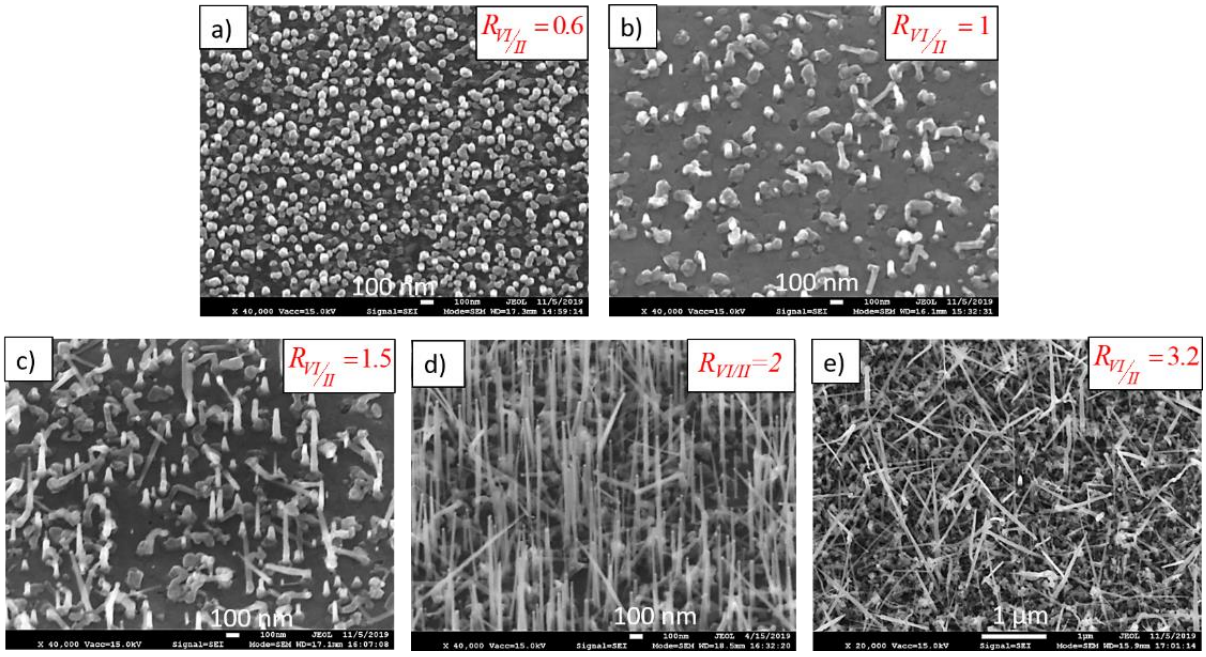

Figure 3.17. 45° tilted SEM images of ZnS NWs with various VI/II ratios: a) 0.6, b) 1, c) 1.5, d) 2, and e) 3.2.

3.5.1.3 Growth on different substrates

After such optimization, NWs growth was also performed on a set of different surfaces, namely GaAs (100), GaAs (111)A, GaAs (111)B, GaP (111), and ZnS buffers deposited on such substrates. SEM images are gathered in Figure 3.18. The growth on GaAs (100) and GaAs (111)A substrates resulted in randomly oriented ZnS NWs. The best uniformity and vertical arrays of NWs have been produced on GaAs (111)B surfaces, in agreement with experimental works reported in the literature. Introducing ZnS buffer leads to mitigated effects concerning GaAs (100) and GaAs (111)A substrates, with no strong improvement in the quality of the NWs arrays. Again the buffer on GaAs (111)B orientation enables the best result. Noticeably, NWs appear much thinner, compared to the case on bare GaAs (111)B. A few 1D nanostructures appear much broader at the base, and possibly flat, like very elongated triangles. In this experimental work, GaP (111) surfaces were also tested. As ZnS is nearly lattice-matched to GaP, it was interesting to study whether arrays of ZnS grown on ZnS (buffer)/GaP would show a strong improvement regarding uniformity and verticality. The results on GaP (111) were found very similar to the case of GaAs (111)B, including TEM results and structural analysis of single NWs so the use of GaP did not bring the expected breakthrough! Therefore, in the following sections, we will focus on NWs grown on GaAs (111)B and ZnS (buffer)/GaAs(111)B. The length and diameter statistics will be presented in Chapter 4 using both SEM and TEM images. The growth and morphology of the particular cases of VLS and VSS on GaAs(111)B and ZnS(buffer)/GaAs(111)B will be more detailed in chapter 4, which will also provide structural analysis by TEM

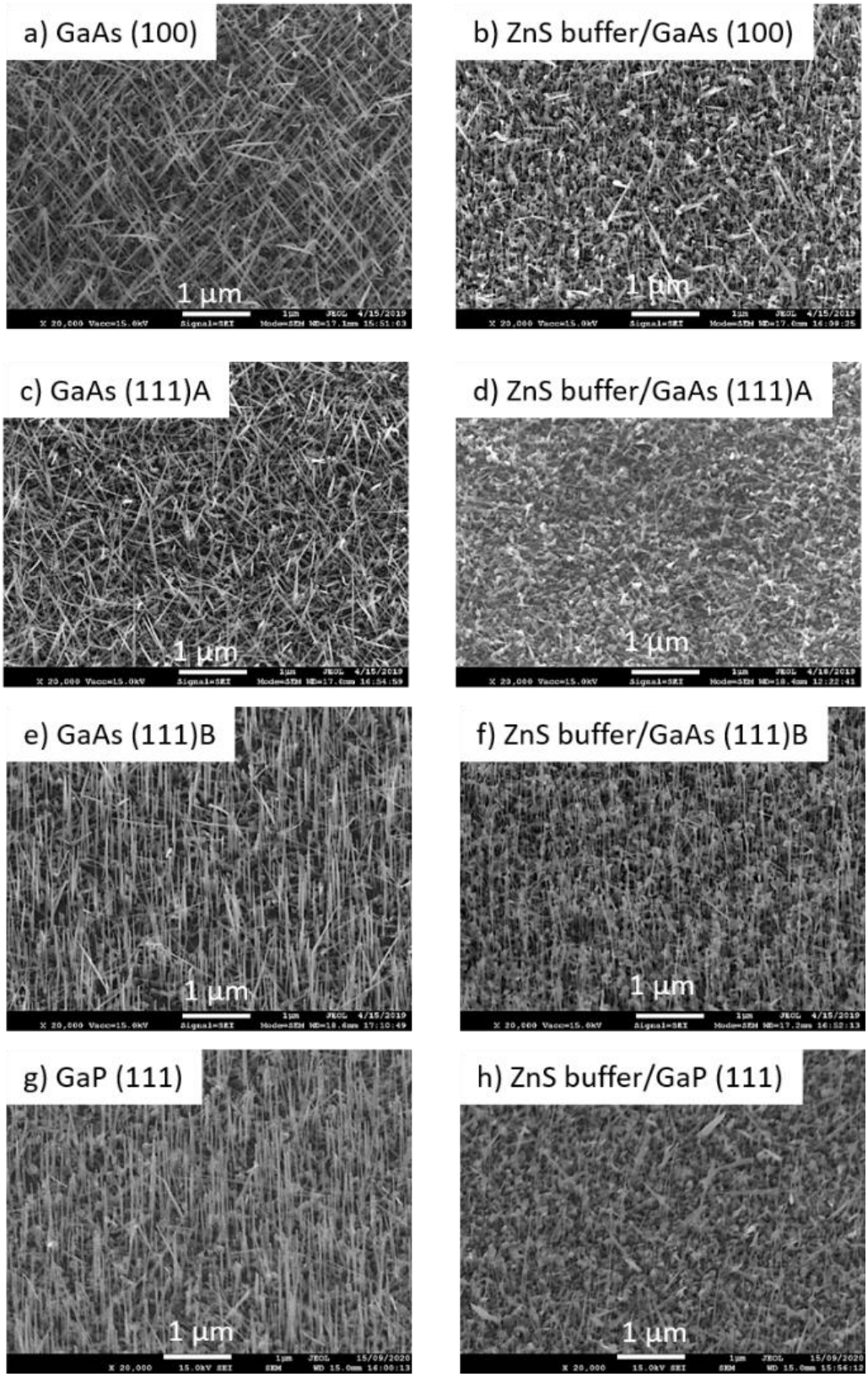

Figure 3.18. 45° tilted SEM images of ZnS NWs grown on GaAs (100), GaAs (111)A, GaAs (111)B, GaP (111), and ZnS buffers.

3.5.1.4 Effect of Au film thickness

In Figure 3.19, we compare the morphologies of two samples grown in the same conditions on GaAs (111)B, one had received a 4 nm thick Au layer before dewetting process and NW growth, the other one only 0.1 nm.

In the first case (4nm, Figure 3.19a), the dewetting process leads to a substrate surface covered by 3D objects, with a high density. They appear faceted and are probably composed of Au-Ga particle and ZnS material. Their diameter is indeed far to be homogeneous, as it lays in a broad range between a few ten and a few hundreds of nm. Indeed, very few ZnS NWs have emerged if one reminds that each droplet may potentially trigger the catalyzed growth. We observe in the SEM image that only the smallest droplets have participated in the NW growth. The biggest particles seem to remain on the substrate and lead to the growth of these big 3D objects.

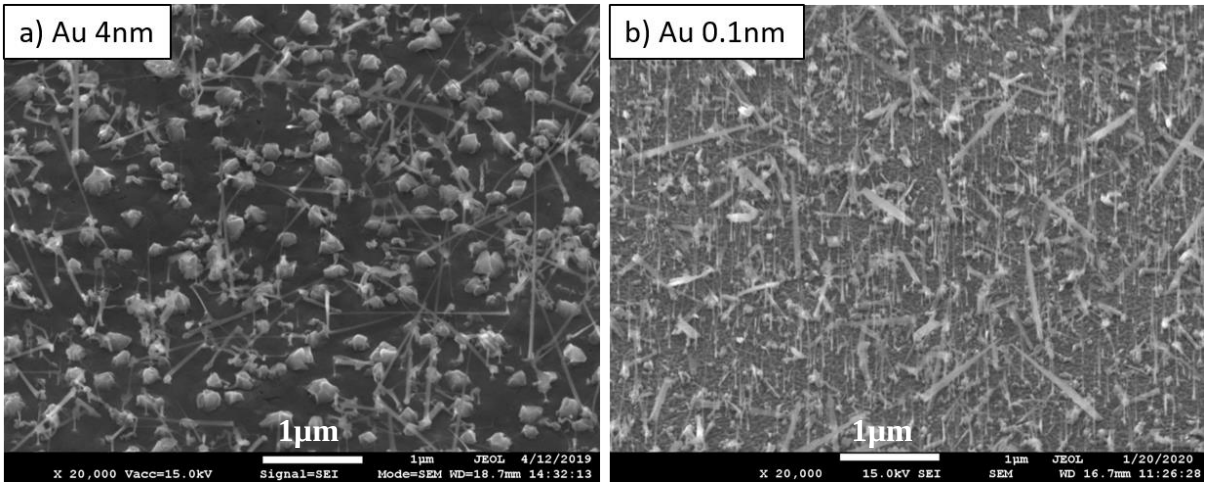

Figure 3.19: The SEM images of ZnS NWs grown on GaAs (111)B with different thicknesses of Au layer a) 0.1 and b) 4nm for 10 min at 550 °C. Scale bar 1 µm

In the second case (0.1 nm, Figure 3.19 b), an attempt was made to deposit a minimum possible Au thickness. After performing dewetting, it was extremely difficult to observe the Au nanoparticles with SEM experiments. Interestingly, after ZnS NW growth, we observed a more homogenous distribution of thin and short NWs with a low density. Such kinds of NWs are interesting to study the quantum effects in II-VI heterostructures based on ZnS NWs, an approach followed in Chapter 7.

3.6 Conclusions

In this chapter, we have presented a comprehensive study on the catalyzed growth of ZnS NWs using MOCVD. We started with basic growth studies on ZnS thin films and defined MOCVD growth regimes based on temperature and VI/II ratio. The structural and morphological characteristics were studied with XRD and SEM experiments, and a detailed analysis was performed to optimize the ideal growth conditions for the buffer layer. Next, we carried out the Au dewetting experiments on GaAs (100) substrates and studied the effect of dewetting temperature, duration, and Au thickness on the distribution of Au nanoparticles. Finally, we investigated the growth of ZnS NWs and it was found that the nanowires emerge in the re-evaporation regime (550°C) and under sulfur-rich conditions (S/Zn ratio of 2). GaAs (111)B substrates are confirmed to give the best arrays of NWs, in terms of verticality and uniformity, in agreement with the literature [121,185].

Chapter 4

VLS *vs* VSS growth mode: Structural properties and growth mechanisms

Contents

ii

When materials are grown as nanowires (NWs), they often adopt crystal structures different from their bulk counterpart. Polytypes of zinc blende and wurtzite phases easily occur in semiconductor NWs, whereas polytypes (such as 4H, 6H) are rare and only exhibit in small segments. In this context, ZnS could prove to be a perfect material to achieve new crystal structures when grown as NW, thanks to its polytypic behavior and small differences in cohesive energy between the 3C, 4H, 6H, 15R, and 2H crystallographic phases. Therefore, a modest change in the growth conditions would be sufficient to attain polytypes. In this chapter, we employed the two different ZnS NW growth approaches, namely vapor-liquid-solid (VLS) assisted by the liquid catalyst, and vapor-solid-solid (VSS) assisted by the solid catalyst. We

[ii]This chapter includes content from our paper: S. Kumar et al. *Nano Res.* **15,** 377–385 (2022) [67].

compared the differences in structural properties induced by the two growth modes. Finally, the involved mechanisms in VLS as well as VSS cases are carefully discussed on the basis of the knowledge related to III-V and II-VI nanowires.

4.1 Introduction

In previous chapter, we carried out an experimental study to grow vertical arrays of ZnS NWs with controlled morphology. In this chapter 4, we wish to deeper understand the crystal structure, and extended defects. Indeed, we predict twins and stacking faults (SFs) to easily occur due to a low formation energy. For comparison, the experimental intrinsic SF energy in zinc blende (E_{ISF}) is less than 6 mJ/m^2, and 45 mJ/m^2 in GaAs [186]. We also wish to identify possible new phases, appearing upon specific growth conditions. In the light of the variety of ZnS polytypes available in the bulk form [68], the occurrence of different crystal structures is highly expected in ZnS NWs with tuning the growth parameters. As the electronic structure varies with crystal structure, the achievement of new phases in semiconductors would pave the way to novel physics and original applications. For example, a new h-Si6 silicon phase with direct bandgap was reported to be an efficient solar absorber [187]. In SiC, well-known material for its polytypism, a quantum crystal phase heterostructure (but homomaterial) was fabricated by embedding a 3C well in 4H barriers [188]. Indeed, similarly to the case of III-V NWs [50,189], we expect that new ZnS polymorphs would be useful for designing crystal phase heterostructures, bandgap engineering, enhanced thermal and mechanical properties, and direct intersubband optical transitions. Boutaiba et al. [168] have calculated the band structures of ZnS 2H, 4H, 6H, and 3C phases, all predicting a direct bandgap, with energy varying from 3.8 (for pure cubic) to 3.88 eV (pure hexagonal). Regarding the 15R phase of ZnS, a change in the band structure is also expected, analogously to the case of 15R ZnO [190]. Hence, controlling the crystal structure (*e.g.* by adjusting the supersaturation during the nanowire growth) would enable the design of original hetero-crystalline (but single ZnS) junctions, without compound intermixing at the interfaces, thus having potential applications in the UV emission.

4.1.1 Occurrence of polytypes in ZnS

As already introduced in chapter 1, we use to consider that a plane is hexagonal (and noted *h*) if sandwiched between a previous plane and a next plane having the same lateral position (e.g. ABA), and cubic (noted *c*) if different positions (e.g. ABC). Another method could better take into account the fact that we are growing material. Considering the crystal projection in the [010] zone axis, if the Zn-S bonds (not normal to the growing plane) of the newly deposited ML are parallel to the corresponding bonds of the previous ML, then the new ML is '*c*', and if not, the new ML is '*h*' (refer Figure 4.1).

The small difference in cohesive energy between ZB and WZ structures (i.e. 7.8 mJ/m^2 [191]) enables the occurrence of twins and SFs in ZB ZnS. Simple calculations have been proposed considering interactions up to the second neighbor monolayer (ML). In this article, the relation between the intrinsic stacking fault (E_{ISF}) and cohesive energy is given by the equation:

$E = 2(\delta_1-\delta_2)$

Here δ_1 is the cohesive energy difference between the cubic and hexagonal layer per unit area of ML, δ_2 is the increase in energy as a result of stacking faults

Consequently, the formation of SFs in a periodic manner qualitatively can result in the formation of high-order polytypes. The cohesive energy calculations of the polytypes in ZnS can give us an idea about their occurrence possibilities. In his calculations, Glas used SF energies and calculated differences of cohesive energies between ZB and WZ forms data to compute the differences of cohesive energies of stacked structures (such as crystals with other types of SFs or twin planes and polytypes) with respect to the reference structure (ZB or WZ). These calculations methodology is similar to ANNNI model (explained in Chapter 2), but simpler because it considers two nearest neighbors (NN) instead of next-nearest neighbor (NNN) interactions [191].

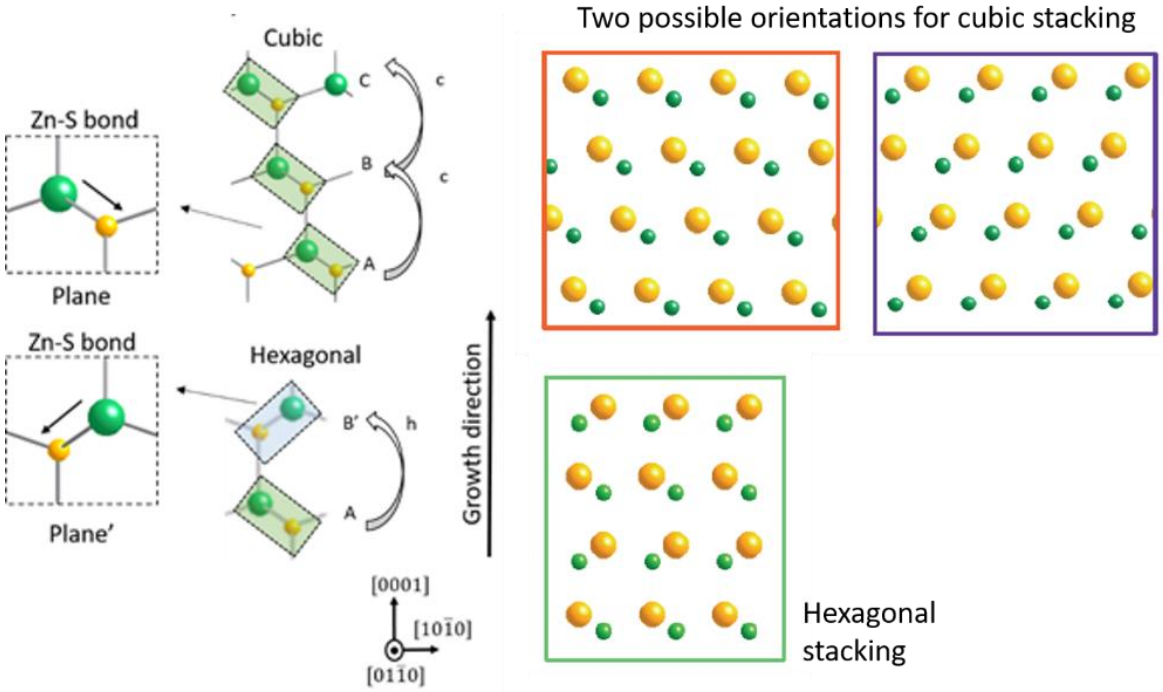

Figure 4.1: Notation of the planes concerning the direction of the Zn-S bond not parallel to the growth direction: the stacking gives either hexagonal *h* or cubic *c* planes.

The expression of the cohesive energies for different ZnS polytypes considering the lattice spacing of 0.31 nm (d_{111} for ZB or d_{0001} for WZ) is written as:

$$\partial E_p = \frac{N_h \partial_1 - 2n\partial_2}{N_h + N_c} \qquad (1)$$

Here again δ_1 is the cohesive energy difference between the cubic and hexagonal layer per unit area of ML, δ_2 is the increase in energy as a result of stacking faults, N_h and N_c are numbers of hexagonal and cubic layers, and n is the number of nonempty sequences of cubic planes.

The hexagonality of a polytype is defined as the ratio of the number of hexagonal layers to the total number of layers in the crystal and can be expressed as,

$$\text{Hexgonality (\%)} = \frac{N_h}{N_h + N_c} \times 100 \qquad (2)$$

Using $\delta_1 = 7.8$ mJ/m^2 and $\delta_2 = 4.8$ mJ/m^2 [191], the cohesive energies of ZnS polytypes are calculated and plotted as a function of their hexagonality. Results are gathered in Table 4.1 and Figure 4.2.

Polytype	**Stacking sequence**	**Hexagonality (%)**	**Formula**	$\partial E_p (\mathrm{mJ/m^2})$
3C	ABC	0	0	0
8L	ABACBACB	25	$\frac{1}{4}\partial_1 - \frac{1}{4}\partial_2$	0.75
6H	ABCACB	33	$\frac{1}{3}\partial_1 - \frac{2}{3}\partial_2$	-0.6
15R	ABCBACABACBCACB	40	$\frac{2}{5}\partial_1 - \frac{4}{5}\partial_2$	-0.72
4H	ABCB	50	$\frac{1}{2}\partial_1 - \partial_2$	-0.9
9R	ABACACBCB	67	$\frac{2}{3}\partial_1 - \frac{2}{3}\partial_2$	2
2H	AB	100	∂_1	7.8

Table 4.1. The table includes the cohesive energy expressions and their calculated values for different ZnS polytypes with their respective hexagonality.

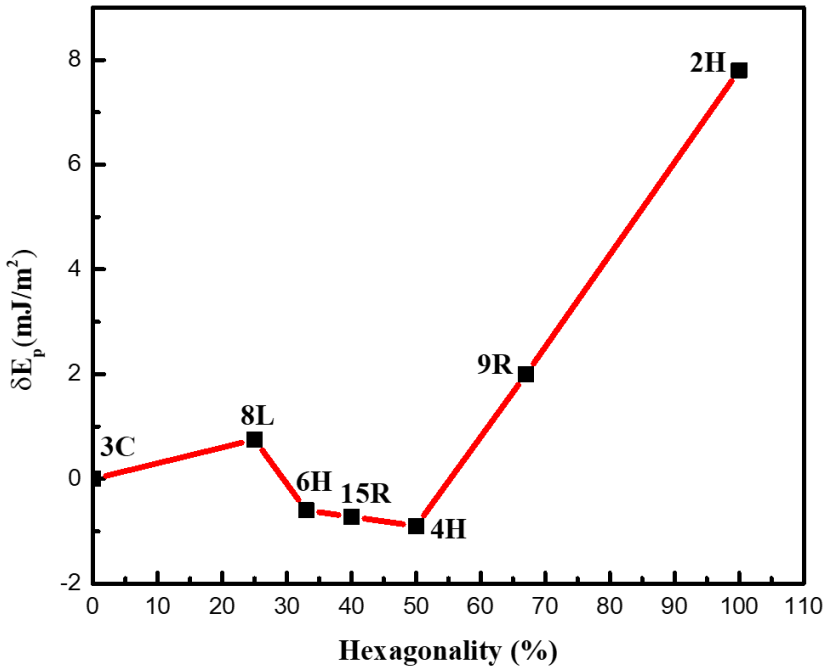

Figure 4.2: The plot of cohesive energies of ZnS polytypes (with respect to 3C (ZB) structure) as a function of their hexagonality (in percentage) shows that 6H, 15R and 4H having the minimum cohesive energies are most stable.

Indeed, the plot show that all cohesive values are very close as regards the different polytypes. Here, the negative energy would simply mean a more stable structure for a given stack compared with 3C (ZB), so that 6H, 15R and 4H structures could be the most stable polytypes of ZnS. The conclusion that all phases from 3C (pure cubic, ZB) to 4H are expected to easily occur, and 2H (pure hexagonal, WZ) is the less favorable (but again with a small increase of the cohesive energy), agrees with previously published calculations [54,192,193]. Let us see now the experiments.

4.2 ZnS NWs growth

4.2.1 Design of experiments

Au-assisted ZnS NWs were grown on GaAs (111)B and ZnS (buffer)/GaAs (111)B. The catalyzed fabrication process is illustrated again in Figure 4.3. In the case of samples with ZnS buffer, GaAs substrates were deoxidized at 550 °C followed by the deposition of a 900 nm thick ZnS layer. Prior to NW growth, a 1-nm-thick Au layer was deposited at room temperature on the substrate surface using thermal evaporation. The samples were then transferred into the MOCVD reactor where 10-min annealing at 500 °C under H2 was performed to ensure Au dewetting. Afterwards, the temperature was fixed to 550 °C for the growth of ZnS NWs for 3 min. The DEZn and DTBS precursor partial pressures were 8 and 16 Pa for zinc and sulfur, respectively, giving a VI/II ratio of 2.

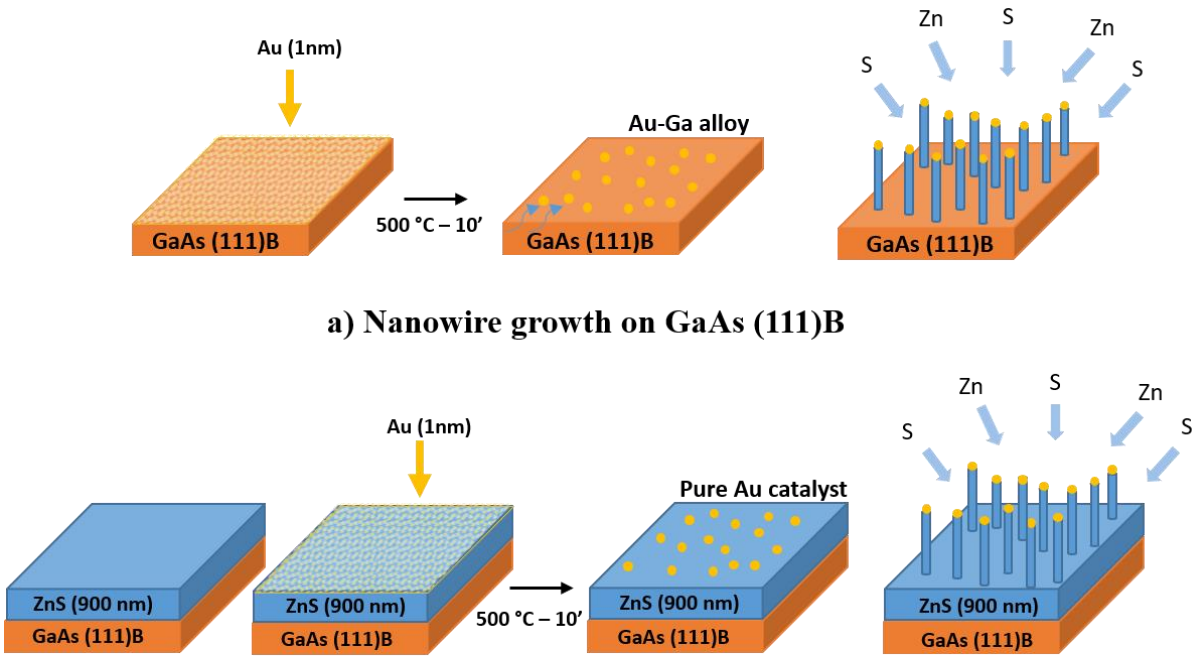

Figure 4.3: The schematic diagram of ZnS NWs growth on (a) GaAs (111)B, and (b) ZnS (buffer)/GaAs (111)B, where a thick buffer layer was prepared to prevent the gold particles from interacting with the substrate.

4.2.2 Nanowire growth and morphology

In this study, we aimed to focus on the influence of a ZnS buffer layer on which Au droplets would lay. To do so, both substrates with and without buffer were kept in the same run, in order to grow the ZnS NWs in the same conditions. The SEM images of the samples are shown in Figure 4.4. Straight and vertically oriented NWs were observed in both cases. NWs grown on the GaAs (111)B substrate have a length in the range 350–1,400 nm with a diameter of 10–35 nm below the droplet. Contrastingly, thinner and shorter NWs were observed on ZnS buffer samples, with length of 230–590 nm and diameter ranging 7–25 nm, as well as worm-like and kinked NWs with a larger diameter around 25–30 nm. The variation in diameter can be correlated to the catalyst size at the top of the nanowire. In addition, on careful analysis of Figure 4.4a-b, it can be seen that the droplet at the top of nanowire grown on GaAs (111)B is larger in size compared to the one of the nanowire with buffer. This behavior suggests that only small catalysts are assisting the nanowire growth in case of “with buffer” growth [194]. In 2014, Zannier et al. similarly observed a diameter dependent morphology of VSS grown ZnSe NWs [195]. Their NWs with a diameter below 15 nm were straight while thicker nanowires showed a “worm like” morphology distinguished by multiple kinks. This supports the idea that there exists a critical diameter of the catalyst above which the growth of straight nanowires is suppressed by either development of kinks or formation of a 2D layer on the catalyst. In our samples, straight and kinked NWs can be seen more clearly in TEM images (Figure 4.5). We measured a maximum growth rate of 7.7 nm/s in the case of ZnS NWs grown on GaAs (111)B, and 3.3 nm/s for NWs on buffer samples. In MOCVD process, this agrees with a preferential adsorption of DEZn and DTBS precursors on the liquid droplet rather than on the solid, or with a higher solubility of one or both of the reactants in the liquid, which leads to an increase in the

reactant flows at the TPL. Such discrepancy of the growth rate between the two processes was also observed in SiGe heterostructure NWs growth [95].

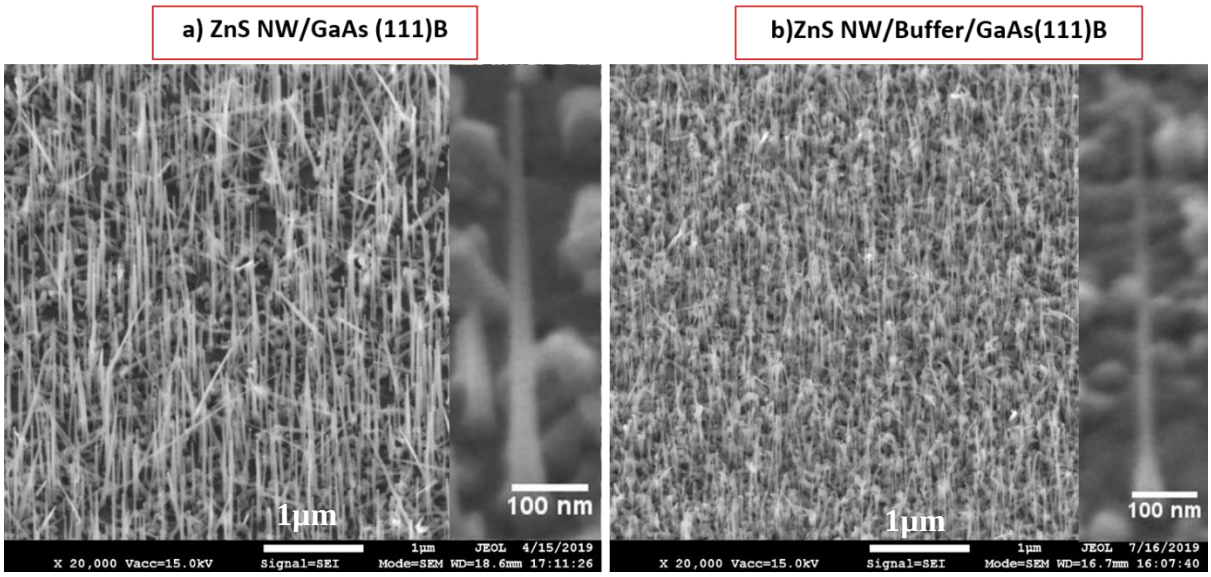

Figure 4.4: 45° tilted SEM images of vertical ZnS nanowires grown on (a) GaAs (111)B, and (b) ZnS buffer/GaAs (111)B.

To get a better idea of the NWs morphology, Figure 4.5 gathers dark field images taken on the two samples grown on GaAs (111)B or ZnS (buffer)/GaAs(111)B. Different kinds of 1D nanostructure can be distinguished, with a bright catalyst droplet on their top. The most important population concerns long and straight nanowires, as indicated by the green arrows. At the tip, their diameter is more or less equal to the droplet, but it weakly increases going toward the base of the nanowires, making them slightly tapered. The tapering angle is small, around 0.5°. Another family of 1D nanostructures presents a much wider base, and the tapering is more pronounced (1.2° in the case of the NW indicated by blue arrow in Figure 4.5a). Actually, such NWs could be flat and hence be nanoribbons [196]. Other ZnS nano-object appear as worm-like structures (pink arrow), or kinked nanowires (orange arrow).

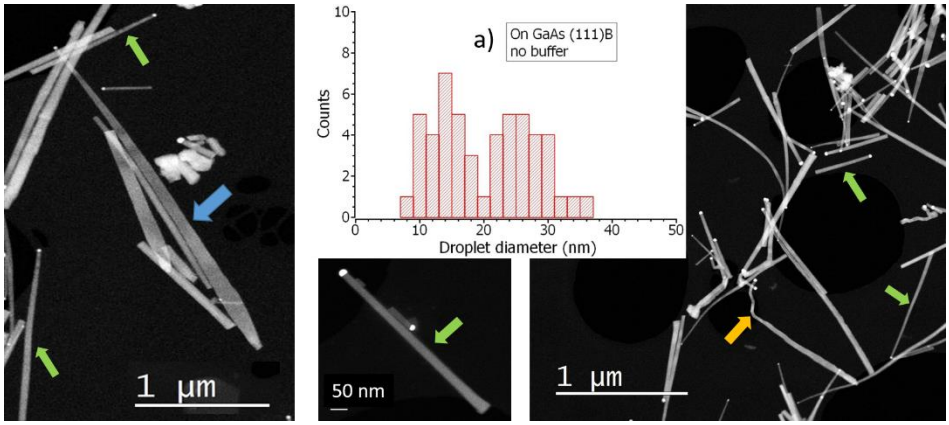

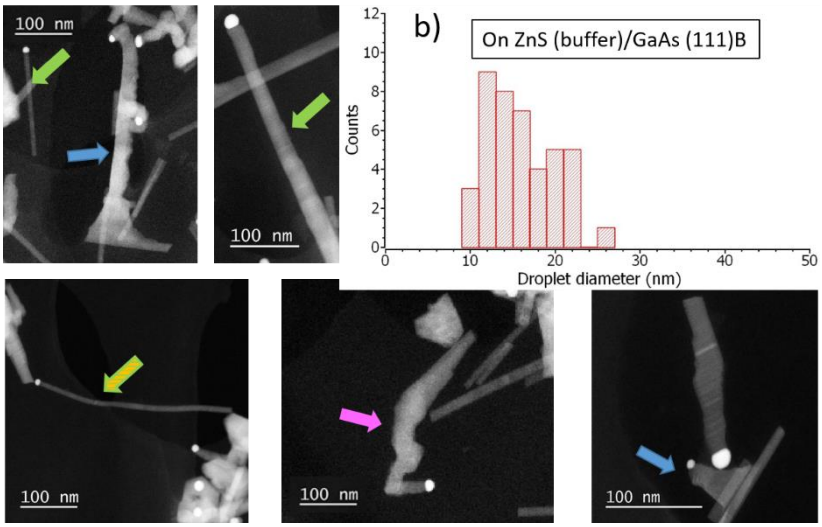

Figure 4.5: TEM image (HAADF) and droplet diameter statistics of ZnS NWs grown on: a) GaAs (111)B, and b) ZnS (buffer)/GaAs (111)B.

In addition, we seized the opportunity to present statistics on the droplet diameter observed at the tip using TEM images. Two statistics are given in the Figure 4.5, corresponding to a collection of ~50 NWs whether grown on one or the other surface. On bare GaAs (no buffer), the droplet diameter spans from 7 to 36 nm. The histogram actually shows two populations, one in the range 7-20 nm (average ~15 nm), the other in the range 20-36 (average ~28 nm). On ZnS (buffer)/GaAs (111)B, the droplet diameter varies between 9 and 26 nm. Here the tendency of forming two populations is not as clear, and the mean size is ~16 nm. In both cases, the histograms are quite different from the ones presented in Chapter 3, Figure 3.14, before the NW growth (i.e. just after dewetting). Indeed, the parts corresponding to the largest droplets are absent in the new histograms, letting us confirm that the small nanowires were preferred during the growth of ZnS NWs.

4.3 Structural analysis of VLS grown NWs on GaAs (111)B substrate

Due to Ga diffusion into the gold droplet during the dewetting process, we anticipated a vapour-liquid-solid (VLS) process, involving a liquid catalyst, for such ZnS NWs directly grown on GaAs (111)B. In the following section, we will verify that assumption and carefully analyze the crystal structure by TEM.

4.3.1 TEM measurements

The STEM/HAADF image of a single nanowire grown on GaAs (111)B is shown in Figure 4.6. The gold catalyst is clearly seen at the top. The diameter below the droplet is 19 nm, and increases to 30 nm at the bottom, suggesting a relatively small contribution of the lateral growth on the NW sides during the process.

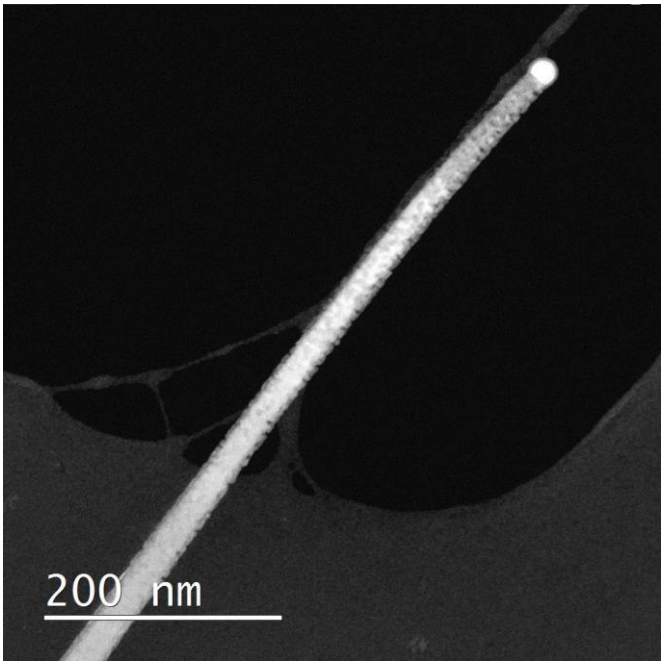

Figure 4.6: STEM/HAADF image of a single NW grown on GaAs (111)B substrate. A catalyst droplet is present at the top the NW.

An HRTEM image taken in the [010] zone axis is given in Figure 4.7, and it shows periodic material stacking along the growth direction, which could correspond to WZ-ZB modulations and/or stacking faults. The thickness of each modulation (as it appears in the image) is around 2 nm. Similar kinds of structural patterned HRTEM images have been observed in the past, showing mixed zinc blende and wurtzite phases and appearance of stacking faults [24,197–201]. In particular, Liang et al. reported the vertically oriented growth of ZnS NWs assisted by Au, Ag and Ga catalysts [20, 24] and emphasized the crystal phase dependence upon NW diameter. In their ZnS NWs, Jiang et al. also described a modulation of structure at the nanometer scale as a stacking of 8H and 10H half-cells [197].

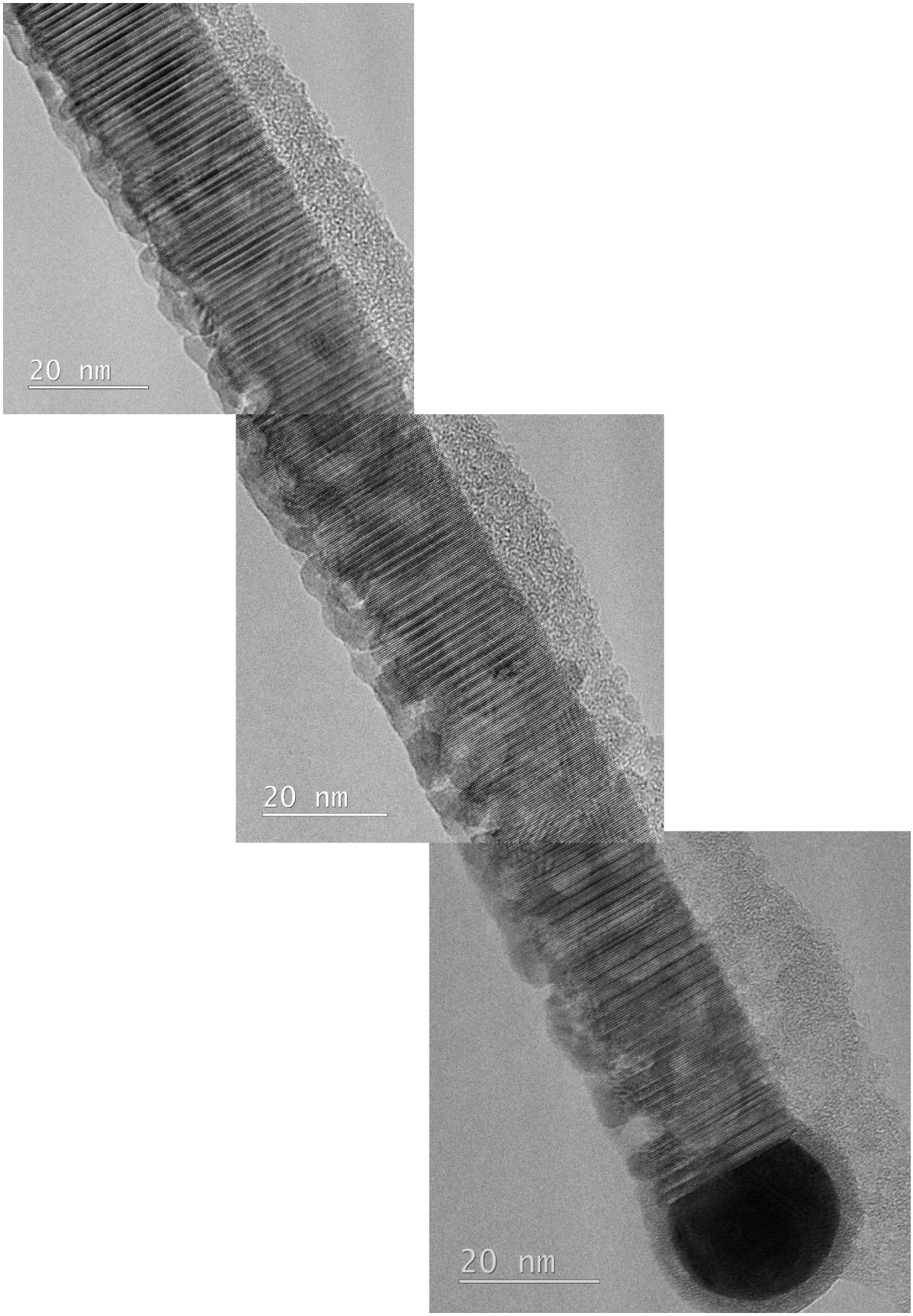

Figure 4.7: HRTEM image of a single NW focusing on the stacking from the different region of the NW. The catalyst droplet can be seen in a dark contrast.

Herein, we seized the opportunity to perform profound investigation on the structural pattern observed in HRTEM image. An accurate analysis of the ordered stacking sequence reveals the formation of a complex structure in a periodical manner along the length of NW. The repeated sequence corresponds to ABCBA-CABAC-BCACB planes, and consists of 3 cycles (each one containing 5 planes with a mirror sequence, e.g. ABCBA) with circular permutations. Such crystal structure is known as 15R [65]. The 15R polymorph crystallizes in the rhombohedral (or trigonal) system, with the space group being R3m. The crystal structure fits well on superimposing a 15R model on the Fourier filtered image of nanowire as shown in Figure 4.8d. This polymorph is highlighted for the first time in ZnS NWs while it is usually observed for SiC [203,204]. The phase transition of ZnS minerals was reported by Akizuki in 1981 and similar stacking pattern of 15R structure was observed by HRTEM [143]. In 1948, Frondel and Palache experimentally observed the three polymorphs (4H, 6H and 15R) in ZnS system and calculated the cell parameters [205]. In Figure 4.8b, the FFT pattern signifies a 5-fold symmetry and confirms the presence of (0 0 15), (107), and ($10\bar{8}$) planes in close agreement with such 15R cell parameters. Conventional TEM images (bright field and dark field) and diffractions have been performed on several tens of nanowires. The signature of the 15R phase given in diffraction by the peculiar pattern (i.e. a 5th order superstructure) has been observed in all investigated wires, with a diameter dispersion from 15 to 40 nm. We have no evidence that a critical diameter prevents or inhibits the 15R growth with respect to this investigated range of nanowire diameters. In addition, dark field images show that the polytype formation is not continuous all along the nanowire, however 15R segments with lengths of a few tens of nanometers are frequently revealed (refer Figure 4.9).

Noticeably, a drastic degradation has been observed under the electron beam for the narrowest NWs (10-15 nm), even if the voltage is reduced from 200 kV to 80 kV, so that their crystal structure could not be investigated. Figures 4.9a-b show HRTEM images of nanowires grown on GaAs (111)B, where the 15R structure is mainly preserved along the segment, with a few tens of nanometers length. HRTEM provides direct evidence of the 15R phase (Figure 4.8) but it is very limited in terms of the investigated area (few tens of nm). To increase the area of investigation, we have performed conventional TEM (bright field and dark field) and diffractions on several tens of nanowires from the 'VLS' sample. Figure 4.9c is the simulated diffraction pattern from the 15R structure. The signature of the 15R phase is given in diffraction by this peculiar pattern (*i.e.* a 5th order superstructure) along this zone axis. Such 15R diffraction pattern has been observed in all investigated wires, with a diameter dispersion from 15 to 40 nm. We have no evidence that a critical diameter prevents or inhibits the 15R growth with respect to this investigated range of nanowire diameters. To evidence the 15R stacking along the nanowire, we have taken dark field images using the {104} diffraction vector, a diffraction condition sensitive to the 15R phase. Figure 4.9e displays a dark field image of a representative NW and it shows that the polytype formation is not observed all along the nanowire but only on certain segments indicated by the blue zones.

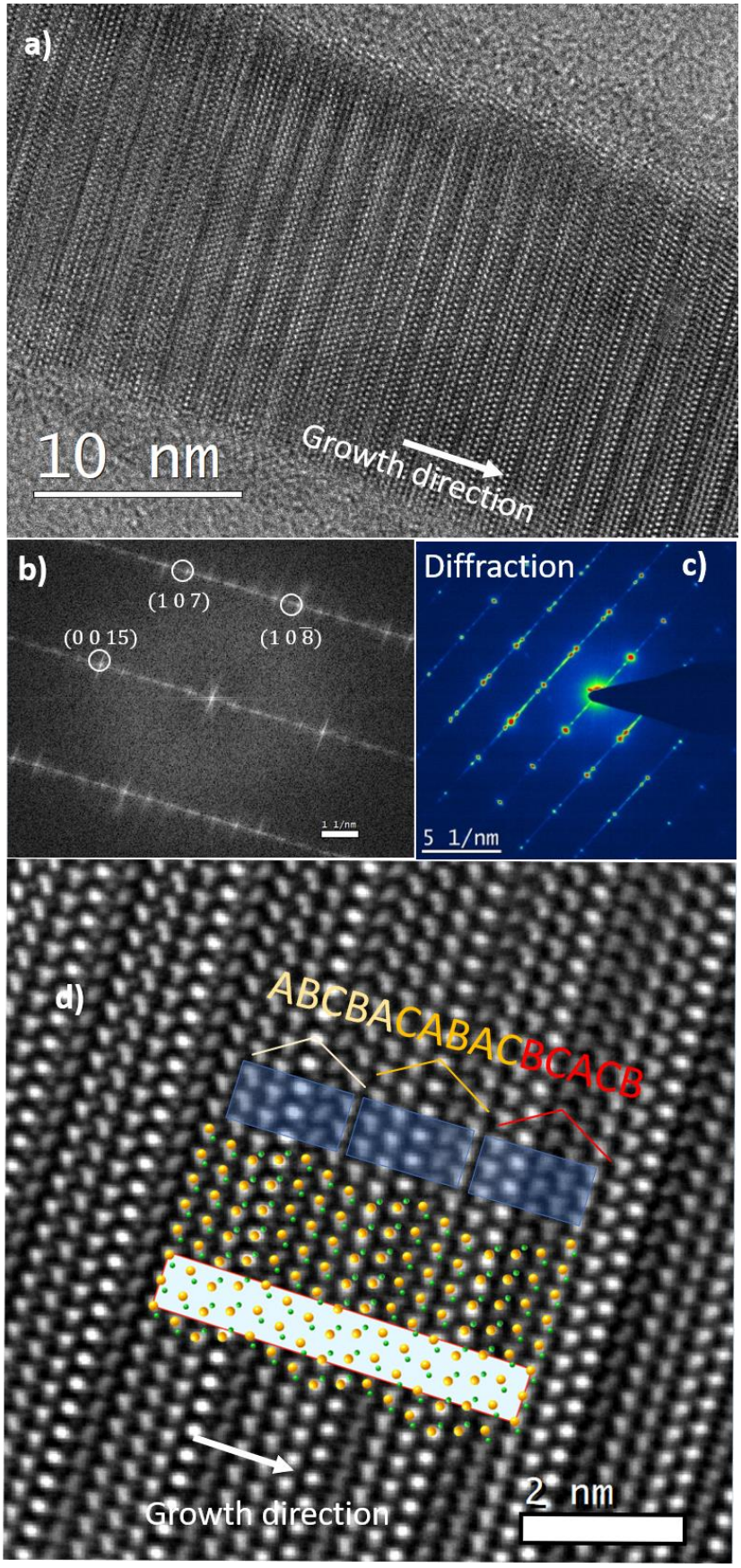

Figure 4.8: a) HRTEM image of the nanowire, B) FFT pattern, c) SAED pattern from a single NW d) Fourier filtered image superposed with 15R structure model and the respective stacking sequence ABCBA–CABAC–BCACB.

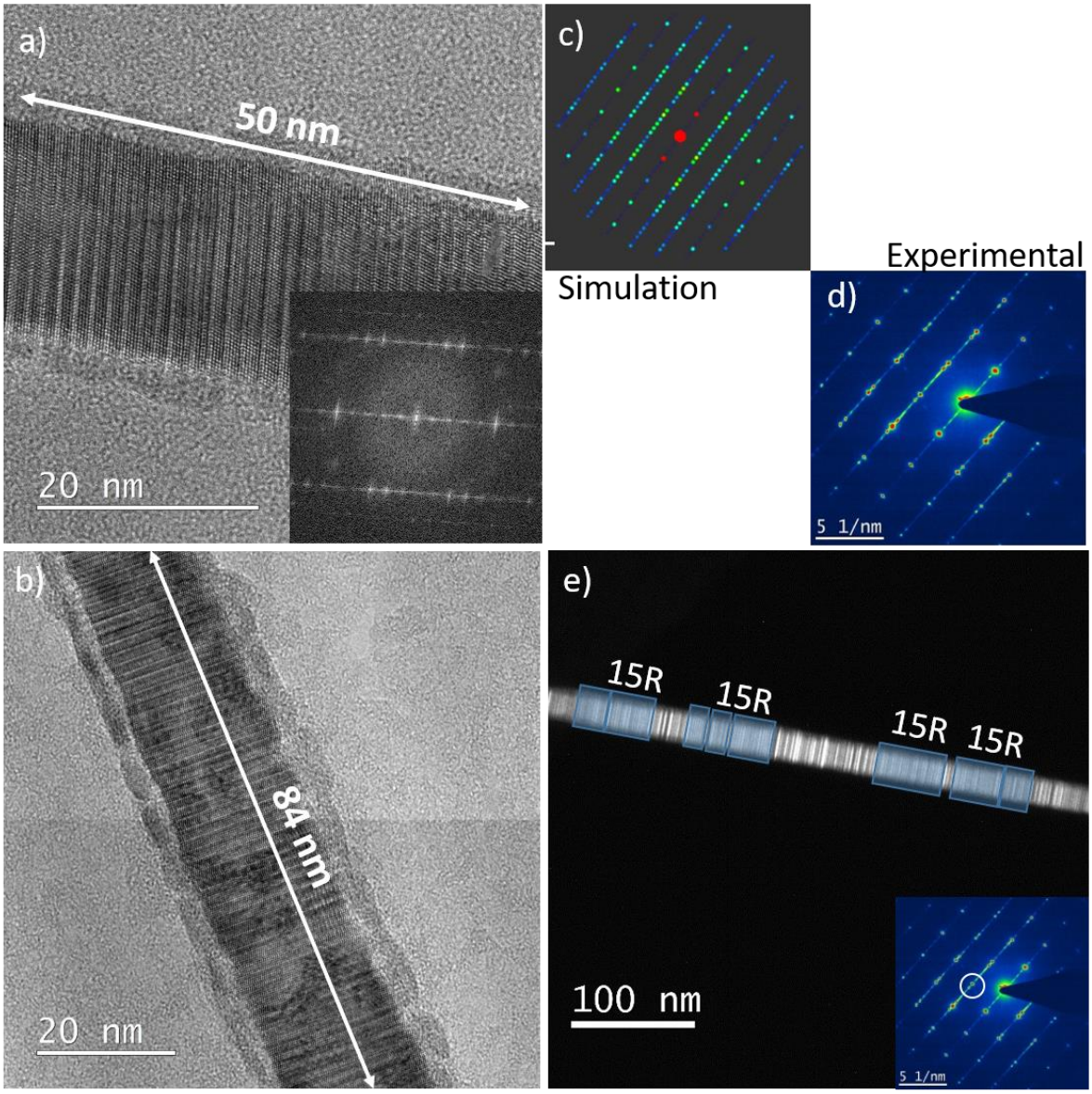

Figure 4.9: TEM analysis of catalyst-assisted ZnS nanowires : a) and b) HRTEM images of nanowires grown on GaAs (111)B, where the 15R structure is mainly preserved along the segment of the nanowire, c) Electron diffraction simulation of the 15R stacking along the <010> zone axis, d) Experimental evidence of the 15R stacking from diffraction taken along the <010> zone axis of the 15R phase, e) Dark field image taken from the same nanowire with the {104} diffraction node as evidenced in the diffraction pattern (given in the insert), the blue zones indicate the possible 15R stacking area.

4.3.2 The catalyst droplet analysis

4.3.2.1 HRTEM of catalyst droplet

The HRTEM analysis also focused on the catalyst droplet at the top of nanowire to validate the VLS credibility. In Figure 4.10, the FFT pattern of HRTEM image corresponds to the Au_7Ga_2 phase of the catalyst at room temperature. However, all the catalyst droplets studied in this sample do not present such a clear signature and are related to neither Au_7Ga_2 nor Au_2Ga, indicating a heterogeneity of the Au-Ga solid phase. More information will be given in the EDS section just below. Surprisingly, in all TEM images (around 20 NWs), we noticed a 2.9 nm thick shell formed around the catalyst droplet.

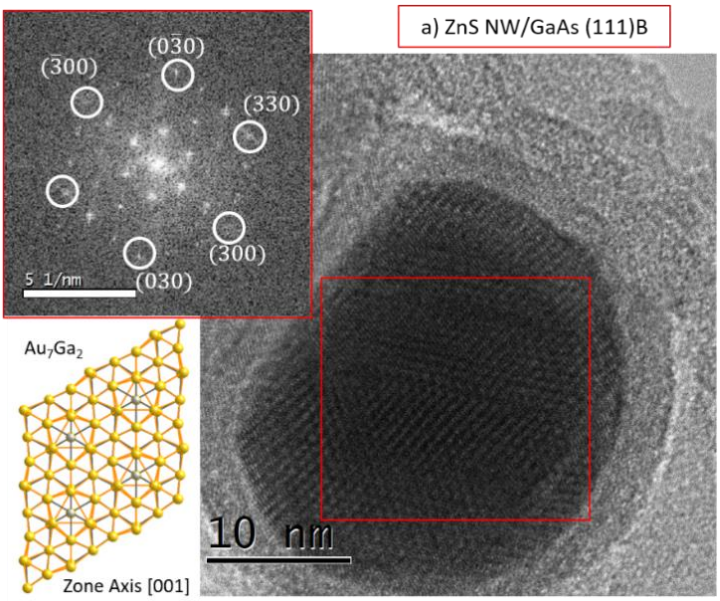

Figure 4.10: HRTEM image of the catalyst present at the top of a ZnS nanowire grown on a) GaAs (111)B, the FFT pattern of the HRTEM image taken in [001] zone axis reveals Au_7Ga_2 phase of the catalyst.

4.3.2.2 EDS of catalyst droplet

EDS analysis of the catalyst droplet present at the top of the nanowire was performed. EDS mappings are illustrated in the Figure 4.11. Regarding NWs grown directly on GaAs (111)B, Ga and Au contents are detected (Figure 4.11c), but no presence of Zn or S (or below the detection limit) has been found. At first sight, the area of Ga mapping appears to be larger than the one of Au, indicating that Au is more distributed at the center. It matches with the HAADF image (Figure 4.11d) which manifests that the droplet is surrounded by two shells, possibly a Ga-rich shell and a GaO shell, respectively. This core/shell structure could be induced during the cooling.

To go further, compositional measurements were carried out on four different catalyst droplets : i) on the whole ensemble of catalyst droplet, and ii) : focusing on the core of the droplet as shown in the Figure 4.12. These measurements were done to study the spread of the gallium inside the droplet. The compositional values of gold and gallium are summarized in Table 4.2. For the ensemble, an Au-rich phase from 61 to 78% Au and 22 to 39% Ga has been perceived. The compositional values of Au and Ga were found to be non-homogenous, and the core of the droplet measured to be richer in Au compared to the whole ensemble (71 to 89%Au at center). Such low composition of Ga in the core suggests that the Ga diffuses towards the surface of the catalyst droplet to get oxidized to form a GaO shell. Consequently, we infer that the catalyst droplet is liquid after the dewetting on GaAs (111)B and would exhibit an Au_2Ga phase (33% Ga, corresponding to the eutectic composition), and that the growth of the NWs takes place via this liquid Au_2Ga alloy [206,207]. Subsequently, during the cooling, the Ga diffuses from the core toward the surface, leaving an Au_7Ga_2 (Figure 4.10) or at least an Au-rich core, and oxidizes on the surface to form a GaO shell.

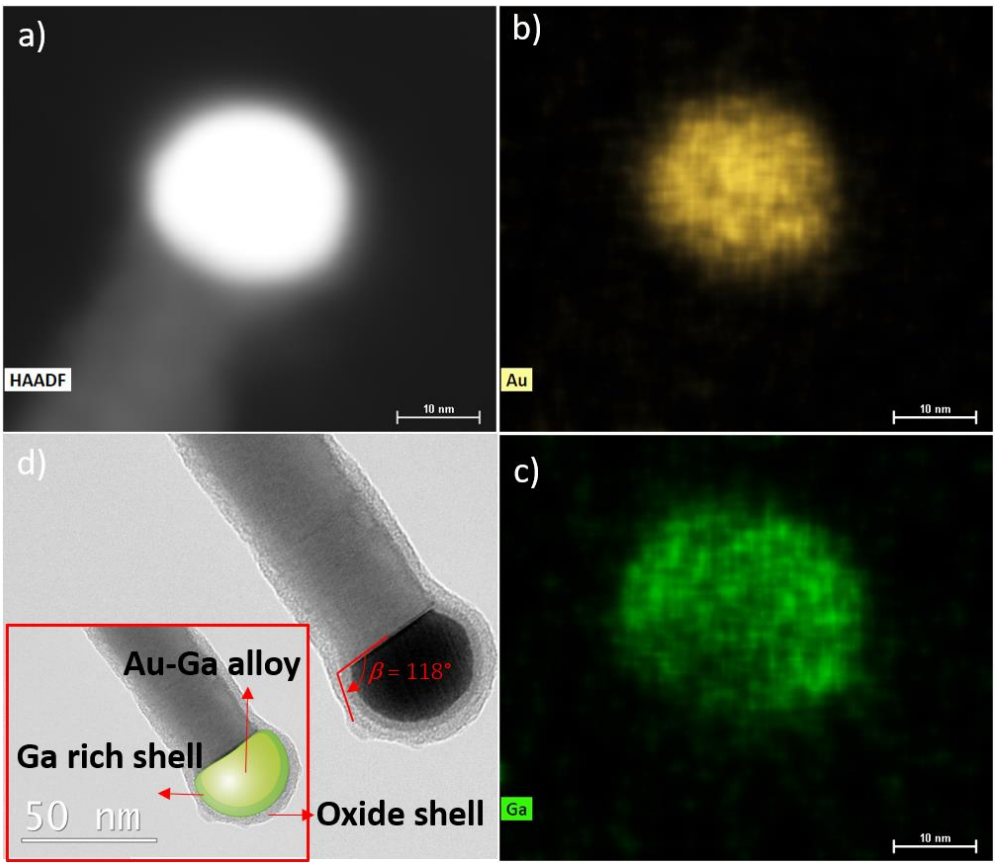

Figure 4.11: a) HAADF image of the catalyst present at the top of VLS grown nanowire, b) EDS gold mapping of VLS ZnS NWs, c) EDS gallium mapping of VLS ZnS NWs, d) Ga-rich shell and oxide shell surrounding the Au-Ga catalyst droplet.

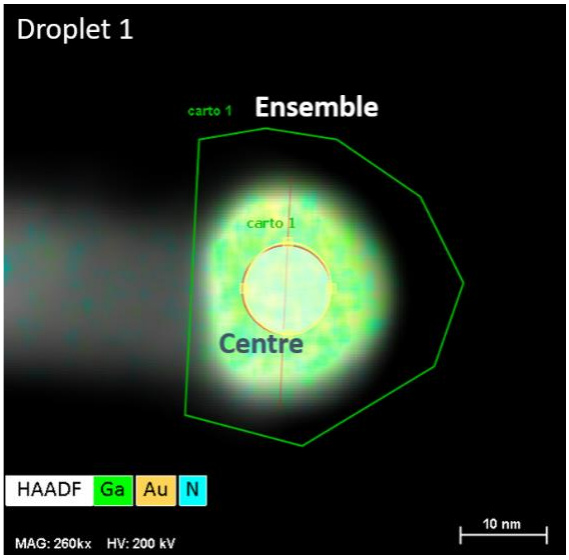

Figure 4.12: EDS measurements were performed on ensemble and at the core (center) of catalyst droplet for VLS grown ZnS NWs. The gallium and gold composition are found to be 10.6 and 89.3 % at center, and 22 and 78 % in the ensemble.

Droplet	Measurements	Gallium (%)	Gold (%)
1.	Center	10.6	89.3
	Ensemble	22.0	78.0
2.	Center	23.7	76.3
	Ensemble	35.8	64.1
3.	Center	22.8	77.2
	Ensemble	38.7	61.3
4.	Center	28.6	71.4
	Ensemble	38.4	61.6

Table 4.2: The compositional values of gold and gallium measured for the different catalyst droplets at their center and for the whole ensemble of droplet. The measurements were carried on four different catalyst droplets.

4.3.3 15R polytype and VLS growth mechanism

TEM analysis revealed a 15R phase in the VLS grown NWs. If we look into the detail of the stacking sequence ABCBA–CABAC–BCACB illustrated in Figure 4.13d, the 15R structure exhibits cubic and hexagonal planes stacked in a periodical manner along the growth direction, <111> for ZB ABCABC…, and <0001> for WZ ABAB.... Expressing the repeated cell with the corresponding "*h*" or "*c*" planes gives an *hcchc–hcchc–hcchc* stacking sequence as shown in Figure 4.13. The 15R crystal structure is referred as 32, a sequence of 3 planes and a sequence of 2 planes repeated three times to give a stacking of 15 planes (see Figure 4.13c) in Zhdanov notation [66]. The first sequence of 3 planes has Zn–S bonds in one direction, and the following 2 planes have corresponding bonds in the other direction, so that the structure can be seen as a ZB zig-zag structure. It can also be described as the stacking of 3 untwinned ZnS tetrahedra followed by 2 twinned tetrahedra [203]. Therefore, we can introduce the notation A', B' and C' to take into account such rotation of the bonds around the vertical direction, as illustrated in Fig. 4.13a. The 15R structure observed in our ZnS NWs is now fully described as ABCB'A'–CABA'C'–BCAC'B'. In the 3 cycles of 5 planes, the periodic rotation of the first plane is noteworthy. Each cycle shows a “mirror” plane, namely the third one at the center, which can be considered as a twin, e.g., plane C in the ABCB'A' cycle. The conditions needed to crystallize the 15R structure could be analyzed by examining the *hcchc–hcchc–hcchc* stacking.

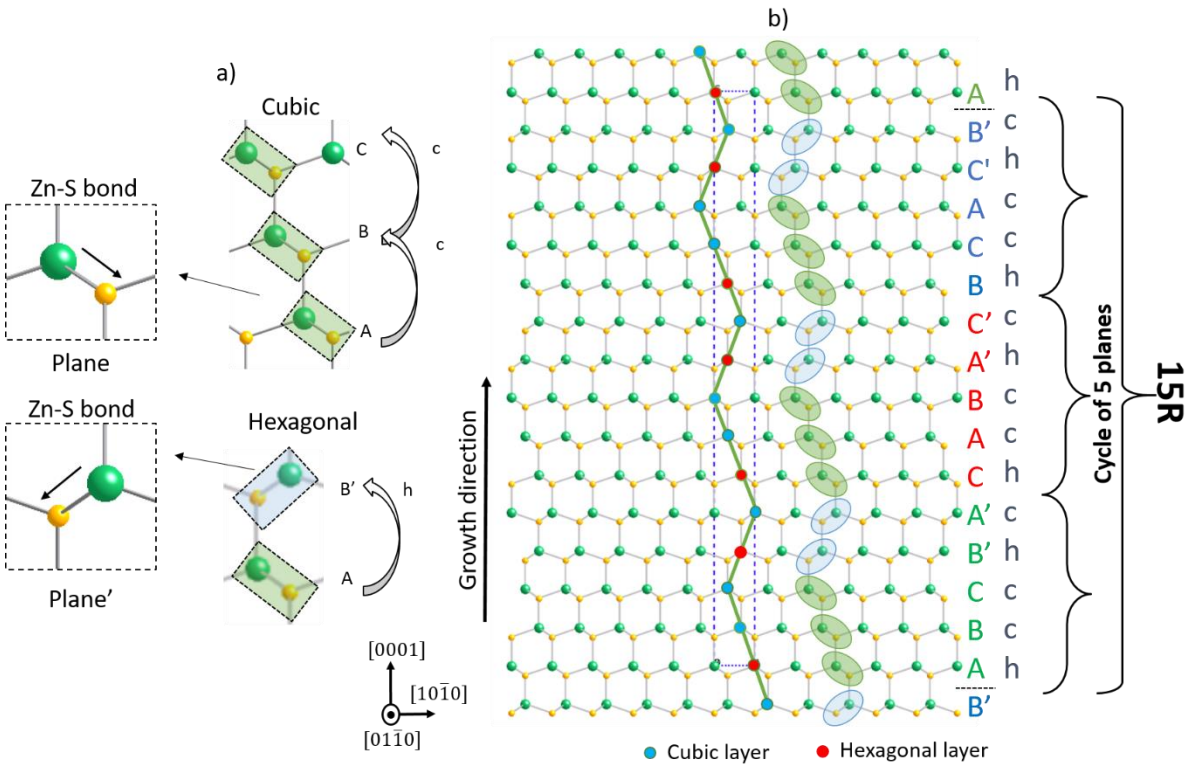

Figure 4.13: (a) Notation of the planes (plane and plane') with respect to the direction of bonds, and the stacking of hexagonal (h) and cubic (c) planes, (b) the structural model of 15R structure with 3 cycles of 5 planes, giving the ABCB'A'–CABA'C'–BCAC'B' sequence.

We introduce two descriptions which can be seen as a growth mechanism with certain rules.

Description 1: growth mechanism considering monolayer by monolayer deposition. The 15R crystal structure can be built with the four following rules:

$$\text{i) h} \rightarrow \text{c, ii) cc} \rightarrow \text{h, iii) cchc} \rightarrow \text{h, and iv) hchc} \rightarrow \text{c}$$

where we put the underlying MLs at the left of the arrow and the new ML at the right. There is no *hh* stacking, letting assume that the hexagonal phase formation is unfavorable, in agreement with cohesive energy calculations. We thus mark that there is a strong tendency to alternate c and h MLs, with only one exception of the 4th transition (i.e. *c* plane is deposited on *c*). This exception makes all the difference between crystallization of 15R with that of 4H (chchch stacking). It implies that, during the growth of a new ML, the interaction can involve up to 4 underlying MLs. Such interaction beyond the nearest neighboring ML has been reported by Johansson [208] and Priante [78] in III-V NWs growth and investigated in the framework of ANNNI model.

Description 2: growth mechanism considering the stacking fault formation. The sequence "*hch*" in ZB structure is labeled as an extrinsic stacking fault (ESF) [191]. On considering the ESF, the crystallization of 15R can be predicted with only one rule:

$$cc \rightarrow hch \text{ (ESF)} \rightarrow cc.$$

where it means after every *cc* (cubic) sequence, the crystallization of a stacking fault is occurring. The energetic calculations for different stacking faults (intrinsic stacking fault (ISF),

twin stacking fault (TSF) and ESF) in ZB ZnS will provide a clear sight on the type of stacking fault to be favored. The different type of stacking faults in WZ and ZB lattices are illustrated in Figure 4.14. We calculated these energy values using the same parameters as presented in Equation (1) [191].

$$
\begin{aligned}
E_{\mathrm{ISF}}^{\mathrm{ZB}} &= 2(\partial_1 - \partial_2) = 6 \text{ mJ/m}^2 \\
E_{\mathrm{twin}}^{\mathrm{ZB}} &= \partial_1 - 2\partial_2 = -1.8 \text{ mJ/m}^2 \\
E_{\mathrm{ESF}}^{\mathrm{ZB}} &= 2(\partial_1 - 2\partial_2) = -3.6 \text{ mJ/m}^2
\end{aligned}
\qquad (3)
$$

Therefore, ESF having the minimum energy will be more likely to occur. It has to be nevertheless noted that having the minimum energy is not the unique condition to favor ESF in ZB, since such occurrence is also dependent on growth conditions as well as on interface and edge energies [11,148].

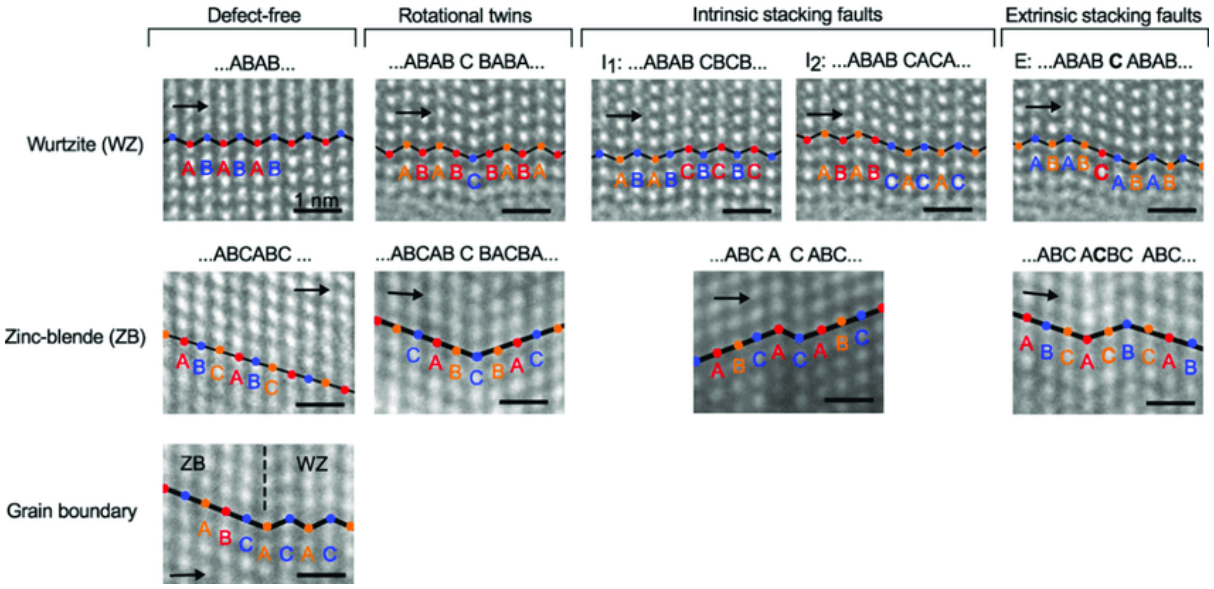

Figure 4.14: TEM images of InAs and $InAs_{1-x}Sb_x$ NWs showing pure WZ and ZB structures with several planar defects including rotational twins and stacking faults. Adapted from [209].

As previously mentioned, twin boundaries, stacking faults and polytypes are commonly observed in semiconductor NWs growth [210–212]. A nucleation-based model has been proposed by Glas et al. [11] and Dubrovskii et al. [213] to explain crystal phase switching between ZB and WZ during the catalyzed growth of NWs. In this model, nucleation at the triple phase line (TPL, at the edge of the solid–liquid interface, thus in contact with the vapor) favors the formation of the WZ structure, while nucleation away from the TPL (within the nanowire–liquid interface) leads to ZB growth. Thus, identification of the exact nucleation site is key to understand the mechanisms of phase selection in NW growth. Experimentally, performing *in situ* GaAs NW growth in a TEM, it has been shown that the crystal phase of the NW is governed by the contact angle of the catalyst droplet [18]. Droplet geometry could be varied with the group III and group V fluxes. A critical contact angle around 125° has been measured which defines a transition between WZ growth at the TPL (< 125° [148],) and ZB growth (> 125°, with edge truncation [18,149]). Interestingly for II-VI compounds, and without carrying out *in situ* observations, Hao et al. [24] have early reported periodic twins in a ZB ZnS NWs and have presented a growth model where the droplet geometry would vary during the growth. They explained that when growth conditions (mainly high growth temperature) lead to

the situation that the diffusion of species in the liquid catalyst is slower than the crystal growth at the L–S interface, periodic depletion of Zn and S results in a modulation of the droplet contact angle, due to a change in the wettability. In our experiments, similarly to III-V NWs, the change in the nucleation site could be related to the modulation of the droplet contact angle. We measured a contact angle between 110° and 123°, close to the critical angle reported for GaAs (125°). Without stating that ZnS and GaAs VLS cases are equal, this may aid the discussion about the involved mechanism. A small variation of the contact angle around its critical value would bring a ZB (*c*) or WZ (*h*) plane formation. At the moment, the origin of this particular hcchc–hcchc–hcchc stacking is still to be specified, but the door is now open for a theoretical study, primarily in the light of the ANNNI model.

On the basis of such knowledge, and considering the interface energies, edge energies and the preference for the nucleation site in ZnS NWs, the motivation is now generated for a subsequent work, where we would model the nucleation mechanism involved in the formation of the 15R phase or other polymorphs. For example, it would be worth investigating theoretically growth parameters having a strong influence on the crystal structure, such as precursor partial pressures (which control the supersaturation) [214]. Actually, this will constitute our chapter 5.

4.4 Structural analysis of VSS grown NWs on ZnS buffer

Introducing ZnS buffer between gold droplets and GaAs substrate, we aimed to suppress the diffusion of Ga into the catalyst. In that case, the NW growth at 550°C would involve pure Au, which would be therefore in the solid state (melting point at 1064°C), and the process should be vapor-solid-solid (VSS).

4.4.1 TEM measurements

The TEM image of a single nanowire grown on ZnS/GaAs (111)B (i.e. with buffer) is shown in Figure 4.15a. Thinner and shorter NWs were observed on ZnS buffer samples, with length of 230-590 nm and diameter ranging 7-25 nm, as well as worm-like and kinked NWs with a larger diameter around 25-30 nm. The straight and worm-like kinked NWs are distinguished with blue and yellow markers, respectively. This supports the idea that there exists a critical diameter of the catalyst above which the growth of straight nanowires is suppressed by either development of kinks or formation of a 2D layer on the catalyst. Interestingly, the stacking sequence of the HRTEM image discloses separate and large domains (Figure 4.15b). The FFT patterns given in Figure 4.15c-d indicate the formation of pure WZ and ZB domains, respectively. More in details, the NW contains large segments of WZ with inclusion of short 1–15 nm thick ZB phases (with an average of 4 nm). The stacking sequence at the interface of WZ and ZB is confirmed to be ABABABCABC. With the help of FFT pattern, we find that the NWs grow in the [0001] and [111] directions for WZ and ZB phases, respectively, which is commonly observed in semiconductor NWs' growth. Moreover, we have not found any visible correlation between the diameter and the length of the observed segments (ZB or WZ).

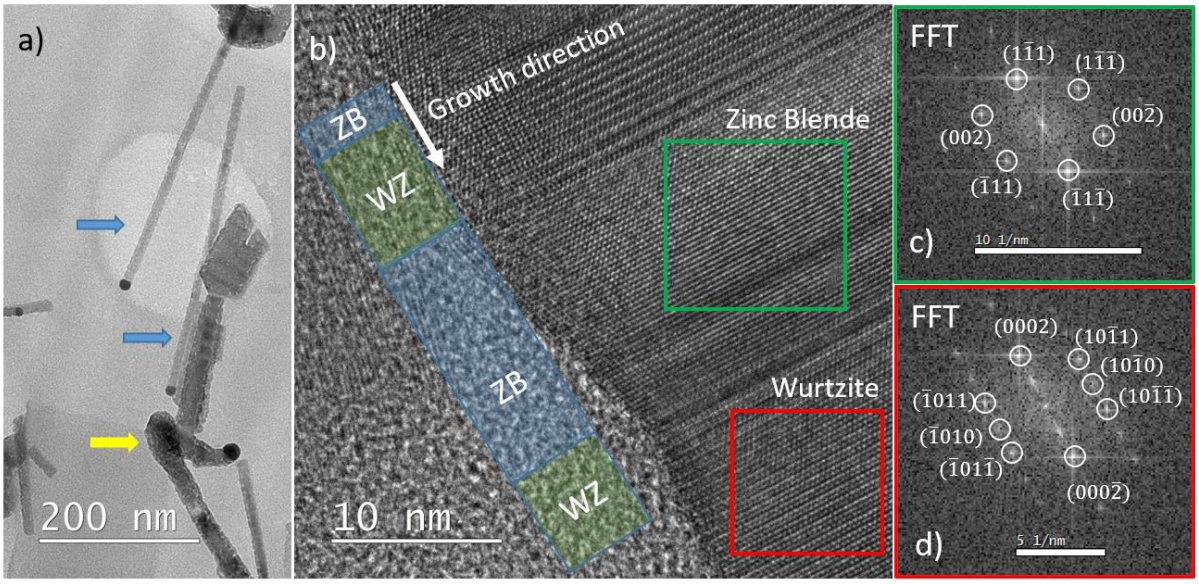

Figure 4.15**:** (a) TEM image of a single nanowire grown on ZnS buffer/GaAs (111)B, (b) HRTEM image with single domains of ZB and WZ phases, (c) FFT pattern of a ZB segment, (d) FFT pattern of a WZ segment.

4.4.2 The catalyst droplet analysis

4.4.2.1 HRTEM of catalyst droplet

In Figure 4.16, the catalyst shows a facetted shape and the FFT pattern confirms the pure gold phase of the catalyst with a face-centered cubic structure. Interplanar distances were calculated as 0.239 nm and 0.206 nm which corresponds to (111) and (002) planes respectively. The [002] axis of the gold catalyst is parallel with the [0001] or the [111] axis of the NW. Moreover, the facets present on the droplet are (111) oriented and compatible with solid gold particles [215]. This occurrence suggests the VSS growth process of the NWs. Noteworthy, no shell was developed for NW grown with ZnS buffer layer, unlike the case of VLS NWs where GaO shell has been previously identified.

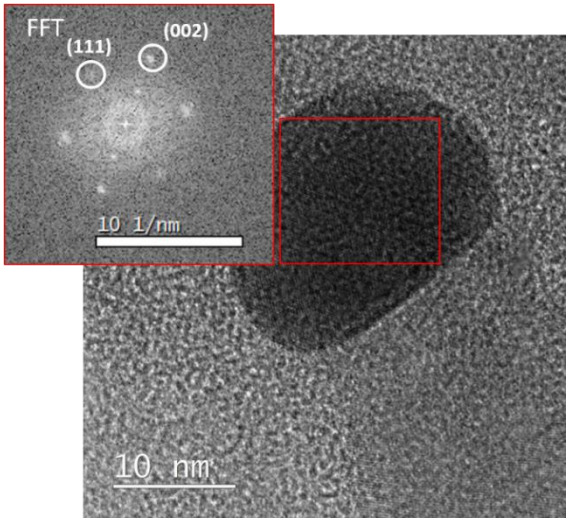

Figure 4.16: ZnS buffer/GaAs (111)B, a faceted catalyst droplet can be seen in the HRTEM image and the corresponding cubic phase from the FFT pattern emphasizes the pure Au solid phase of the droplet.

4.4.2.2 EDS of catalyst droplet

EDS analysis (Figure 4.17) of the tip of a nanowire grown with ZnS buffer only shows the presence of gold with no detectable traces of gallium, Zn, or S, in agreement with FFT pattern observations.

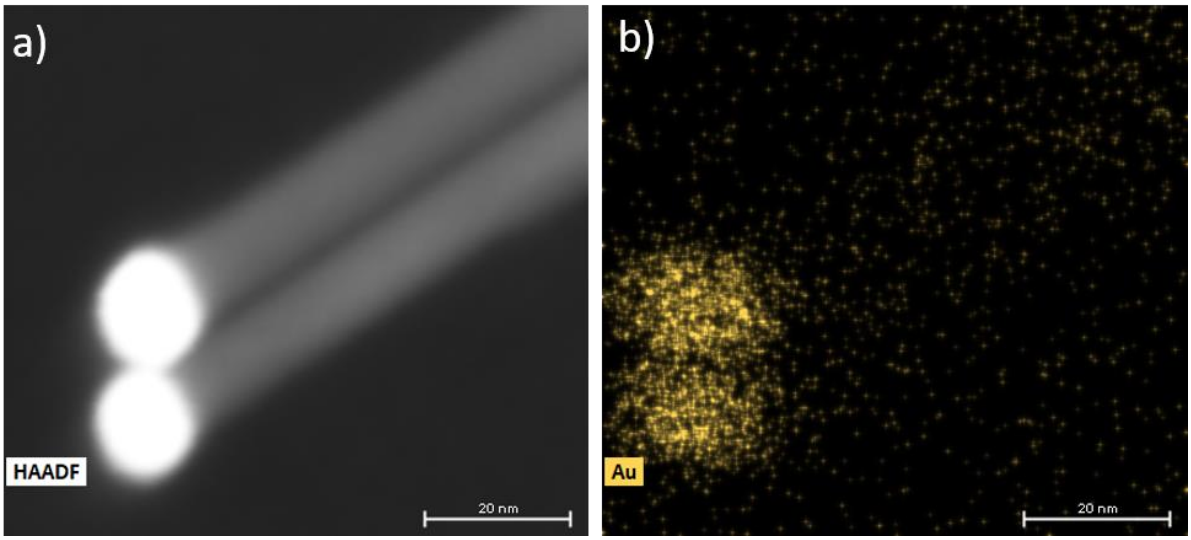

Figure 4.17: a) HAADF image of the catalyst for VSS grown nanowire, b) EDS gold mapping of VSS ZnS NWs.

4.4.3 VSS growth mechanism

VSS growth involving solid Au-catalyst has been reported for many semiconductors such as GaAs, InAs, Si, Ge, ZnSe, ZnTe, and ZnO [94,95,195,216–218]. In this process, atoms from the vapor phase adsorbing on the Au particle would diffuse in the body towards the growing interface. However, it is still not clear whether the reactants are actually incorporated into the catalyst or would diffuse on the surface to reach the interface edge (similar to the TPL in VLS, in the following section referred as "pseudo-TPL"), and further crystalize at the solid-solid (droplet-NW) interface. Like in VLS, diffusing adatoms from the substrate and from the NW sidewalls could also contribute to the growth. In our case, we assume that there is no incorporation of S in the Au-droplet at 550 °C due to high volatilization of sulfur [219]. The Au2S alloy may exist, and has been synthesized and investigated by Ishikawa et al. [220], but it was shown to decompose at temperatures above ~ 500 K. It is difficult to state if Zn diffuses in the droplet. At 550 °C, considering the phase diagram, the Au-Zn alloy can be in the liquid state but only for high Zn contents, in the range of 85%–100% [221]. Such strong diffusion of Zn in the Au-particle is not expected. In the literature, there is no evidence of liquid Au-Zn alloy catalyzing the NW growth, e.g. in the case of ZnTe or ZnSe at temperatures between 350 and 450 °C. Interestingly, at a much higher temperature (900 °C), Simon et al. [218] proposed a growth model involving an Au-Zn (8.5%–12.5% Zn) liquid skin at the surface of the catalyst to describe the growth of ZnO NWs, where zinc atoms diffuse towards the pseudo-TPL and react with oxygen atoms. In our grown ZnS samples, EDS analysis of the catalyst shows no detectable Zn, nor S, letting impede that the droplet remains solid, leading to a VSS growth. Reactant species are believed to be mainly transported via diffusing through the solid Au surface, as well as along the NW sidewalls [26,222]. However, a contribution of a small fraction of Zn or S diffused in the solid cannot be fully rejected, as we know that, for example, GaAs NWs are grown using an As content in the Au-Ga catalyst as low as 0.01% [223].

In contrast with VLS, ZnS NWs grown with solid catalysts exhibit pure WZ and ZB domains and frequently switch between these two structures. Due to the solid state of the Au-particle, the diffusion of Zn and S atoms at the solid–solid interface is reduced and their transport towards the inner part of the growth front is slow [195]. Consequently, a new growing plane could start to nucleate before the last one has completed [218]. This may lead to instabilities affecting the growth front geometry, which could be either flat, symmetrically or asymmetrically facetted (illustrated in Figure 4.18), as well as impacting surface energies and the contact angle at the pseudo-TPL. Then, nucleation can occur at different sites leading to stacking defects, kinks and crystalline phase changes.

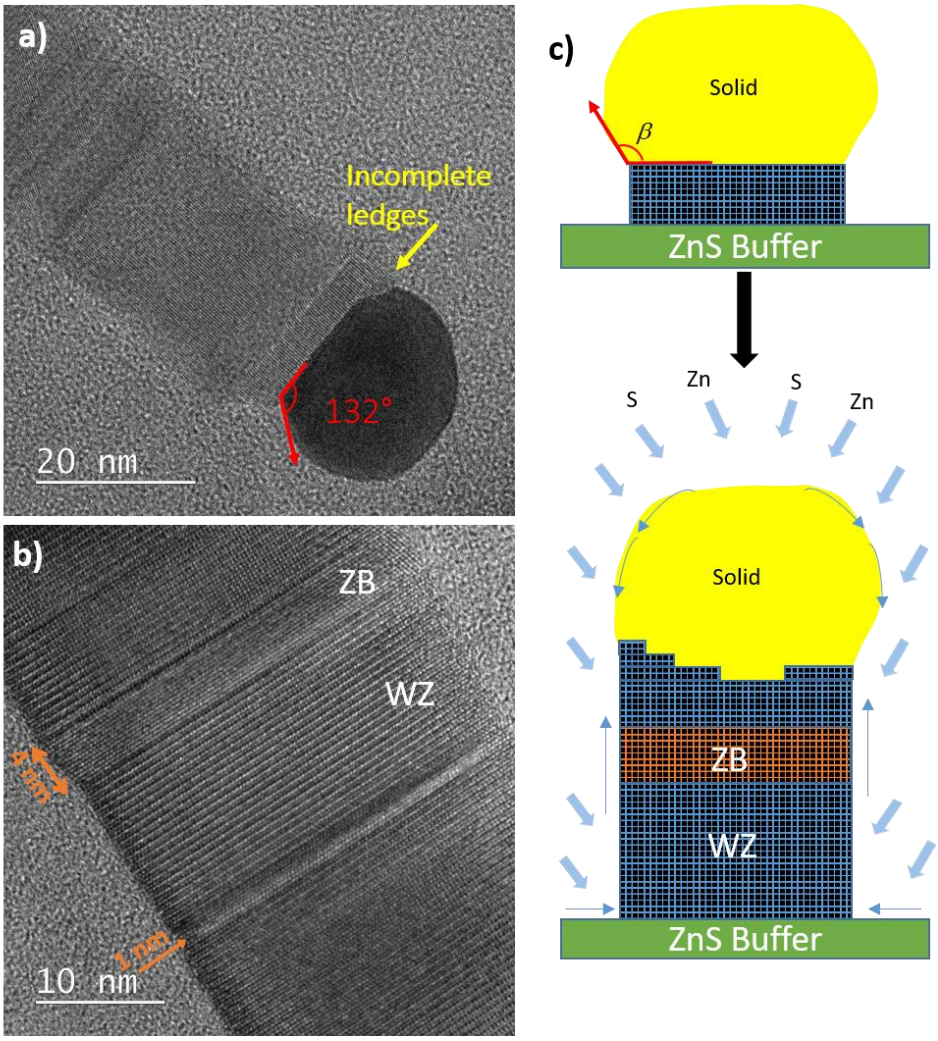

Figure 4.18: (a) The faceted droplet with incomplete ledges (or layers). (b) The stacking of small ZB segments (1 and 4 nm) in the WZ structure. (c) The model showing formation of ledges (incomplete layers) with a faceted solid droplet at the top.

In particular, it has been suggested that slow growth kinetics in VSS process produce the wormlike nanowires [195,224,225]. Similar to the case of ZnSe NW growth [195], we observe that small catalyst particles (10–20 nm in diameter) lead to a flat droplet–NW interface and hence straight NWs growth, whereas worm-like and kinked nanostructures are induced by large and facetted Au-droplets. Rueda et al. [217] also demonstrated that the crystal structure of VSS grown ZnTe nanowires is gold particle geometry dependent. A half sphere catalyst (i.e.,

small contact angle) matching the diameter of the NW resulted in a WZ crystal phase, whereas a full sphere gold catalyst particle (i.e., large contact angle) was found at the tip of ZB NW.

At the difference of VLS process involving a liquid droplet, high order polytypes are not observed when the catalyst remains solid. This could be understood by the modified growth kinetics, as well as the surface energy difference between pure Au and Ga-Au surface [226]. Also, the 15R could occur in a particular range of supersaturation in VLS, as proposed in the work of Johansson et al. [227], where the density of stacking faults and WZ segments in ZB GaP NWs is related to the concentration of reactants in the catalyst. This will be further modeled and discussed in the following chapter 5, where we will emphasize the opening of a "high order polytypes window" in certain conditions. In addition, the liquid or solid state of the catalyst may involve distinct growth processes at the droplet/NW interface: ML by ML growth observed as *in situ* grown GaAs can be assumed for VLS NWs, in contrast with multiple nucleation at the solid–solid interface in VSS.

Finally, a last feature is that VSS involves segments of pure hexagonal phase in the NW. This particular growth condition overcomes the limitation of 2H crystal phase due to a higher cohesive energy. This confirms that the occurrence of a particular phase in semiconductor NW growth is not only dependent on the cohesive energy but also on thermodynamics and growth conditions.

4.5 Conclusions

In conclusion, we have demonstrated that different crystallographic phases in ZnS nanowires could be achieved by varying the NW growth mechanisms. Two different Au-catalyzed growth approaches, namely VLS and VSS, were employed to grow vertically aligned ZnS NWs by MOCVD. In the VLS case, the growth of ZnS nanowires directly on GaAs (111)B was assisted by Au_2Ga alloyed droplets in the liquid state, which would subsequently change to a core-shell structure (Au_7Ga_2 core surrounded by Ga-rich Au_xGa_y and Ga_xO_y shells) during the cooling to room temperature and air exposure. On the other hand, the VSS growth involved a ZnS buffer layer to prevent Au–Ga interaction with the substrate and to enforce a pure solid Au catalyst. A comprehensive structural analysis was performed to study the different crystallographic phase in the NWs. The HRTEM images analysis of VLS grown samples undoubtedly identified a 15R crystal phase, which had never been observed in ZnS nanowires. We detailed such 15R sequence and proposed selection rules to illustrate its formation. Regarding the NWs grown on ZnS buffer (VSS mode, solid catalyst), an HRTEM study of straight wires revealed large segments of WZ with inclusion of small ZB segments.

Finally, with this study, we emphasize that ZnS is a perfect material to study polytypes in semiconductor nanowires as cohesive energy differences are small between the available crystal phases.

Chapter 5

Emergence and control of polytypes: theoretical modeling

Contents

In this chapter, we will offer a theoretical model based on previously developed nanowire growth models which combine two contributions: i) classical nucleation theory-based nanowire growth dynamics, and ii) probabilistic polytype calculation. At first, we will present and apply Johansson's approach for calculating the probability of formation of the 3C, 4H, 6H, and 2H polytypes in GaAs, and further introduce 15R as another potential crystal phase. In the second part of the chapter, we will extend this model to better describe the surface energies of the developing nucleus at the TPL. The extended model will be applied to GaAs as well as ZnS nanowires.

Unit conversions: 1J = 1e+7 erg = 6.24e+18 eV

5.1 Introduction

The nanowire growth dynamics is based on classical nucleation theory (refer section 2.1.1). It states that a nucleus initiates at the interface between the catalyst droplet and the solid top of the nanowire, and that this nucleus then expands across the entire interface to form a single bilayer (e.g., bilayer of Ga and As atoms for GaAs, but will be referred to as monolayer (ML) in the following text). In 2012, Johansson provided formation probability estimates to explain how polytypes develop in III-V semiconducting nanowires [161]. Next sections 5.2 and 5.3 will discuss the ANNNI model and Johansson's technique.

5.2 State of the art

We present below the model developed by Johansson, based on the ANNNI model [160].

5.2.1 Classical nucleation theory

In this section, we will quickly explain the adaptation of classical nucleation theory, introduced in chapter 2. In their model, Johansson and co-authors have considered a 2D semicircular geometry of the nucleus with the straight edge of the nucleus along the triple-phase line (TPL) and the curved edge in the interior of the catalyst-nanowire interface, as illustrated in Figure 5.1 [160].

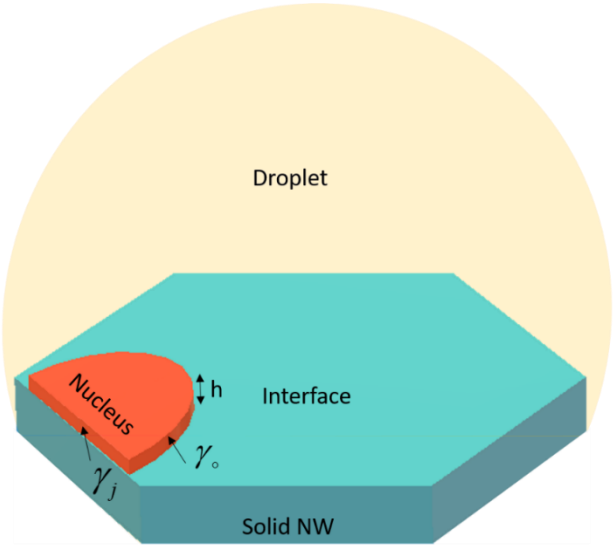

Figure 5.1: The bird eye view of nanowire-droplet interface with formation of a 2D semicircular nucleus (in red) of height *h* and other respective surface energies.

For this nucleus geometry, the critical formation energy of a nucleus is given by:

$$\Delta G_j^* = \frac{\Gamma_j^2}{2\pi\left(\frac{\Delta\mu}{s} - \sigma_j\right)} \qquad (5.1)$$

Where $\Delta\mu$ is the chemical potential difference of reacting species in the droplet (also called supersaturation), s is the area of the molecular site on the {111} interface, Γ_j is the step energy, and σ_j is the interface energy between nucleus and solid NW. The subscript j stands for cubic (c) or hexagonal (h) type of nucleus, the step and surface energy are different for each of them.

The effective edge energy for such nucleus is given by,

$$\Gamma_j = (2\gamma_j + \pi\gamma_\circ)h \qquad (5.2)$$

Where, γ_j is the straight edge energy at TPL for j stacking, $\gamma_\circ$ is the interior edge energy and h is the height of the bimolecular step.

Like in chapter 2, the nucleation rate of a specific island (j) on the top of previous stacked layer is given by,

$$N_j = AZ_j \exp\left(\frac{-\Delta G_j^*}{k_B T}\right) \qquad (5.3)$$

Where A is a function of attachment frequency of III-V pairs to the critical radius and their concentration in the droplet, k_B is the Boltzmann's constant, Z_j is the Zeldovich factor, and T is the growth temperature in kelvin.

The Zeldovich factor is expressed as,

$$Z_j = \sqrt{\frac{1}{2k_B T}}\frac{s}{\Gamma_j}\left(\frac{\Delta\mu}{s} - \sigma_j\right)^{3/2} \qquad (5.4)$$

Furthermore, and interestingly, Johansson applied the ANNNI model to the interface energy taking upon the interaction up to the third layer. Thus, the interface interaction energy could be expressed as,

$$\begin{aligned}\sigma_{j|klm} &= \sigma_\circ - s_j \sum_{i=1}^{3} J_i s_i \\ &= \sigma_\circ - J_1 s_0 s_1 - J_2 s_0 s_2 - J_3 s_0 s_3\end{aligned} \qquad (5.5)$$

Where σ_o is the energy of the stacked layer if no interactions are present, s_0 is the spin of j nucleus, and s_1, s_2, and s_3 are the spins of previous stacked layers k, l and m respectively.

Notations Used: To define spins of stacked layers, we need to consider a reference spin +1. For instance, to define interface interaction energy of $c|ch$ sequence (nucleation of c on ch sequence i.e. $j = c$, $k = c$, $l = h$) we consider $s_3 = +1$, see Figure 5.2. The conversion from h-c notation to spin assignment can be referred from Table 1.

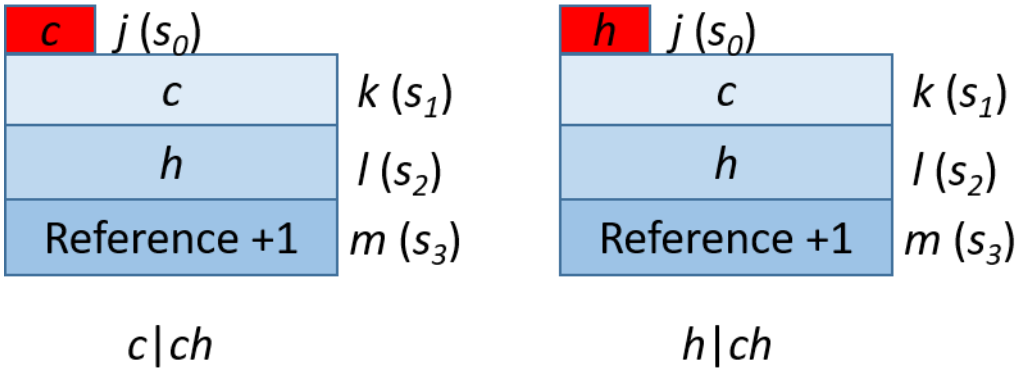

Figure 5.2: Illustration of the sequences $c|ch$ (c on ch) and $h|ch$ (h on ch).

The interface energy (σ) for different sequences can be expressed as following:

$$\sigma_{c|cc} = -J_1 - J_2 - J_3 \quad (5.5a)$$

$$\sigma_{h|hh} = J_1 - J_2 + J_3 \quad (5.5b)$$

$$\sigma_{h|ch} = J_1 + J_2 - J_3 \quad (5.5c)$$

$$\sigma_{c|hc} = -J_1 + J_2 + J_3 \quad (5.5d)$$

$$\sigma_{h|cc} = J_1 + J_2 + J_3 \quad (5.5e)$$

$$\sigma_{c|ch} = -J_1 - J_2 + J_3 \quad (5.5f)$$

$$\sigma_{c|hh} = -J_1 + J_2 - J_3 \quad (5.5g)$$

$$\sigma_{h|hc} = J_1 - J_2 - J_3 \quad (5.5h)$$

Here, $\sigma_o = 0$ is considered since this term is the energy of a non-interacting layer and does not contribute to the interface energy.

5.2.2 The polytype formation probabilities

The probabilities of stacked layers are defined using the nucleation rate. Johansson et al generalized this expression for the nucleation of a particular layer *j* (*j* = *c* or *h*) on previously stacked layers *uv* (*u* and *v* can be *c* or *h* layers) [160],

$$p_{j|uv} = \frac{N_{j|uv}}{N_{j|uv} + N_{j'|uv}} \quad (5.6)$$

Where *j'* stacking is different from *j* stacking. If *j* is *c*, *j'* will be *h* and vice versa.

For example, the probability of a particular sequence *c*|*ch* is given by the nucleation rate for *c* on *ch* divided by the sum of the two nucleation rates: *c* on *ch* and *h* on *ch*. In the same way, the probability of complementary sequence *h*|*ch* is expressed in equation 8b:

$$p_{c|ch} = \frac{N_{c|ch}}{N_{c|ch} + N_{h|ch}} \quad (5.7a)$$

$$p_{h|ch} = \frac{N_{h|ch}}{N_{h|ch} + N_{c|ch}} \quad (5.7b)$$

Using these probabilities representation, we can express the probabilities of all polytypes [160],

$$\rho_{3C} = \left(p_{c|cc}^3\right)^{N/3} \quad (5.8a)$$

$$\rho_{2H} = \left(p_{h|hh}^2\right)^{N/2} \quad (5.8b)$$

$$\rho_{4H} = 2\left(p_{h|ch}^2 p_{c|hc}^2\right)^{N/4} \left(\text{degeneracy} = 2\right) \quad (5.8c)$$

$$\rho_{6H} = 3\left(p_{h|cc}^2 p_{c|hc}^2 p_{c|ch}^2\right)^{N/6} \left(\text{degeneracy} = 3\right) \quad (5.8d)$$

Where, the factors 2, and 3 are the degeneracy factors of these polytypes compared to 2H and 3C. For example, 4H can be described as *hchc* or *chch* (hence two possibilities), and 6H as *hcchcc*, or *chcchc, or cchcch* (3 possibilities).

For easy comparison, same number of layers for each polytypes have considered, thus N = 6 represents one 6H, two 3C, three 2H, one and a half 4H. Again, normalization of all polytypes is required to express the final polytype probability that is given by [160],

$$P_q = \frac{\rho_q}{\sum_Q \rho_Q} \tag{5.9}$$

Where q and Q are one of the polytypes (3C, 2H, 4H, 6H) and the summation in the denominator represents the sum of all four polytypes.

For example, the 3C polytype probability can be expressed as:

$$P_{3C} = \frac{\rho_{3C}}{\rho_{3C} + \rho_{2H} + \rho_{4H} + \rho_{6H}} = \frac{\left(p^3_{c|cc}\right)^2}{\left(p^3_{c|cc}\right)^2 + \left(p^2_{h|hh}\right)^3 + 2\left(p^2_{h|ch} p^2_{c|hc}\right)^{3/2} + 3\left(p^2_{h|cc} p^2_{c|hc} p^2_{c|ch}\right)} \tag{5.9a}$$

5.2.3 Results of the model

The polytype formation probabilities were calculated from equations (9) introducing the parameter values given in the Table 5.1 for GaAs. Here γ_o is the interior step energy of the nucleus. In his work, Johansson sets the edge energy of a cubic nucleus γ_c. equal to γ_o so that $\gamma_o = \gamma_c$. He also sets the edge energy ratio between hexagonal and cubic as $\gamma_h / \gamma_c = 0.4$ [160]. Noticeably, he makes no distinction between the inner edge energy (in contact with the liquid) and the edge in contact with the vapor. As we will see later, this leads to a strong limitation of this model.

γ_o (erg/cm^2)	J_1 (erg/cm^2)	J_2 (erg/cm^2)	J_3 (erg/cm^2)	γ_h/γ_c	T
119.3	10	-1	-1	0.4	500 °C

Table 5.1: The values of surface energies and interaction energies for GaAs taken from Johansson [160].

The polytype formation probabilities are plotted as a function of supersaturation per area (Δ/s) in Figure 5.3.

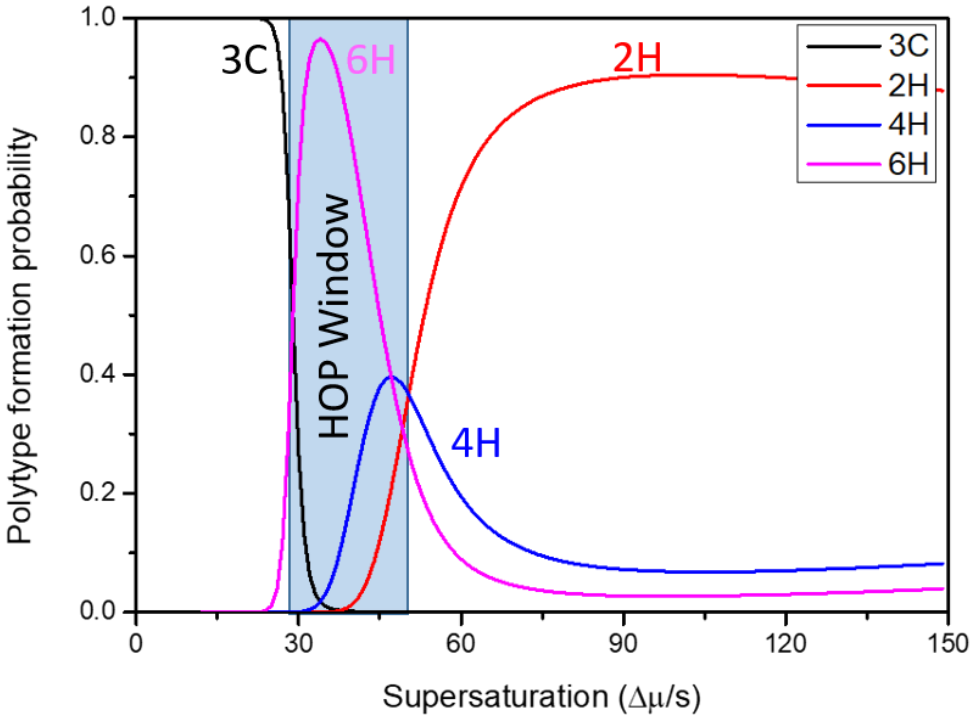

Figure 5.3: The polytype formation probabilities of 3C, 2H, 4H, 6H are plotted as a function of supersaturation. The 3C polytype dominates at low supersaturation values, as supersaturation increases high order polytypes starts to dominate for a certain range, and then after 2H polytype dominates. Unit of supersaturation $\Delta\mu/s$ is erg/cm^2.

The plot in Figure 5.3 clearly suggests that the most common polytypes 3C and 2H dominate at low and high supersaturation values respectively. This follows well in accordance with experimental and theoretical findings [162,164]. The high order polytypes (4H and 6H) occur in an interval of supersaturation values that we will call "high order polytypes (HOP) window". Further, Johansson demonstrated that this window is dependent on the J_2 and J_3 interaction parameters. Playing with the combination of these two interaction parameters can affect the HOP window as well as the probabilities of 4H and 6H probabilities (or dominancy) can be altered.

The nine combinations of J_2 and J_3 interaction energies are depicted in Figure 5.4 [160]. At low and high supersaturations, respectively, the 3C and 2H polytypes invariably dominate. For J_2 values ranging from -1 to 1 erg/cm^2, both the HOP window and the 4H and 6H probability decline dramatically for all J_3 values. In a small supersaturation interval for J_2 = 1 erg/cm^2, the probability of 4H is dominant. This probability, however, reduces as J_3 is reduced from 1 to 1 erg/cm^2. Simultaneously, the probability of 6H increases. All four polytypes are theoretically possible when $J_2 = J_3 = -1$ erg/cm^2.

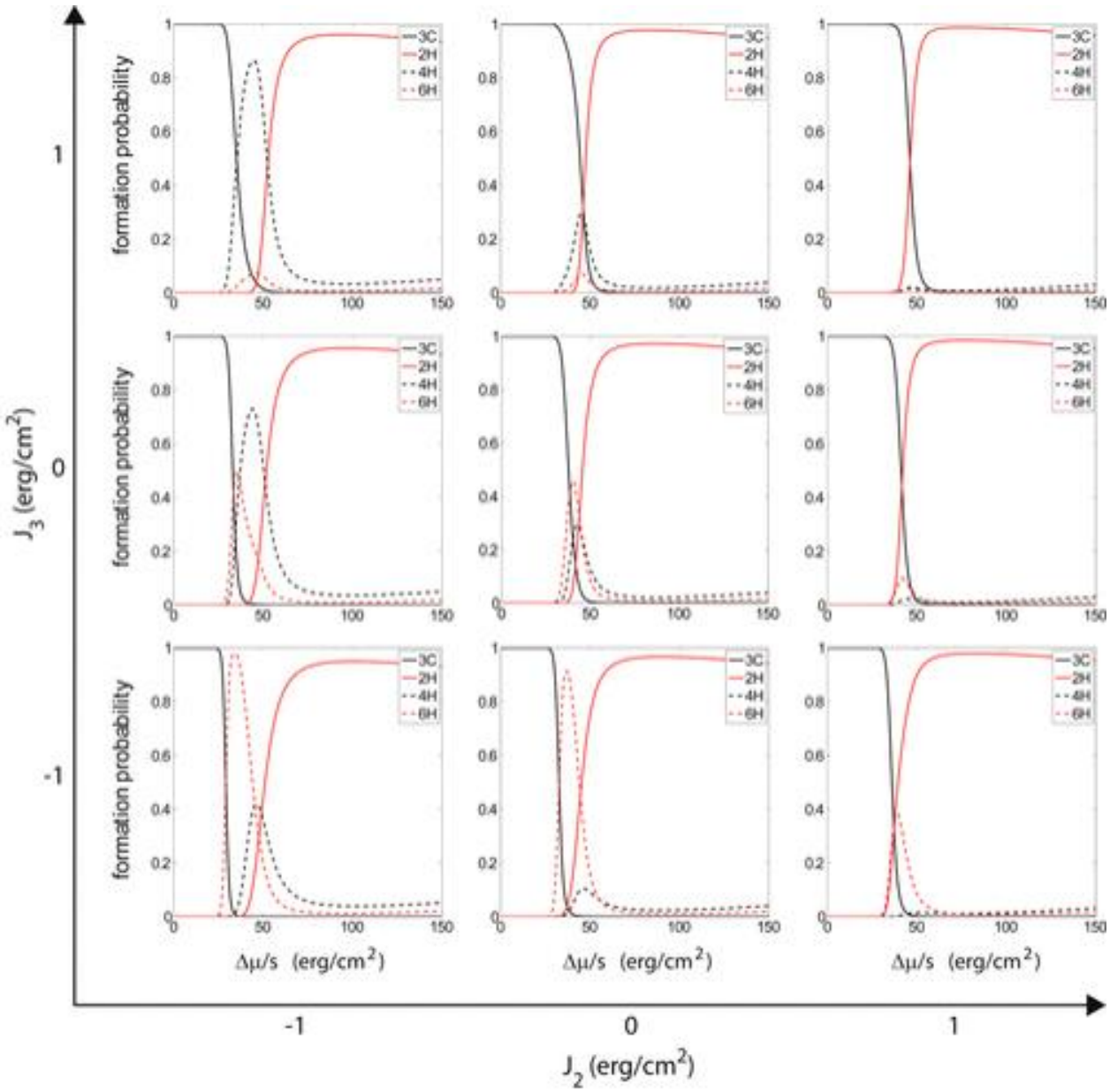

Figure 5.4: The nine combinations of polytype formation probabilities for different values of J2 and J3 (-1, 0 and 1 erg/cm^2). Adapted from Ref. [160].

To sum up, we repeated here and explained the calculations of Johansson, and, fortunately, got the same results! However, this model assumes the formation of a limited number of polytypes, namely four, and does not include other possible polytypes such as 15R, which has been observed in our ZnS nanowires. Thus, the question that arises is: where would 15R probability incorporate in such graphs? Would it even appear? Would it be dominant in a certain range of supersaturation? Let us see below…

5.2.4 Calculations with 15R polytype

As a next step, we included the 15R polytype in the probability calculations. The equation (5.9) for 15R polytype can be expressed as,

$$\rho_{15R} = 5\left(p_{c|hc}^2 p_{h|ch} p_{c|ch} p_{h|cc} \right)^{1/5} \left(\text{degeneracy} = 5\right) \qquad (5.8e)$$

The equation (10) for 15R polytype formation probability can be expressed as,

$$p_{15R} = \frac{\rho_{15R}}{\rho_{3C} + \rho_{2H} + \rho_{4H} + \rho_{6H} + \rho_{15R}} \qquad (5.10)$$

The polytype formation probabilities are plotted again as a function of supersaturation per area ($\Delta\mu$/s) in Figure 5.5. Note that this is again for GaAs material.

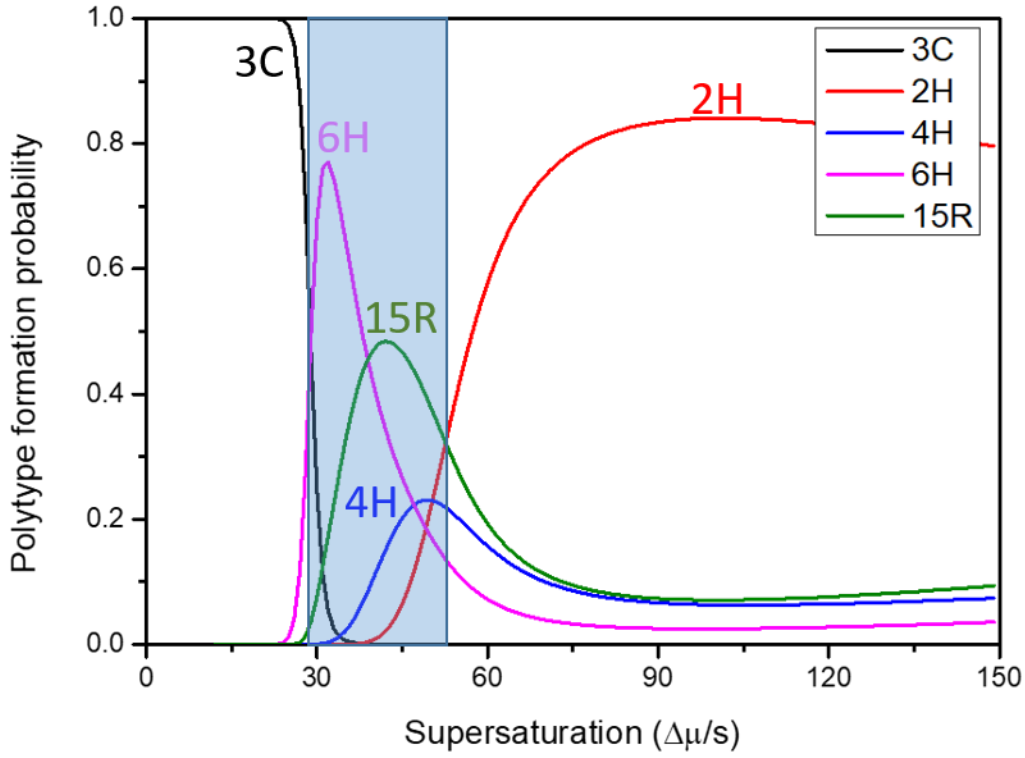

Figure 5.5: The 15R polytype included in the probability calculations, the plot shows that 15R can dominate in a certain range of supersaturation. Unit of supersaturation $\Delta\mu$/s is erg/cm^2.

The inclusion of 15R polytype does not affect the results of 3C and 2H occurrence as well as the HOP window. The results are quite interesting, the 15R polytype formation probability lies in between the 6H and 4H. As the supersaturation in the catalyst droplet increases, the phase still changes from 3C to 2H with formation of some high order polytypes, including that time 15R which is observed in our ZnS nanowires. The probability of 6H is maximum (0.8) amongst high order polytypes, 15R and 4H have a probability of 0.5 and 0.2 respectively. As we saw, these probabilities can be altered with the values of J_1, J_2 and J_3. Interestingly, the results observed here are plotted for GaAs parameters, hence the occurrence of 15R polytype is anticipated in GaAs nanowires! Why hasn't anyone ever reported on 15R-GaAs? Either 15R polytype never dominated in GaAs NWs or it went unnoticed till now because the high order polytypes in GaAs nanowires occur in a very small segment. Moreover, we must emphasize that identifying a very small 15R segment can be a tedious task. In the case of ZnS NWs, the length of the 15R segments (up to 80nm, Figure 5.6i) are quite large compared to the ones of high order polytypes (4H or 6H) observed in GaAs (just few nms, Figure 5.6ii). In addition to

the great expertise and obstinacy of our microscopist (Fréderic Fossard), such lengths could explain why 15R has been more easily evidenced in ZnS, and stayed hidden in GaAs.

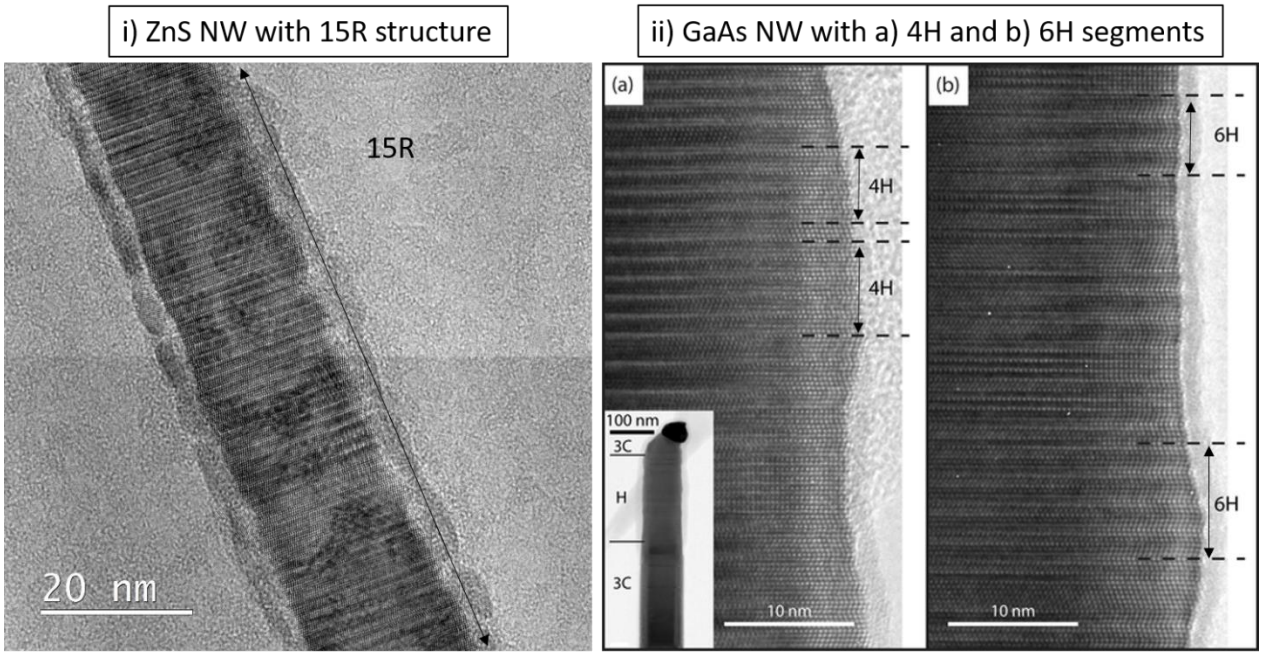

Figure 5.6: segment of NWs with HOP occurrence: i) ZnS with 15R (long segment, around 80 nm), ii) GaAs with short 4H and 6H segments. Figure 5.6ii Adapted from Ref. [161].

5.2.5 Summary and limitations of the model… and the modifications required

This approach is based on the classical nucleation theory that considers the formation of a nucleus at the interface between the catalyst droplet and the substrate. The characteristics of this nucleus are supposed to be critical to define the crystalline structure of the entire monolayer that completes afterwards. In this model, simple probability calculations were proposed. For example, the nucleation of a cubic nucleus is governed by an exponential distribution with probability,

$$P(c) = \frac{\exp\left(-\frac{\Delta G_c^*}{k_B T}\right)}{\sum_{j=c,h} \exp\left(-\frac{\Delta G_j^*}{k_B T}\right)} \qquad (5.11)$$

Where *j* represents the *c* and *h* orientation of the nucleus. And similarly, the same probabilistic expression was used to calculate the probabilities of particular sequences that represent the different polytypes. The long-range interaction was considered using the ANNNI model applied to the interface energy. Therefore, this approach is very effective to precisely study the formation phenomenon of polytypes in nanowires.

Johansson, in this model, shows that the interval of supersaturation in which high order polytypes occur could be controlled with the J_1, J_2, and J_3 interaction parameters affecting the interface energy (σ). All these J_i's are of course material dependent. We must notice that the values of J_1, J_2 and J_3 given in literature were calculated for bulk interactions and these values can be a little (or quite) different for the nanowire dynamics.

In the above model, the defined expression of nucleus edge energy Γ_j is very simple. Too simple, actually. This might be a concern since this step energy is considered to be the dominant parameter that allows nucleation of a WZ ML in NW geometry. Indeed, some growth dependent parameters were not considered for the calculation of effective edge energy of the nucleus. These growth dependent parameters are droplet contact angle, liquid-vapor interface energy (γ_{LV}), and surface energies of the possible lateral facets of nucleus (WZ, ZB (111)A or ZB (111)B). Recently, researchers developed various unique models to explain the dependence of crystal phase on such parameters [162,228]. Thus, it is need of the hour to include the NW growth dynamics in the above-calculated probabilities in order to precisely explain the crystal phase selection and occurrence of high order polytypes in nanowires.

5.3 The new (extended) model

The geometry of the nucleus is always being a topic of argument and it highly depends on the facets and surface energies present at the interface. However, recently, the group of Harmand, Glas et al. reported the possible rhombus geometry of the smallest nucleus they have observed during the in-situ TEM measurement of GaAs NW growth [148].

Herein the extended model, we will try to include the nanowire growth dynamics from Glas approach combined with the probability calculations proposed by Johansson. Clearly, the new expression of the nucleus edge energy Γ_j will be adapted to nanowire growth dynamics. We will also take the opportunity to compare the triangular nucleus shape with a rhombus geometry. We continue with the case of GaAs, to compare with the previous model. But in the last part, we will investigate ZnS polytype probabilities by inserting ZnS parameters (as far as we know them) in our model.

5.3.1 The effective edge energy

We keep in mind that, if hexagonal, the nanowires grow along the [0001] direction, and, if cubic, they follow the [111]B direction ([111]-As terminated as reported in [229]). For a given nucleus formed at the vapor-liquid-solid triple phase line (TPL), the effective energy $\bar{\gamma}_{eV,j}$ of the lateral (edge) surface in contact with the vapor depends on its position j (j = ZB, WZ). The grown lateral planes are different for WZ and ZB nuclei, namely {10-10} and {111}. {10-10} are vertical facets, as shown in Figure 5.7. In the case of a cubic nucleus, two possibilities arise as the ZB facets can be tilted inwards (j =111A) or outwards (j = 111B) with an angle 19.5° from the wire axis. As a result, the nucleus type modifies the areas of the solid-liquid and liquid-vapor interfaces. The expression for the effective surface energy at TPL has been proposed by Ross and Glas [162,230], and hence, is much more complex than in our previous calculation (i.e. following Johansson's approach).

$$\bar{\gamma}_{eV,j} = \gamma_{eV,j} / \cos\theta_j + \left(\gamma_{LS} + \gamma_{LV}\cos\beta\right)\sin\theta_j \qquad (5.12)$$

Where $\gamma_{eV,j}$ is the energy of the lateral facet (in j position) in contact with vapor, θ_j is the angle of lateral facet with the wire axis, γ_{LS} and γ_{LV} are the energy per unit area of the liquid-nanowire interface and liquid-vapor interface, and β is the droplet contact angle. It is important to note that, since the edge facet of a ZB nucleus may have different angle θ, +19.5° or -19.5°, we now have to consider 3 cases for j: WZ, ZB (111)A, or ZB (111)B

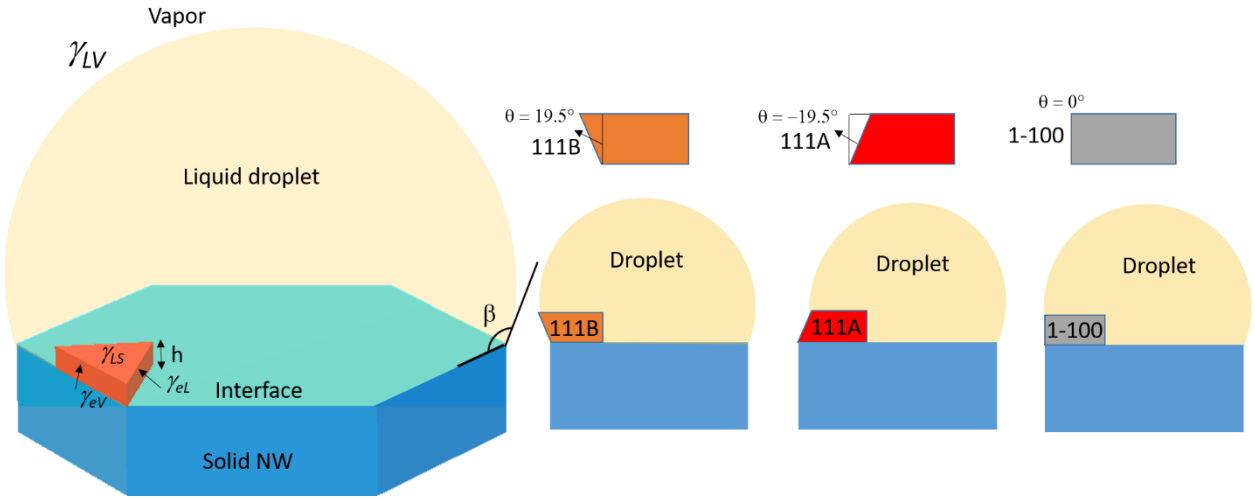

Figure 5.7: The growth dynamics of the nanowire with the respective surface energies for WZ, ZB ((111)A and (111)B) nucleus and contact angle are represented.

In order to calculate the effective edge energy of the nucleus, we must consider that the lateral facet of nucleus in contact with the vapor eliminates part of the liquid-vapor (LV) interface and replaces it by a nucleus-vapor (eV) interface. If α is the fraction of the nucleus in contact with the vapor, then the effective edge energy can be expressed as [11],

$$\Gamma_j = (1-a)\gamma_{eL} + a\left(\bar{\gamma}_{eV,j} - \gamma_{LV}\sin\beta\right) \qquad (5.13)$$

Where γ_{eL} is the lateral (edge) energy of the nucleus facet inside the liquid droplet. Hence, Γ_j is the sum of the edge energy in contact with liquid (i.e., inside the droplet) plus the edge energy in contact with vapor (i.e., outside), minus the energy of the eliminated droplet surface. This latter estimated by Glas as $\gamma_{LV}\cdot\sin\beta$.

Here, α = 1/3 for an equilateral triangular nucleus. Thus, the equation (5.13) becomes,

$$\Gamma_j = \frac{1}{3}\left(2\gamma_{eL} + \bar{\gamma}_{eV,j} - \gamma_{LV}\sin\beta\right) \qquad (5.14)$$

Let us remind again from equation (2.4) the corresponding critical energy ΔG^* is,

$$\Delta G^* = \Delta G|_{a^*} = \frac{3\sqrt{3}}{2}\frac{h\Gamma^2}{(\Delta\mu - \sigma/h)} \qquad (5.15)$$

And the nucleation rate is given by,

$$N = AZ\exp\left(\frac{-\Delta G^*}{k_B T}\right) \qquad (5.16)$$

Hence, since we have a new expression of Γ_j, we get a new expression of the nucleation rate (and consequently the polytype probability) in our extended.

5.3.2 Probability calculation of polytypes

This section follows the same probability calculation approach proposed by Johansson, explained in section 5.3.2 [160]. The principal change is for the calculation of the effective edge energy Γ_j. The shape of the nucleus, triangular instead of semicircular, has a minor effect.

The probabilities of all polytypes are same as before,

$$\rho_{3C} = \left(p_{c|cc}^{3}\right)^{N/3} \qquad (5.8a)$$

$$\rho_{2H} = \left(p_{h|hh}^{2}\right)^{N/2} \qquad (5.8b)$$

$$\rho_{4H} = 2\left(p_{hch}^{2} p_{chc}^{2}\right)^{\frac{N}{4}} (\text{degeneracy} = 2) \qquad (5.8c)$$

$$\rho_{6H} = 3\left(p_{hcc}^{2} p_{chc}^{2} p_{cch}^{2}\right)^{\frac{N}{6}} (\text{degeneracy} = 3) \qquad (5.8d)$$

$$\rho_{15R} = 5\left(p_{chc}^{2} p_{hch} p_{cch} p_{hcc}\right)^{\frac{N}{5}} (\text{degeneracy} = 5) \qquad (5.8e)$$

The final polytype probability that is given by equation (5.9),

$$P_q = \frac{\rho_q}{\sum_Q \rho_Q}$$

Where q and Q are one of the polytypes (3C, 2H, 4H, 6H, and 15R) and the summation in the denominator represents the sum of all five polytypes.

5.3.3 Results of this model for GaAs

Before presenting the results, let us go back to one important point. The WZ nucleation is favored when $\Delta G_{WZ}^{*} < \Delta G_{ZB}^{*}$. Reminding the expression of the critical barrier energy ΔG^{*}, as calculated in chapter 1, that means:

$$\Delta G_{WZ}^{*} < \Delta G_{ZB}^{*}$$

$$\frac{3\sqrt{3}}{2}\frac{h\Gamma_{WZ}^{2}}{\Delta\mu^{*} - \frac{\sigma}{h}} < \frac{3\sqrt{3}}{2}\frac{h\Gamma_{ZB}^{2}}{\Delta\mu^{*}}$$

$$\Delta\mu^{*} > \frac{\sigma/h}{\left(1 - \frac{\Gamma_{WZ}^{2}}{\Gamma_{ZB}^{2}}\right)}$$

Looking carefully, the second inequality requires two conditions to be valid:

1) At numerator, $\Gamma_{WZ} < \Gamma_{ZB}$, the effective surface energy for WZ should be less than ZB, since at denominator we have always $\Delta\mu - (\sigma/h) < \Delta\mu$.
2) At denominator, the supersaturation should be high enough to overcome the interface energy (stacking fault) σ. For example, if we highly increase Δμ so that Δμ-σ/h ≈ Δμ, then the inequality is easily satisfied. Hence, the supersaturation should be larger than a critical value expressed as:

$$\Delta\mu^{*} > \frac{1}{1 - R^{2}}\left(\frac{\sigma}{h}\right) \qquad (5.17)$$

Where, $R = \frac{\Gamma_{WZ}}{\Gamma_{ZB}}$ is the ratio of the effective edge energy of WZ nucleus with respect to the ZB nucleus. Conditions 1) imposes *R* to be less than 1, if not the NW grows cubic. It is clear that small ratios R will favor the occurrence of WZ phase.

If we consider the equation 5.17, the value of critical supersaturation varies as an inverse function of Ratio (1/1-R^2) and as a direct function of interface energy (σ). If we plot the function of 1/1-R^2 in Figure 5.8, it is interesting to note that, small differences between Γ_{WZ} and Γ_{ZB} (i.e., *R* close to 1) lead to very high values of the critical supersaturation Δμ*above which we achieve the hexagonal phase. Hence, we anticipate that the variation of *R* in the range [0.9 – 1] will have a strong impact, and should be worth investigating.

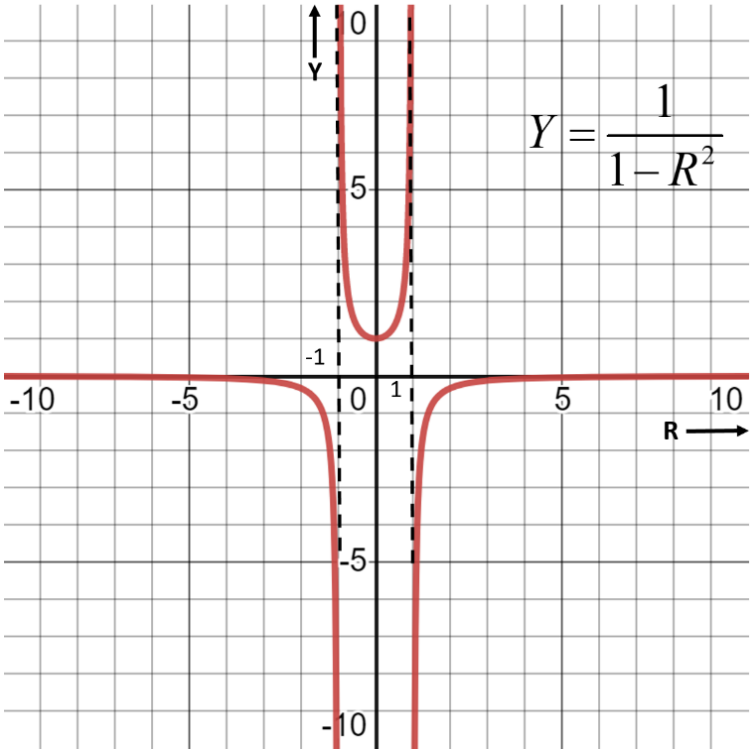

Figure 5.8: The plot of Y = 1/1-R^2, Y (supersaturation, Δμ) increases as a parabolic function for values of R between -1 and 1 exclusively. Physically, *R* varies between 0 and 1.

The surface energies and other growth parameters for GaAs are gathered in Table 5.2.

γ_{111B} (J/m^2) [231]	γ_{111A} (J/m^2) [231]	$\gamma_{1\bar{1}00}$ (J/m^2) [232]	θ_{111B} (°)	θ_{111A} (°)	$\gamma_{LV,Au}$ (J/m^2) [233]	$\gamma_{LV,Ga}$ (J/m^2) [233]	β (°)	γ_{LV,Au_2Ga} (J/m^2)	J1 (mJ/m^2) [234]	J2 (mJ/m^2) [234]	J3 (mJ/m^2) [234]
0.69	0.82	0.70	19.5	-19.5	1.14	0.72	120	1	13.9	-0.67	-0.56

Table 5.2: GaAs surface energies values used to plot Figure 5.9.

Finally, the polytype formation probabilities in GaAs are plotted as a function of supersaturation (meV/pair), and gathered in Figure 5.9. The cubic plane is considered as 111A

and *R* has a value of 0.78. The catalyst is considered to be Au_2Ga and the contact angle is 120° for all the calculations, unless specifically mentioned.

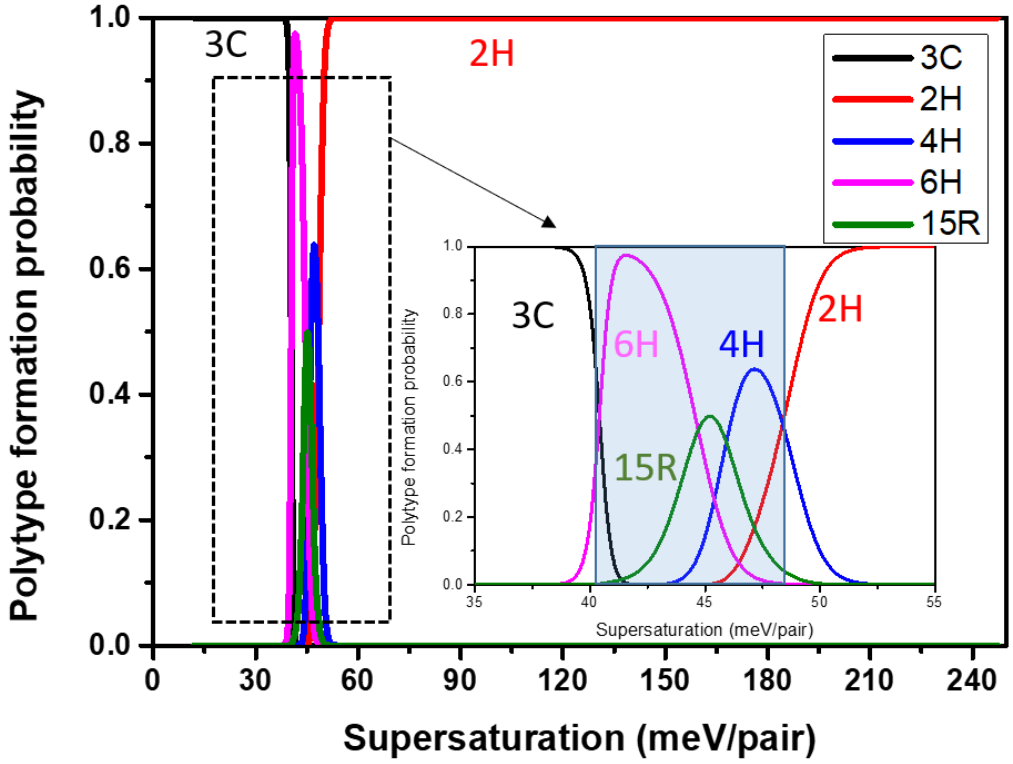

Figure 5.9: The polytype formation probabilities of 3C, 2H, 4H, 6H, 15R are plotted as a function of supersaturation for a well described triangular nucleus.

The results are in good agreement with Johansson's model that we used previously. Actually, we do not want to contradict this previous model, but rather extend it, and explore new tracks. Importantly, in our new model, we have now the ability to study the variation imposed by the growth parameters and/or the material-related parameters. For example, the change in the surface energies due to the growth in III or V rich conditions could be considered. Indeed, we want to go further than Johansson's paper where only J_2 and J_3 had been varied. In the next subsections we study the effect of some key parameters on the high order polytypes occurrence window.

5.3.3.1 The effect of edge energy ratio (R)

$R = \frac{\Gamma_{WZ}}{\Gamma_{ZB}}$, the ratio between the effective edge energy of WZ and ZB nucleus, appears to play a major role in the expression of ΔG^*. The effect of different values of *R* is illustrated in the Figure 5.10. For values *R* less than 0.8 (that means significant difference between ZB and WZ edge energies), the HOP window is very narrow, and it reduces further with decreasing the value of R. This is illustrated in Figure 5.10a with $R = 0.6$, where the probability of 3C is 1 for low supersaturation in the range (0-20 meV/pair) and directly goes to 2H at $\Delta\mu > 25$. For $R > 0.8$ (smaller difference of energies), the HOP window opens up with increasing the value of *R*. For example, for $R = 0.9$, it extends between 75 and 125 meV/pair of supersaturation.

Noticeably, the range of 3C also increases, and in fact all curves are shifted to high supersaturation values.

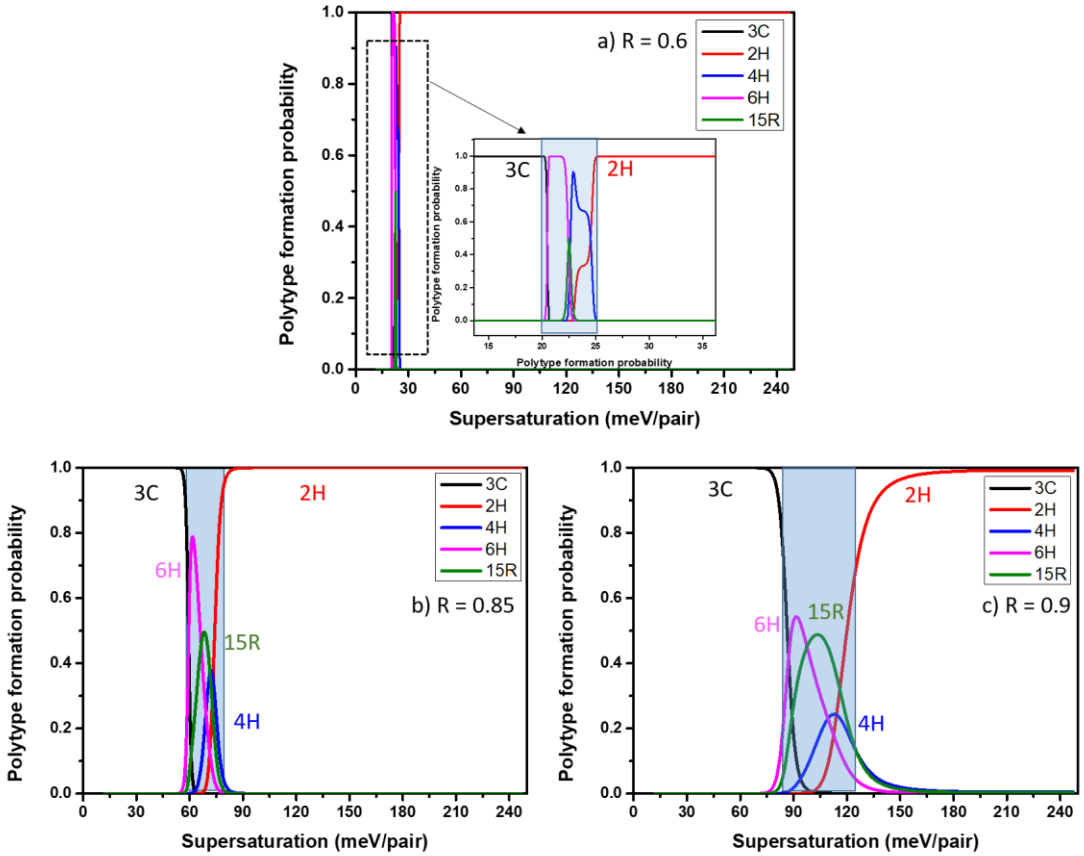

Figure 5.10: The effect of increasing the value of *R* (i.e., when edge energy difference between WZ and ZB is close), the supersaturation range of 3C and HOP window increase, a) *R* = 0.6, b) *R* = 0.85, and c) *R* = 0.9.

Clearly, the difference of effective edge energy between WZ to ZB defines the opening and closing of the high order polytypes window, that means favors or hinders the emergence of HOP. We also check that R strongly impacts the transition supersaturation from 3C to 2H, as it was expected from the expression of ΔG^*. We can go now more into the details, since $R = \frac{\Gamma_{WZ}}{\Gamma_{ZB}}$ is related to various parameters. If consider the expression of Γ_j (equation 13), we see that *R* is naturally material dependent, but also growth dependent as it is function of the droplet contact angle (β), tapering angle (θ), and liquid-vapor interface energy (γ_{LV}). Below, we take the time to consider these parameters.

5.3.3.2 The effect of zinc blende (111)A and (111)B planes

It is worth considering that the cubic nucleus have two possible sidewall facets, namely Ga-terminated (111)A, or As-terminated (111)B. GaAs NWs can grow along [111]B or [111]A direction [235]. As it has been mentioned previously, edge facets of the ZB nucleus can be tilted inwards (*j* =111A) or outwards (*j* = 111B) with an angle of 19.5° from the wire axis. The effect of choosing one plane or the other on the HOP window is presented in Figure 5.11. The

results are pretty interesting. We can see that, if the 3C nucleation is (111)A type at TPL, the HOP window is narrow, whereas it widens for (111)B nucleation. It is due to the difference in the surface energies of the (111)A and (111)B planes, respectively 0.82 and 0.69 J/m^2. This gives a ratio *R* of 0.78 if (111)A side facet, and 0.94 if (111)B. In the latter case, it is striking to observe that 2H phase disappears on the high supersaturation side, and 15R would be the most probable polytype.

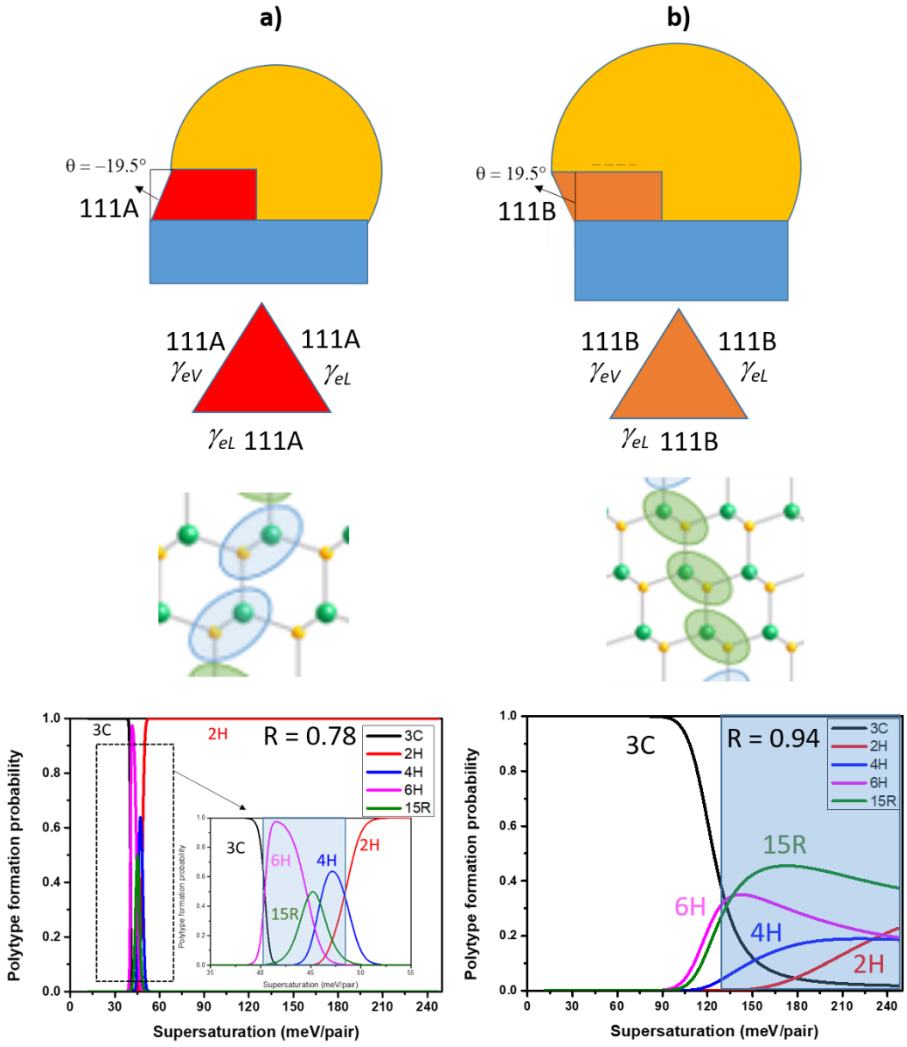

Figure 5.11: The polytype formation probabilities curve changes significantly for the two ZB nucleus i.e., a) 111A and b) 111B. The value of *R* is different for 111A and 111B nucleus that changes the HOP window for the two cases.

5.3.3.3 The effect of contact angle (β)

The ratio R also depends on the contact angle β. In Figure 5.12a, the effective edge energy (Γ_j) of WZ, ZB (111)A and ZB (111)B nucleus are plotted as a function of contact angle (β). In addition, a change in contact angle alters the capillary forces balance at the TPL. Thus, it may change the nucleation site favorable for one phase with respect to the other (3C/HOP/2H) [18].

In the range 60-140°, WZ has the minimum edge energy so that $R < 1$, and this allows WZ to dominate when the critical supersaturation condition satisfies. Regarding ZB edge,

(111)A has a lower energy than (111)B between 60° and 95°. It is the opposite between 95° and 180°, making (111)B edge facet more favorable in the case of a ZB nucleus.

As a result of the variation of Γ_j, the variation of R is also plotted in Figure 5.12b, for the two cases: $\Gamma_{WZ} / \Gamma_{j,ZB(111)A}$ in red, and $\Gamma_{WZ} / \Gamma_{j,ZB(111)B}$ in blue. In the graph, we arbitrarily introduced three regions: region 1 for $R > 1$ (called pure 3C favored), region 2 for $0.9 < R < 1$ (HOP and 3C favored), and region 3 for $R < 0.9$ (2H favored). We employed the term "favored" because, again, the conditions of supersaturation must satisfy. Let us look again at the different domains of β. At low droplet angle (60-95°), (111)A is favored in case of a cubic nucleus, and R is considered from the red curve, which crosses two zones: the HOP/3C favored zone between 60-80° and the WZ favored zone between 80-95°. With 95° < β < 180°, (111)B is favored for a cubic nucleus and the blue curve stands for R. In this range, R increases as β increases, starting from low values below 0.9 (2H favored), then reaching the HOP/3C favored zone. Above 140°, $R > 1$ and we have seen the NW should be 3C (region 1).

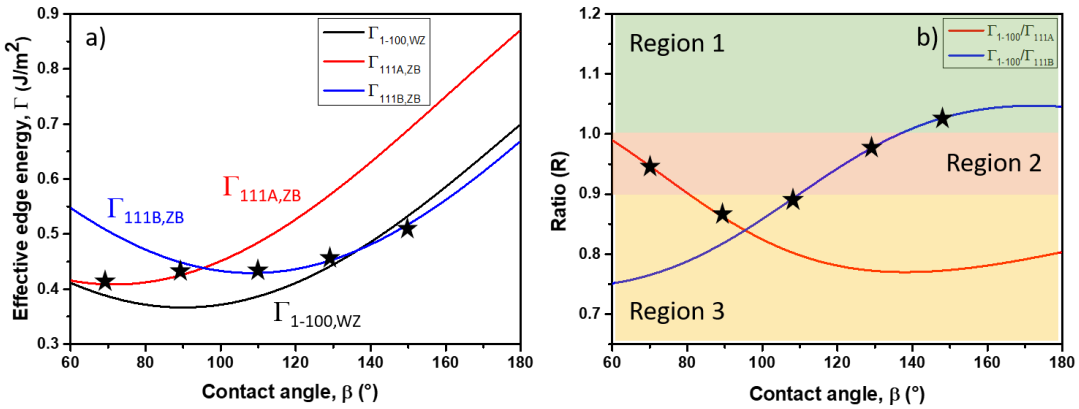

Figure 5.12: a) The effective edge energy of the zinc blende and wurtzite planes are plotted as a function of contact angle and its dependence on the b) Ratio (R).

To illustrate these results, five graphs are given (refer to five stars in Figure 5.12b) corresponding to β angles of 70°, 90°, 110°, 130° and 150° in Figure 5.13. At small contact angle 70°, 3C is highly favored (see Figure 5.13a). For intermediate contact angles between 90° and 110°, 3C/HOP/2H could be favored depending upon the supersaturation (Figure 5.13b-c). Further increase in contact angle, at 130°C, lowers the probability of 2H at the expense of HOP (figure 5.13d). At β = 150° (large contact angle), 3C phase dominates at all values of supersaturation (Figure 5.13e).

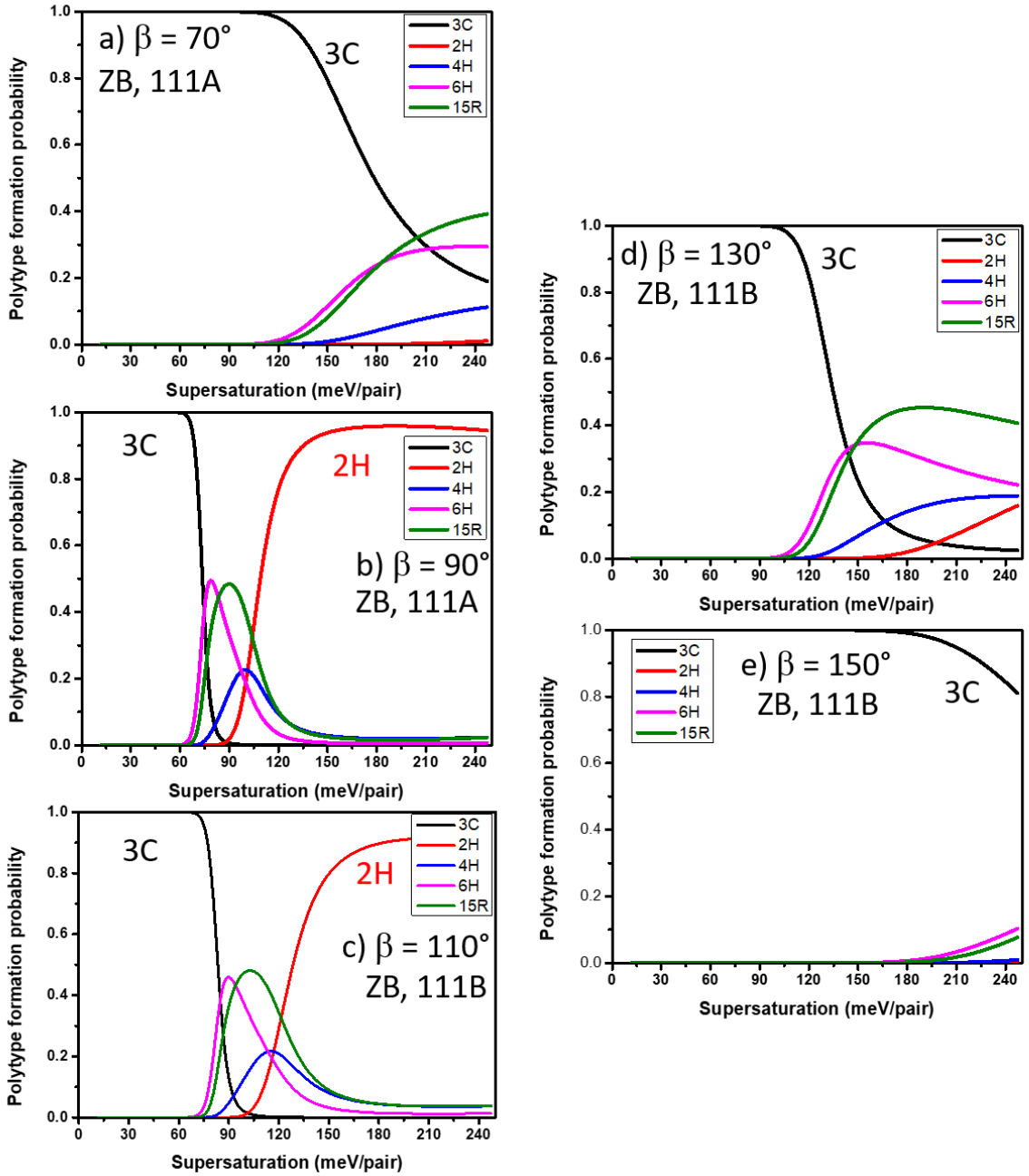

Figure 5.13: The polytype formation probabilities are plotted for different contact angles: a) 70° (111)A, b) 90° (111)A, c) 110° (111)B, d) 130° (111)B, and e) 150° (111)B. At a low contact angle, 111A is dominant; at a medium or high contact angle, 111B takes control. At low and high contact angles, 3C structure dominates, while HOP/2H favors at intermediate contact angles.

Indeed, it is interesting underline that, increasing droplet angle β, phase transitions are induced from ZB to WZ, and then from WZ to ZB. Such tendency in the role of contact angle successfully fits the experimental results observed in real time TEM measurements, i.e. a transition from ZB to WZ and then WZ to ZB while increasing the droplet contact angle β [228]. In their article, Panciera and coauthors proposed a model that fits with experimental observations of a WZ phase for intermediate contact angles (100 to 125°), whereas for smaller and larger contact angles the tapered and "truncation-assisted" ZB nanowires occur. These findings are represented in Figure 5.14, reproduced from [228].

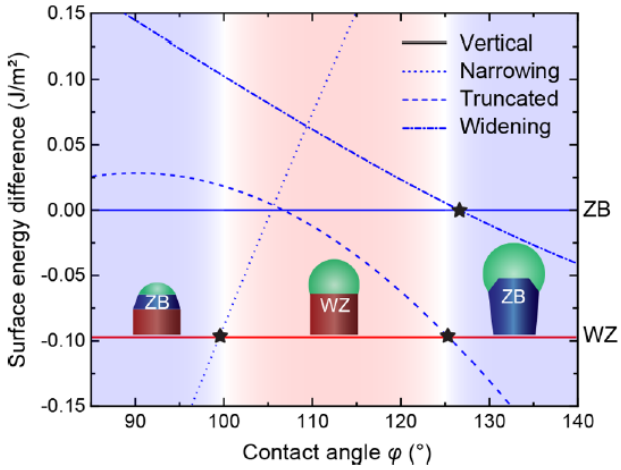

Figure 5.14: Contact angle dependent phase selection model for self-catalyzed GaAs NWs. At small and large contact angle ZB favors with tapering and truncation, whereas between 100° and 125° WZ phase was observed. Adapted from [228].

Our model successfully matches with the in-situ observations for GaAs. The intermediate range between 90° and 130° favors 2H nucleation if high supersaturation conditions meet. For small and high contact angles, we also predict 3C dominant phase. However, we have not considered the truncation and tapering in our model. The observed truncation at large contact angle still remains in debate.

5.3.3.4 The effect of γ_{LV} (composition of the droplet)

The liquid-vapor interface energy depends on the composition of droplet, and it is also involved in the expression of effective edge energy Γ_j. Let's take an example of catalyst droplet used for GaAs NW growth. It is possible to grow the nanowire with pure gold, Au-Ga alloy, and pure Ga catalyst droplet. Consequently, the liquid-vapor surface energy may vary between 1.14 (pure Au) to 0.72 J/m^2 (pure Ga) [233]. In Figure 5.15, the effective edge energies of ZB (111)A, ZB (111)B and WZ (10-10) nuclei are plotted as a function of liquid vapor energy. γ_{LV} is varied in the range 0.2-1.4 J/m^2. The effective edge energy of WZ remains the lowest while (111)B is lower than (111)A for most of the values of γ_{LV}.

The ratio (R) is decreasing with γ_{LV}, from 0.91 to 0.65 for (111)A edge, while it is increasing for (111)B, from 0.9 to 1. It implies that with increasing the γ_{LV}, 111A will shrink the HOP window and favor 3C, whereas 111B will do the opposite. Hence, we emphasize here that the composition of the droplet may have an impact on the polytypes formation. Even in the cases where the effect of γ_{LV} on R is very small; it can bring significant change to HOP window if R is close to 1 (refer to Figure 5.8). We have noticed an opposite trend for ZnS compared to GaAs, where the ratio (R) increases with γ_{LV} (refer appendix A.1.2).

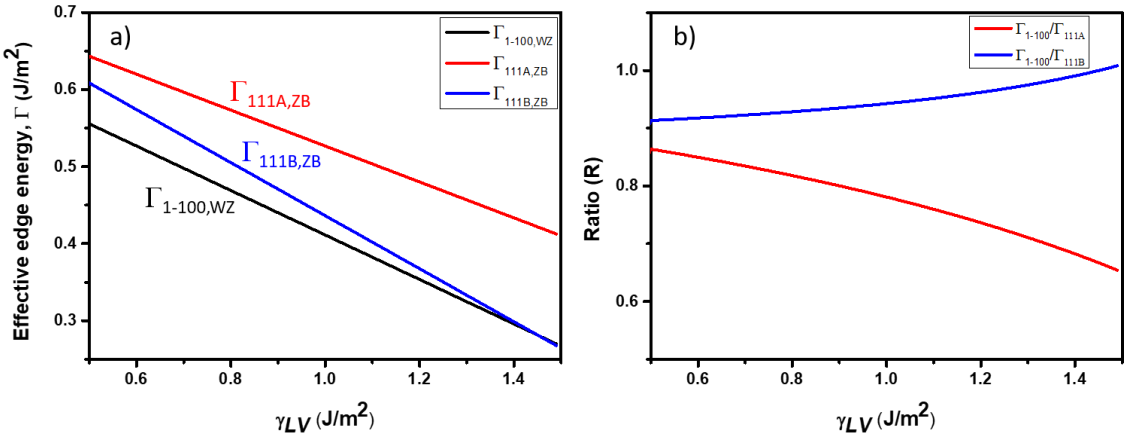

Figure 5.15: The effective edge energy of the zinc blende and wurtzite planes are plotted as a function of γ_{LV}. (left) and its dependence on the Ratio (R) (right).

5.3.3.5 The interface energy

ANNNI model is applied to the interface energy via the interaction parameters (J_1, J_2, and J_3). The first interaction J_1 is always the principal and strong compared to J_2 and J_3 (usually smaller by one or two orders). The effect of interaction parameters J_2 and J_3 on the polytype formation probabilities has already been discussed in Figure 5.4. Both Γ (effective edge energy) and σ (interface energy) would be altered significantly if the metallic droplet-semiconductor materials system will change. In the case of σ, the change can occur due to a change in the interaction parameters, J_1, J_2, and J_3 resulting from a switch in the polarity of the nanowire, that is, growth along [111]A instead of the much more common [111]B [235]. It is worth noting here that when the ANNNI model is used in traditional equilibrium thermodynamics [157,234], the total energy of the various polytypes do not depend on their polarity. This is because, in the absence of surfaces or interfaces, A-polar material is simply B-polar material reversed. In this work dealing with NWs, we consider that variations in the interaction parameters J_i (taken from the bulk) can be caused primarily by changes in the droplet-NW materials combination, also by changes in the droplet's physical state, but the possible switch of polarity will not be taken into account.

Here, we decreased the principal interaction parameter J_1 while keeping the other parameters the same. The results are plotted in Figure 5.16 for two values of J_1, 13.9 mJ/m^2 (GaAs value) and 3.5 mJ/m^2 (4 times smaller value).

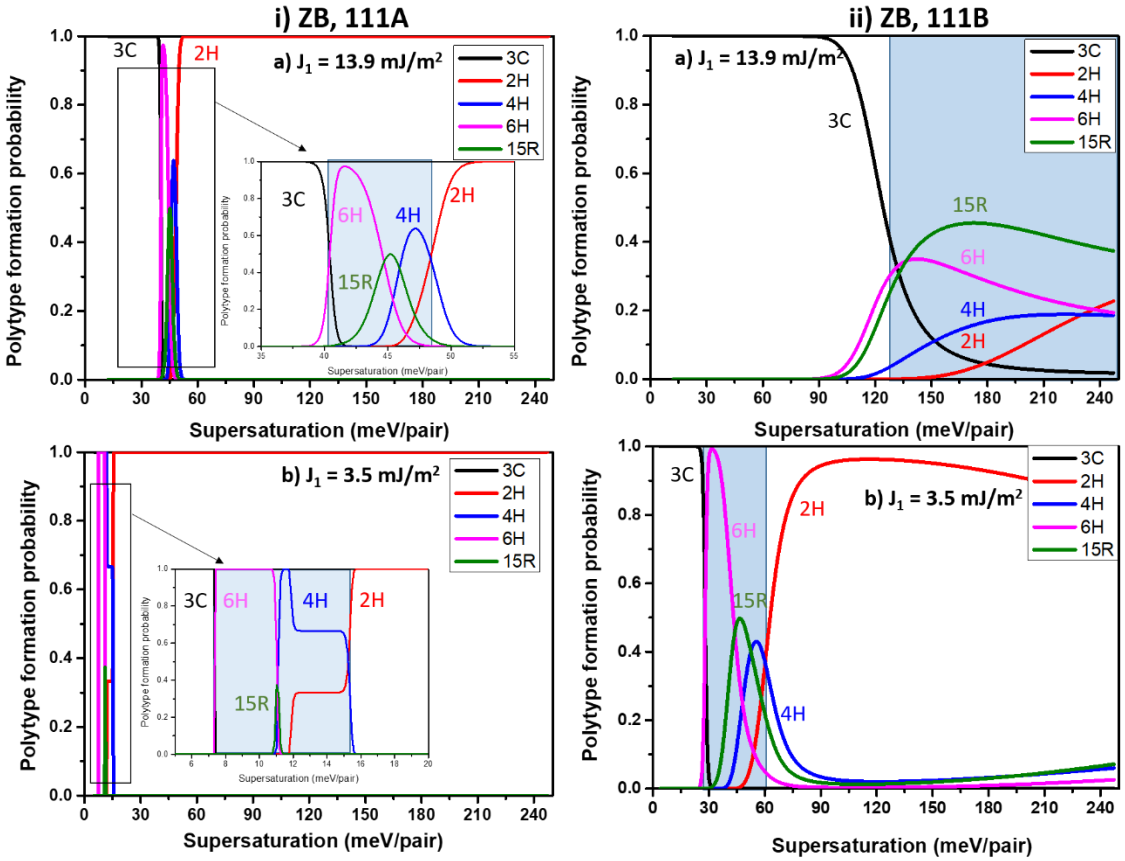

Figure 5.16: The change in the critical supersaturation range has been plotted for different principal interaction parameter J_1.

The plots obtained by decreasing the J_1 value could be explained using the equation of critical supersaturation $\Delta\mu^*$ (allowing the occurrence of the WZ phase), i.e.

$$\Delta\mu^* > \frac{\sigma / h}{\left(1 - R^2\right)}$$

This equation simply suggests that by decreasing the J_1 value, σ will decrease, resulting in the decrease in the critical supersaturation. This is consistent with plots in Figure 5.16. The domain of supersaturation for 3C is reduced at the expense of the other potytypes, especially 2H. For example in the case of (111)B edge, 3C extends from 0 to 130 meV/pair with J_1 = 13.9 mJ/m^2, and only from 0 to 30 meV/pair with J_1 = 3.5 mJ/m^2. In fact, it is relevant that materials having low J_1 values need smaller critical supersaturation values to overcome the stacking fault energy, or interface energy (σ). Thus, the HOP and 2H phase can occur more easily and at very low supersaturation in such materials.

For semiconductors, III-V, II-VI, and IV-IV with a stable cubic structure, J_1 must be large and positive, while J_2 and J_3 are negative and smaller than J_1. The polytypic behavior in semiconductors is believed to be controlled by the J_1/J_2 ratio, which is about -21 for GaAs, -14 for InP, -7.5 for ZnS and -0.5 for SiC [192,234] that explains the occurrence of high order polytypes (around 200 different types) in both SiC and ZnS. In the case of ZnS, it will be now interesting to investigate theoretically the polytypic behavior, as J_1 is much lower, as compared to GaAs.

5.3.4 The case of ZnS

The previous calculations were done for GaAs nanowires. This allowed to assess and compare the results with the literature. In this section, we tried to apply our model to the case of ZnS. The growth parameters and relevant surface energies from the literature are gathered in Table 5.4. However, there is limited literature available on the surface energies of ZnS.

γ_{111B} (J/m^2) [236]	γ_{111A} (J/m^2) [236]	$\gamma_{1\bar{1}00}$ (J/m^2) [236]	θ_{111B} (°)	θ_{111A} (°)	$\gamma_{LV,Au}$ (J/m^2) [233]	$\gamma_{LV,Ga}$ (J/m^2) [233]	β (°)	γ_{LV,Au_2Ga} (J/m^2)	J1 (mJ/m^2) [192]	J2 (mJ/m^2) [192]	J3 (mJ/m^2) [192]
1.01	0.87	0.52	19.5	-19.5	1.14	0.72	120	1	4.30	-0.58	-0.20

Table 5.4: Surface energies and parameter values given in the literature for ZnS.

We have calculated the polytype formation probabilities for ZnS. The plot is illustrated in Figure 5.17.

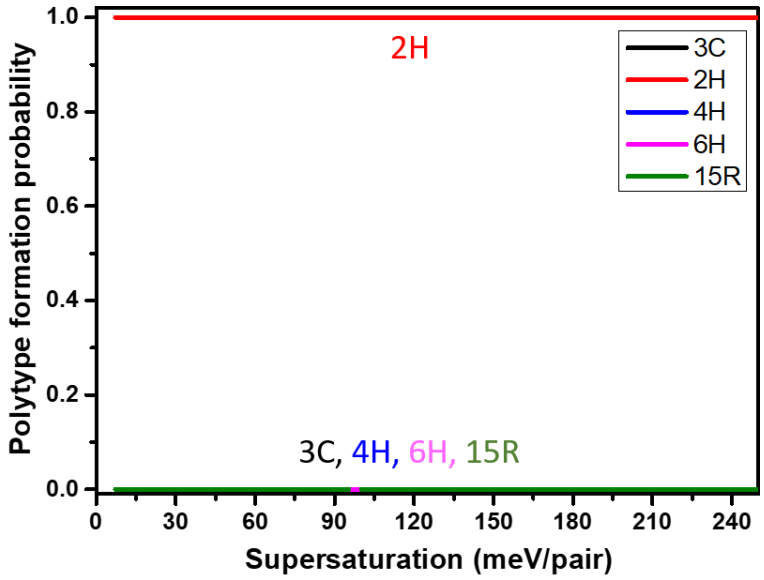

Figure 5.17: The polytype formation probabilities plotted for the ZnS surface energies. The formation probability of 2H polytype is 1 for all range of supersaturations.

Striking at first sight, the ZnS model suggests 2H formation for all values of supersaturation. The curve follows the same behavior for both ZB, 111A and 111B. Thinking about it, this is not so surprising. With the given surface energy values, the ratios (R) (1-100)/(111)A = 0.43 and (1-100)/(111)B = 0.29 are very small (i.e., a large difference between ZB and WZ energies), hence that is favoring drastically the 2H phase. Indeed, the surface energy of {1-100} plane is very low. This is also due to the low interface energy for ZnS, related to J_1.

Let us compare ZnS and GaAs materials. Firstly, the stacking fault energy is almost one order of magnitude lower in ZnS (6 mJ/m^2, 45 mJ/m^2 in the case of GaAs). Secondly, the ratio of hexagonal (1-100) to cubic (111A and 111B) surface energies are 0.78 and 0.94 for GaAs, but they are only 0.427 and 0.29 for ZnS. Consequently, considering such parameters, the hexagonal phase should be strongly favored in ZnS. But experimentally, with MOCVD growths, we have shown it is not entirely the case. If we have actually observed dominant 2H phase in VSS ZnS nanowires, the VLS ones show 15R polytype. And this first calculation in Figure 5.17 does not indicate any preferential window of supersaturation for the occurrence of such 15R phase.

The discrepancy between experiments and model may come from considering the low value of {1-100} plane taken from the literature. We believe this is right to consider lower interface energy (*Ji* interaction parameters) since it appears well-known in the bibliography that ZnS has a low stacking fault energy. We would rather incriminate the surface energy values found for ZnS, which indeed may undergo high variations, depending on the environment and reconstruction. Hence, we consider in the Figure 5.18 increasing values of $\gamma_{1\text{-}100}$ (>0.75 J/m^2) that results in an increase in the ratio $R = \frac{\Gamma_{WZ}}{\Gamma_{ZB}}$ for ZnS.

As expected, increasing *R* leads to an opening of the HOP window, as well as an increasing supersaturation range of 3C. At *R* = 0.97, the HOP window is wide open with 15R being the most dominating polytype. Thus, we need a high value of *R* in ZnS to open up the window and for the 15R dominance. However, it also depends on the supersaturation, how much it is varying during the growth. In Figure 5.18d, the variation of Ratio (*R*) with change in the surface energy of WZ (1-100) plane is plotted for ZB, 111A, and 111B. Looking at the blue line, the maximum possible R value for WZ/ZB 111B is still too low (*R* = 0.65) to open up the HOP window, as *R* = 0.65 only results in the 2H dominancy for all values of supersaturations (similar to Figure 5.17). This is why we have only considered ZB, 111A in the first three plots 5.18a-b-c. In Figure 5.18d, the red line represents the ratio of WZ/ZB, 111A and we highlight the suitable region (green + blue overlay) for the 15R occurrence).

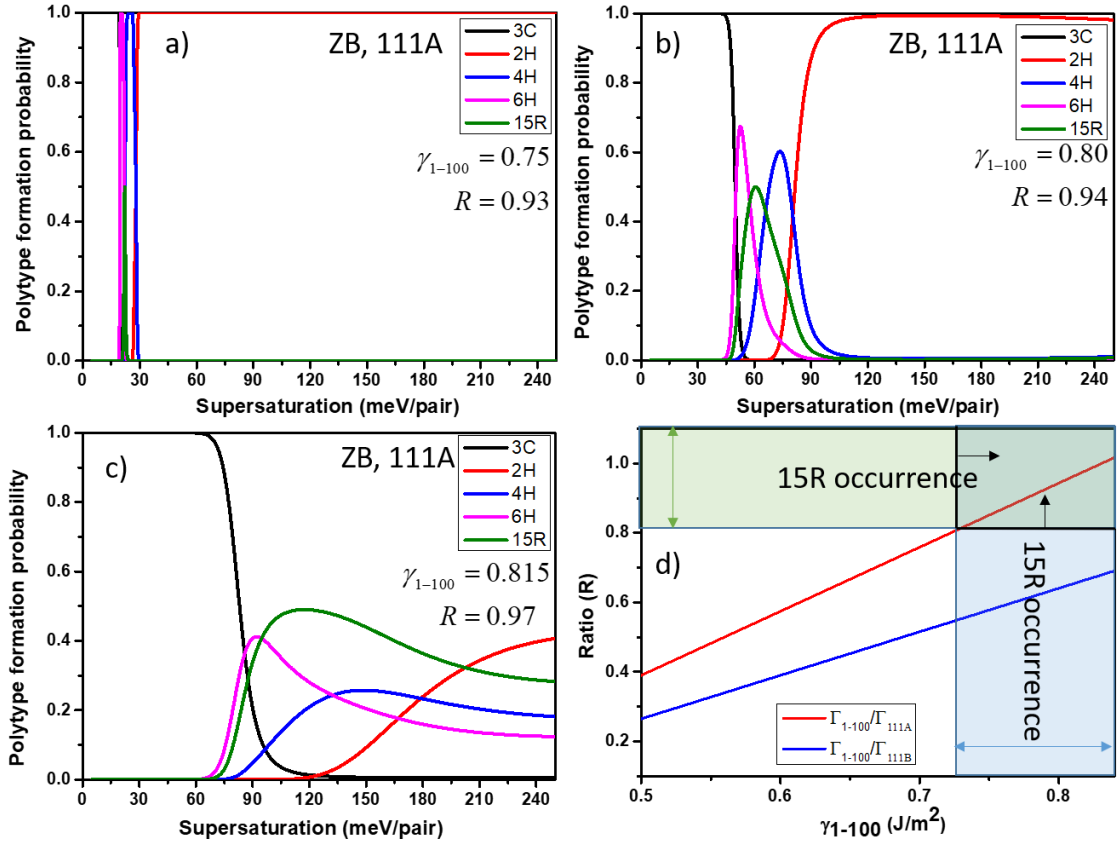

Figure 5.18: The surface energy of WZ (1-100) is increased between 0.75 and 0.815 J/m^2. The plot represents the respective effect on the polytype probability of polytypes for a) 0.75 J/m^2, b) 0.80 J/m^2, c) 0.815 J/m^2, and d) the plot shows a linear correlation between (1-100) surface energy and *R* value. The black arrow shows the HOP favored region.

5.4.1 The role of interaction parameters (J_2 and J_3)

Similar to Figure 5.4, we plotted ZnS polytype formation probabilities for nine combinations of J_2 and J_3 values (plotted at -1, 0, and 1 mJ/m^2) at constant J_1 = 4.3 mJ/m^2. Like in the case of GaAs, the different simulations reveal how HOP window can open or shrink depending on the values of J_2 and J_3, and how one particular high order polytype can be favored at the expense of the others. Indeed, among the three 4H, 6H and 15R HOPs considered here, it is not always the same that has the maximum probability. For example, the 15R phase is strongly enhanced in HOP window when the interaction parameters J_2 and J_3 are zero. Whereas, 6H is favored compared to the two others if J_3 = -1, whatever the value of J_2. 4H polytype would occur at J_2 = -1 and J_3 = 0 or 1. These simulations also suggest that the 15R occurrence is enhanced when J_2 and J_3 interactions have equal values, at least between -1 and 0.

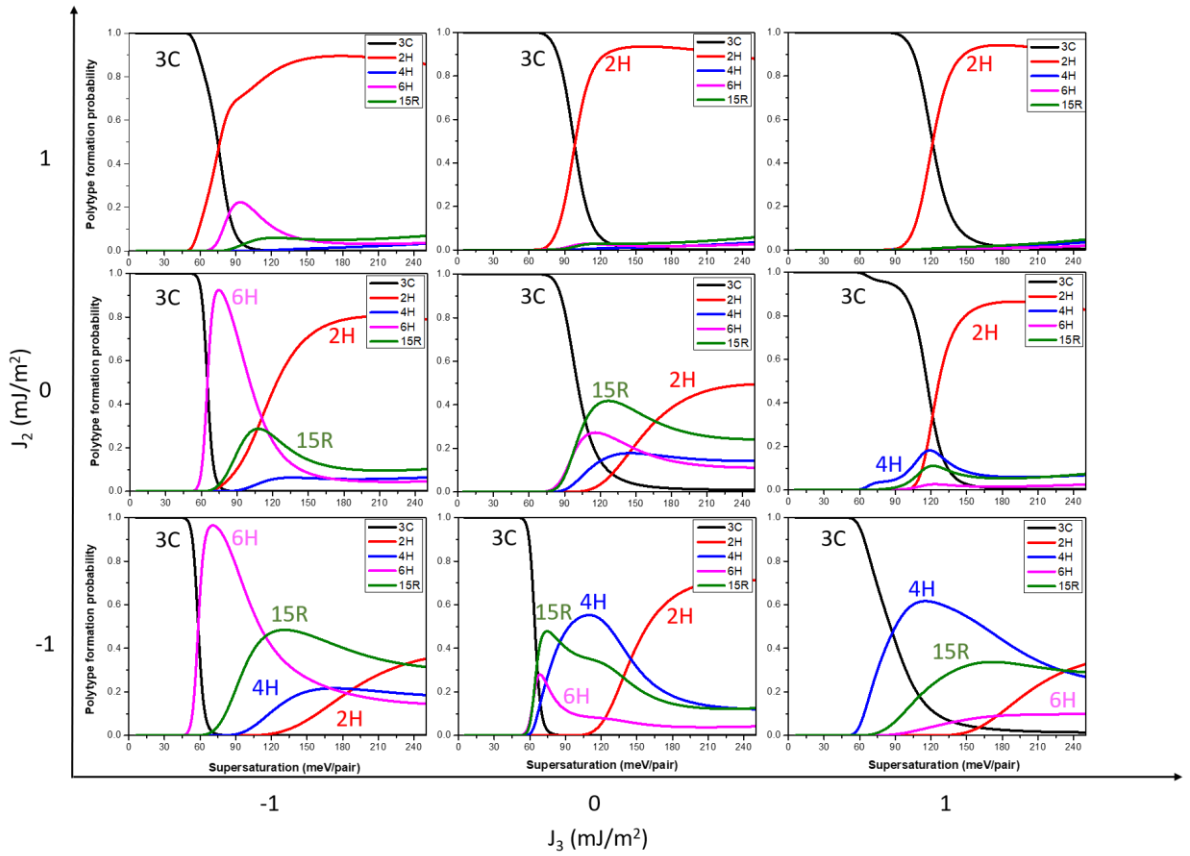

Figure 5.19: The nine combinations of polytype formation probabilities for different values of J_2 and J_3 (-1, 0 and 1 mJ/m^2) keeping J_1 = 4.3 mJ/m^2.

5.4 Conclusions

In conclusion, we started with the calculations of Johansson taking into account classical nucleation theory and ANNNI model to study the polytypism in semiconducting NWs. This model was proposed for a limited number of polytypes, namely four, and did not include other possible polytypes such as 15R, which has been observed in our ZnS nanowires. Thus, we took the opportunity to introduce the 15R polytype and carried out the calculations. This model successfully predicts the 15R occurrence in a narrow window of supersaturation. However, it did not allow us to integrate the NW growth dynamics in the calculations due to the simple assumptions made on the nucleus step energy. Therefore, we have extended this model by integrating NW growth model proposed by Glas et al. [11] in the calculations.

In this extended model, and considering a triangular nucleus, the first result follows closely with the outcomes of Johansson's model. Thus, as a next step, we detailed this model and investigated the ratio of WZ/ZB effective edge energies (R), on which polytype probabilities show a strong dependence. We found two possible ZB faceted geometries of nucleus termed as (111)A and (111)B. Noticeably, due to different surface energies of these facets, the effective edge energies are different and so does the ratio (R), leading to either an opening or a narrowing of the HOP window.

We continued our study by investigating the effect of other parameters involved in the effective edge energy values: contact angle and liquid-vapor surface energy. The contact angle study brings out interesting results. Our model successfully predicts the crystal phase transition from ZB to WZ at small contact angles, and WZ to ZB for large contact angles, in agreement with in-situ TEM experiments performed on self-catalyzed GaAs NWs. Subsequently, we

discussed the effect of liquid-vapor (LV) energy and show how it could play a significant role to open the HOP window when R is close to 1.

Now, coming back to the 15R crystal phase; we studied the case of ZnS NWs, by applying our extended model. First, we reconsidered the low surface energy of {10-10} WZ plane given in the literature, that does not allow any other phase than 2H. Then, a strong dependence has been observed on decreasing the first interaction parameter J_1. The J_1 parameter i.e., stacking fault energy is very small for ZnS 6 mJ/m^2 compared to GaAs 45 mJ/m^2 that means it is much easier to create a stacking fault in ZnS than GaAs. The WZ stacking can be considered as a stacking fault. Thus, it is easier to nucleate WZ stacking in ZnS and the same is predicted by our calculations. We further discussed the formation of 15R in ZnS NWs and suggested the favorable conditions for its occurrence.

Chapter 6

Emergence and control of polytypes: experimental findings

Contents

This chapter implements our model findings to achieve pure phases (WZ, ZB, and 15R) in ZnS NWs. We know that controlling and selecting crystal phases with no extended effect is crucial. Herein, we first pursue the idea that supersaturation in the catalyst droplet plays a significant role in controlling crystal phases in NWs. Thus, we will vary the supersaturation through variation in Zn and S partial pressures and study the impact on the structural properties of ZnS NWs. In a second part, we emphasize how the composition of the catalyst particle may change the growth mechanism and consequently the crystal phase of the growing NW.

6.1 Introduction

In chapter 4, we have observed a 15R structure with stacking faults and ZB/WZ polytypism in ZnS NWs grown by VLS and VSS growth mode, respectively. We thus underlined how the state and composition of the catalyst particle might change the growth mechanism and consequently the crystal phase of the NW. Stacking faults and defects have an adverse effect on the optical and electrical properties of semiconductor nanowires, lowering the quantum efficiency, carrier lifespan, and mobility of carriers. Indeed, the presence of such extended defects would hinder their applications. Therefore, it is crucial to explore all growth conditions to achieve and control the best crystal quality. Many research groups have carried out studies based on varying the nanowire diameter, growth temperature, VI/II (III/V) ratio, and adding dopants to control the morphology and crystal phase of the NWs [17,61,237]. For example, the crystal structure of nanowires was found to be diameter dependent, with smaller diameter nanowires gravitating toward a WZ phase and larger diameter nanowires tending toward a ZB phase [17]. Recently, the group of Harmand at C2N reported the phase selection in GaAs NWs by controlling the contact angle of the catalyst droplet [149].

In this chapter, we first pursue the idea that supersaturation in the catalyst droplet plays a significant role and gives an explanation behind the selection of phases in semiconductor nanowires: the WZ phase occurs at high supersaturation, whereas ZB is favored at the beginning of growth when supersaturation stays low [227,238]. The polytype models presented in Chapter 5 are consistent with such experimental findings. Herein the MOCVD process, we attempted to control the supersaturation through the variation in Zn and S fluxes. We could reduce Zn and S partial pressures by four times compared to the reference samples, allowing NW to grow in minimum supersaturation conditions. Below these partial pressures, no homogenous deposition was observed on the samples. On the other hand, we could increase the precursor fluxes by 1.6 times (reaching the maximum flow allowed by the DTBS mass-flow controller) with the aim of imposing high supersaturation. We thus assume that varying precursor partial pressures leads to a modulation of the supersaturation in the catalyst particle. This assumption seems relevant in the case of a liquid droplet, where elements would diffuse. It can be debatable in the case of a solid droplet; thus, here, we only considered VLS growth. However, a case study of VSS growth flux is presented in appendix (A.2). Anyway, by varying the precursor partial pressures, we try to achieve a pure ZB phase for NWs grown at a low growth flux (low supersaturation) and WZ for NWs grown at a high growth flux (high supersaturation), as it is expected from our model.

In the second part of this chapter, we show that it is possible to modify the composition of Au-Ga droplet by "feeding" it with a Ga flux, which has a substantial impact on the crystal structure of the ZnS NWs.

6.2 The key role of supersaturation

6.2.1 Impact of high growth flux on VLS grown ZnS NWs

The sample series is presented in Table 6.1. The reference sample (NW4) is the 15R sample studied in Chapter 4.

In this section, ZnS NWs were grown at a high growth flux (NW13, Table 6.1), 1.6 times higher than the reference sample. We increased the partial pressures of Zn and S sources, maintaining the same ratio, VI/II = 2. The growth duration was reduced to two minutes, while the growth temperature remained the same (550° C).

The SEM image of the NW morphology is shown in Figure 6.1. If we compare with the reference sample, the NWs are thicker and appear to be shorter. The density is significantly reduced at a higher growth flux. The observed length of the NWs is in the range of 500-700 nm, definitely shorter than the reference sample. The NWs have a conically tapered shape due to higher lateral growth. The axial growth of the NW might be compromised at the expense of increased lateral growth. The conical shape of NW is particularly interesting for the applications such as single-photon emission, where the single photon is guided inside the NW [239]. Moreover, an increase in the lateral growth with increasing the NW growth flux can be modeled to achieve the optimized tapered ZnS NWs for single-photon applications [239].

Table 6.1: The series of samples prepared at low and high growth fluxes.

	Study	Reference	Tg (°C)	P_{DEZn} (Pa)	P_{DTBS} (Pa)	VI/II ratio	Growth time (min)	Substrate
Nanowires	Reference sample	NW 4	550	7.8	15.6	2	3	GaAs (111)B
	High growth flux	NW13	550	12	24	2	2	GaAs (111)B
	Low growth flux	NW14	550	1.95	3.9	2	12	GaAs (111)B

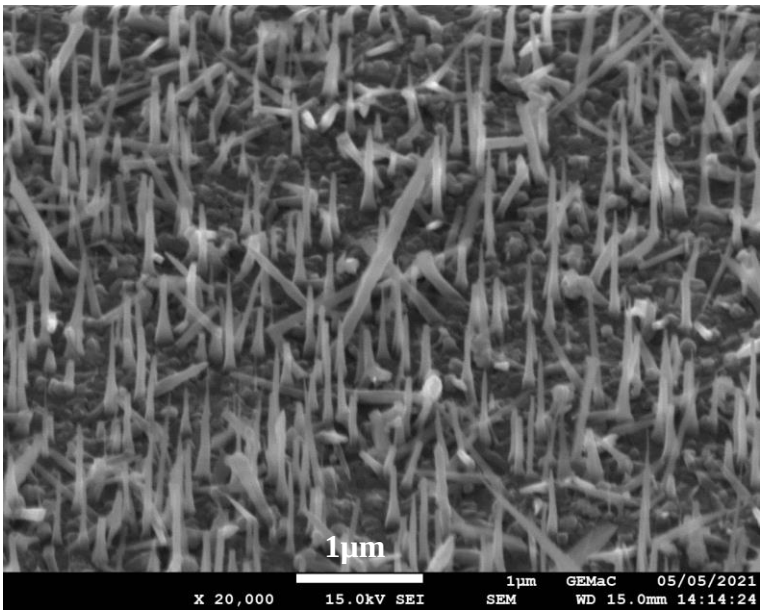

Figure 6.1: 45° tilted SEM images of ZnS NWs grown on GaAs (111)B with a high growth flux.

We performed TEM experiments on several NWs grown with higher supersaturation. The bright-field (BF) TEM image of a single NW is illustrated in Figure 6.2a. The diameter is 10 nm below the droplet and 25 nm at the bottom, suggesting a significant lateral growth flux. In Figure 6.2b, we present the HRTEM image of the NW. Remarkably, the NW is defect-free and exhibits a pure WZ structure. The Selective Area Electron Diffraction (SAED) pattern in Figure 6.2c confirms the pure WZ phase for ZnS NW. Hence, an increase in the growth flux

has changed the crystal phase from 15R to WZ. These results provide clear evidence to the reported theoretical works predicting that the pure WZ phase can occur at high supersaturation and agrees with our polytype modeling in Chapter 5. For ZnS NWs, we notice that a relatively small increase in the growth flux has brought a pure WZ phase.

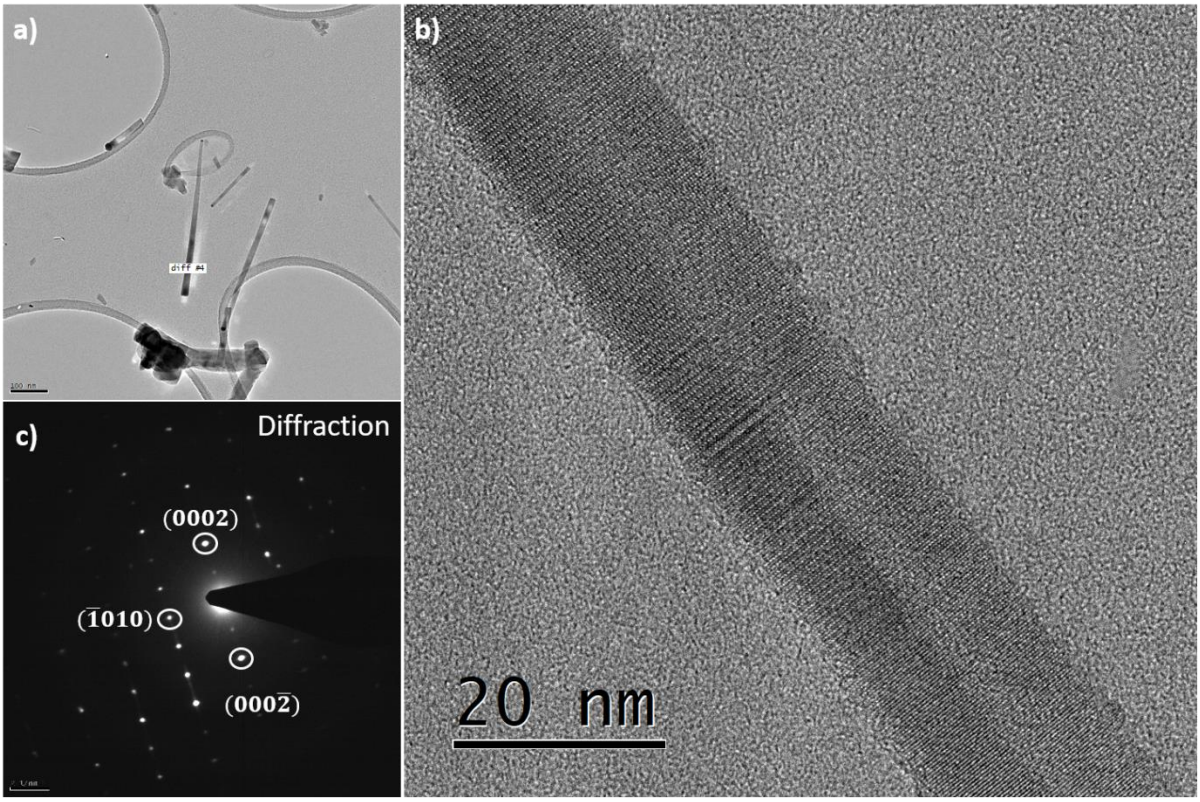

Figure 6.2: a) A bright-field TEM image of the single NW, b) the HRTEM image of NW revealing a pure WZ phase, c) SAED pattern of the NW presenting WZ-like footprint.

6.2.2 Impact of low growth flux on VLS grown ZnS NWs

In this experiment, ZnS NWs were grown this time at a lower growth flux (NW 14), four times less than the reference sample, by decreasing the fluxes of Zn and S precursors. We have also increased the growth duration to 12 min, i.e., four times. Like in the case of a high growth flux, it allows us to compare the morphology with reference samples (growth duration × growth flux = constant). SEM images in Figure 6.3 depict the NW morphology. When compared to reference and high growth flux samples, the NWs are cylindrical and straight. The NWs are comparatively larger in length, i.e., 0.9 – 1.5 µm as a result of lower lateral growth. The density is definitely lowered. We will use TEM images for more analysis.

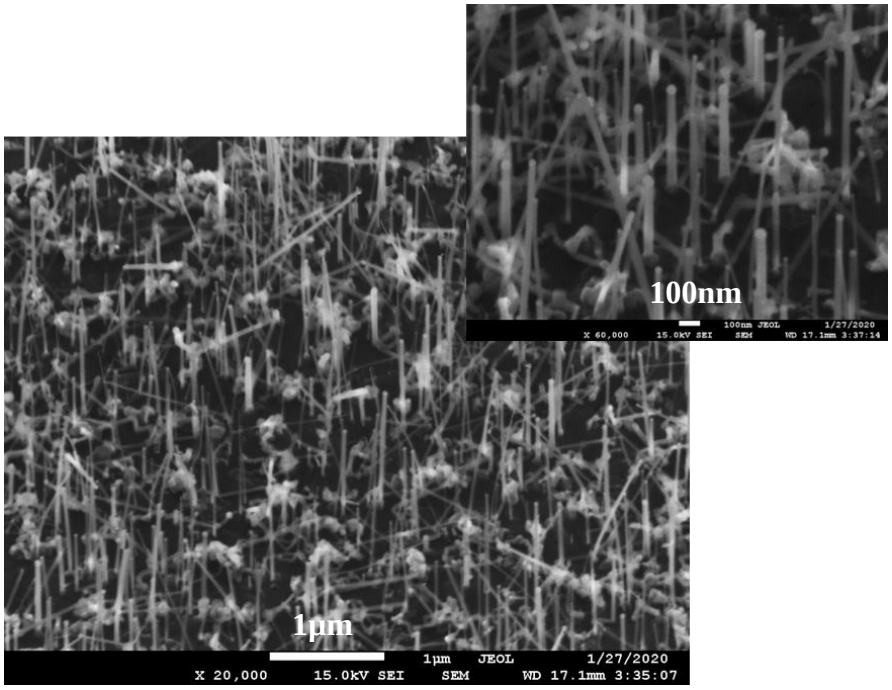

Figure 6.3: 45° tilted SEM images of ZnS NWs grown on GaAs (111)B with a low growth flux.

The structural properties and crystal phase were again studied using bright field, diffraction, and HRTEM. The bright-field TEM image of a single NW taken in <010> zone axis is shown in Figure 6.4a. The catalyst droplet can be seen at the top with a darker spherical contrast. The NW diameter below the catalyst is 45 nm and 50 nm at the bottom, making it almost a perfect cylindrical NW. This slight difference in diameter implies a decrease of the lateral growth using a low growth flux, compared to the cases of both reference and high growth flux samples.

In Figure 6.4b, the HRTEM image provides visuals of a 15R crystal phase stacking. The diffraction image in Figure 6.4c confirms the typical diffraction pattern of a 15R structure observed before for the reference sample. Additionally, the 15R would have an improved tendency and quality in low growth flux NWs, as it appears to dominate with fewer stacking faults.

A detailed TEM analysis using STEM and HRTEM was performed on different sections of the NW, presented in Figure 6.5. The dark stacks in BF-TEM image refer to the stacking faults. A magnified image in orange box focuses on such stacking faults. The green circle highlights the presence of small ZB segments (<5nm) and stacking faults. Above and below these stacking faults, a pure 15R crystal phase was observed. The HRTEM image (in black) shows a stacking very similar to the 15R crystal phase observed for the reference sample but, noteworthy, with few stacking faults.

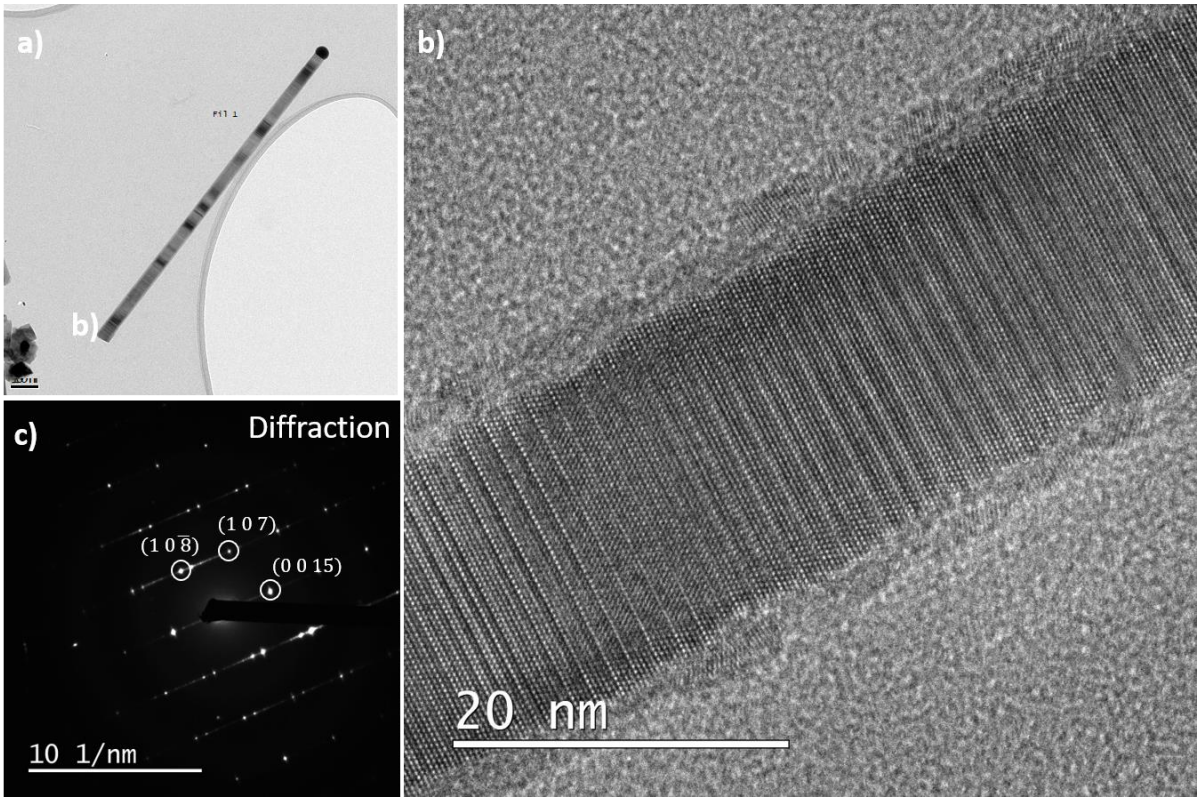

Figure 6.4: a) bright-field TEM image of a single NW with a catalyst droplet at the top, b) HRTEM image of NW revealing a 15R phase, and c) SAED pattern of the NW shows a 15R footprint.

Let's discuss these results in light of the theoretical work reported in our previous chapter. In typical "probability *vs.* supersaturation" graphs, three domains were defined. At low $\Delta\mu$, the cubic phase 3C is predicted, with 100% probability. At high $\Delta\mu$, the hexagonal structure 2H is expected with a probability close to 1. In between, and depending on several parameters such as the interaction between the forming nucleus and the previously grown layers (namely the J_i parameters of the ANNNI model), a window of supersaturation opens for the occurrence of high order polytypes (HOP) such as 4H and 6H. Interestingly, here, we turn the crystal phase of ZnS NWs from 15R to 2H by increasing supersaturation, thus in full agreement with these theoretical predictions. We notice that a relatively small increase in the growth flux (by 1.5) has brought a pure WZ phase, so that the reference 15R sample may have been grown at the upper limit of the HOP window. In the case of our ZnS NWs grown with low supersaturation, we were expecting a possible ZB crystal phase, which would indeed follow the predicted tendency. This is not the case, as the 15R phase is still found, remarkably, with lower stacking faults (see Figure 6.5). One explanation could be that the HOP window is much larger for ZnS and/or the 3C domain is much reduced for ZnS as compared to GaAs. This can be understood by the large difference of stacking fault energy between these two materials, as mentioned in the previous chapter, so that, in ZnS, the occurrence of high order polytypes and 2H crystal phase is favored at the expense of the cubic structure.

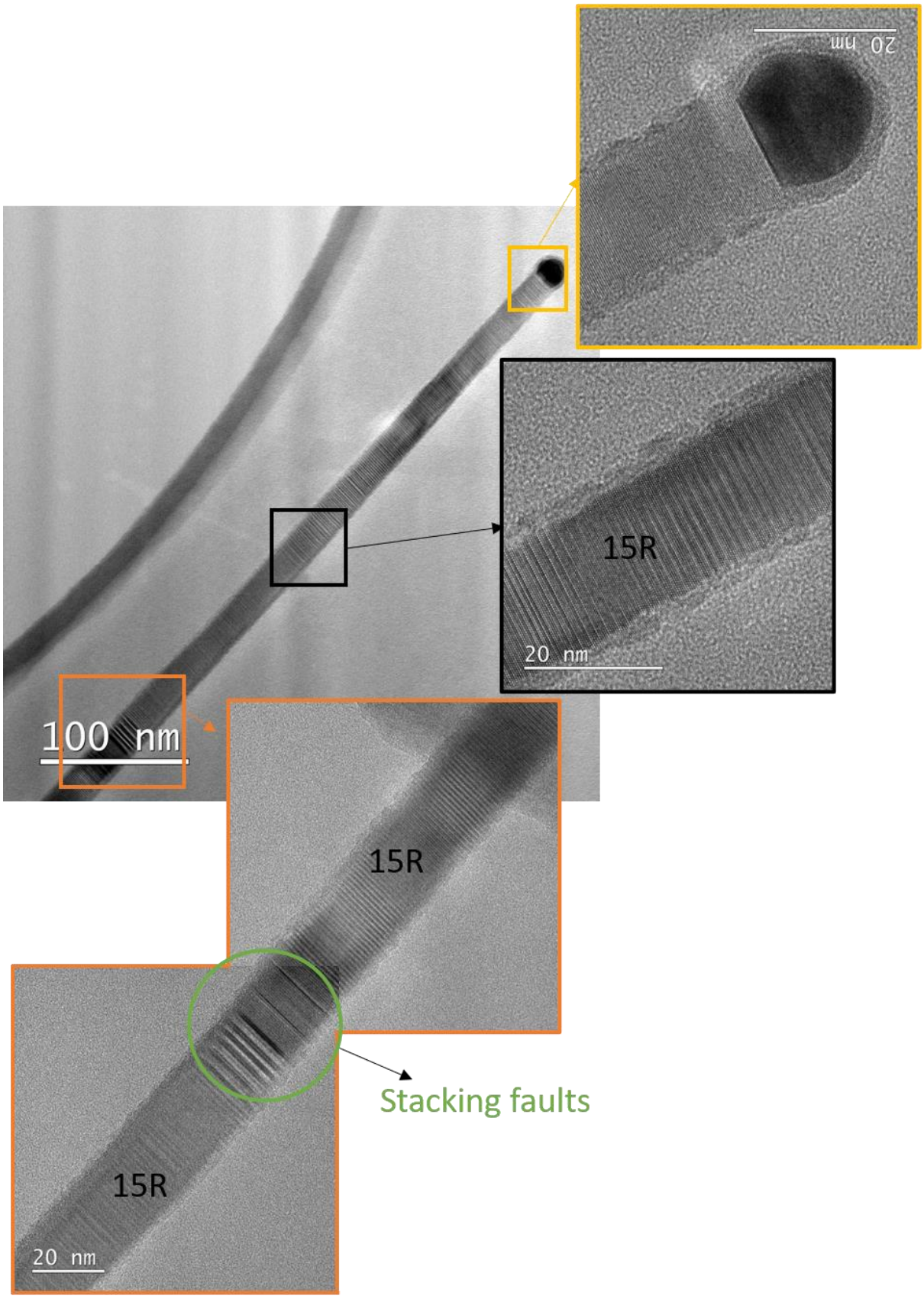

Figure 6.5: Different sections of a single NW are studied with the help of high magnification bright-field TEM images (orange boxes) with few stacking faults (in green) and HRTEM image (in black). The NW exhibit large segments of the 15R crystal phase (several hundred nm).

6.3 Impact of imposing high Ga concentration in Au-droplets: the key role of catalyst composition

We have just achieved pure WZ and extended the 15R crystal phase by controlling the sole parameter: growth flux or supersaturation. We have observed very small segments of ZB while growing at low supersaturation. Our inability to further reduce the supersaturation limits us from getting a pure ZB phase in ZnS NWs.

This section will show that we can achieve large segments of the ZB phase, periodically twinned, by imposing high Ga composition in the catalyst droplet, i.e., playing with the catalyst composition.

6.3.1 The origin of the idea (by chance!)

On one occasion, while growing ZnS NWs on the buffer layer (VSS growth mode), we observed the formation of strange discs, as presented in Figure 6.6. We focused on one of the discs (highlighted in orange). The zoomed images from different disc zones are given in orange, yellow, and blue boxes and a cross-sectional view (green). The presence of a hole at the center of each disc was persistent. However, the diameter of each disc is different, and so does the hole size, and there might be some correlation between them. The cross-sectional view shows that the hole is deep inside the buffer layer.

The growth conditions were similar to the reference sample (NW 4, Table 3.1) except for the deoxidation temperature before the deposition of the ZnS buffer layer on GaAs (111)B. For this sample, the deoxidation was done at 600°C instead of 550°C. Consequently, the high deoxidation temperature might have damaged the GaAs substrate because of As evaporation. Thus, without knowing the exact mechanism, it has led to holes in the buffer layer. We performed a step-by-step analysis, as shown in Figure 6.7. The holes were present after the ZnS buffer layer deposition (Figure 6.7a), and the formation of a disc can already be seen after dewetting the Au layer on such buffer (Figure 6.7b).

Thus, if we summarize the effect: there are pinholes in the buffer layer due to the deoxidation of GaAs substrate at high temperature. When Au dewetting is performed, Ga might diffuses from the hole to form Au-Ga alloy particles (Ga rich). The Ga diffusion would have a limit on the surface; it creates a disc with a specific diameter depending upon the size of the hole.

To our surprise, the results are fascinating because the morphology of NWs is highly aligned, homogenous, and straight (without any noise, see Figure 6.6 in blue) inside the disc. We conclude that this might be an interesting effect of increased Ga compositions in the droplet. As a result, we propose that we control the Ga composition inside the droplet by supplying Ga from an external source. Thus, this could open up new possibilities for us to achieve aligned and controlled morphology of NWs.

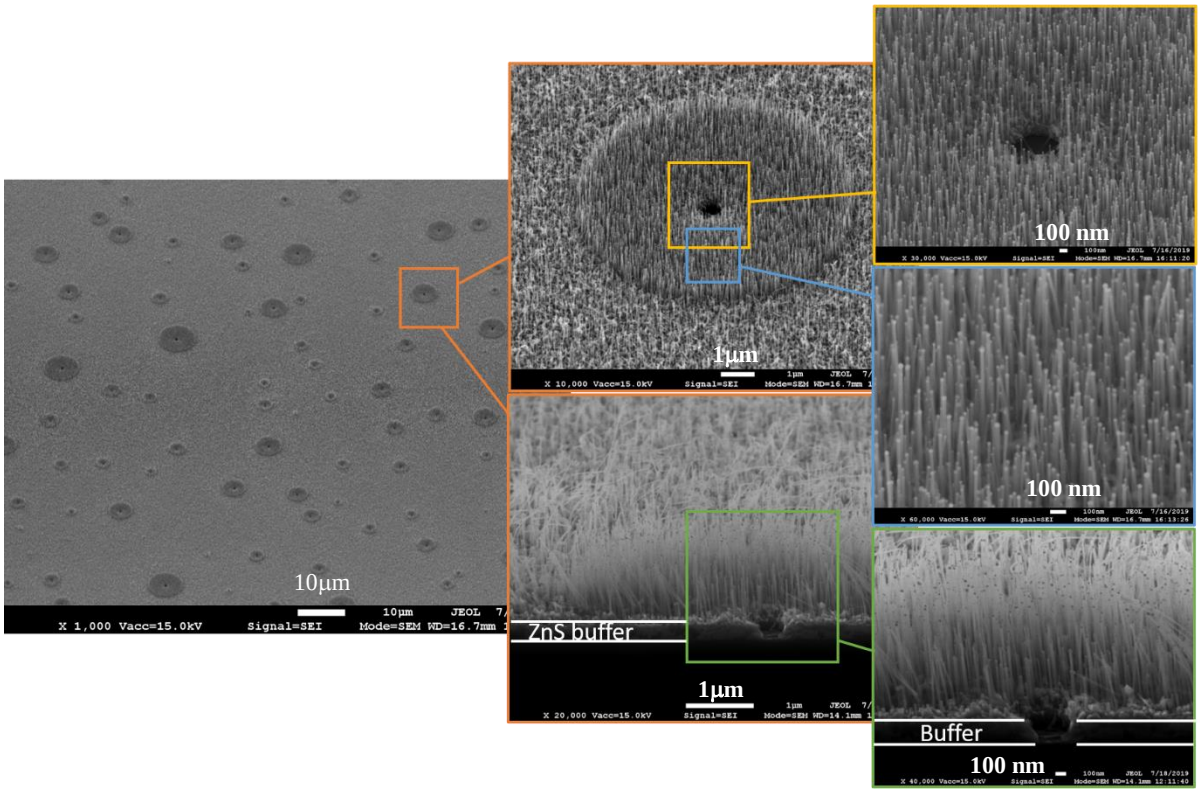

Figure 6.6: The SEM images of the sample with formation disc. In zoomed images, we show 45° tilted and cross-sectional views of the disc. The NWs morphology inside the disc (straight and highly aligned) is different from the NWs outside.

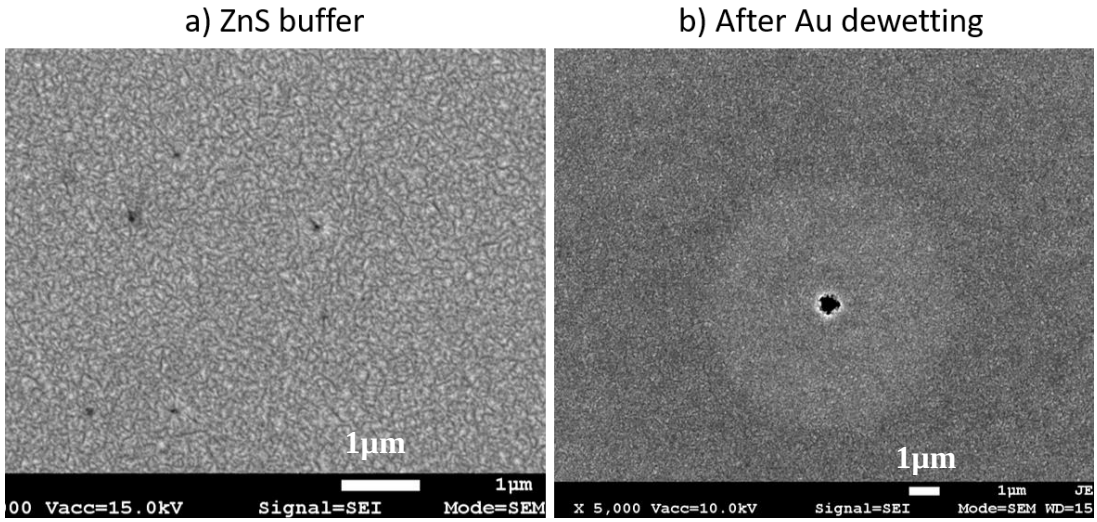

Figure 6.7: SEM images of a) ZnS buffer with the presence of holes as a result of high-temperature deoxidation of GaAs substrates, b) the formation of a disc around the hole after Au dewetting.

6.3.2 The "Ga feeding" experiments

Herein, we aimed to increase the Ga content in the catalyst. This can be easily done and controlled by exposing the Au-particles to a trimethyl-gallium (TMGa) flow before dewetting. Hence, it is possible to intentionally "feed" the droplet with Ga atoms in the MOCVD reactor before growing the ZnS NW.

We performed the following growth experiment in "normal" conditions of deoxidation. GaAs (111)B and ZnS buffer/GaAs (111)B substrates with 0.1 nm Au-deposition were

introduced into the reactor. A 1 sccm TMGa flow (corresponding to a partial pressure of 4.5 Pa) was supplied during the increase in the temperature between 450-500°C to allow Ga diffusion into the Au droplets. The TMGa flow was stopped after a purge time of 30 sec. Then, dewetting was done at 500°C for 10 min. DEZn and DTBS flows were sent with Zn and S partial pressures, 2 and 4 Pa, respectively, corresponding to low growth flux conditions. On both substrates with or without buffer, the NW follows the VLS growth mode. The SEM images of the samples are given in Figure 6.8. It was great to find out very particular NWS due to the "Ga-feeding": vertically well-aligned, exhibiting a big droplet on their top, and quasi-periodic micro-facets on the lateral surfaces. We observed big NWs diameter in the range 35-150 nm with big catalyst droplet present at the top for both samples. Indeed, previous ZnS NWs were somewhat limited in diameter, as the largest catalyst particles (without Ga feeding) were buried under a 2D layer or were forming the so-called 3D objects. Thus, 'Ga fed' droplets can open up new possibilities for us.

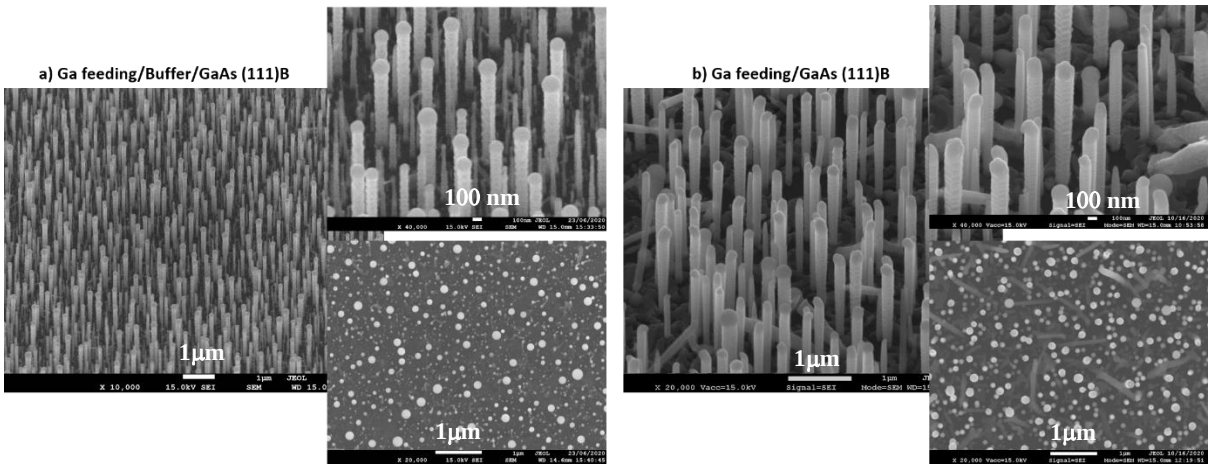

Figure 6.8: 45° tilted SEM images of ZnS NWs grown using "Ga-fed" Au-droplets on a) ZnS (buffer)/GaAs (111)B, b) GaAs (111)B. (A 45° tilted and top view are presented in pop-up images).

6.3.3 Structural properties

We perform a detailed structural analysis on Ga-fed NWs grown on buffer samples using TEM measurements. The catalyst droplet can be seen at the top of the NW in Figure 6.9a. The diameter of the NW is around 140 nm, and a zig-zag faceted structure can be seen on the sidewalls. The related SA Electron diffraction pattern is shown in Figure 6.9b. The diffraction pattern of the whole NW shows a symmetry that suggests the presence of twinning. The NW would be periodically twinned, made of an alternating structure involving the two possible orientations of the ZB structure (refer to Figure 4.1). To confirm that, we select two different spots related to each orientation (see orange and green circles in Figure 6.9c) and perform dark field images. DF images are shown in Figures 6.9d and 6.9e. It is clear that the contrast comes from different orientations: if we select the diffraction spot #1 (in green), we see bright segments related to this orientation in Figure 6.9d, and, on the other hand, the selection of spot #2 (in orange) gives bright zones corresponding to the other orientation (Figure 6.9e). In Figure 6.9f, the composite image alternates green and orange segments and clearly illustrates the zig-zag structure. The period is here ~40 nm.

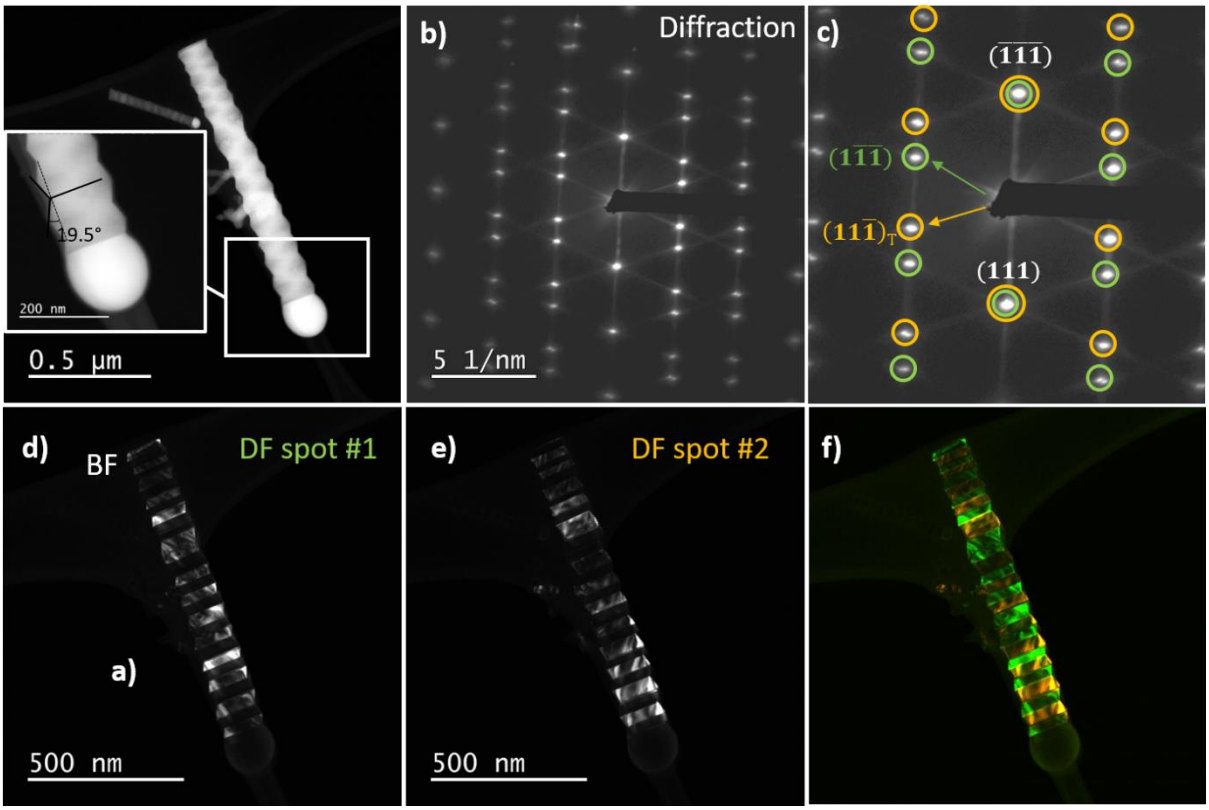

Figure 6.9: a) HAADF image of a single NW; b) SAED pattern of the NW indicates a ZB twinning symmetry, c) marked diffraction twinning spots with green and orange circles; d) dark field (DF) image with spot #1 (green), highlights segments from one ZB orientation; e) DF image created from spot #2 (orange), highlights segments from the other ZB orientation; f) composite DF image made of ZB segments with two different orientations marked in green and orange.

6.3.3.1 HRTEM analysis

HRTEM measurements were performed on the Ga-fed NWs to study the crystal phase in detail and the transition interface between the two ZB orientations. An HRTEM image is given in Figure 6.10a. The zig-zag structure with a ZB stacking can be better seen, and such periodical lattice is called “twinning superlattice (TSL)” [25,61,240]. A careful analysis of the interface between these periods reveals stacking faults or restricted 15R phases. We use inverse Fast Fourier transform (IFFT) to study the interface transition. The FFT of the HR image is shown in Figure 6.10b; we can notice bright ZB spots with the presence of some other weak spots between (000) and (111). We performed Fourier filtered images corresponding to the intensity delimited by the three circles (#1 orange, #2 green, #3 yellow) marked in Figure 6.10b. The resulting lattice correspondences to these three spots are shown in Figures 6.10c-d-e-f. Spot #1 and #2 show the two orientations of the ZB structure, while yellow spot #3 corresponds to the periodic modulation related to stacking faults or restricted 15R phases.

We further focus our detailed study on the transition stacking faults. The magnified HRTEM image shown in Figure 6.11 reveals complicated transient sequences, and some could be high-order polytypes. We considered the different segments of the crystal phase observed in this magnified HR image. The usual green and orange box represent the ZB structure, while the yellow box focuses on the transient stacking. Their corresponding FFT patterns are shown on the right.

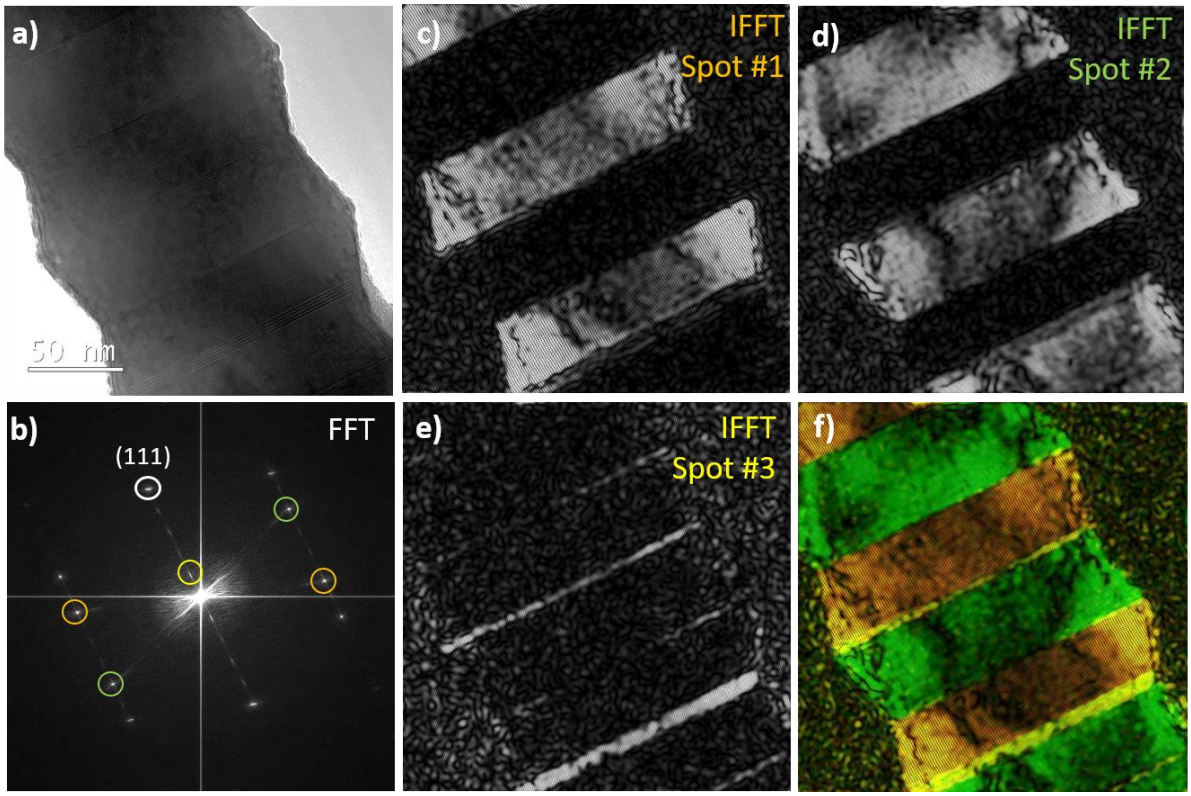

Figure 6.10: a) An HRTEM image of the zig-zag structure called “twinning superlattice (TSL)”, b) FFT of the HR image, c) IFFT image corresponding to spot #1 (orange), d) IFFT image corresponding to spot #2 (green), e) IFFT image corresponding to spot #3 (yellow), and f) composite representation of the HR lattice (orange, green and yellow).

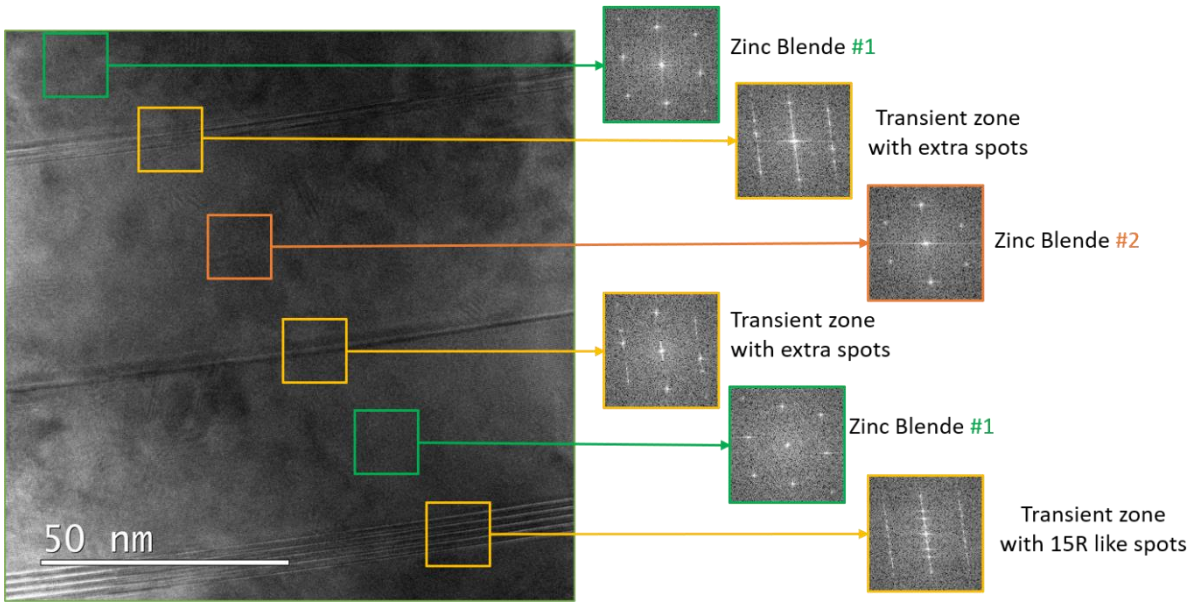

Figure 6.11: The HRTEM image of NW lattice focusing on the transient zone between two orientations of the ZB phase. The green and orange zone represents the ZB stacking (type #1 and #2). The transient zones are given in yellow.

The first and second transition interfaces on the top of the image are short (~2 nm). Extra spots can be seen in the FFT pattern that might be due to random stacking faults. Below, the third transient zone has a larger period (~10 nm), and the corresponding FFT pattern is similar to the 15R spots. Hence, it is possible that at this transition interface, we get a short sequence of the high order 15R polytype which was previously identified in our VLS ZnS NWs. A more detailed high magnification HR image focusing on the transition interface is shown in Figure 6.12 and confirms that point. The transition lattice sequence looks like the 15R structure (Figure 6.12b). Additionally, the angle between the droplet and the twinning plane is measured at around 130 ° (Figure 6.12c).

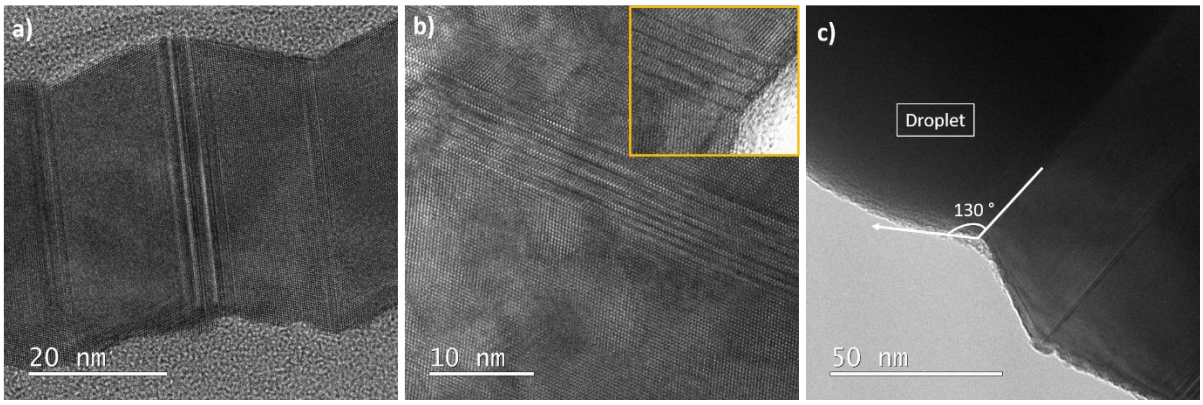

Figure 6.12: a-b) A highly magnified HR image focusing at the transition interface revealing a 15R alike lattice sequence, and c) we measured an angle around 130° between the droplet and the transition interface plane.

6.3.3.2 EDS mapping

As Ga atoms from outside fed the Au-droplets, big Au-Ga catalyst particles might be the reason behind the presence of a wide range of NW diameters (35-150 nm). To quantify the Ga content inside the droplet, we have performed EDS measurements and mappings. The EDS mapping of a large droplet (diameter >100nm) is illustrated in Figure 6.13. A two-phase composite can be seen in the droplet. The droplet is non-homogenous, as Au is more concentrated at a specific place near the surface of the droplet in the form of a core. Contrastingly, the EDS mapping of smaller droplets (~50 nm) shows a more homogenous distribution of the Au and Ga (see Figure 6.14). The compositional measurements on the droplet reveal a Ga rich droplet for both cases (small and large droplets). For the large droplet, EDS measurement performed on a selected volume outside the Au-core (see circle in Figure 6.13) indicates quasi-pure Ga composition with 99.7 ± 0.2 % Ga and 0.3 ± 0.2 % Au distribution. On the smaller droplet, EDS analyzes a volume close to the droplet-NW interface (circle in Figure 6.14), and gives a composition of 84 ± 2 % Ga and 16 ± 2 % Au. Thus, the intentional Ga supply and diffusion increase the diameter of the catalyst droplet. In addition, we have observed a sharp droplet-NW interface and found no detectable traces of Zn and S inside the droplet. Another point we noticed is that larger droplets are elongated along the growth direction, while smaller droplets are spherical.

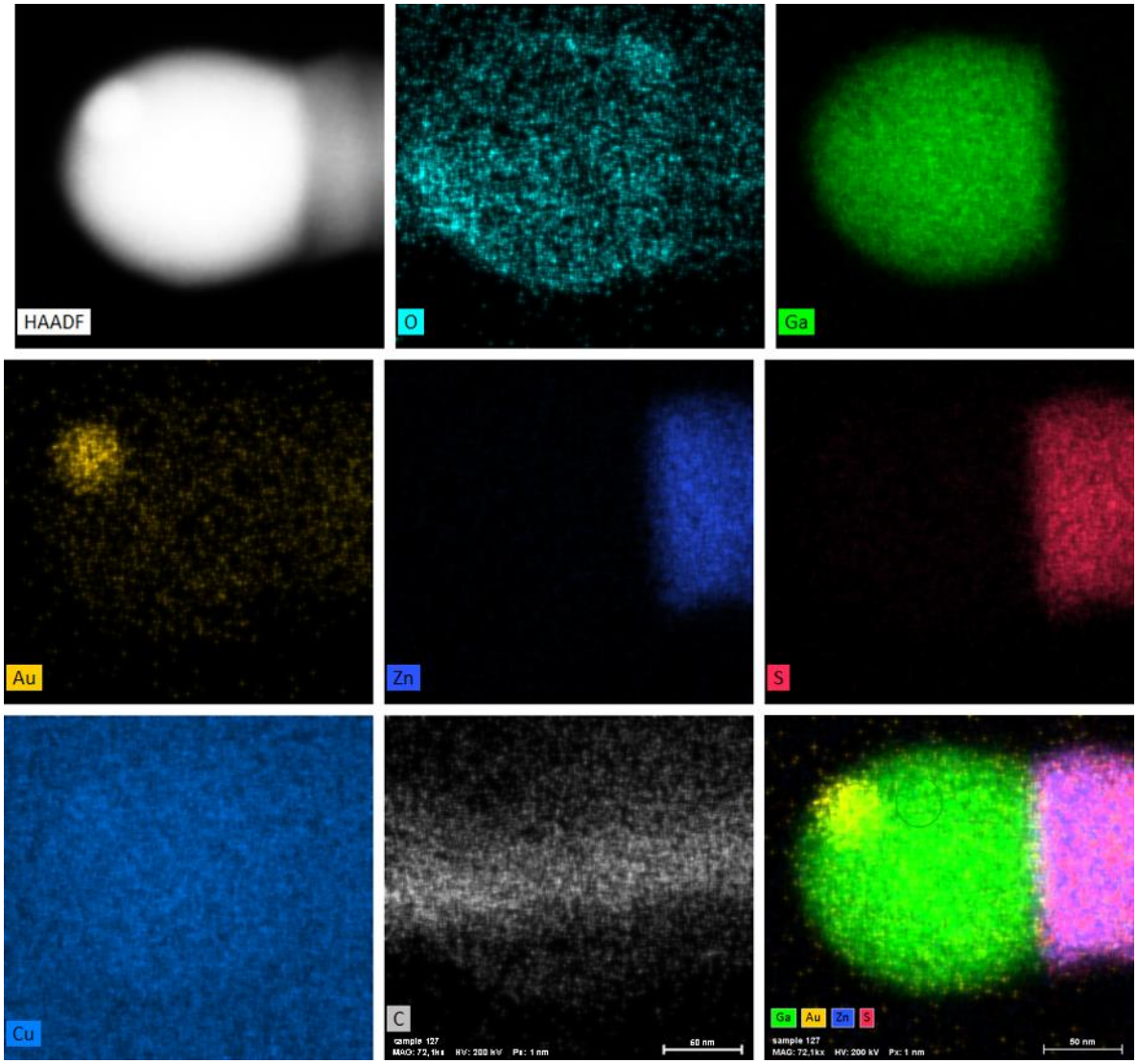

Figure 6.13: The EDS mapping of a big catalyst droplet; Ga is homogenously dispersed inside the catalyst, while Au is concentrated in a specific zone near the edge; no presence of Zn and S detected inside the droplet.

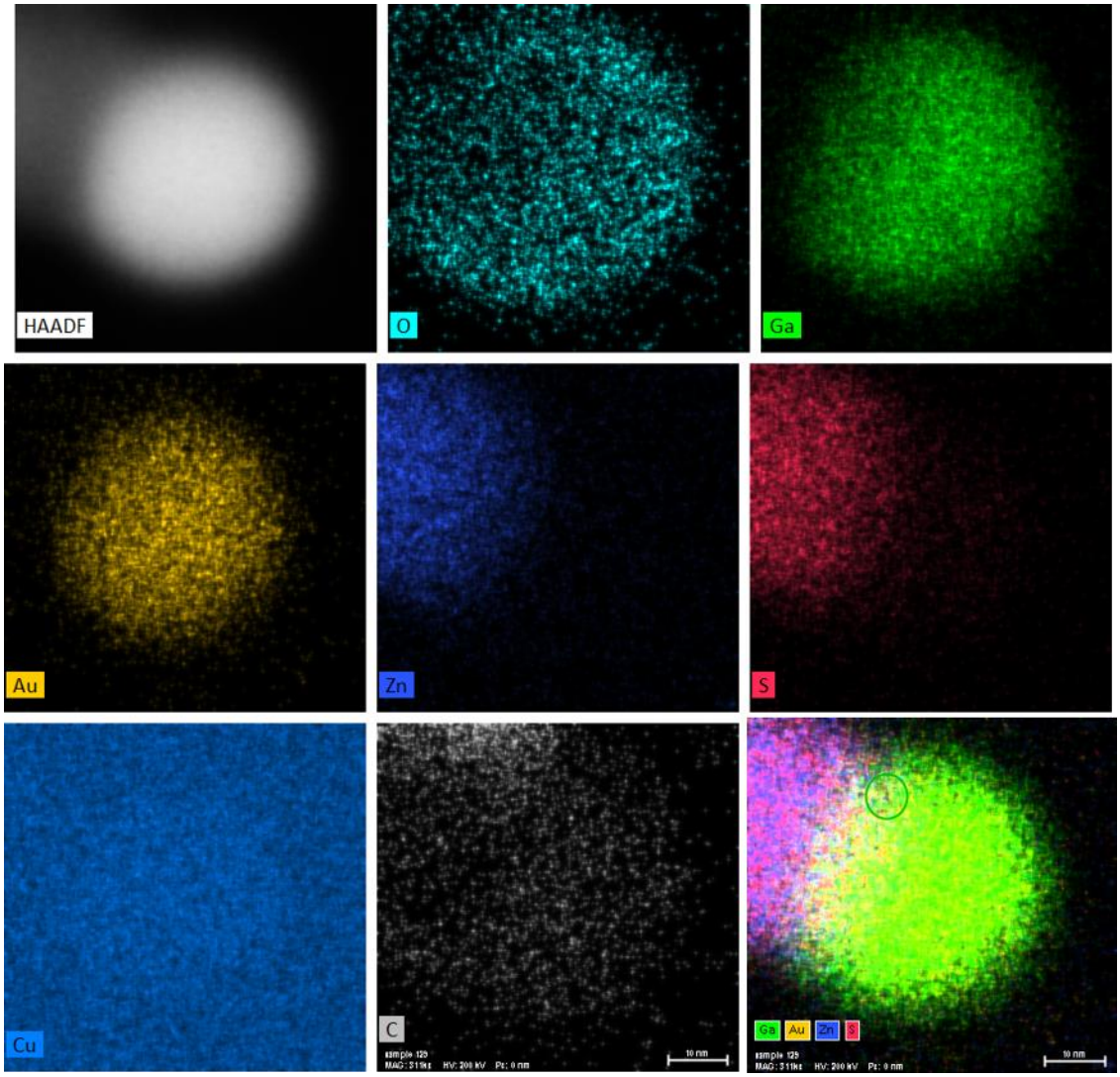

Figure 6.14: The EDS mapping of a small catalyst droplet; Ga and Au are more homogenously dispersed inside the catalyst.

6.3.3.3 Correlation between NW diameter and segment length

In this section, we studied the periodic oscillation of the Ga-fed low growth flux ZnS NWs. The correlation between the NW diameter and segment length is plotted in Figure 6.15. It follows a linear correlation, i.e., the period of oscillation increases with increasing the nanowire diameter. Previous studies have reported linear and non-linear relationships between NW diameter and twin segment length [61,241–243]. Burgess et al. discussed GaAs TSL fabricated using Zn as a twinning enabler [241]. They found a linear correlation between diameter and superlattice length for GaAs similar to SiC [242] but contrasting with previous GaP and InP studies [243,244]. The authors gathered the results, reproduced here in Figure 6.14. The plots represent the correlation between twin plane spacing and NW diameter for GaAs (linear) and GaP and InP (non-linear). Building a model, they relate such different behaviors to the higher twin plane surface energy of GaAs and the lower supersaturation in the Au droplet. Herein this thesis, ZnS TSL would show the same tendency as GaAs TSL.

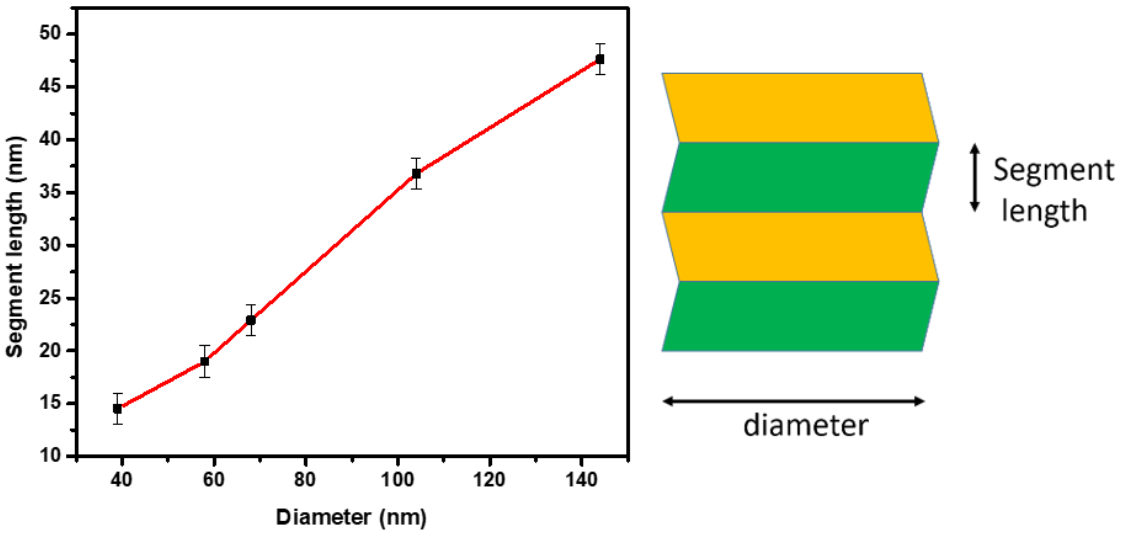

Figure 6.15: The plot between NW diameter and TSL segment length shows a linear correlation between them.

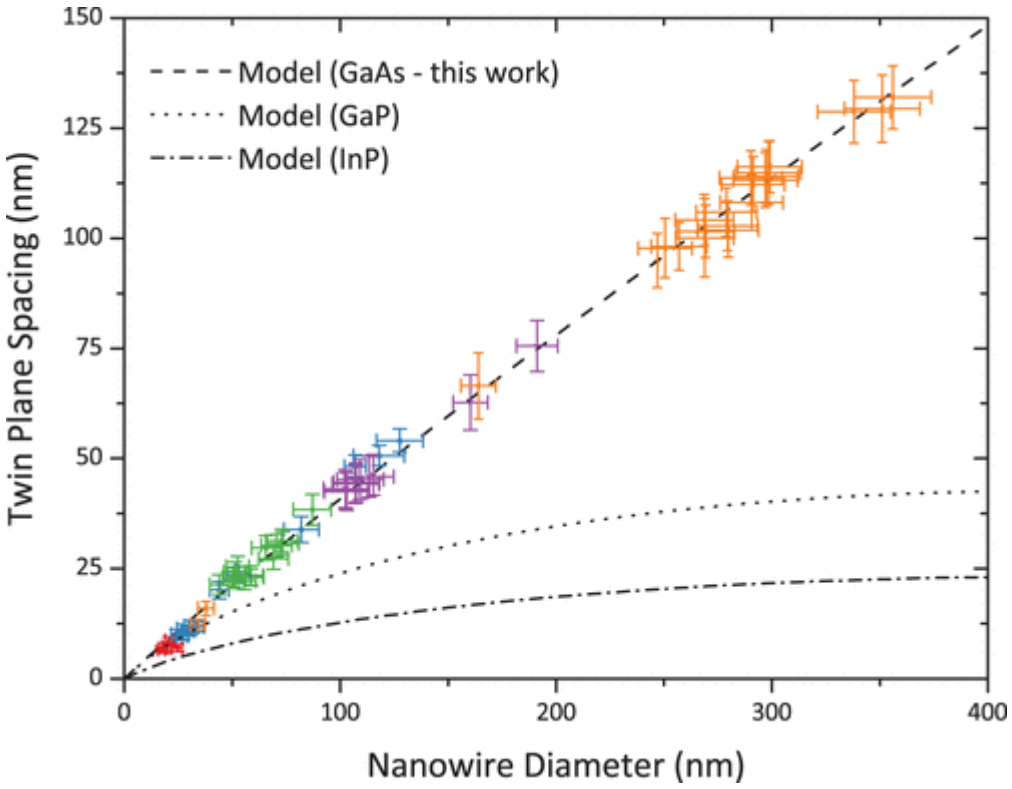

Figure 6.16: The plot depicts a correlation between twin plane spacing and NW diameter for GaAs, GaP, and InP. GaAs NWs follow a linear behavior, while GaP and InP follow a non-linear behavior. Results from different NWs treatments are shown in different color. Adapted from [241].

6.3.4 Discussion

In recent years, the twinning superlattices, i.e. the formation of periodic rotational twins, have been introduced intentionally, or unknowingly in a number of III-V (InP [61,240,244], InAs [17,77,245,246], GaP [240,247,248], and GaAs [241], II-VI (ZnS [24,142,199], ZnSe [25,249], ZnTe [250], and ZnO [251]), and IV-IV (SiC [242]) semiconductor nanowires. Apart from providing fundamental insight into the growth process [61,211], periodic twinning was anticipated for bandgap engineering and the generation of direct intersubband optical transitions [252–256], increased mechanical strength [257,258], and phonon engineering [248]. A twinning superlattice is predicted to induce a direct bandgap in normally indirect semiconductors, such as silicon, germanium, and gallium phosphide. However, controlling and maintaining periodic rotational twins in the NW structure is challenging.

Recent studies on III-V semiconductor nanowires have revealed periodic zinc-blende twins, which are typically created due to a high impurity dopant (Zn, Te, or Be) concentration in the nanowires structure [61,211,241,244,254]. For example, Algra et al. commonly observed the WZ phase in undoped InP NWs grown by MOCVD, but the addition of DEZn in the gas phase, used for p-type doping, resulted in the formation of a zinc blende crystal structure which was periodically twinned [61]. On the base of a nucleation model, they argued for a strong relationship between the Zn atoms and the InP growth interface, leading to a decrease of the liquid-solid (LS) step energy for a ZB nucleus, compared to the WZ case. Interestingly, they demonstrate how the cross-sectional shape of the growing NW, constantly evolving from hexagonal to triangular and *vice versa*, induces the periodic distortion of the catalyst droplet (to be relaxed via a twin creation) and hence explain the formation of a twinning superlattice.

Let us go into the details of the TSL formation mechanism. The TSLs are due to side facets {111}A and {111}B that are inclined in opposite directions ($\theta_A = 19.5°$, $\theta_B = -19.5°$) with respect to the NW axis. At a certain point during growth (situations 1 and 3), the top surface of the nanowire is hexagonal, and the catalyst droplet attached to this surface is very close to spherical, as schematically represented in Figure 6.17 (taken from [61]). When the NW grows, the {111}A edges move inward, and their length increases, while the {111}B edges move outward, and their length decreases. As a result, the shape of the nanowire–droplet interface becomes more and more triangular, as depicted in Figure 6.17b for conditions 2 and 4. This bends the catalyst droplet to reduce its surface area, forcing it to lean toward the catalyst droplet's long 111A edges. After a certain point, it becomes more advantageous to establish a twin plane and begin reducing the distortion of the catalyst particle by re-growing towards a hexagonal shape, rather than continuing development toward an entirely triangular shape. This method of inverting triangularly created interfaces is repeated indefinitely, resulting in the NW's periodic structure [61].

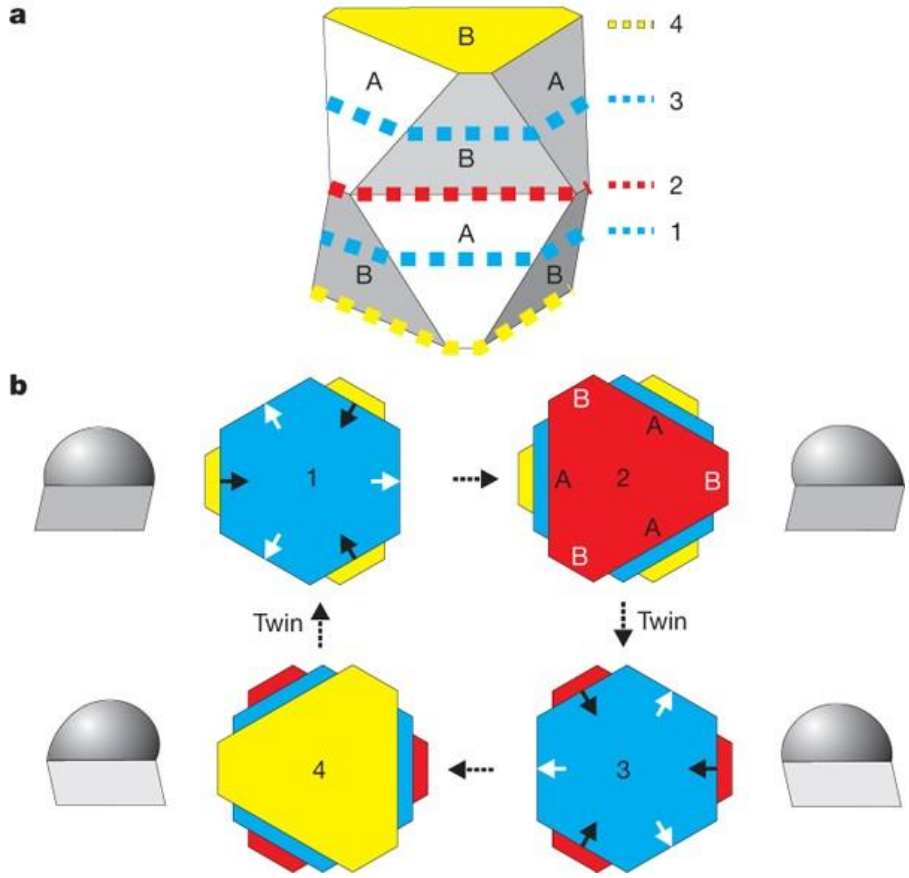

Figure 6.17, reproduced from ref. [2]: a) Schematic representation of the morphology of a twinned nanowire with the ZB crystal structure with non-parallel {111} side facets, b) The cross-sectional shapes of the top facet of the nanowire crystal at the solid-liquid interface during growth. The numbers correspond to the positions indicated in a. Owing to the non-parallel orientation of the side facets, {111}A edges increase and {111}B edges decrease in length during vertical growth. As a result, a hexagonal interface develops into a triangle-like shape. At a specific moment, it is energetically more favorable to create a twin plane rather than to continue growing towards an entirely triangular top interface. After twin formation, a triangle-like shape evolves back to a hexagonal shape, and the cycle is repeated as schematized in b. To the left or right, the corresponding calculated shape of the catalyst particle on a hexagonal (1 and 3) and a triangularly deformed (2 and 4) interface is depicted, showing the skewing of the droplet towards the long {111}A side edge and demonstrating that the contact angles depend sensitively on the cross-sectional shape.

In another example, Goktas et al. used Be and Te dopants to initiate the TSL formation in self-catalyzed (with Ga droplet) GaAs NWs growth. Their proposed model is based on surface energetics to explain the formation of TSLs: the accumulation of dopants on the NW sidewalls is expected to decrease the surface energies of (111)A and (111)B side facets with respect to vertical facets, which makes the formation of TSLs energetically preferred. They have also found that the TSL period is dependent on NW diameter and contact angle-dependent. Interestingly, they have suggested an important idea that the TSLs could be simply controlled by the VLS surface energetics rather than the growth kinetics.

However, some experimental works produced TSL without dopant [17,242]. Caroff et al. showed a dependence of crystal structure on diameter for InAs NWs and growth temperature. For small nanowires (<40 nm), they reported a WZ structure with few stacking faults. With a further increase in the diameter, they observed an increase in the stacking faults

density and inclusions of small ZB segments. For large diameters (>100 nm), they found InAs coherent twin-plane superlattices.

To conclude this brief state of the art, the following conditions favor the formation of TSL in semiconductor NWs:

1) First, we need the cubic growth of NWs.
2) The presence of stable {111} lateral facets, possibly favored by dopants.

In our case of ZnS 1D nanostructures, TSLs are achieved by increasing the Ga composition of the droplet. Such difference in the droplet composition would significantly affect the droplet contact angle, interface energies between droplet and NW (liquid-solid, LS), and between droplet and vapor (liquid-vapor, LV). In the reported nucleation models [11], this variation of the catalyst composition has possibly a strong impact and may favor the formation of ZB polytypes. Then, if we assume that (111)A and (111)B side facets are favored and kept as long as the distortion of the Ga-rich droplet allows it, a periodically twinned ZB structure would grow following the mechanism described above III-Vs.

In addition, the droplet contact angle β is worth considering. The recent article of Panciera et al.(detailed in Chapter 1 and 4) demonstrated the ZB phase selection at high (>125°) and low (<100°) values of contact angle [149]. We have observed a contact angle between 110 and 123° after growth for our reference ZnS NWs (Chapter 4). Feeding the Au droplet with Ga, we increased its volume, and hence high contact was achieved (~130°), favorable to ZB nucleus formation. Additionally, the extra Ga composition might have helped to decrease the surface energy of the droplet (γ_{LV}), causing an increase in the value of ratio (*R*) (refer appendix to see the impact of contact angle and γ_{LV} in the case of ZnS NWs).

In the literature, ZnS TSL has also been reported without additional doping. As already mentioned, Hao achieved ZB periodic structure, however, with a very short period of a few nanometers [24]. To the best of our knowledge, our ZnS TSLs are the first achieved with a large period of 40 nm. Actually, achieving ZB phase perfection in ZnS NWs is rare in the literature, and we discussed previously that the small stacking fault energy would favor other polytypes. The scarcity of ZB in ZnS NWs explains the difficulties of achieving it. Interestingly, our results agree with the work of Liang et al. [202]. They also used pure Ga as catalyst on GaAs (111)B substrates to obtain vertical arrays of ZnS NWs (exhibiting diameters >100 nm) and reached a ZB structure with frequent inclusions of stacking faults, nevertheless not showing periodicity.

6.4 Conclusions

Our TEM results presented in chapter 4 showed that catalyzed growth in the VSS conditions involving a pure solid Au-droplet leads to a mixed WZ (dominant)-ZB structure, while in VLS conditions (liquid Au-Ga droplet), an original 15R high order polytype is observed. From that starting point, the partial pressures of precursors were varied in the MOCVD reactor, and the role of supersaturation was demonstrated to play a major role in the crystal phase selection: we turned 15R ZnS NW into 2H by increasing the growth flux. At low growth flux, large 15R segments with small inclusions of 3C/stacking faults were observed. For intermediate growth flux, a 15R structure with increased stacking faults was observed and detailed in Chapter 4. For this case, HOP/2H supersaturation range is predicted. Regarding high growth flux, a pure 2H phase was favored. This phase confirms the growth at high supersaturation values with a 2H preferred crystal phase. The 3C phase was not induced by reducing the supersaturation. Finally, the key role of droplet composition was also demonstrated: another remarkable

structure, a twinning superlattice made of zinc-blende segments of a few tens of nanometers sandwiched between twin boundaries, was achieved by increasing the Ga composition of the Au-Ga alloy catalyst, and is possibly be explained in the framework of our theoretical model. Indeed, the richness and the variety of the crystal phase attainable in ZnS make this material particularly interesting for the study and general comprehension of polytypism in semiconductor nanowires.

Chapter 7

Optical properties and towards II-VI based heterostructure NWs

Contents

This chapter provides optical studies of our grown materials using photoluminescence and cathodoluminescence. We start with thin films, ZnS as well as ZnSe (zinc selenide), which was the chosen material to investigate the growth of heterostructures. Subsequently, we carry out CL on single ZnS nanowires. The benefit of coating the NW with a $Zn_xMg_{1-x}S$ shell will be emphasized. Finally, ZnS/ZnSe axial heterostructures are investigated. This latter case will actually correspond to preliminary studies since we faced difficulties in the preparation of the samples. However, we hope this gives nice perspectives and insights into future work.

7.1 Optical properties of thin films

7.1.1 ZnS thin films

7.1.1.1 Photoluminescence

The PL measurements were performed at cryogenic temperature (~4K). Importantly, in this PL measurements, the collected energy is limited to ~3.78 eV at maximum. This is intrinsic to our PL set-up: the excitation is given by the 325 nm line (3.81 eV) of a He-Cd laser. In addition, a filter with cut-off at 328 nm (3.78 eV) is introduced to avoid overwhelming the rather weak ZnS emission with the Rayleigh diffusion of the laser.

In the PL spectrum of a ZnS thin film presented in Figure 7.1, the near band edge (NBE) emission is measured in the range 3.5-3.78 eV, and includes several sharp transitions. A broad emission centered around 3.2 eV is also observed, and attributed to point and extended defects in the material.

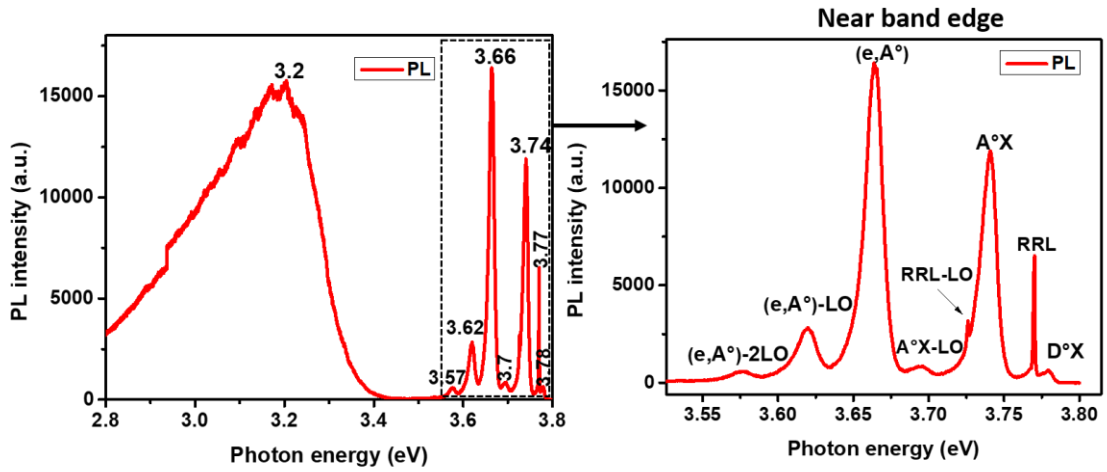

Figure 7.1: PL spectra of ZnS thin films, with a focus on near band edge emission.

Looking carefully at the NBE emission, and comparing it with the ZnS PL emission reported in 2000 by the group [259], we underline that:

- the light-hole free exciton (LHX) transition, which was the dominant feature in 2000, is missing at 3.797eV because of the cut-off. As well, the first excited state n=2 is not observed at 3.825 eV. The small peak at 3.78 eV could be the foot of donor bound exciton (D°X, at 3.789 eV in 2000).
- acceptor bound exciton (A°X) is seen at 3.74 eV, with LO-phonon replica at 3.69 eV (LO-phonon energy around 42 meV in ZnS)
- electron acceptor (e, A°) transition is measured at 3.66 eV, with two LO-phonon replicas at 3.62 eV and 3.57 eV.
- 3.726 and 3.77 eV are resonant Raman lines (RRL) of the laser at 3.815 eV, which again is consistent with LO phonon value of 42 meV

7.1.1.2 Cathodoluminescence

CL enabled to collect light emission at higher energy, revealing the missing peaks of ZnS spectrum.

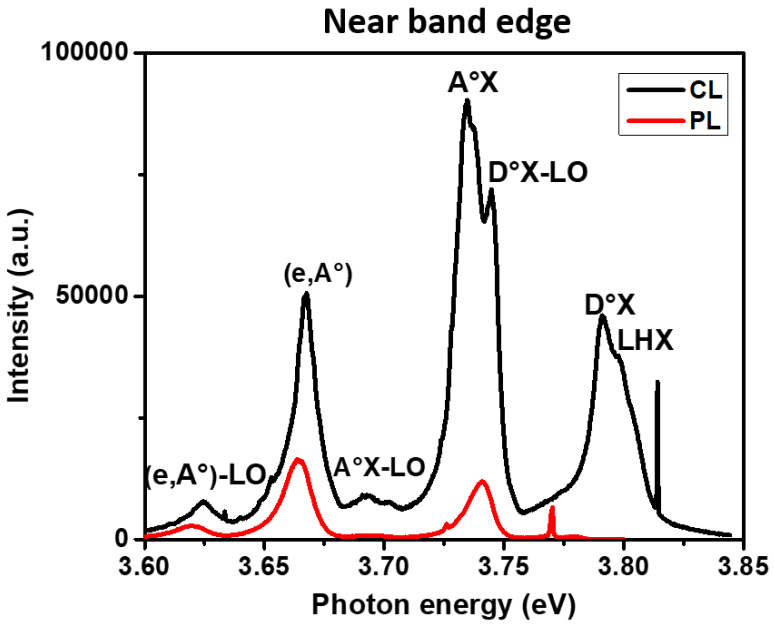

Figure 7.2: CL and PL NBE spectra of ZnS thin films.

The Figure 7.2 gathers and allows to compare PL and CL spectra. CL adds additional information on the high energy missing part. D°X and LHX are now clearly seen at 3.79 and 3.797 eV, respectively. The peak at 3.74 eV is better resolved and shows the contribution of LO-phonon replica of D°X at 3.744 eV. Noticeably, there is a nice agreement between PL and CL emissions.

7.1.2 Photoluminescence of ZnSe thin film

In the same way, we compare the photoluminescence properties of a reference ZnSe thin film grown for this thesis, with the ones reported by the group in 1998. The MOCVD reactor is the same, but in the previous work, dimethylzinc-triethylamine (DMZn-TEN) had been used as the zinc precursor. In 1998-ZnSe films [260], PL spectrum was dominated by the free exciton (labelled Ex in the article) and the donor bound excitation (labelled I_2 in the article) at 2.8 and 2.794 eV, respectively. A Y_0 transition at 2.6 eV was related to excitons trapped on dislocations. [see also detailed transitions in Thesis of C. Thiandoume, University Cheikh Anta Diop of Dakar, Sénégal, 1997]. We can point out that, many years later, the quality of our layer is not as good the old one. The contribution of free and donor bound excitons is weak, in the range 2.79-2.8 eV. The line at 2.6 eV is again attributed to Y_0. The emission at 2.71 eV could be acceptor bound excitons but was not seen in our previous samples, nor the deep emission at 2.46 eV which could be also related to defects in the grown material. Hence, the optical quality of ZnSe would be worth optimizing a bit, but this was not the scope of the thesis. We will see below that we had to face other issues.

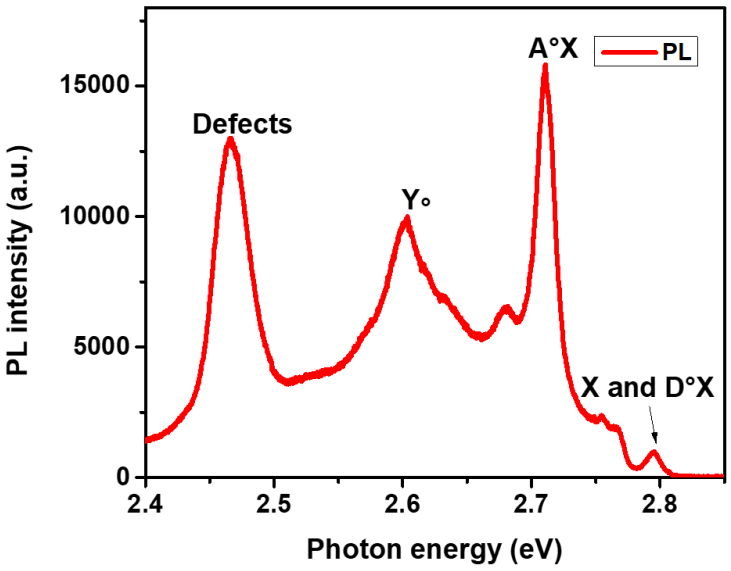

Figure 7.3: PL spectra of ZnSe thin films.

7.1.3 Cathodoluminescence of $Zn_xMg_{1-x}S$ thin film

We have carried out cathodoluminescence measurements on $Zn_xMg_{x-1}S$ thin films with ~10% Mg content. The CL spectrum presented in Figure 7.4 is dominated by the excitonic transition at 3.89 eV, and a deep level emission at 3.13 eV could be related to the defects in the grown thin films. Therefore, the bandgap of the alloy is larger, and an increase of the Mg composition could shift further the free exciton transition (MgS ~ 4.5 eV). In this work, we will use $Zn_xMg_{x-1}S$ as a shell material to cover the ZnS NWs.

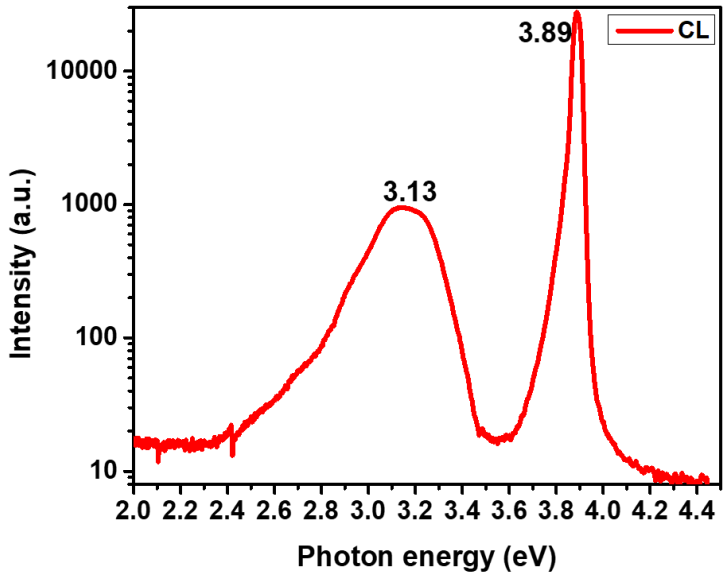

Figure 7.4 CL spectra of ZnMgS thin films.

7.2 Optical properties of ZnS NWs

We have performed nano-cathodoluminescence measurements on single NWs at cryogenic temperature (~4K). The NWs were scratched from the substrate, and spread on a holy carbon TEM grid for the CL measurements. Table 7.1 gathers the list of NW samples studied.

Table 7.1: NW samples studied for CL.

Sample	Growth mode	Crystal phase	ZnMgS Shell
NW4	VLS	15R	No
NW15	VLS	15R	Yes
NW16	VSS	WZ/ZB	Yes
NW17	VSS-Low growth flux	Pure WZ	Yes
NW18	VLS-Ga feeding	ZB TSL	No
NW19, NW20 and NW21 (ZnS/ZnSe)ZnMgS heterostructure	VLS-Low growth flux	15R with less stacking faults	Yes

7.2.1 VLS grown NWs

The reference sample (with 15R polytype) is studied for its optical properties. The CL spectrum in Figure 7.5a (black) corresponds to the as grown 15R NW. Bare ZnS nanowires do not emit, or only very weakly, even at low temperatures. This is probably due to their high-density surface states that act as non-radiative carrier traps. These surface states affect the optical properties and quench semiconductor NW light emission [261]. Thus, we attempted to grow a 30-40 nm thick $Zn_{0.9}Mg_{0.1}S$ shell around the NWs. The NW morphology is shown in Figure 7.5b. The shell is non homogenous with more deposition on the top around Au droplet. The CL spectrum of such ZnS/ZnMgS (core/Shell) NW is presented in red color. The emission around 3.95 eV comes from the shell, while a broad peak centered at 3.2 eV is attributed to ZnS core, and might appear due to the defects, similarly to ZnS thin films. In addition, it is not forbidden to consider a contribution from ZnMgS shell in this broad emission. We must note that we have observed weak luminescence from these NWs even after covering with a shell.

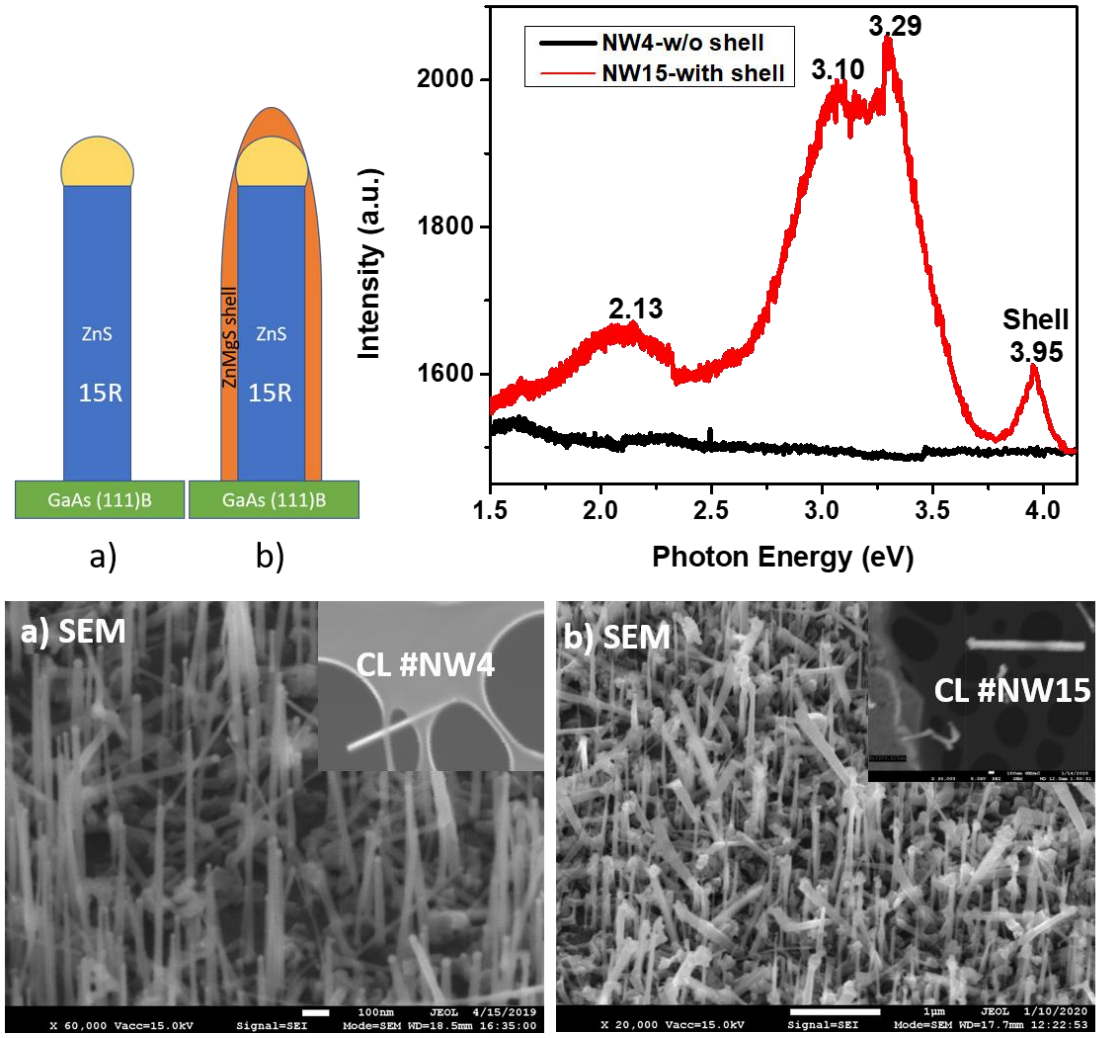

Figure 7.5: The CL spectra of a) bare ZnS NWs (in black), b) ZnS NWs covered with a ZnMgS shell (in red). The luminescence at 3.95 comes from the shell, while a broad emission might appear from the shell + core ZnS 15R NW.

7.2.2 VSS grown NWs

In the same way, we performed optical measurements on VSS reference samples (with alternate WZ/ZB structure) after growing a shell around them. The NWs morphology is shown in Figure 7.6a. The shell is again deposited non homogenously with a very fat rounded top. The peak around 4 eV belongs to the emission from ZnMgS shell. For this sample, we would see a near band edge emission from core ZnS NW at 3.74 and 3.77 eV. These peaks might correspond to A°X and D°X transitions similar to ZnS films. Another possibility can be a luminescence coming from ZB and WZ segments (Eg =3.72 and 3.77 eV at RT, respectively), therefore giving two contributions, and the NW would act like a crystal phase heterostructure. But we recognize this is very speculative at that point, and it will be contradicted just after.

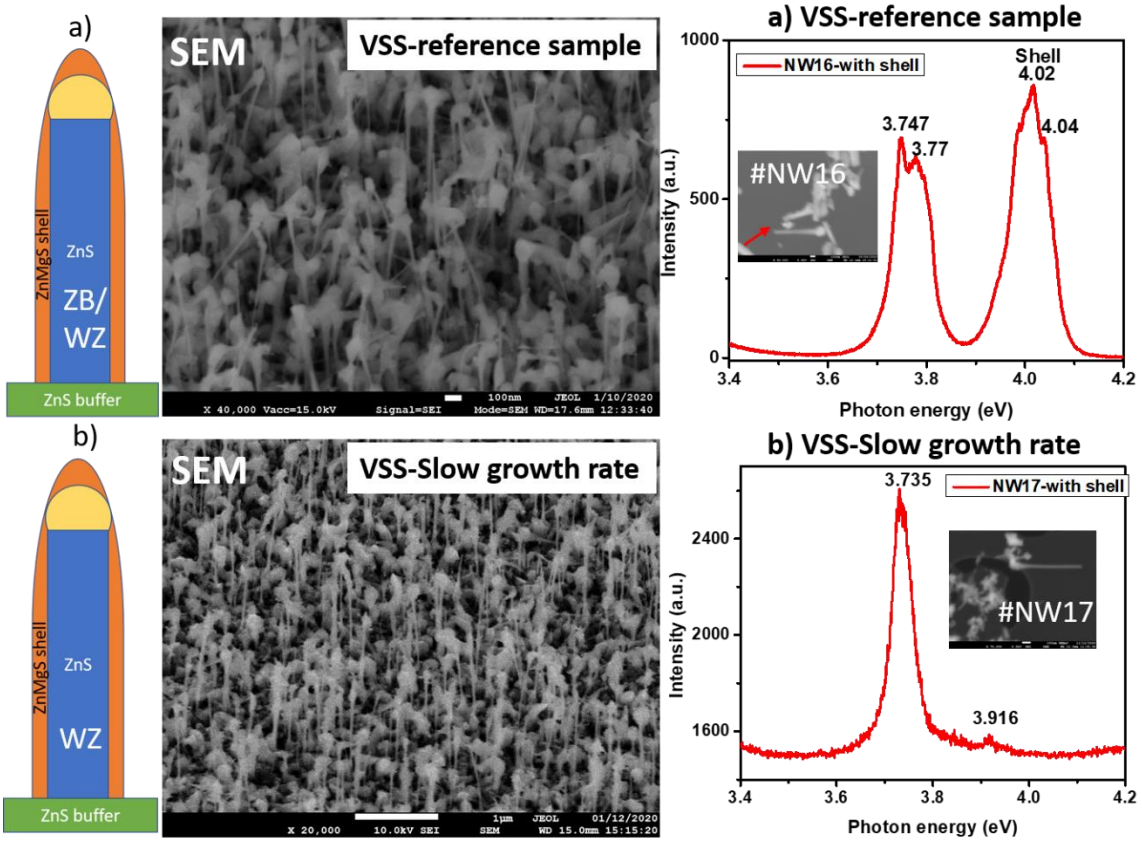

Figure 7.6: The CL spectra of VSS grown NW: a) reference sample (WZ/ZB structure) with shell and b) low growth flow (pure WZ) sample with a shell.

We carried out CL measurements on another VSS sample grown with low growth flux that inherits a pure WZ structure (refer to the appendix). The core/shell NW morphology is given in Figure 7.6b. The CL performed on NW4 shows emission peaks at 3.9 eV and 3.735 eV that are attributed again to the luminescence from shell and the core, respectively. The presence of a single peak at 3.735 eV appears due to the presence of single WZ phase. However, that result disagrees with the assumption of ZB and WZ separated contributions in the previous sample, since we would expect the WZ emission energy to be higher that the ZB one, at 3.77 eV (if transitions are of the same nature, i.e., acceptor bound exciton).

To conclude, we collected a better CL emission from VSS grown ZnS nanowires, as compared to VLS nanowires. In VSS case, the excitonic transition is observed with a significant intensity, due to pure phase segments, WZ and/or ZB. 15R NWs (VLS) appear to have degraded optical properties, and this could be explained by the repeated stacking faults involved in the polytype formation

7.2.3 Ga feeding

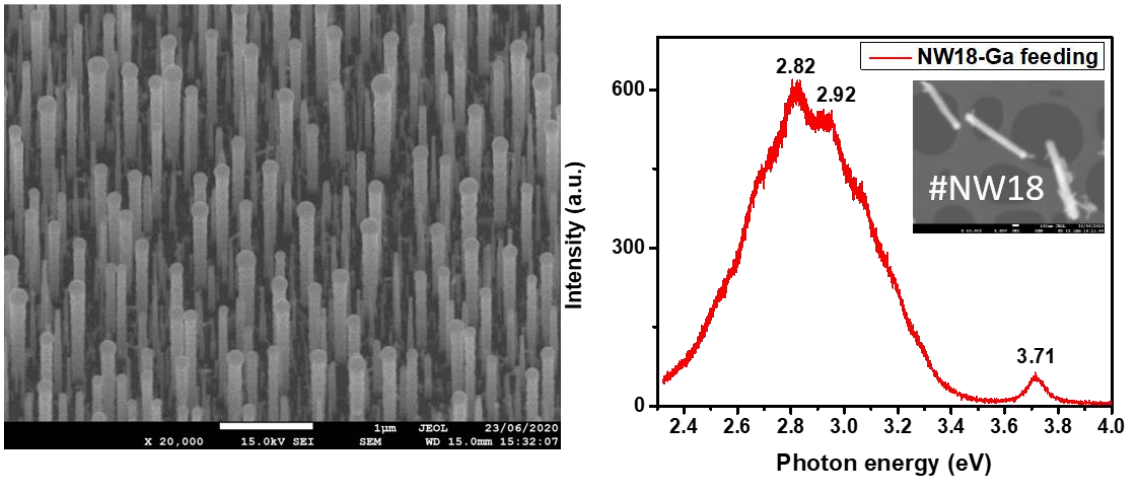

Figure 7.7: The CL spectra corresponding to ZnS NWs grown with a Ga fed droplet (ZB TSL sample). The NBE emission is observed at 3.71 eV, while a broad DLE reflects presence of periodic stacking faults (twinning, 15R transitions).

We also took the opportunity to study the CL of the so-called Ga-fed ZnS NWs. Figure 7.7 presents the SEM image of the sample, and the CL spectrum recorded on a single NW. A weak NBE emission is seen at 3.71 eV. Since this NW was NOT covered with any ZnMgS shell, it confirms that such peak is originating from ZnS material, and so it should be the same for the previous samples. Hence, the transitions observed in this work between 3.7 – 3.8 eV are attributed to excitonic emissions in ZnS. In Ga-fed NWs, the spectrum is strongly dominated by deep emissions in the broad range 2.4-3.4 eV. Again, the presence of stacking faults at the interface between ZB segments (see chapter 6) might alter the NBE emission intensity.

7.3 Towards ZnS/ZnSe axial heterostructure NWs

To prepare axial heterostructures based on ZnS, we tried inserting ZnSe segments during the growth. The bandgap of ZnSe is 2.8 eV at RT. The ZnS/ZnSe heterojunction is illustrated in Figure 7.8, which also presents the band alignments for the other usual semiconductors.

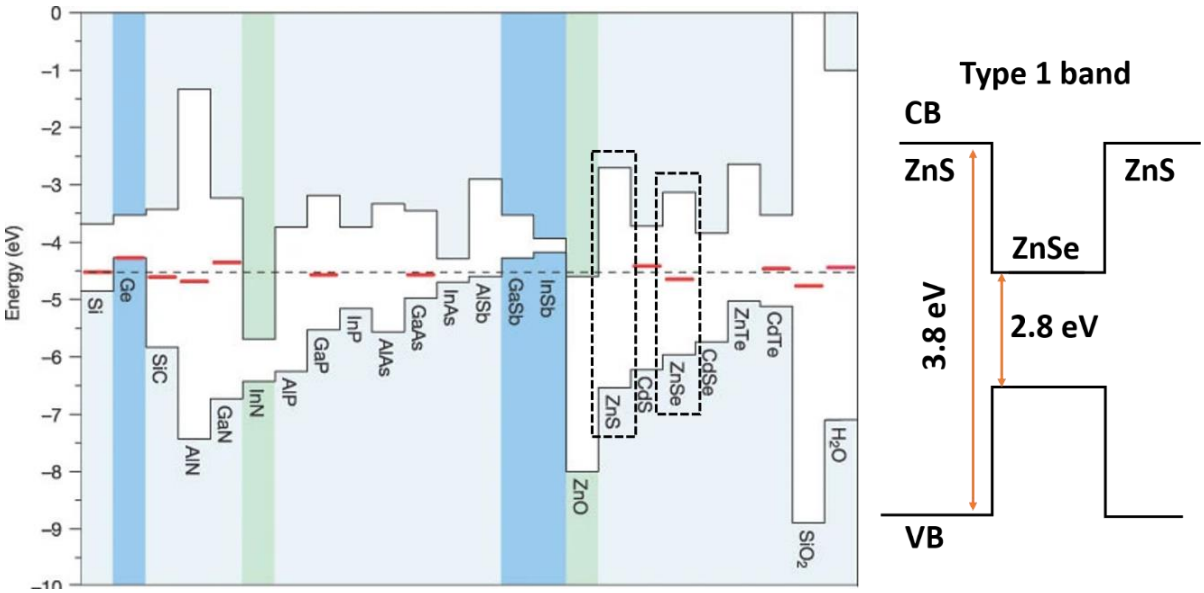

Figure 7.8: The alignments of bands calculated for some materials of columns IV, III-V and II-VI. The type 1 heterojunction band structure of ZnS/ZnSe heterostructure. Adapted from [262]

Type I band alignment is thus expected between ZnS and ZnSe. From the illlustration, we note that CdS would also be a good candidate to build 1D II-VI based heterostructures.

7.3.1 VLS growth of ZnS/ZnSe heterostructures

We tried to grow ZnS/ZnSe heterostructures in our MOCVD system. We followed many recipes, varying the size of ZnSe segments, type of growth mode, etc... Indeed, we found it difficult to characterize and control the ZnSe insertion in ZnS NWs. Such dense and insulating nanostructures are hard to observe using SEM, and TEM experiments were dedicated in priority to ZnS polytypes analysis. In addition, another difficult step has been to cover with a ZnMgS shell, as it appeared to be strongly inhomogeneous.

Here, we selected a (ZnS/ZnSe)ZnMgS heterostructure sample (NW6, Table 7.1), see schematic and SEM image in Figure 7.9. In this sample, several ZnSe segments were inserted for different growth duration (1', and 20"). We started the growth on bare GaAs (111)B in VLS mode with ZnSe, and then switched between ZnS and ZnSe segments. After axial growth, we decreased the temperature and started the lateral growth of ZnMgS shell. SEM image shows different nanostructures. We will skip the biggest ones (indicated by the yellow arrow) and will be more interested in the "nail-like" nanowires (green arrows), hardly seen in this image, but better shown in the following.

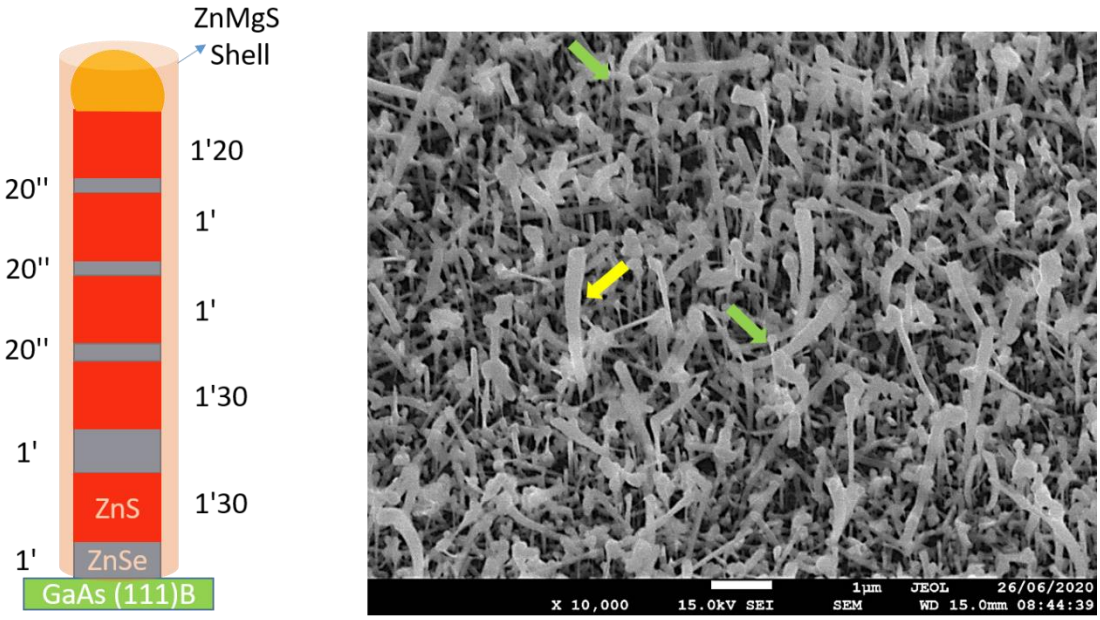

Figure 7.9: A 45 tilted SEM image of ZnS/ZnSe heterostructures covered with a ZnMgS shell ; the NW structure is represented with growth time scale

As a next step, we carried out additional SEM, TEM and EDS studies on this sample. To tell the story, two colleagues from GEMAC had the opportunity to visit JEOL facilities and test their equipments: i) JSM-7900F Schottky field emission SEM, equipped with a new Back Scattered Electron Detector (BSED) claimed reach extreme high-resolution imaging, and ii) JEM-F200 field emission transmission electron microscope.

Results from 7900F SEM analysis are gathered in Figure 7.10. The "nail-like" shape is clearly observed in image 7.10a. The core-shell structure is distinguished, and it is confirmed that ZnMgS shell is not uniform. Remarkably, different segments with a higher Z contrast are observed from Figure 7.10b and 7.10d. But the EDS mappings performed on the NW are indeed tricky. In figure 7.10c, Se distribution would tend to show two or three diffused ZnSe segments. Looking at Au mapping, it is obvious that there is a big discrepancy with the presence of a small Au-droplet on the top of the NW, as indicated by the yellow arrow. We should not find Au all along the NW has it is suggested. Hence the EDS mappings are not correct and do not reflect the real distribution, due to low signal/noise level. Coming back to the SEM image in figure 7.10b, the two brighter segments indicated by the red arrows, which might be attributed to ZnSe, appear ~30 and 50 nm long and are positioned within the 200 nanometers at the top of the NW. However, we stay careful on any conclusion.

Thankfully, more relevant results from JEM-F200 analysis focusing on another NW are presented in Figure 7.11. A STEM HAADF image of the NW is shown Figure 7.11a. The Z contrast reveals two bright segments in the NW. Going further, the EDS images identify these two sharp segments as ZnSe (purple Se mapping, Figure 7.11f). The sulfur mapping is consistent with remaining ZnS and ZnMgS parts of the NW. Again, the background signal or Au spreading on the NW sidewalls during or after the growth artificially suggests Au concentration in the whole NW, but here the signal/noise level is much higher, so that we can rely on these results. Noticeably, the last ZnSe segment is 130 nm long and is located 250 nm below the top of the NW, and the ZnS segment inserted between the two ZnSe can also be measured around 130 nm. This will help to build the stacking geometry, at least with relative segment lengths.

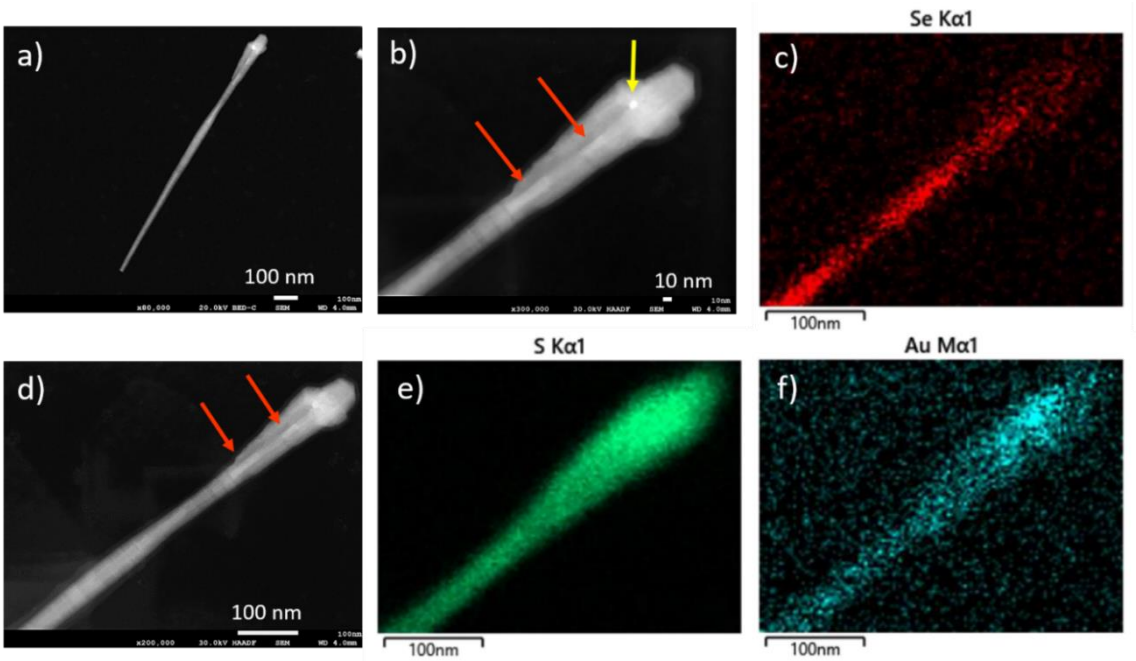

Figure 7.11: a-b-c) Backscattered (BSED) SEM image of a single (ZnS/ZnSe)ZnMgS heterostructure NW, two high contrast segments are highlighted by red arrows, Au-droplet by yellow arrow ; c-e-f) represent EDS mappings.

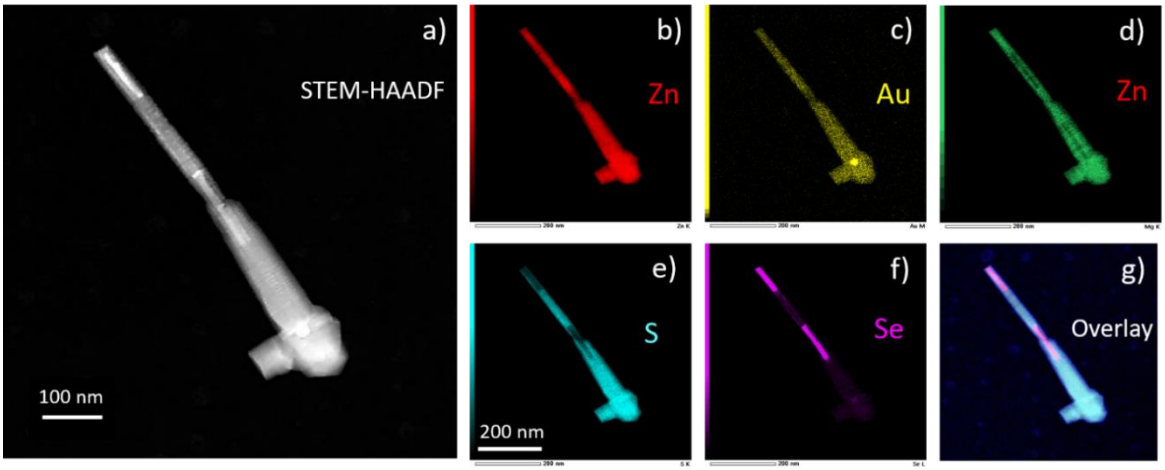

Figure 7.12: a) A STEM-HAADF image of the NW, b-c-d-e-f-g) EDS mappings

To sum up, we have a more detailed information on the grown heterostructure. ZnSe segments are clearly distinguished. However, these two NWs come from the same sample but the lengths and positions of the ZnSe segments seem different. This is not so surprising since heterostructures are not homogenous over the sample.

7.3.1.1 Cathodoluminescence and TEM

CL measurements were performed on several single NWs. The CL spectra of two NWs are shown in Figure 7.13. The emission at high energy is consistent with previous measurements, i.e., emission from the ZnMgS shell at 3.96 eV. We also observe strong emission peaks in the range 2.89 to 3.02 eV. There is no NBE emission from ZnS core, expected around 3.7 eV. However, as the heterostructure is grown in the VLS mode, we expect the ZnS crystal phase to

be 15R, and we previously observed that 15R does not bring a nice CL. The emission around 2.9 eV is too high in energy to be undoubtedly attributed to ZnSe, or it would come from a ZnSSe alloy. In the latter case, the mechanism would be hard to understand: strong diffusion at ZnS/ZnSe interface? Strong memory effect of the droplet?

Interestingly, CL allows monochromatic mapping, i.e., a cartography of the emission at a precise wavelength. Such mappings of the two NWs are presented in the lower part of Figure 7.13. To help imagine the heterostructure, a schematic of the geometry is tentatively built, including all segments with relative lengths. At 3.96 eV, we clearly observe an emission originating for the shell, with accumulation on the top (forming the head of the nail). Whereas, at 2.89 eV, we can see the luminescence emerging mostly at the bottom of the NWs. The length of the emitting parts is a few hundreds of nanometers, and these parts are located more than 1µm below the top of the heterostructure (indeed, the droplet is our landmark). Consequently, the emitting segments are not the short ZnSe segments that were identified by TEM and located in the ~ 500 nm long region just below the Au-droplet.

A further CL analysis is illustrated in Figure 7.14. For this third NW, in addition to the shell emission around 3.9 eV, we collect two signals at 2.88 and 3.05 eV. Interestingly, these two peaks correspond to two adjacent segments of the NW, as shown in the monochromatic images. Again, the schematic of the heterostructure is tentatively given and overlaid to the SEM image. Then we tried to fit the CL emissions with the heterostructure geometry. It appears that the emission at 3.05 eV could be attributed to a ZnS segment, and the one at 2.88 eV to a ZnSe segment. If this was right, we would still face the discrepancy between ZnSe bangap energy and collected CL at 2.88 eV. We believe quantum confinement is not enough. As a comparison, the emission of 10 nm thick quantum well in ZnSSe barriers was measured at 2.811 eV [260]. Hence, diffusion in ZnSe segment must be considered. One explanation could be related to S or Mg diffusion during the growth of the ZnMgS shell. Indeed, since the diameter of the core is ~20 nm, the required diffusion length would be only 10 nm. The energy shift around 80 -100 meV roughly corresponds to a ZnS_xSe_{1-x} alloy with 10% of sulfur.

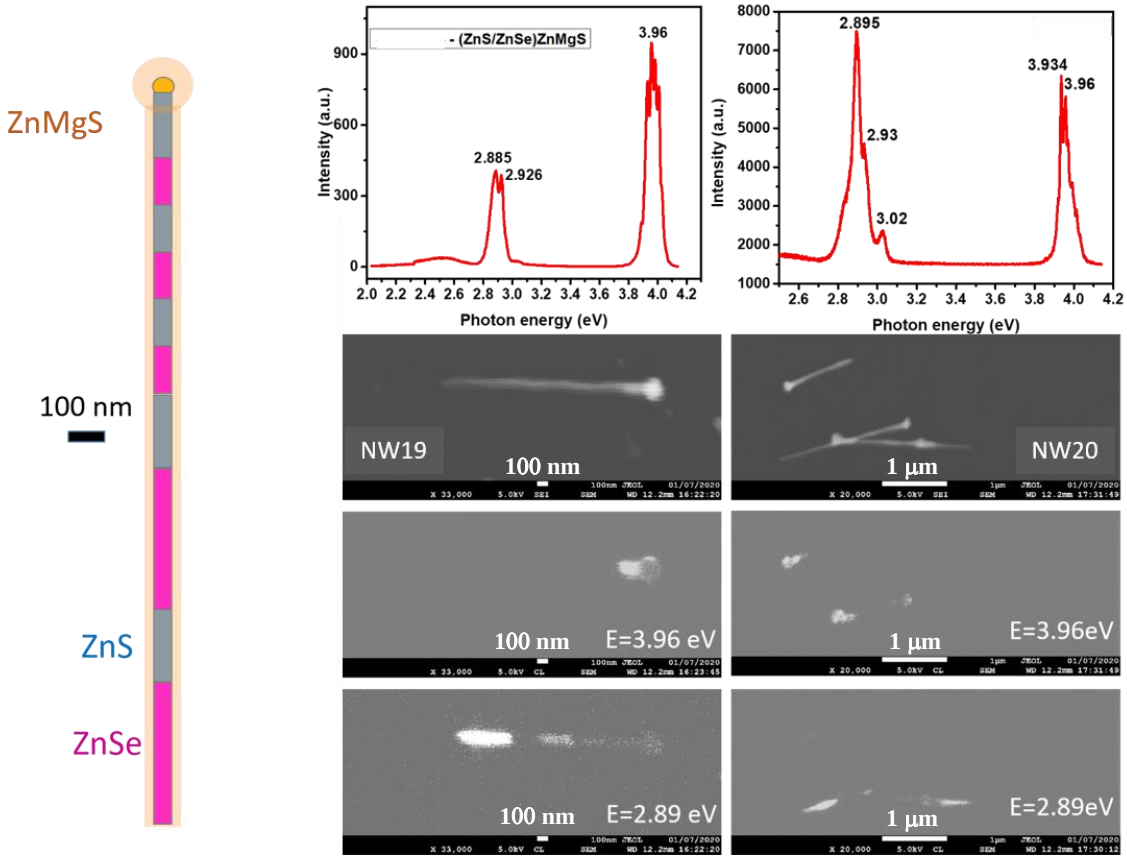

Figure 7.13: The CL spectrum of two ZnS/ZnSe heterostructure NWs covered with a shell. Below spectrum, monochromatic CL image of the NWs are shown for 3.96 and 2.89 eV.

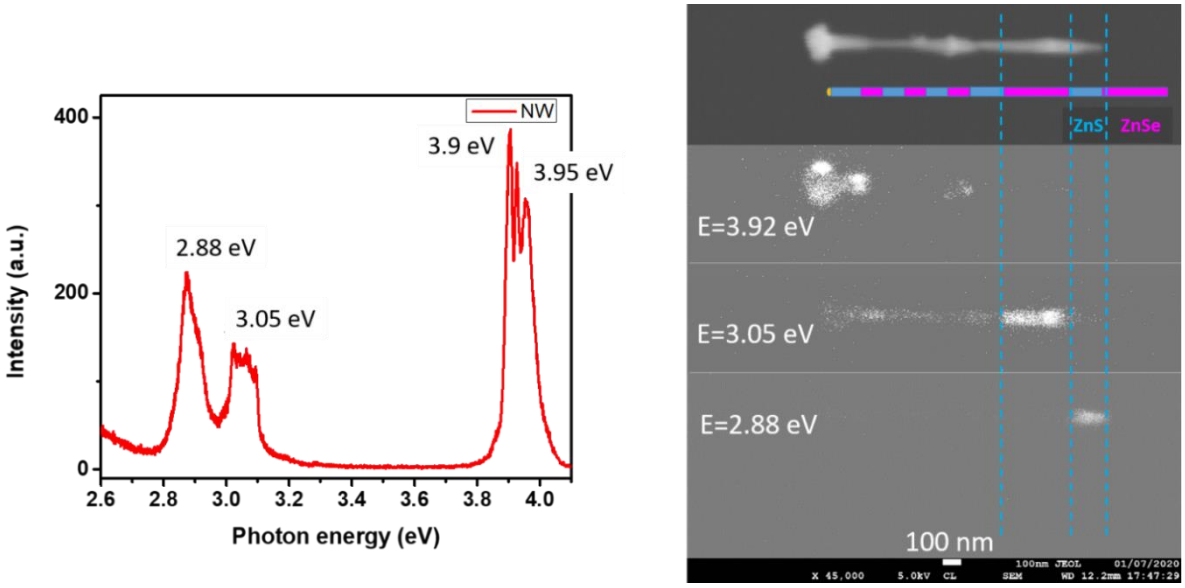

Figure 7.14: CL spectrum of a third NW (left) and monochromatic images taken at 2.88, 3.05 and 3.92 eV (right). The emitting segments are tentatively attributed.

7.3.2 Difficulties to grow axial ZnS/ZnSe heterostructures

In our experiments, we found difficulties controlling the ZnS/ZnSe heterostructures and even growth of ZnMgS shell. In Figure 7.13a-b, we show the initial stage of the ZnS and ZnSe NW growth on GaAs (111)B. In next step, we tried to grow axial heterostructures, i.e., ZnS on ZnSe, and ZnS on ZnSe, following the two stages in the same run. SEM images are presented in Figure 7.13 c-d. When we introduced the other materials for axial heterostructures growth, the NW lose its vertical alignment and frequent kinking was observed for many of the NWs.

We have observed the same difficulties while growing with VLS, VSS and Ga feeding experiments. However, growing axial and lateral heterostructures with VLS are better than the other two. In this work, I prepared heterostructures with several conditions but a deep study is required in the future to optimize the growth.

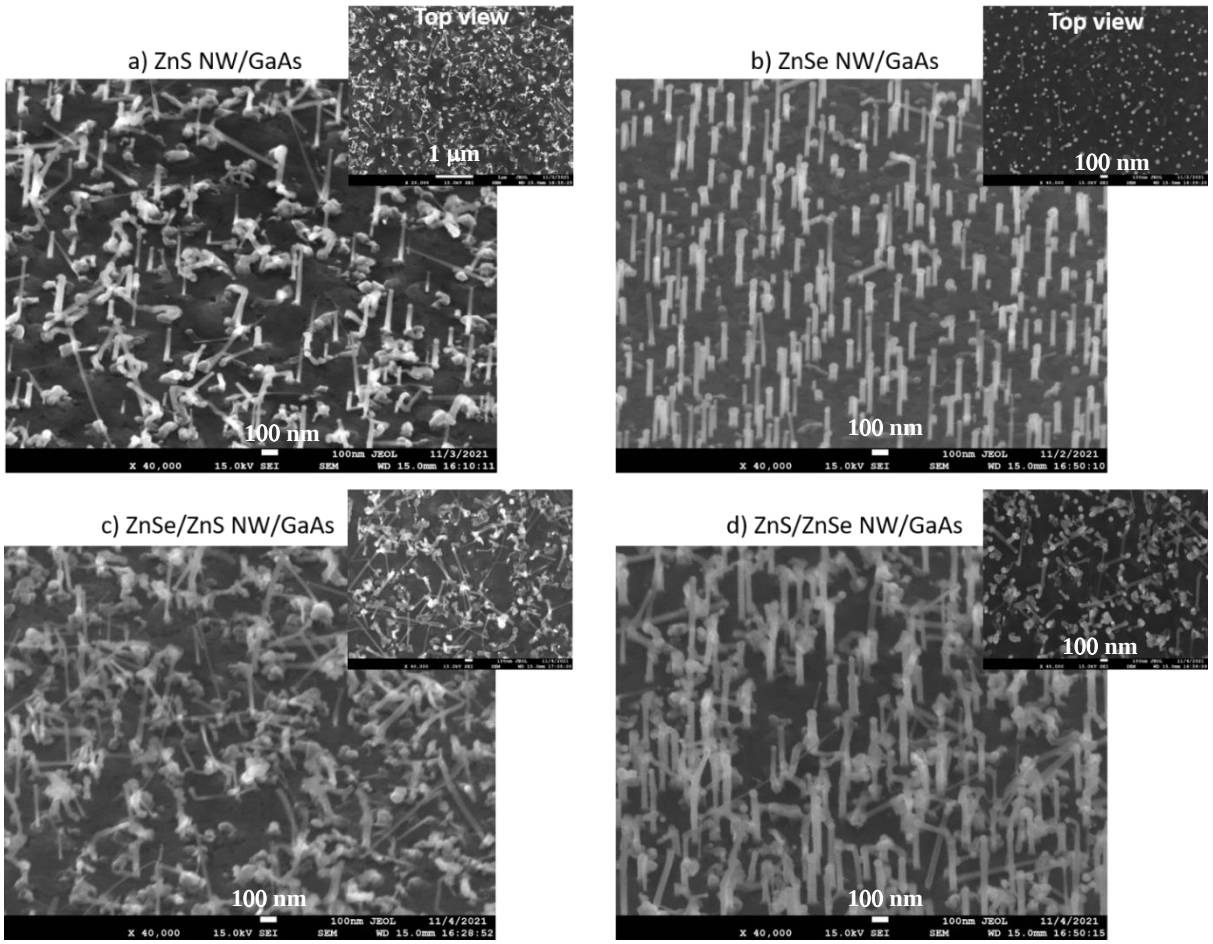

Figure 7.15: Top and 45°tilted SEM images of a) Initial growth phase of ZnS NW on GaAs (111)B, b) ZnSe NW, c) ZnSe axial growth on ZnS NWs shown in a), and d) ZnS axial growth on ZnSe NWs shown in b). The growth of heterostructures leads to the kinking when switched between two materials.

7.4 Conclusions

In this last chapter, photoluminescence and cathodoluminescence spectra of ZnS, ZnMgS and ZnSe thin films are first given as references. Then, the optical properties of several ZnS NWs have been investigated by CL in a SEM. VSS grown nanowires with pure wurzite phase appear to bring the best quality, with an excitonic transition at 3.735 eV. In a second part, we report

on the growth and CL investigation of (ZnS-ZnSe)/ZnMgS core/shell heterosturcture, where the core is made of distinct ZnS or ZnSe segments. CL spectra are collected, as well as monochromatic images of the emission. Results are not fully understood, however we emphasized distinct emission peaks corresponding to ZnSe or ZnS insertions, at 2.88 eV and 3.05 eV, without being sure on their exact attribution. What is certain is that a lot of insertion do not generate any light emission. Hence, at this point, it is difficult to give a definitive conclusion, however it is clear that more work is needed on such 1D ZnS-ZnSe heterostructures.

General conclusions and prospects

In this final section, we summarize the primary results of this thesis. The first goal of this thesis was to grow ZnS NWs with controlled morphology and orientation. In the light of ZnS polytypic behavior, we next aimed to achieve new crystal phases in ZnS NWs on providing a modification in growth mechanism. The achievement of new phases in ZnS could pave the way to novel physics and original applications. We faced several challenges in this work and sometimes get lucky too! We utilized both challenges and luck to drive science that helped us to discover some unexpected results and opportunity to have new ideas.

The first part of this work (Chapter 3) was experimental and devoted to a comprehensive study on the catalyzed growth of ZnS NWs using MOCVD. We began with fundamental growth research on ZnS thin films. This allowed us to developed temperature and VI/II ratio dependent MOCVD growth regimes. XRD and SEM techniques were used to investigate the structural and morphological properties, and a detailed study was undertaken to optimize the optimal growing conditions for the buffer layer. Following that, we dewetted Au on different surfaces and got optimized conditions: dewetting temperature of 500°C, duration 10 min, and Au thickness 1 nm to achieve a suitable distribution of Au nanoparticles, with average diameter ~25 nm on GaAs(111)B and ~13 nm on Zns/GaAs(111)B. Finally, we studied the formation of ZnS NWs and discovered that they emerge under re-evaporation conditions (550°C) and in sulfur-rich environments (S/Zn ratio of 2). GaAs (111)B substrates are confirmed to give the best arrays of NWs, in terms of verticality and uniformity, in agreement with the literature.

Then we followed the idea to provide a change in the growth mechanism via physical state of catalyst droplet (liquid or solid) and hence, study the induced polytypism in ZnS NWs (Chapter 4). To do so, we used two different Au-catalyzed growth approaches, namely VLS and VSS. In the VLS case, the growth of ZnS nanowires directly on GaAs (111)B was assisted by Au_2Ga alloyed droplets in the liquid state. On the other hand, the VSS growth involved a ZnS buffer layer to prevent Au–Ga interaction with the substrate and to enforce a pure solid Au catalyst. A comprehensive structural analysis was performed to study the different crystallographic phases in the NWs. The HRTEM images analysis of VLS grown samples undoubtedly identified a 15R crystal phase, which had never been observed in ZnS nanowires. We detailed such 15R sequence and proposed selection rules to illustrate its formation. Regarding the NWs grown on ZnS buffer (VSS mode, solid catalyst), an HRTEM study of straight wires revealed large segments of WZ with inclusion of small ZB segments. Figure C.1 illustrates the VLS and VSS mechanisms that lead to different crystal phase in ZnS NWs.

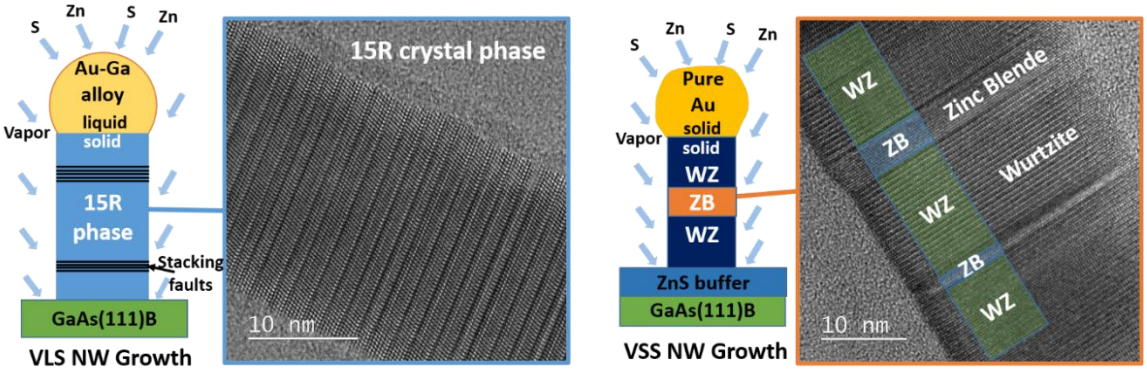

Figure C.1: The schematics of VLS and VSS NW growth mode with their corresponding HRTEM images. VLS growth mode favors a 15R crystal phase, where as pure WZ/ZB domains were observed for VSS.

To investigate the occurrence of 15R crystal phase in ZnS NWs, we explored theoretical aspects of polytypism occurrence (chapter 5). The phenomenon of polytypism in semiconductors have been studied using axial-next nearest neighbor Ising (ANNNI model). We started with the calculations of Johansson performed in the framework of classical nucleation theory and ANNNI model [214]. This model was developed for a limited number of high order polytypes (HOP), specifically four, and did not include additional feasible polytypes such as 15R, which was observed in our ZnS nanowires. As a result, we took the opportunity to introduce the 15R polytype and perform the calculations. This model accurately predicts the occurrence of 15R within a small window of supersaturation. However, due to the basic assumptions made about the nucleus step energy, it prevented us from going more into the details of the NW growth dynamics. As a result, we extended this growth model by introducing more precise effective edge energy equations from Glas et al. [11] into the computations. This extended model considers a triangular nucleus, and allows to detail key parameters on which polytype probabilities show a strong dependence, namely the ratio of WZ/ZB effective edge energies (R), and the interface energy. We found two possible ZB faceted nucleus geometries termed as (111)A and (111)B. Noticeably, due to different surface energies of these facets, the effective edge energies are different and so does the ratio (R), leading to either an opening or a narrowing of the HOP window, as illustrated in Figure C.2. We examined the effect of two additional parameters on the effective edge energy values: droplet contact angle and liquid-vapor surface energy. The contact angle analysis reveals some intriguing facts about GaAs nanowires. Our model accurately predicts the crystal phase transition from ZB to WZ at small contact angles and from WZ to ZB at large contact angles, which is consistent with in-situ TEM measurements on self-catalyzed GaAs NWs. Following that, we explored the effect of liquid-vapor (LV) energy and indicated how it could be a substantial factor in opening the HOP window when R is near 1.

Coming back to the 15R crystal phase, we applied our extended model to the case of ZnS NWs. A strong dependence has been observed on decreasing the first interaction parameter J_1. The J_1 parameter i.e., stacking fault energy is very small for ZnS 6 mJ/m^2 compared to GaAs 45 mJ/m^2 that means it is much easier to create a stacking fault in ZnS than GaAs. The 2H stacking can be considered as a stacking fault. To begin, we reconsidered the low surface energy of {10-10} WZ plane given in the literature, that precludes any other phase than 2H. Indeed, easy nucleation of WZ stacking is predicted in ZnS by our calculations. We further discussed the formation of 15R in ZnS NWs and suggested the favorable conditions for its occurrence. 15R occurrence is highly favorable in ZnS if we consider a higher value of {10-10} surface energy around 0.81 J/m^2. For this value, the ratio R is close to 1, the corresponding plot is shown in Figure C.3 for ZnS NW. In the wide HOP window, crystallization of 15R phase is most likely.

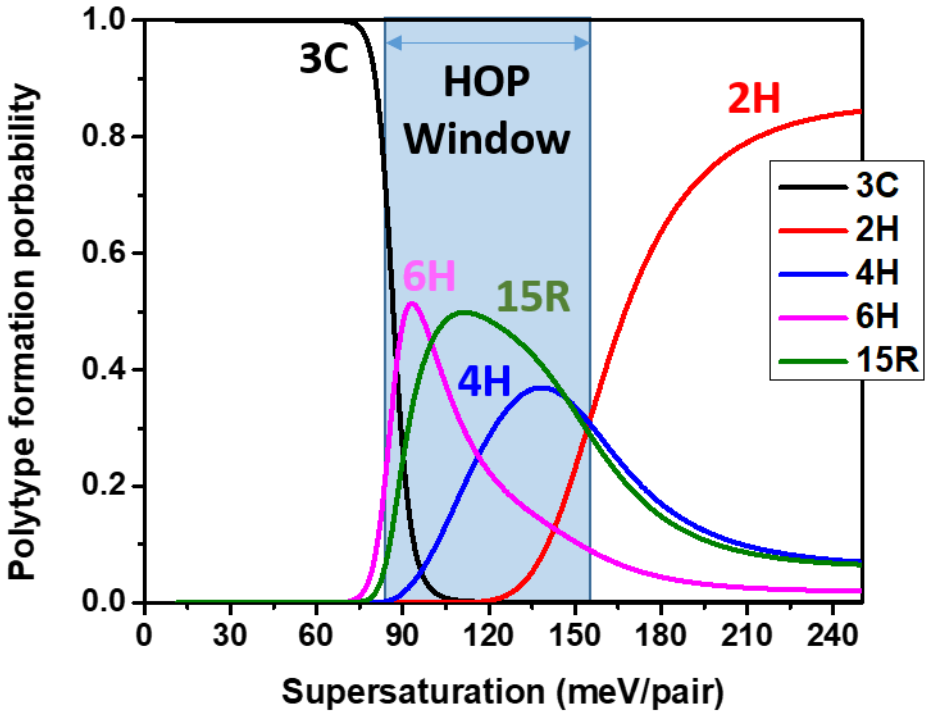

Figure C.2: The plot of polytype formation energy of five polytypes as a function of supersaturation for ZnS NWs. Here we consider a high surface energy of {10-10} facet to favor 15R, observed experimentally in our VLS grown NWs.

We designed new experiments to validate our theoretical findings (chapter 6). The supersaturation is predicted to be critical for the crystal phase selection in NWs. Hence, we performed experiments to control the supersaturation via the variation of the NW growth flux i.e., playing with the incoming Zn and S fluxes. The effect of supersaturation variation on crystal phase is illustrated in Figure C.3. At low growth flux, large 15R segments with small inclusions of 3C/stacking faults were observed. This result suggests a 3C/HOP favored supersaturation range. For intermediate growth flux, a 15R structure with increased stacking faults was observed and detailed in Chapter 4. For this case, HOP/2H supersaturation range is predicted. Regarding high growth flux, it confirms a pure 2H phase is induced by going toward high supersaturations, as predicted by the model.

Likewise, a graphical summary of NW growth with different droplet composition, from pure Au to Ga-rich Au-Ga, is illustrated in Figure C.4. We presented in chapter 4 structural results of VSS grown NW assisted by a pure Au droplet. It shows 3C inclusions in dominant WZ crystal phase (fig. C.4a). It suggests that the HOP window is narrow and a quick transition takes place from 3C to 2H. Our theoretical model for ZnS agrees with that, as it predict a decrease in the *R* value for pure Au droplet (γ_{LV} = 1.14 J/m^2, explained in appendix). For NW grown with Au_2-Ga alloy (Au-rich), we have observed a 15R crystal phase (fig. C.4b). This time, the *R* value increases (near 1) with Ga diffusion inside the Au droplet that decreases the LV surface energies (γ_{LV} = 1 J/m^2 for Au_2Ga). Regarding Ga rich droplet (99% Ga, "Ga-fed" droplet), a 3C phase with twinning superlattice was observed (fig.C.4c), using low growth flux. For such conditions, we decreased supersaturation and γ_{LV} (0.72 J/m^2), and that might have helped to reach *R* value very close or above 1. In that case, 3C/15R could be the possible range of supersaturation. Remarkably, we have found highlights of 15R/stacking faults in our ZB twinning superlattices.

Therefore, our model reasonably supports all the experimental crystal phase observations for the VLS growth mode of ZnS NWs. However, the NWs grown with VSS growth mode at a lower growth flux still exhibits a pure WZ phase (detailed in appendix), and so, do not follow the model predicting 3C. This might be due to the effect of diameter, as we have observed a diameter less than 10 nm for such NWs. Our extended model does not consider the effect of diameter currently. In the future studies, we could consider introducing other growth parameters in our model.

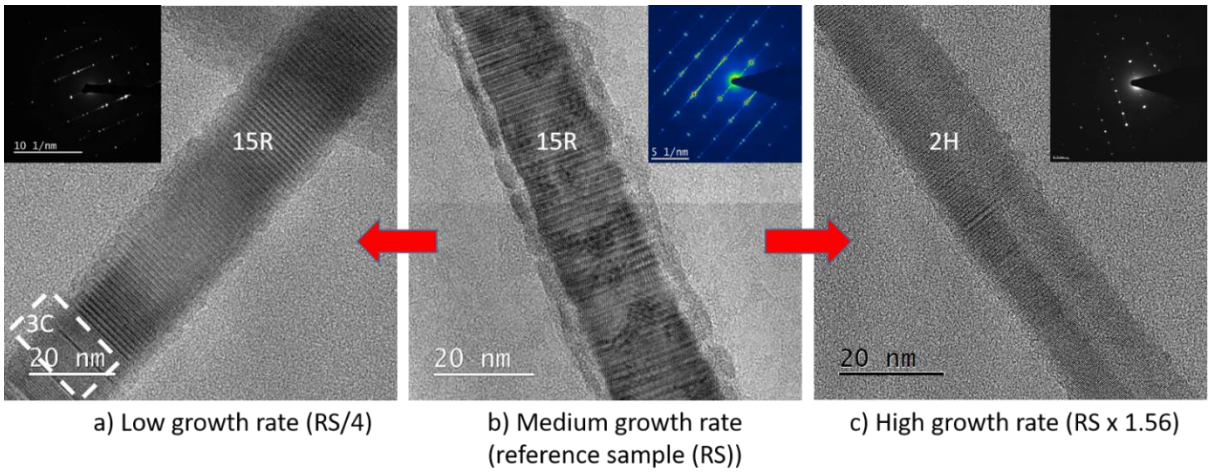

Figure C.3: The HRTEM images of NW segments grown at different growth fluxes, a) low growth flux, with 15R/3C phase, b) medium growth flux, with 15R/stacking faults, and c) high growth flux, with pure WZ phase.

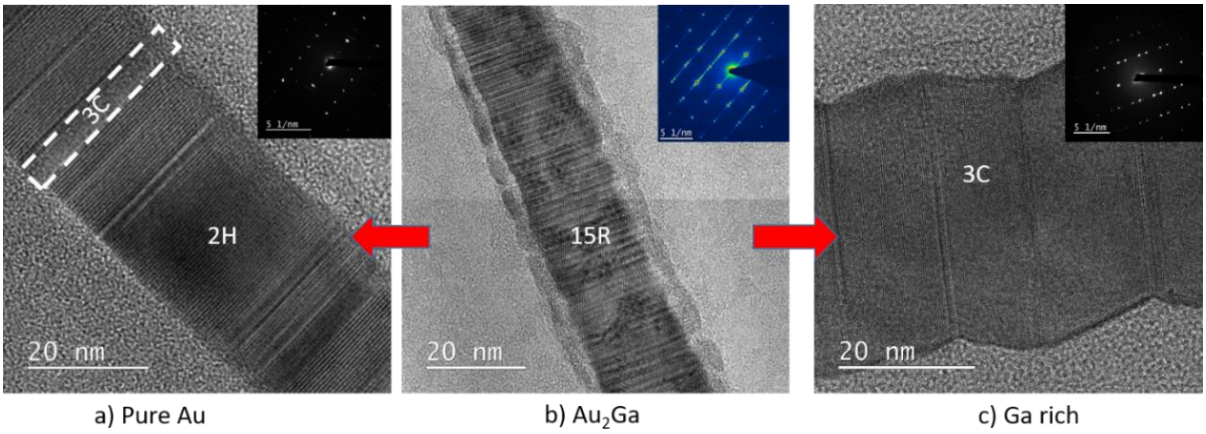

Figure C.4: The HRTEM images of NW segments grown with different droplet catalyst, a) pure Au, with 2H/3C phase, b) Au_2Ga (Au-rich), with 15R/stacking faults, and c) Ga rich, with twinned ZB phase.

Last but not the least, we have studied optical properties of thin films and NWs. The photoluminescence (PL) and cathodoluminescence (CL) spectra of ZnS, ZnSe, and ZnMgS thin films were discussed. Then, using CL in a SEM, the optical characteristics of different ZnS NWs were studied. VSS grown NWs with pure WZ phase appear to be the highest quality. Finally, the growth and CL study of (ZnS-ZnSe)/ZnMgS core/shell heterostructures with different ZnS or ZnSe segments was performed. CL spectra and monochromatic images of the emission were collected. Although the results were not completely understood, we highlighted unique emission peaks that, we believe, are related to ZnSe or ZnS insertions. What is certain is that a large number of insertions do not produce any emission. As a result, it is difficult to draw a firm conclusion of such preliminary work.

Future prospects

We divide the prospects in four categories: growth, structural aspects, theoretical modeling, heterostructures, and optical measurements.

1. *Growth of ZnS NWs*

   Vertically aligned ZnS NWs were achieved in this thesis by the use of VLS and VSS growth modes. However, we aim to exert exact control over the density of NWs, and in particular reach low densities. We noticed that the growth flux of NWs had an effect on their density and form. Such an impact can be investigated in detail in order to optimize the geometry of ZnS NWs for a particular application. By employing a physical mask and depositing smaller droplets (gold thickness below 0.1 nm), we may succeed in reducing the density of NWs.

2. *Structural aspects*

   We have explored various possibilities to control the crystal properties of ZnS NWs. We have successfully studied polytypic behavior and discover new phases in ZnS. But in particular, twinning superlattice (TSL) could be investigated further. Moreover, in-situ TEM observations of high order polytypes such as15R crystal phase in ZnS as well as in GaAs could open new or answer previous questions on NW fundamentals.

3. *Theoretical modeling*

   Our proposed theoretical model could be developed more by including further parameters such as role of diameter of NW. From ANNNI model point of view, it can be applied to the edge energy interactions (in this work it was applied to interface energy)

4. *Heterostructures based on II-VI semiconductors*

   In this work, we have already employed different methods to prepare heterostructures. We have tried VLS, VSS and Ga feeding methods for ZnS/ZnSe axial heterostructures. But none has been completely successful, and the control over morphology, precise insertion of segments needs to be achieved for potential application. Moreover, ZnMgS passivation shell plays a crucial role, thus, a control over its homogenous growth is essential.

5. *Optical properties*

   In the last chapter, we have seen interesting optical results from ZnS NWs. More optical experiments and a deep analytical study is required to understand the emission behavior and possible quantum confinement. In addition, CL experiment in a TEM would be quite interesting to investigate the optical properties of this original 15R polytype in ZnS, and compare with ZB and WZ phases.

APPENDIX

A.1 Theoretical modeling results

A.1.1 The role of contact angle: ZnS

Similar to GaAs, the role of contact angle has been studied for ZnS. We have considered R = 0.97, as it supports the 15R occurrence in ZnS nanowires. The plots are illustrated in Figure A.1.

The effective edge energy plot as a function of contact angle suggests that ZB, 111B is highly unlikely to occur having a large value of Γ. At low contact angle (60-100°), the ratio with 111A is higher than 1 suggesting 3C dominant structure. The value of R, decreases with increasing in the contact angle (pink curve). It implies that, if contact angle increase from a very low to high value, the crystal phase switches between polytypes, beginning with 3C at very low contact angle to 2H at high contact angle (above 125°). At intermediate contact angles (100-125°), we get the high probability of high order polytypes as the HOP window is wide. Indeed, we have found the similar contact angle range in our experiments for the 15R crystal phase NWs [67].

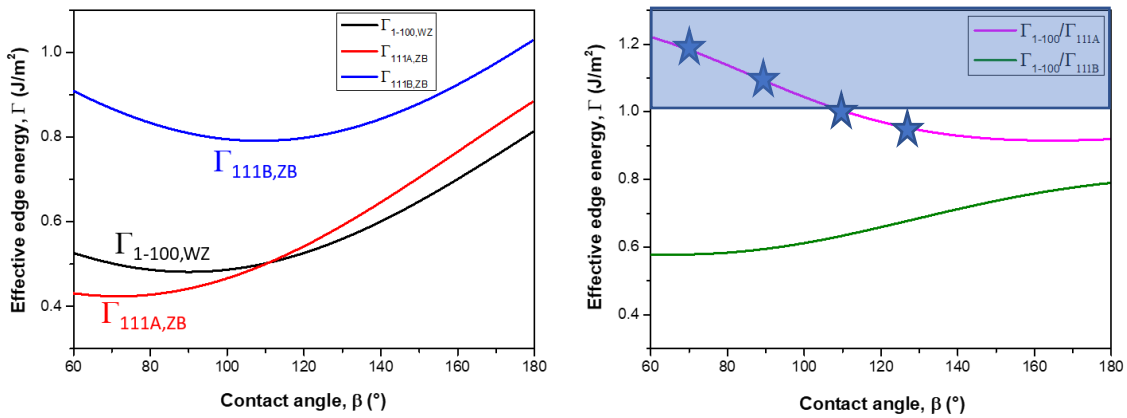

Figure A.1: The effective edge energy of the zinc blende and wurtzite planes are plotted as a function of contact angle. (left) and its dependence on the Ratio (R) (right).

A.1.2 The role of γ_{LV} (composition of the droplet): ZnS

In Figure A.2, the liquid-vapor surface energy doesn't show a large effect on the effective edge energy of ZB and WZ planes, especially when we see the effect on the ZB/WZ ratio. However, it is worth mentioning again that, a small change in the ratio (R) near the value 1 can significantly impact the result.

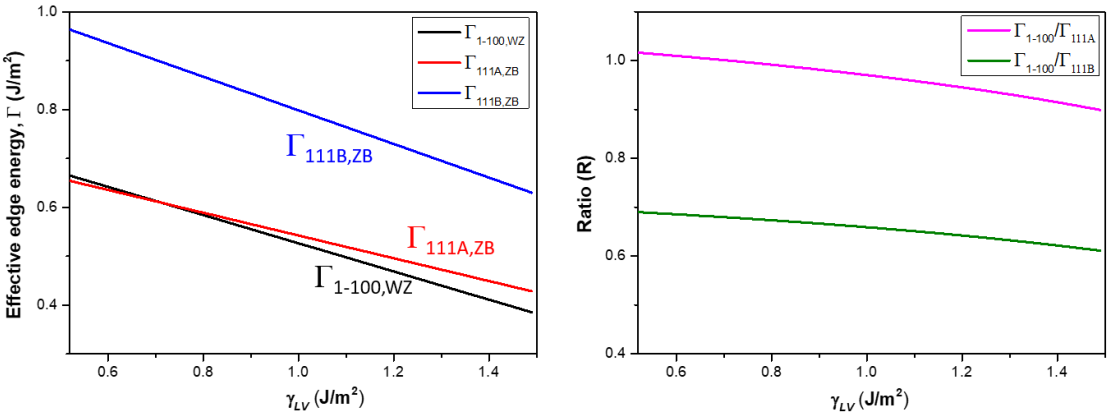

Figure A.2: The effective edge energy of the zinc blende and wurtzite planes are plotted as a function of γ_{LV} (left) and its dependence on the Ratio (R) (right).

A.1.3 Rhombus nucleus

In this appendix, we aim to compare different possible nucleus; semicircular, triangular, and rhombus. The nucleus geometry has always been a topic of argument and many groups have proposed different geometries [148,160,162,163]. Due to inability of in-situ TEM experiments to capture the birth of nuclei, the nucleus geometry remains a mystery. Meanwhile, here, we offer a nucleus geometry comparison based on our model and results reported in the literature. Interestingly, we found different results for different geometries. We started chapter 5 with the semicircular nucleus. But, recent in-situ studies reported a faceted asymmetrical rhombus geometry of the smallest nucleus they have observed [148]. Thus, spherical geometry is not expected. We used triangular nucleus for our extended model calculations (such as Glas calculations). Remarkably, this triangular nucleus geometry works perfectly with our model. The studied behavior of NW growth parameters makes good agreement with the literature. As a next step, we considered the rhombus geometry of the nucleus and performed similar calculations. The rhombus nucleus is symmetrical with two side facets in contact with vapor and two inside the liquid, as shown in Figure A.3. The rhombus averages the discrepancy created by ZB {111}A and {111}B facets unlike triangular, where this difference was significant for effective edge energy. Thus, we have only one possibility of the rhombus-ZB nucleus.

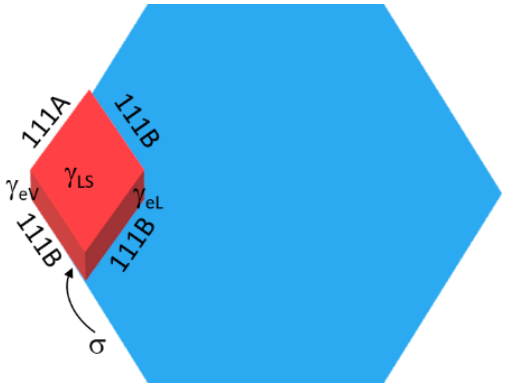

Figure A.3: ZB nucleus with two side facets (111A and 111B) in contact with vapor and the other two inside the liquid. The nucleus is symmetrical.

For rhombus geometry, equation (5.13) can be expressed as for ZB (Γc) and WZ (Γ_h):

$$\Gamma_c = \left(\frac{1}{4}\right)\left(\gamma_{eL,111A} + \gamma_{eL,111B}\right) + \frac{1}{4}\left(\left(\bar{\gamma}_{eV,111A} + \bar{\gamma}_{eV,111B}\right) - 2\gamma_{LV}\sin\beta\right) \quad \text{(A.1a)}$$

$$\Gamma_h = \left(\frac{1}{2}\right)\left(\gamma_{eL,h} + \gamma_{eV,h} - \gamma_{LV}\sin\beta\right) \quad \text{(A.1b)}$$

The polytype formation probability is plotted for GaAs calculated for a rhombus nucleus, as shown in Figure A.4. The calculated *R* value is 0.774 in this case. This plot is similar to the case of triangular nucleus with ZB-(111)A (Figure 5.9). The HOP window is narrow and 2H is highly probable at supersaturation, $\Delta\mu$ > 50 meV/pair. Unlike triangular (111)B (*R* = 0.97), we have no possibility to increase the *R* value in the case of rhombus.

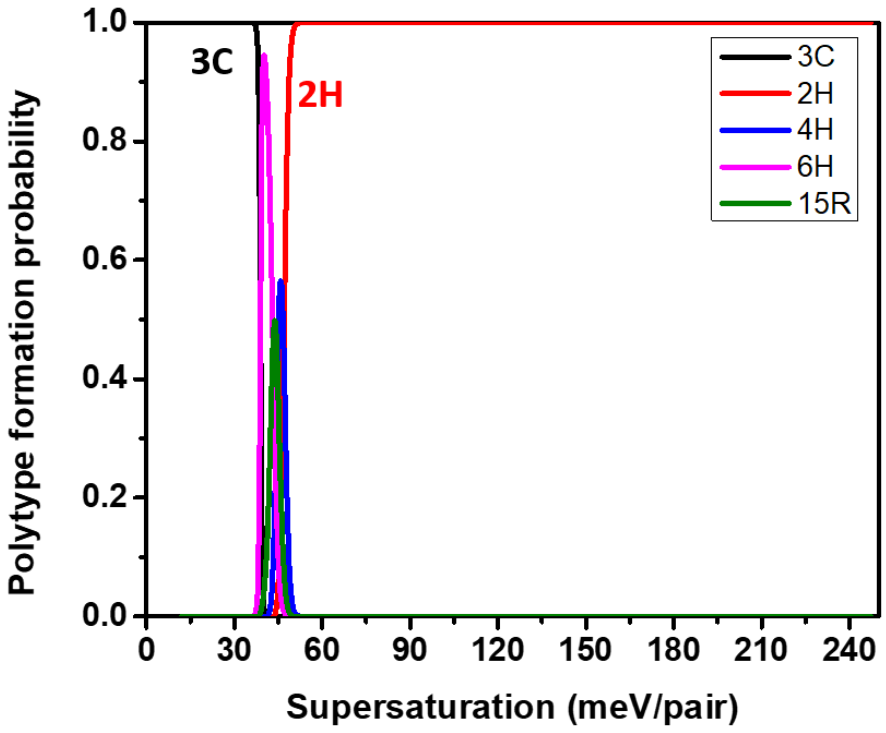

Figure A.4: The polytype formation probability plot for a rhombus geometry of nucleus. The curve is plotted for the case of GaAs.

It implies that considering rhombus results in a quick transition from 3C to 2H with an increase in supersaturation for GaAs NWs. Hence, the occurrence of HOP is not anticipated for GaAs NWs. We now focus on the effect of contact angle for rhombus nucleus. The effective edge energy for ZB (Γ_c) and WZ (Γ_h) is plotted as a function of contact angle, illustrated in Figure A.5a. The WZ effective edge energy always stays lower than ZB. In Figure A.5b, their ratio (*R*) dependence on contact angle is plotted. In the full range 60-180°, *R* never reaches a value higher than 0.9 and stays below the blue region marking the "HOP/3C favored" window. Thus, the rhombus nucleus fails to explain the opening of the HOP window, and the occurrence of new polytypes such as 4H, 6H and 15R. We support the idea of a probable triangular nucleus,

nucleating from a corner of hexagon at TPL. This triangular nucleus then spread out and form the rhombus asymmetrical facets observed in the in-situ experiments [148].

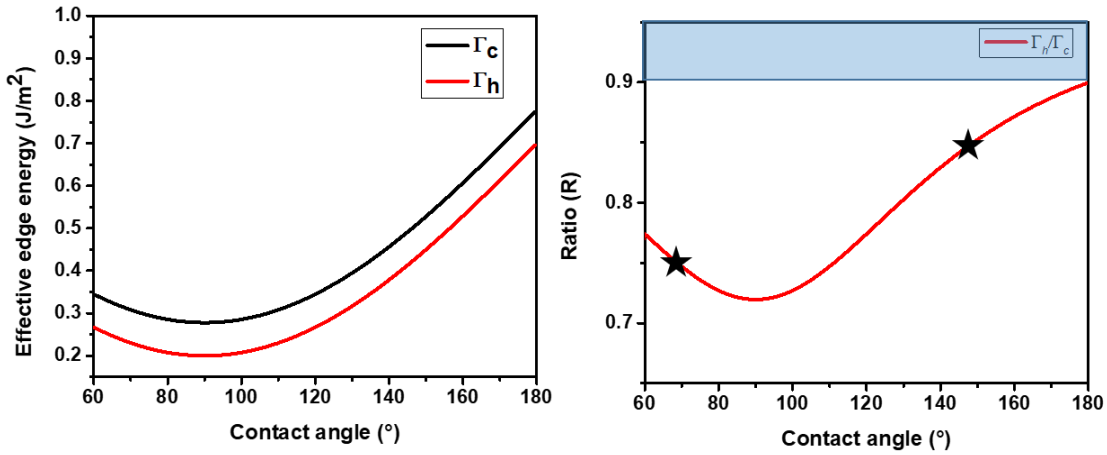

Figure A.5: The effective edge energy for ZB and WZ is plotted as a function of contact angle and b) their ratio dependence on contact angle. In whole range of contact angle, *R* value remains < 0.85 to favor a pure ZB or a high order polytype for GaAs.

A.2 Pure wurtzite phase in VSS NWs imposing high growth flux

We tried to apply the idea (increase growth flux to achieve pure WZ structure) for the growth of VSS NWs. However, expecting an increase in the supersaturation for VSS by increasing the growth flux might be a tedious assumption because we are not sure if the growing species diffuse through the whole body of the catalyst droplet, or diffuse on the droplet surface to reach pseudo TPL, and further diffuse at the NW-droplet interface. In the latter case, supersaturation in the droplet does not exist.

For high growth flux VSS, we lose the vertical aligned NWs, as shown in Figure A.6. We did not perform any TEM measurements on these NWs. For the reference VSS sample (let's say normal "growth flux ") we had observed large segments of WZ phase with frequent inclusions of small ZB segments. So that we don't know whether increasing supersaturation changed the crystalline properties of the NWs, e.g., suppressing the cubic segments and hence achieving pure hexagonal NWs.

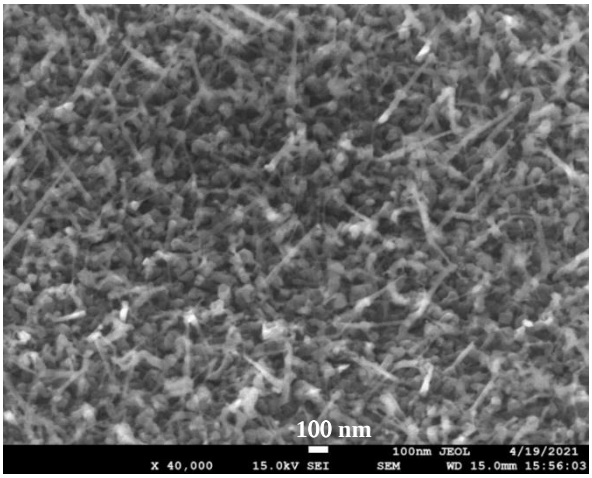

Figure A.6: VSS ZnS NW grown with a high growth flux. The NWs lose their homogeneity and vertical growth.

A.2.1 Attempt to get zinc blende phase in VSS NWs imposing low growth flux

In this experiment, we grow VSS assisted ZnS NWs with a low growth flux. Normally, doing so, one should expect (at least) an increase in the size or frequency of ZB segments. Therefore, to compare to the reference sample, we reduced the growth flux by a factor of four.

From SEM images of these samples, we have already observed a reduction in the diameter as well as a significant downfall in the density of NWs (Figure A.7). The bright field TEM image of single NWs taken in <010> zone axis is shown in Figure A.8a. A lot of NWs are indeed thin and cylindrical with constant diameter, such as the one indicated by the arrow. We measured the diameter of these NW around 10 nm or less. A few other NWs appear more tapered, or totally unsymmetrical and/or kinked. We focused our structural analysis on the long straight NWs. In Figure A.8b, the HRTEM image shows the catalyst droplet present at the top, which is clearly faceted. The ZnS crystal structure is pure WZ just below the droplet. We performed the HRTEM analysis for a large segment of NW. To our surprise, the NW adapted a pure WZ structure without any insertion ZB phase or even stacking faults. The FFT of the HRTEM image shows evidence of a pure WZ phase, in Figure A.8d.

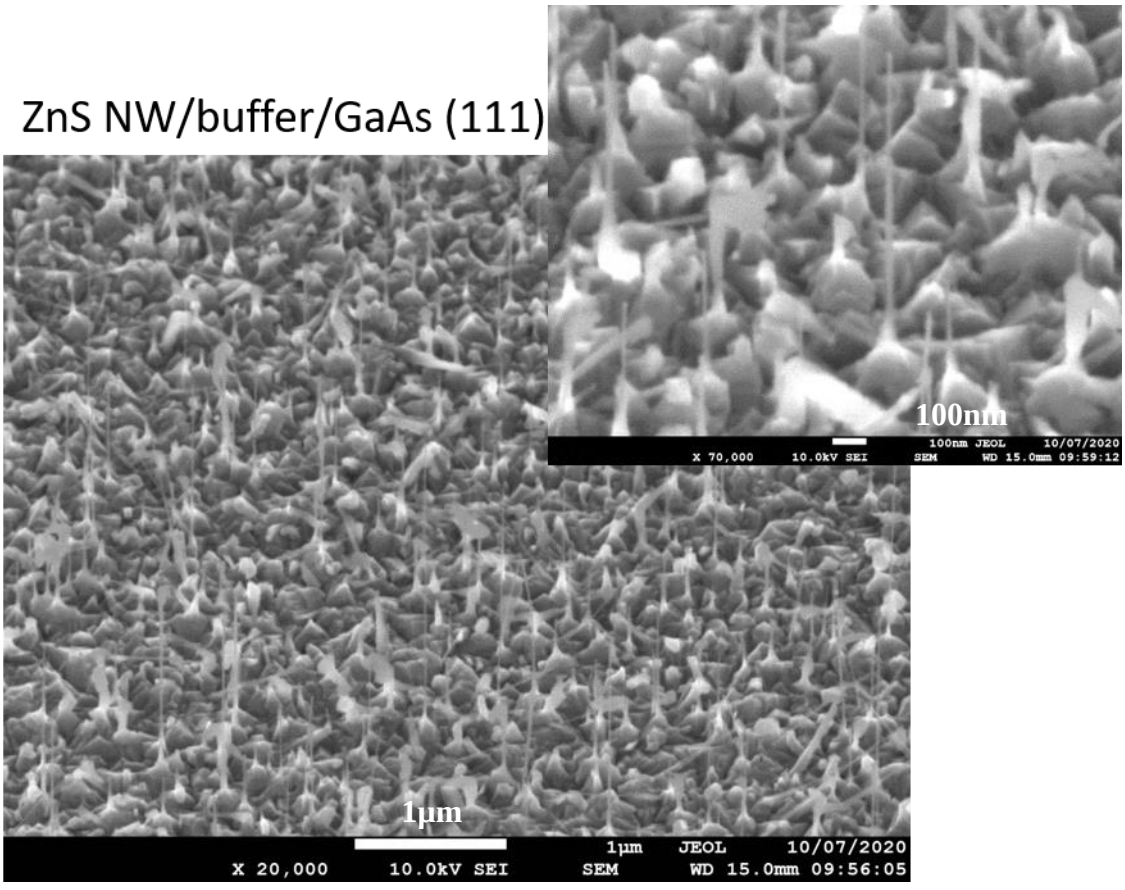

Figure A.7: ZnS NWs grown with VSS mode at low growth flux. The NWs are thin and straight with a pyramid at the base.

As we discussed before, we were expecting more inclusions of ZB in the crystal phase when the NW is grown at low growth flux, but instead the NW prefers to adopt a pure WZ structure. We have no clear explanation for that. The significant decrease in the NW diameter could be one possible reason behind this observation as well as the argument on the supersaturation in the case of VSS might be another reason.

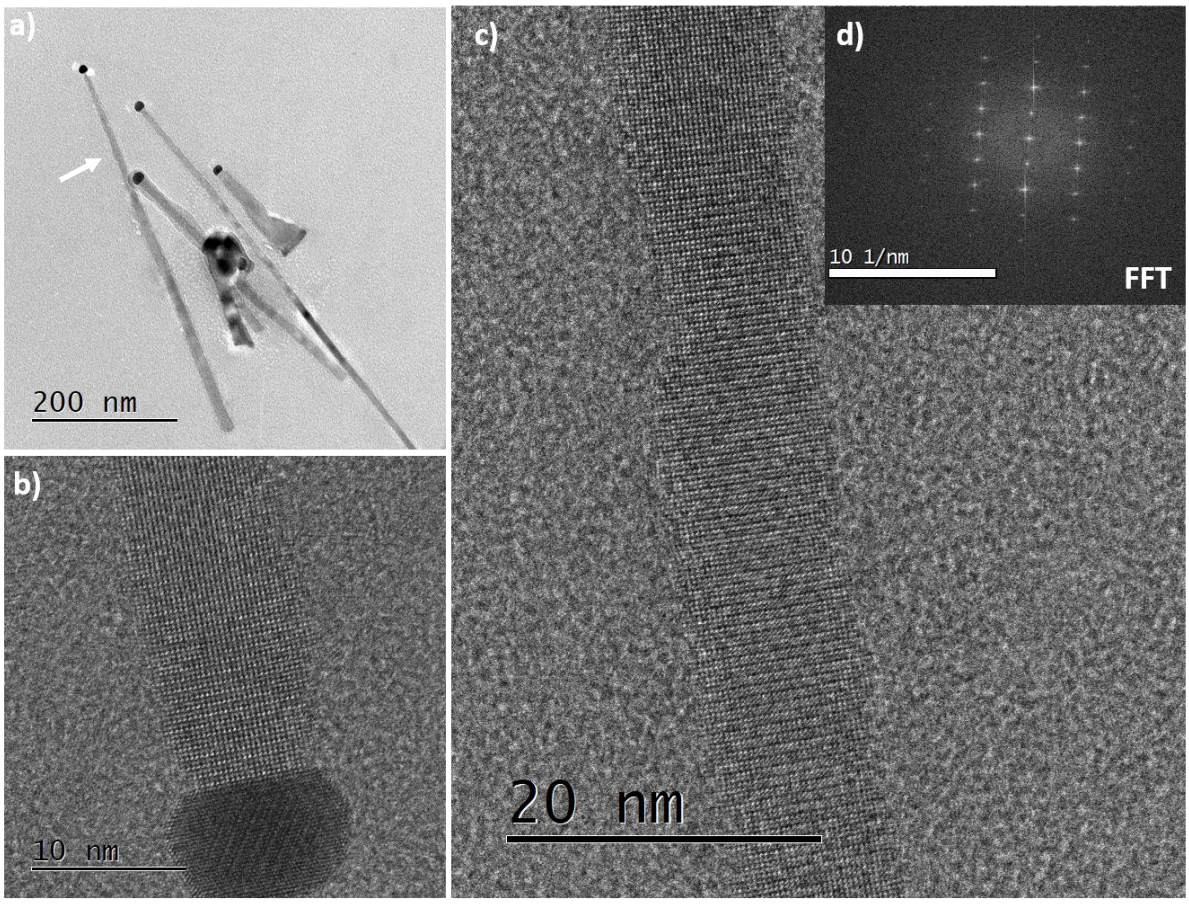

Figure A.8: a) A bright field TEM image of the single NWs, b) An HRTEM image focused on the top of the NW, the droplet is clearly faceted and the NW adapt a pure WZ phase, c) An HRTEM image focusing on a larger section of NW revealing pure WZ structure, d) the FFT pattern of HRTEM image shows a WZ crystal phase diffraction pattern.

Résumé substantiel en français

L'objectif premier de cette thèse était de faire croître des nanofils (NFs) du semiconducteur ZnS avec une morphologie et une orientation contrôlée. A la lumière du comportement "polytypique" du ZnS, nous avons ensuite cherché à obtenir de nouvelles phases cristallines (les polytypes) dans ces NFs de ZnS, cela en modifiant le mécanisme de croissance. L'obtention de nouvelles phases dans le ZnS pourrait ouvrir la voie à une nouvelle physique et à des applications originales. Nous avons relevé plusieurs défis dans ce travail et avons même parfois eu de la chance, ce qui nous a permis de découvrir des résultats inattendus et de développer de nouvelles idées.

Dans ce manuscrit, le chapitre 1 a pour but d'introduire le lecteur au contexte, aux concepts de base et aux principes fondamentaux nécessaires à la compréhension des résultats issus de la thèse. Nous détaillons les propriétés des nanofils semiconducteurs, le phénomène de polytypisme, et les mécanismes de croissance de ces nanofils. Dans la deuxième partie, nous nous concentrons sur l'état de l'art des NFs II-VI avec une attention particulière accordée au matériau ZnS, à ses phases cristallines, et aux études TEM in-situ. A la suite de cette introduction, le chapitre 2 donne un aperçu des aspects théoriques et des techniques expérimentales utilisées dans cette thèse. La première partie est consacrée à un résumé de la théorie de la nucléation et du modèle ANNNI. Dans la deuxième partie, nous nous concentrons sur la description de la croissance MOCVD (dépôt en phase vapeur par décomposition d'organométalliques) et les principales techniques de caractérisation.

Une part importante de ce travail était expérimentale et consacrée à une étude complète de la croissance catalysée des NFs de ZnS par MOCVD (chapitre 3). Nous avons commencé par une recherche fondamentale sur la croissance des films minces de ZnS. Ceci nous a permis d'identifier les régimes de croissance MOCVD dépendant de la température et du rapport VI/II des précurseurs injectés en phase gazeuse. Les techniques de diffraction de rayons X (DRX) et de microscopie électronique à balayage (MEB) ont été utilisées pour étudier les propriétés structurales et morphologiques, et une étude détaillée a été entreprise pour optimiser les conditions optimales de croissance de la couche tampon ZnS. Ensuite, nous avons démouillé un fim d'or sur différentes surfaces et obtenu des conditions optimales (à savoir : température de 500°C, durée de 10 min, et épaisseur de l'Au de 1 nm) pour obtenir une distribution appropriée de nanoparticules d'Au avec un diamètre moyen de ~25 nm sur GaAs(111)B et ~13 nm sur ZnS/GaAs(111)B. Enfin, nous avons étudié la formation des NFs de ZnS et découvert qu'ils émergent dans des conditions de ré-évaporation (550°C) et dans des environnements riches en soufre (rapport S/Zn de 2). Les substrats GaAs (111)B sont confirmés comme donnant les meilleurs réseaux de NFs, en termes de verticalité et d'uniformité, en accord avec la littérature.

Nous avons ensuite suivi l'idée d'apporter un changement dans le mécanisme de croissance via l'état physique de la gouttelette de catalyseur (liquide ou solide) et donc d'étudier le polytypisme induit dans les NWs de ZnS (Chapitre 4). Pour ce faire, nous avons utilisé deux approches différentes de croissance catalysée par Au, à savoir VLS (vapeur-liquide-solide) et VSS (vapeur-solide-solide). Dans le cas de la VLS, la croissance des nanofils de ZnS directement sur GaAs (111)B a été assistée par des gouttelettes alliées Au_2Ga à l'état liquide. D'un autre côté, la croissance VSS impliquait une couche tampon de ZnS pour empêcher l'interaction Au-Ga avec le substrat et conserver un catalyseur Au solide pur. Une analyse structurale complète a été réalisée pour étudier les différentes phases cristallographiques dans les NFs. L'analyse des images de microscopie électronique en transmission haute résolution (HRTEM) des échantillons obtenus par VLS a permis d'identifier une phase cristalline 15R,

qui n'avait jamais été observée dans les nanofils de ZnS. Nous avons détaillé cette séquence 15R et proposé des règles de sélection pour illustrer sa formation. En ce qui concerne les NFs élaborés sur le tampon ZnS (mode VSS, catalyseur solide), une étude HRTEM des fils droits a révélé de longs segments de phase wurzite (WZ, 2H, hexagonal) avec inclusion de petits segments de phase blende de zinc (ZB, 3C, cubique). La figure C.1 illustre les mécanismes VLS et VSS qui conduisent à différentes phases cristallines dans les NFs de ZnS.

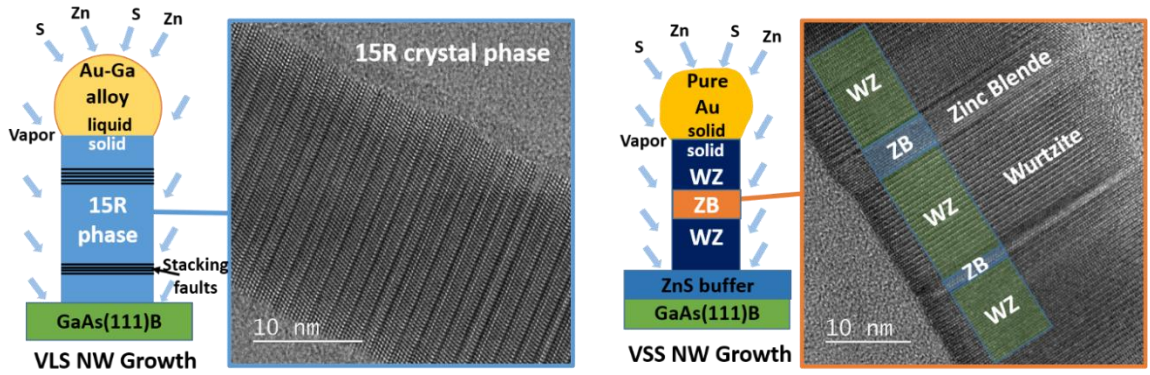

Figure C.1 : Schémas des modes de croissance VLS et VSS NW avec leurs images HRTEM correspondantes. Le mode de croissance VLS favorise une phase cristalline 15R, alors que des domaines WZ/ZB purs ont été observés pour VSS.

Pour modéliser l'apparition de la phase cristalline 15R dans les NFs de ZnS, nous avons exploré les aspects théoriques de l'émergence du polytypisme (chapitre 5). Le phénomène de polytypisme dans les semiconducteurs a été étudié à l'aide du modèle d'Ising ANNNI (axial next nearest neighbour Ising). Nous avons commencé par les calculs de Johansson effectués dans le cadre de la théorie classique de la nucléation et du modèle ANNNI [214]. Ce modèle a été développé pour un nombre limité de polytypes d'ordre élevé (high order polytypes, HOP), à savoir quatre, et n'incluait pas d'autres polytypes réalisables comme le 15R, qui a été observé dans nos nanofils de ZnS. Par conséquent, nous avons saisi l'occasion d'y introduire le polytype 15R et d'effectuer à nouveau les calculs. Ce modèle prédit avec précision l'apparition du 15R dans une petite fenêtre de sursaturation. Cependant, en raison des hypothèses simplifiées faites sur les énergies de surface du germe de croissance (nucleus), il ne permet pas d'entrer dans les détails de la dynamique de croissance du NF. Par conséquent, nous avons étendu ce modèle de croissance en introduisant dans les calculs des équations d'énergie de marche du nucleus plus précises, issues de Glas et al. [11]. Ce modèle étendu considère un nucleus triangulaire, et permet de préciser les paramètres clés dont les probabilités de polytype montrent une forte dépendance, à savoir le rapport des énergies effectives de marche entre nucléation cubique et hexagonale ($R_{WZ/ZB}$), et aussi l'énergie d'interface catalyseur/nanofil. Nous avons trouvé deux géométries de nucleus à facettes ZB possibles, appelées (111)A et (111)B. En raison des différentes énergies de surface de ces facettes, les énergies effectives des bords sont différentes, tout comme le rapport $R_{WZ/ZB}$, ce qui entraîne une ouverture ou un rétrécissement de la fenêtre HOP, comme l'illustre la figure C.2. Nous avons examiné l'effet de deux paramètres supplémentaires sur les valeurs de l'énergie effective de bord : l'angle de contact des gouttelettes et l'énergie de surface liquide-vapeur. L'analyse de l'angle de contact révèle certains faits intéressants sur les nanofils de GaAs. Notre modèle prédit avec précision la transition de phase cristalline de ZB à WZ pour les petits angles de contact et de WZ à ZB pour les grands angles de contact, ce qui correspond aux mesures TEM in situ sur les nanofils de GaAs auto-catalysés. Ensuite, nous avons exploré l'effet de l'énergie liquide-vapeur (LV) et indiqué comment elle pourrait être un facteur substantiel dans l'ouverture de la fenêtre HOP lorsque $R_{WZ/ZB}$ est proche de 1.

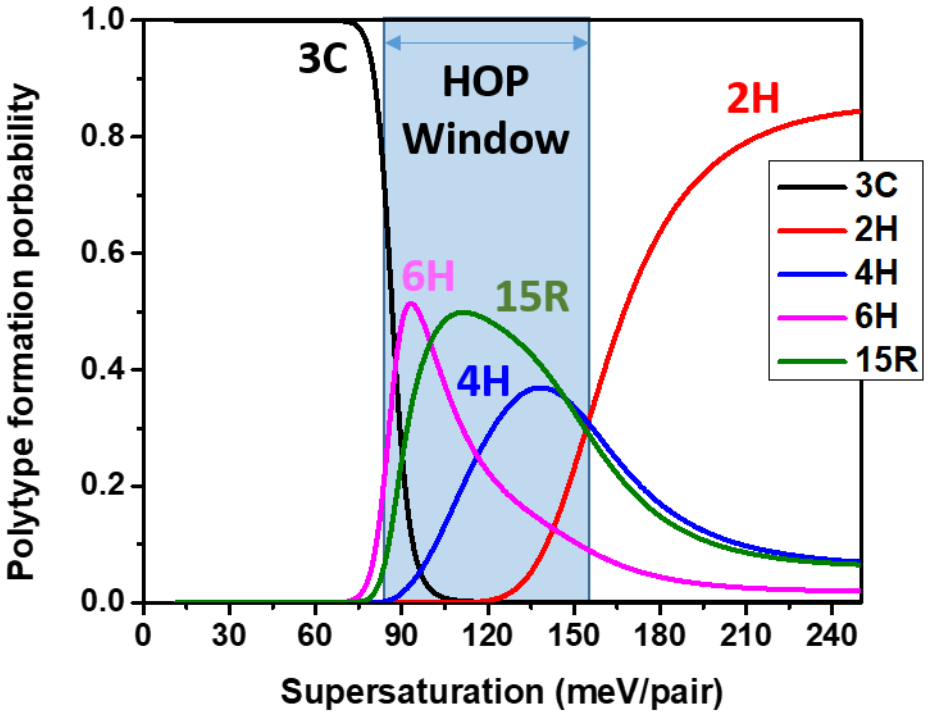

Figure C.2 : Graphique de l'énergie de formation de polytypes de cinq polytypes en fonction de la sursaturation pour les NW de ZnS. Ici, nous considérons une énergie de surface élevée de facette {10-10} en faveur de 15R, observée expérimentalement dans nos NW développés par VLS.

En revenant à la phase cristalline 15R, nous avons appliqué notre modèle étendu au cas des NFs de ZnS. Une forte dépendance a été observée en diminuant le premier paramètre d'interaction J_1. Le paramètre J_1, c'est-à-dire l'énergie de faute d'empilement, est très faible pour ZnS (6 mJ/m^2) comparé à GaAs (45 mJ/m^2), ce qui signifie qu'il est beaucoup plus facile de créer un défaut d'empilement dans ZnS que dans GaAs. L'empilement 2H peut être considéré comme un défaut d'empilement. Pour commencer, nous avons reconsidéré la faible énergie de surface du plan {10-10} WZ donnée dans la littérature, qui exclut toute autre phase que 2H. En effet, la nucléation facile de l'empilement WZ est prédite dans ZnS par nos calculs. Nous avons également discuté de la formation de 15R dans les NFs de ZnS et suggéré les conditions favorables à son apparition. L'apparition de 15R est très favorable dans ZnS si nous considérons une valeur plus élevée de l'énergie de surface {10-10} autour de 0,81 J/m^2. Pour cette valeur, le rapport R est proche de 1, le graphique correspondant est illustré à la figure C.3 pour le ZnS NW. Dans la large fenêtre HOP, la cristallisation de la phase 15R est la plus probable.

Nous avons mis en place de nouvelles expériences pour valider nos résultats théoriques (chapitre 6). La sursaturation est censée être critique pour la sélection de la phase cristalline dans les NFs. Nous avons donc réalisé des expériences pour contrôler la sursaturation par la variation du flux de croissance des NFs, c'est-à-dire en jouant sur les flux de Zn et de S entrants. L'effet de la variation de la sursaturation sur la phase cristalline est illustré dans la figure C.3. À faible flux de croissance, de grands segments 15R avec de petites inclusions de 3C et fautes d'empilement ont été observés. Ce résultat suggère une plage de sursaturation à la frontière des domaines 3C et HOP. Pour un flux de croissance intermédiaire, une structure 15R avec une augmentation des défauts d'empilement a été observée et détaillée au chapitre 4. Dans ce cas, une gamme de sursaturation HOP/2H est prédite. En ce qui concerne le flux de croissance

élevé, nous confirmons qu'une phase 2H pure est induite en allant vers des supersaturations élevées, comme le prédit le modèle.

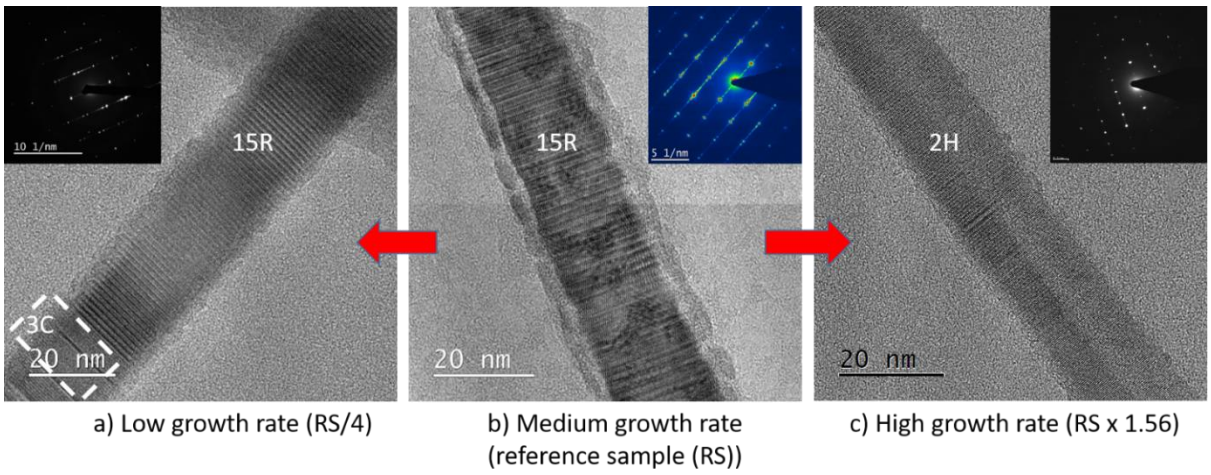

Figure C.3 : Les images HRTEM des segments NW cultivés à différents flux de croissance, a) flux de croissance faible, avec phase 15R/3C, b) flux de croissance moyen, avec 15R/défauts d'empilement, et c) flux de croissance élevé, avec Phase WZ.

De même, un résumé graphique de la croissance de NFs avec différentes compositions de gouttelettes, de l'Au pur à un alliage Au-Ga riche en Ga, est illustré dans la Figure C.4. Nous avons présenté au chapitre 4 l'analyse structurale de la croissance de NFs par VSS assistée par une gouttelette d'Au pur. Elle montre des inclusions 3C dans la phase cristalline dominante WZ (fig. C.4a). Cela suggère que la fenêtre HOP est étroite et qu'une transition rapide a lieu de 3C à 2H. Notre modèle théorique pour ZnS est en accord avec cela, car il prédit une diminution de la valeur R pour la gouttelette d'Au pur (γ_{LV} = 1,14 J/m^2, expliqué en annexe). Pour le NF cru avec l'alliage Au_2Ga (riche en Au), nous avons observé une phase cristalline 15R (fig. C.4b). Cette fois, la valeur de R augmente (proche de 1) avec la diffusion de Ga à l'intérieur de la gouttelette d'Au qui diminue les énergies de surface des LV (γ_{LV} = 1 J/m^2 pour Au_2Ga). En ce qui concerne la gouttelette riche en Ga (99% Ga, gouttelette "Ga-fed"), une phase 3C avec super-réseau de macles (twinning superlattice, TSL) été observée (fig.C.4c), en utilisant un faible flux de croissance. Pour de telles conditions, nous avons diminué la sursaturation et l'énergie γ_{LV} (0,72 J/m^2), ce qui a pu contribuer à atteindre une valeur de R très proche ou supérieure à 1. Dans ce cas, 3C/15R pourrait être la gamme possible de sursaturation. De manière remarquable, nous avons bien mis en évidence une structure 3C cubique dans nos super-réseaux de jumelage ZB.

Par conséquent, notre modèle soutient raisonnablement toutes les observations expérimentales de phase cristalline pour le mode de croissance VLS des NWs de ZnS. Cependant, les NFs élaborés avec le mode de croissance VSS avec un flux de croissance plus faible présentent toujours une phase WZ pure (détaillée en annexe), et ne suivent donc pas le modèle prédit 3C. Cela pourrait être dû à l'effet du faible diamètre, car nous avons observé un diamètre inférieur à 10 nm pour ces NFs. Notre modèle étendu ne prend pas en compte l'effet du diamètre actuellement. Dans les études futures, nous pourrions envisager d'introduire d'autres paramètres de croissance dans notre modèle.

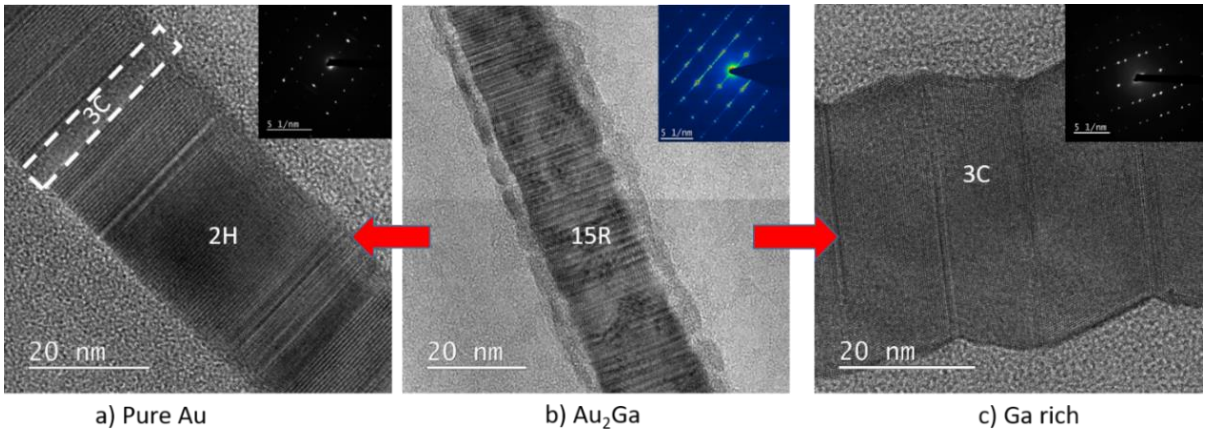

Figure C.4 : Les images HRTEM de segments NW cultivés avec différents catalyseurs de gouttelettes, a) Au pur, avec phase 2H/3C, b) Au2Ga (riche en Au), avec 15R/défauts d'empilement, et c) Ga riche, avec phase ZB jumelée.

Enfin, nous avons étudié les propriétés optiques des films minces et des NFs. Les spectres de photoluminescence (PL) et de cathodoluminescence (CL) des films minces de ZnS, ZnSe et ZnMgS ont été discutés. Ensuite, en utilisant la CL dans un MEB, les caractéristiques optiques de différents NFs de ZnS ont été étudiées. Ceux développés par VSS avec une phase WZ pure semblent être de meilleure qualité. Enfin, la croissance et l'étude par CL d'hétérostructures cœur/coquille (ZnS-ZnSe)/ZnMgS avec différents segments de ZnS ou ZnSe ont été réalisées. Des spectres CL et des images monochromatiques de l'émission ont été collectés. Bien que les résultats n'aient pas été complètement compris, nous avons mis en évidence des pics d'émission uniques qui, selon nous, sont liés à des insertions de ZnSe ou de ZnS. Ce qui est certain, c'est qu'un grand nombre d'insertions ne produisent aucune émission. Par conséquent, il est difficile de tirer une conclusion ferme d'un tel travail préliminaire.

Bibliography

[1] Feynman R 1960 “There is plenty of room at the bottom” California Institute of Technology *Journal of Engineering Science* **4** 23–36

[2] Wagner R S and Ellis W C 1964 VAPOR-LIQUID-SOLID MECHANISM OF SINGLE CRYSTAL GROWTH *Applied Physics Letters* **4** 89–90

[3] Givargizov E I 1975 Fundamental aspects of VLS growth *Journal of Crystal Growth* **31** 20–30

[4] Yazawa M, Koguchi M, Muto A, Ozawa M and Hiruma K 1992 Effect of one monolayer of surface gold atoms on the epitaxial growth of InAs nanowhiskers *Appl. Phys. Lett.* **61** 2051–3

[5] Yazawa M, Koguchi M, Muto A and Hiruma K 1993 Semiconductor nanowhiskers *Adv. Mater.* **5** 577–80

[6] Haraguchi K, Katsuyama T and Hiruma K 1994 Polarization dependence of light emitted from GaAs *p* - *n* junctions in quantum wire crystals *Journal of Applied Physics* **75** 4220–5

[7] Hu J, Ouyang M, Yang P and Lieber C M 1999 Controlled growth and electrical properties of heterojunctions of carbon nanotubes and silicon nanowires *Nature* **399** 48–51

[8] Güniat L, Caroff P and Fontcuberta i Morral A 2019 Vapor Phase Growth of Semiconductor Nanowires: Key Developments and Open Questions *Chem. Rev.* **119** 8958–71

[9] Tao A, Kim F, Hess C, Goldberger J, He R, Sun Y, Xia Y and Yang P 2003 Langmuir−Blodgett Silver Nanowire Monolayers for Molecular Sensing Using Surface-Enhanced Raman Spectroscopy *Nano Lett.* **3** 1229–33

[10] Li D, Wu Y, Kim P, Shi L, Yang P and Majumdar A 2003 Thermal conductivity of individual silicon nanowires *Appl. Phys. Lett.* **83** 2934–6

[11] Glas F, Harmand J-C and Patriarche G 2007 Why Does Wurtzite Form in Nanowires of III-V Zinc Blende Semiconductors? *Phys. Rev. Lett.* **99** 146101

[12] Duan X and Lieber C M 2000 General Synthesis of Compound Semiconductor Nanowires *Adv. Mater.* **12** 298–302

[13] Wu Y, Fan R and Yang P 2002 Block-by-Block Growth of Single-Crystalline Si/SiGe Superlattice Nanowires *Nano Lett.* **2** 83–6

[14] Wu Y and Yang P 2000 Germanium Nanowire Growth via Simple Vapor Transport *Chem. Mater.* **12** 605–7

[15] Woodruff J H, Ratchford J B, Goldthorpe I A, McIntyre P C, and Chidsey 2007 Vertically Oriented Germanium Nanowires Grown from Gold Colloids on Silicon Substrates and Subsequent Gold Removal *Nano Lett.* **7** 1637–42

[16] Duan X and Lieber C M 2000 Laser-Assisted Catalytic Growth of Single Crystal GaN Nanowires *J. Am. Chem. Soc.* **122** 188–9

[17] Caroff P, Dick K A, Johansson J, Messing M E, Deppert K and Samuelson L 2009 Controlled polytypic and twin-plane superlattices in iii–v nanowires *Nature Nanotechnology* **4** 50–5

[18] Jacobsson D, Panciera F, Tersoff J, Reuter M C, Lehmann S, Hofmann S, Dick K A and Ross F M 2016 Interface dynamics and crystal phase switching in GaAs nanowires *Nature* **531** 317–22

[19] Caroff P, Wagner J B, Dick K A, Nilsson H A, Jeppsson M, Deppert K, Samuelson L, Wallenberg L R and Wernersson L 2008 High-Quality InAs/InSb Nanowire Heterostructures Grown by Metal–Organic Vapor-Phase Epitaxy *Small* **4** 878–82

[20] Krogstrup P, Popovitz-Biro R, Johnson E, Madsen M H, Nygård J and Shtrikman H 2010 Structural Phase Control in Self-Catalyzed Growth of GaAs Nanowires on Silicon (111) *Nano Lett.* **10** 4475–82

[21] Dick K A, Thelander C, Samuelson L and Caroff P 2010 Crystal Phase Engineering in Single InAs Nanowires *Nano Lett.* **10** 3494–9

[22] Yang P, Yan H, Mao S, Russo R, Johnson J, Saykally R, Morris N, Pham J, He R and Choi H-J 2002 Controlled Growth of ZnO Nanowires and Their Optical Properties *Adv. Funct. Mater.* **12** 323

[23] Lee C J, Lee T J, Lyu S C, Zhang Y, Ruh H and Lee H J 2002 Field emission from well-aligned zinc oxide nanowires grown at low temperature *Appl. Phys. Lett.* **81** 3648–50

[24] Hao Y, Meng G, Wang Z L, Ye C and Zhang L 2006 Periodically Twinned Nanowires and Polytypic Nanobelts of ZnS: The Role of Mass Diffusion in Vapor−Liquid−Solid Growth *Nano Lett.* **6** 1650–5

[25] Li Q, Gong X, Wang C, Wang J, Ip K and Hark S 2004 Size-Dependent Periodically Twinned ZnSe Nanowires *Adv. Mater.* **16** 1436–40

[26] Rueda-Fonseca P, Bellet-Amalric E, Vigliaturo R, den Hertog M, Genuist Y, André R, Robin E, Artioli A, Stepanov P, Ferrand D, Kheng K, Tatarenko S and Cibert J 2014 Structure and Morphology in Diffusion-Driven Growth of Nanowires: The Case of ZnTe *Nano Lett.* **14** 1877–83

[27] Zhang H-F, Wang C-M and Wang L-S 2002 Helical Crystalline SiC/SiO_2 Core−Shell Nanowires *Nano Lett.* **2** 941–4

[28] Wang D-H, Xu D, Wang Q, Hao Y-J, Jin G-Q, Guo X-Y and Tu K N 2008 Periodically twinned SiC nanowires *Nanotechnology* **19** 215602

[29] Young Kim H, Park J and Yang H 2003 Synthesis of silicon nitride nanowires directly from the silicon substrates *Chemical Physics Letters* **372** 269–74

[30] Li W, Gan L, Guo K, Ke L, Wei Y, Li H, Shen G and Zhai T 2016 Self-supported Zn $_3$ P $_2$ nanowire arrays grafted on carbon fabrics as an advanced integrated anode for flexible lithium ion batteries *Nanoscale* **8** 8666–72

[31] Escobar Steinvall S, Tappy N, Ghasemi M, Zamani R R, LaGrange T, Stutz E Z, Leran J-B, Zamani M, Paul R and Fontcuberta i Morral A 2020 Multiple morphologies and functionality of nanowires made from earth-abundant zinc phosphide *Nanoscale Horiz.* **5** 274–82

[32] Krogstrup P, Jørgensen H I, Heiss M, Demichel O, Holm J V, Aagesen M, Nygard J and Fontcuberta i Morral A 2013 Single-nanowire solar cells beyond the Shockley–Queisser limit *Nature Photon* **7** 306–10

[33] Li Z, Tan H H, Jagadish C and Fu L 2018 III–V Semiconductor Single Nanowire Solar Cells: A Review *Adv. Mater. Technol.* **3** 1800005

[34] Duan X, Huang Y, Cui Y, Wang J and Lieber C M 2001 Indium phosphide nanowires as building blocks for nanoscale electronic and optoelectronic devices *Nature* **409** 66–9

[35] Hayden O, Greytak A B and Bell D C 2005 Core-Shell Nanowire Light-Emitting Diodes *Adv. Mater.* **17** 701–4

[36] Guan N, Dai X, Babichev A V, Julien F H and Tchernycheva M 2017 Flexible inorganic light emitting diodes based on semiconductor nanowires *Chem. Sci.* **8** 7904–11

[37] Friedler I, Sauvan C, Hugonin J P, Lalanne P, Claudon J and Gérard J M 2009 Solid-state single photon sources: the nanowire antenna *Opt. Express* **17** 2095

[38] Claudon J, Bleuse J, Malik N S, Bazin M, Jaffrennou P, Gregersen N, Sauvan C, Lalanne P and Gérard J-M 2010 A highly efficient single-photon source based on a quantum dot in a photonic nanowire *Nature Photon* **4** 174–7

[39] Lodahl P, Mahmoodian S and Stobbe S 2015 Interfacing single photons and single quantum dots with photonic nanostructures *Rev. Mod. Phys.* **87** 347–400

[40] Reimer M E, Bulgarini G, Akopian N, Hocevar M, Bavinck M B, Verheijen M A, Bakkers E P A M, Kouwenhoven L P and Zwiller V 2012 Bright single-photon sources in bottom-up tailored nanowires *Nat Commun* **3** 737

[41] Bao Q, Li W, Xu P, Zhang M, Dai D, Wang P, Guo X and Tong L 2020 On-chip single-mode CdS nanowire laser *Light Sci Appl* **9** 42

[42] Bermúdez-Ureña E, Tutuncuoglu G, Cuerda J, Smith C L C, Bravo-Abad J, Bozhevolnyi S I, Fontcuberta i Morral A, García-Vidal F J and Quidant R 2017 Plasmonic Waveguide-Integrated Nanowire Laser *Nano Lett.* **17** 747–54

[43] Mourik V, Zuo K, Frolov S M, Plissard S R, Bakkers E P A M and Kouwenhoven L P 2012 Signatures of Majorana Fermions in Hybrid Superconductor-Semiconductor Nanowire Devices *Science* **336** 1003–7

[44] Deng M T, Vaitiekėnas S, Hansen E B, Danon J, Leijnse M, Flensberg K, Nygård J, Krogstrup P and Marcus C M 2016 Majorana bound state in a coupled quantum-dot hybrid-nanowire system *Science* **354** 1557–62

[45] Mauthe S, Baumgartner Y, Sousa M, Ding Q, Rossell M D, Schenk A, Czornomaz L and Moselund K E 2020 High-speed III-V nanowire photodetector monolithically integrated on Si *Nat Commun* **11** 4565

[46] Li Z, Allen J, Allen M, Tan H H, Jagadish C and Fu L 2020 Review on III-V Semiconductor Single Nanowire-Based Room Temperature Infrared Photodetectors *Materials* **13** 1400

[47] Kong J, Franklin N R, Zhou C, Chapline M G, Peng S, Cho K and Dai H 2000 Nanotube Molecular Wires as Chemical Sensors *Science* **287** 622–5

[48] Cui Y, Wei Q, Park H and Lieber C M 2001 Nanowire Nanosensors for Highly Sensitive and Selective Detection of Biological and Chemical Species *Science* **293** 1289–92

[49] de la Mata M, Magén C, Caroff P and Arbiol J 2014 Atomic Scale Strain Relaxation in Axial Semiconductor III–V Nanowire Heterostructures *Nano Lett.* **14** 6614–20

[50] Akopian N, Patriarche G, Liu L, Harmand J-C and Zwiller V 2010 Crystal Phase Quantum Dots *Nano Lett.* **10** 1198–201

[51] Lin M E, Xue G, Zhou G L, Greene J E and Morkoç H 1993 *p* -type zinc-blende GaN on GaAs substrates *Appl. Phys. Lett.* **63** 932–3

[52] Park C H, Cheong B-H, Lee K-H and Chang K J 1994 Structural and electronic properties of cubic, 2 *H* , 4 *H* , and 6 *H* SiC *Phys. Rev. B* **49** 4485–93

[53] Bechstedt F, K�ckell P, Zywietz A, Karch K, Adolph B, Tenelsen K and Furthm�ller J 1997 Polytypism and Properties of Silicon Carbide *phys. stat. sol. (b)* **202** 35–62

[54] Engel G E and Needs R J 1990 Total energy calculations on zinc sulphide polytypes *Journal of Physics: Condensed Matter* **2** 367–76

[55] Huang Z, Lü T-Y, Wang H-Q and Zheng J-C 2015 Thermoelectric properties of the 3C, 2H, 4H, and 6H polytypes of the wide-band-gap semiconductors SiC, GaN, and ZnO *AIP Advances* **5** 097204

[56] Wang L, Xiong K, He Y, Huang X, Xia J, Li X, Gu Y, Cheng H and Meng X 2017 Epitaxial growth of wafer-scale two-dimensional polytypic ZnS thin films on ZnO substrates *CrystEngComm* **19** 2294–9

[57] Maurice J-L, Tang J, Florea I, Fossard F, Roca i Cabarrocas P, Johnson E V and Foldyna M 2016 TEM characterisation of diamond-hexagonal silicon nanowires

European Microscopy Congress 2016: Proceedings ed European Microscopy Society (Weinheim, Germany: Wiley-VCH Verlag GmbH & Co. KGaA) pp 488–9

[58] Hauge H I T, Verheijen M A, Conesa-Boj S, Etzelstorfer T, Watzinger M, Kriegner D, Zardo I, Fasolato C, Capitani F, Postorino P, Kölling S, Li A, Assali S, Stangl J and Bakkers E P A M 2015 Hexagonal Silicon Realized *Nano Lett.* **15** 5855–60

[59] Vincent L, Patriarche G, Hallais G, Renard C, Gardès C, Troadec D and Bouchier D 2014 Novel Heterostructured Ge Nanowires Based on Polytype Transformation *Nano Lett.* **14** 4828–36

[60] Fadaly E M T, Dijkstra A, Suckert J R, Ziss D, van Tilburg M A J, Mao C, Ren Y, van Lange V T, Korzun K, Kölling S, Verheijen M A, Busse D, Rödl C, Furthmüller J, Bechstedt F, Stangl J, Finley J J, Botti S, Haverkort J E M and Bakkers E P A M 2020 Direct-bandgap emission from hexagonal Ge and SiGe alloys *Nature* **580** 205–9

[61] Algra R E, Verheijen M A, Borgström M T, Feiner L-F, Immink G, van Enckevort W J P, Vlieg E and Bakkers E P A M 2008 Twinning superlattices in indium phosphide nanowires *Nature* **456** 369–72

[62] Montgomery K H and Woodall J M 2010 Moving past 2.0eV: Engineered ZnSe-GaAs alloys for multijunction solar cells *2010 35th IEEE Photovoltaic Specialists Conference* 2010 35th IEEE Photovoltaic Specialists Conference (PVSC) (Honolulu, HI, USA: IEEE) pp 003369–73

[63] Averous M and Balkanski M 1991 *Semimagnetic Semiconductors and Diluted Magnetic Semiconductors* (Boston, MA: Springer US)

[64] Rutter M J 1997 Growth and stability of silicon carbide polytypes

[65] Ramsdell L S 1947 Studies on silicon carbide *American Mineralogist* **32** 64–82

[66] Zhdanov G S 1945 The numerical symbol of close packing of spheres and its application in the theory of close packings *Compt. Rend. Acad. Sci. URSS* **48** 11

[67] Kumar S, Fossard F, Amiri G, Chauveau J-M and Sallet V 2022 Induced structural modifications in ZnS nanowires via physical state of catalyst: Highlights of 15R crystal phase *Nano Res.* **15** 377–85

[68] Mardix S 1986 Polytypism: A controlled thermodynamic phenomenon *Phys. Rev. B* **33** 8677–84

[69] Trigunayat G C and Verma A R 1976 Polytypism and Stacking Faults in Crystals with Layer Structure *Crystallography and Crystal Chemistry of Materials with Layered Structures* ed F Lévy (Dordrecht: Springer Netherlands) pp 269–340

[70] Yeh C-Y, Lu Z W, Froyen S and Zunger A 1992 Zinc-blende–wurtzite polytypism in semiconductors *Phys. Rev. B* **46** 10086–97

[71] Patrick L, Hamilton D R and Choyke W J 1966 Growth, Luminescence, Selection Rules, and Lattice Sums of SiC with Wurtzite Structure *Phys. Rev.* **143** 526–36

[72] Jagodzinski H 1954 Polytypism in SiC crystals *Acta Crystallographica* **7** 300

[73] Kawanishi S and Mizoguchi T 2016 Effect of van der Waals interactions on the stability of SiC polytypes *Journal of Applied Physics* **119** 175101

[74] Mardix S, Brafman O and Steinberger I T 1967 The zinc sulphide polytypes 14L(7 7); 18L(4 2)3; 24L(7 5 5 7) and 36L(6 2 2 2)3 *Acta Cryst* **22** 805–7

[75] Jagodzinski H and Kunze G 1954 The Rolled Structure of Chrysotile. II. Far Winklen Interferences *Neues Jahrb. Mineral Monatsh* **6** 113–30

[76] Heine V, Cheng C and Needs R J 1991 The Preference of Silicon Carbide for Growth in the Metastable Cubic Form *J American Ceramic Society* **74** 2630–3

[77] Johansson J, Dick K A, Caroff P, Messing M E, Bolinsson J, Deppert K and Samuelson L 2010 Diameter Dependence of the Wurtzite−Zinc Blende Transition in InAs Nanowires *J. Phys. Chem. C* **114** 3837–42

[78] Priante G, Harmand J-C, Patriarche G and Glas F 2014 Random stacking sequences in III-V nanowires are correlated *Phys. Rev. B* **89** 241301

[79] Lopez F J, Hemesath E R and Lauhon L J 2009 Ordered Stacking Fault Arrays in Silicon Nanowires *Nano Lett.* **9** 2774–9

[80] Biswas S, Doherty J, Majumdar D, Ghoshal T, Rahme K, Conroy M, Singha A, Morris M A and Holmes J D 2015 Diameter-Controlled Germanium Nanowires with Lamellar Twinning and Polytypes *Chem. Mater.* **27** 3408–16

[81] Dheeraj D L, Patriarche G, Zhou H, Hoang T B, Moses A F, Grønsberg S, van Helvoort A T J, Fimland B-O and Weman H 2008 Growth and Characterization of Wurtzite GaAs Nanowires with Defect-Free Zinc Blende GaAsSb Inserts *Nano Lett.* **8** 4459–63

[82] Jiang Y, Meng X-M, Liu J, Hong Z-R, Lee C-S and Lee S-T 2003 ZnS Nanowires with Wurtzite Polytype Modulated Structure *Adv. Mater.* **15** 1195–8

[83] Liu X and Wang D 2009 Kinetically-induced hexagonality in chemically grown silicon nanowires *Nano Research* **2** 575–82

[84] Cui Y, van Dam D, Mann S A, van Hoof N J J, van Veldhoven P J, Garnett E C, Bakkers E P A M and Haverkort J E M 2016 Boosting Solar Cell Photovoltage via Nanophotonic Engineering *Nano Lett.* **16** 6467–71

[85] Waldron N, Merckling C, Teugels L, Ong P, Ibrahim S A U, Sebaai F, Pourghaderi A, Barla K, Collaert N and Thean A V-Y 2014 InGaAs Gate-All-Around Nanowire Devices on 300mm Si Substrates *IEEE Electron Device Lett.* **35** 1097–9

[86] Zhang J, Dhindsa N, Chia A, Boulanger J, Khodadad I, Saini S and LaPierre R 2014 Multi-spectral optical absorption in substrate-free nanowire arrays *Appl. Phys. Lett.* **105** 123113

[87] Lang D V, Grimmeiss H G, Meijer E and Jaros M 1980 Complex nature of gold-related deep levels in silicon *Phys. Rev. B* **22** 3917–34

[88] Hillerich K, Ghidini D S, Dick K A, Deppert K and Johansson J 2013 Cu particle seeded InP-InAs axial nanowire heterostructures: Cu particle seeded InP-InAs axial nanowire heterostructures *Phys. Status Solidi RRL* **7** 850–4

[89] Lindberg C, Whiticar A, Dick K A, Sköld N, Nygård J and Bolinsson J 2016 Silver as Seed-Particle Material for GaAs Nanowires—Dictating Crystal Phase and Growth Direction by Substrate Orientation *Nano Lett.* **16** 2181–8

[90] Sun R, Jacobsson D, Chen I-J, Nilsson M, Thelander C, Lehmann S and Dick Kimberly A 2015 Sn-Seeded GaAs Nanowires as Self-Assembled Radial *p–n* Junctions *Nano Lett.* **15** 3757–62

[91] Wang Y, Schmidt V, Senz S and Gösele U 2006 Epitaxial growth of silicon nanowires using an aluminium catalyst *Nature Nanotech* **1** 186–9

[92] Ford A C, Ho J C, Fan Z, Ergen O, Altoe V, Aloni S, Razavi H and Javey A 2008 Synthesis, contact printing, and device characterization of Ni-catalyzed, crystalline InAs nanowires *Nano Res.* **1** 32–9

[93] Boulanger J P, Chia A C E, Wood B, Yazdi S, Kasama T, Aagesen M and LaPierre R R 2016 Characterization of a Ga-Assisted GaAs Nanowire Array Solar Cell on Si Substrate *IEEE J. Photovoltaics* **6** 661–7

[94] Persson A I, Larsson M W, Stenström S, Ohlsson B J, Samuelson L and Wallenberg L R 2004 Solid-phase diffusion mechanism for GaAs nanowire growth *Nature Materials* **3** 677–81

[95] Wen C-Y, Reuter M C, Bruley J, Tersoff J, Kodambaka S, Stach E A and Ross F M 2009 Formation of Compositionally Abrupt Axial Heterojunctions in Silicon-Germanium Nanowires *Science* **326** 1247–50

[96] Kodambaka S, Tersoff J, Reuter M C and Ross F M 2007 Germanium Nanowire Growth Below the Eutectic Temperature *Science* **316** 729–32

[97] Krogstrup P, Yamasaki J, Sørensen C B, Johnson E, Wagner J B, Pennington R, Aagesen M, Tanaka N and Nygård J 2009 Junctions in Axial III−V Heterostructure Nanowires Obtained via an Interchange of Group III Elements *Nano Lett.* **9** 3689–93

[98] Dick K A, Bolinsson J, Borg B M and Johansson J 2012 Controlling the Abruptness of Axial Heterojunctions in III–V Nanowires: Beyond the Reservoir Effect *Nano Lett.* **12** 3200–6

[99] Joyce H J 2009 *Growth and Characterisation of III-V Semiconductor Nanowires for Optoelectronic Device Applications* PhD Thesis (Australia: Australian National University)

[100] Zhai T, Fang X, Li L, Bando Y and Golberg D 2010 One-dimensional CdS nanostructures: synthesis, properties, and applications *Nanoscale* **2** 168

[101] Wang R P, Xu G and Jin P 2004 Size dependence of electron-phonon coupling in ZnO nanowires *Phys. Rev. B* **69** 113303

[102] Wang Z L 2004 Zinc oxide nanostructures: growth, properties and applications *J. Phys.: Condens. Matter* **16** R829–58

[103] Utama M I B, Zhang J, Chen R, Xu X, Li D, Sun H and Xiong Q 2012 Synthesis and optical properties of II–VI 1D nanostructures *Nanoscale* **4** 1422

[104] Fang X, Wu L and Hu L 2011 ZnS Nanostructure Arrays: A Developing Material Star *Adv. Mater.* **23** 585–98

[105] Kar S and Chaudhuri S 2006 Cadmium Sulfide One-Dimensional Nanostructures: Synthesis, Characterization and Application *Synthesis and Reactivity in Inorganic, Metal-Organic, and Nano-Metal Chemistry (formerly Synthesis and Reactivity in Inorganic and Metal-Organic Chem* **36** 289–312

[106] Hajer J, Mantei W, Kessel M, Brüne C, Wenner S, van Helvoort A T J, Buhmann H and Molenkamp L W 2020 Selective area grown ZnTe nanowires as the basis for quasi-one-dimensional CdTe-HgTe multishell heterostructures *Phys. Rev. Materials* **4** 066001

[107] Sallet V, Sartel C, Vilar C, Lusson A and Galtier P 2013 Opposite crystal polarities observed in spontaneous and vapour-liquid-solid grown ZnO nanowires *Appl. Phys. Lett.* **102** 182103

[108] Subannajui K, Wongchoosuk C, Ramgir N, Wang C, Yang Y, Hartel A, Cimalla V and Zacharias M 2012 Photoluminescent and gas-sensing properties of ZnO nanowires prepared by an ionic liquid assisted vapor transfer approach *Journal of Applied Physics* **112** 034311

[109] Di Carlo V, Prete P, Dubrovskii V G, Berdnikov Y and Lovergine N 2017 CdTe Nanowires by Au-Catalyzed Metalorganic Vapor Phase Epitaxy *Nano Lett.* **17** 4075–82

[110] Bellet-Amalric E, Elouneg-Jamroz M, Rueda-Fonseca P, Bounouar S, Hertog M D, Bougerol C, André R, Genuist Y, Poizat J P, Kheng K, Cibert J and Tatarenko S 2013 Growth of II–VI ZnSe/CdSe nanowires for quantum dot luminescence *Journal of Crystal Growth* **378** 233–7

[111] Bellet-Amalric E, Panciera F, Patriarche G, Travers L, Hertog M den, Harmand J-C, Glas F and Cibert J 2021 Regulated dynamics with two-monolayer steps in vapor-solid-solid growth of nanowires *arXiv:2112.06493 [cond-mat]*

[112] Zannier V, Grillo V, Martelli F, Plaisier J R, Lausi A and Rubini S 2014 Tuning the growth mode of nanowires via the interaction among seeds, substrates and beam fluxes *Nanoscale* **6** 8392–9

[113] Bakti Utama M I, Zhang Q, Zhang J, Yuan Y, Belarre F J, Arbiol J and Xiong Q 2013 Recent developments and future directions in the growth of nanostructures by van der Waals epitaxy *Nanoscale* **5** 3570

[114] Biswas S, Ghoshal T, Kar S, Chakrabarti S and Chaudhuri S 2008 ZnS Nanowire Arrays: Synthesis, Optical and Field Emission Properties *Crystal Growth & Design* **8** 2171–6

[115] Chan S K, Lok S K, Wang G, Cai Y, Wang N, Wong K S and Sou I K 2008 MBE-Grown Cubic ZnS Nanowires *Journal of Electronic Materials* **37** 1433–7

[116] Meng X M, Liu J, Jiang Y, Chen W W, Lee C S, Bello I and Lee S T 2003 Structure- and size-controlled ultrafine ZnS nanowires *Chemical Physics Letters* **382** 434–8

[117] Barrelet C J, Wu Y, Bell D C and Lieber C M 2003 Synthesis of CdS and ZnS Nanowires Using Single-Source Molecular Precursors *J. Am. Chem. Soc.* **125** 11498–9

[118] Liang, Shimizu Y, Sasaki T, Umehara H and Koshizaki N 2004 Au-Mediated Growth of Wurtzite ZnS Nanobelts, Nanosheets, and Nanorods via Thermal Evaporation *J. Phys. Chem. B* **108** 9728–33

[119] Lin M, Sudhiranjan T, Boothroyd C and Loh K P 2004 Influence of Au catalyst on the growth of ZnS nanowires *Chemical Physics Letters* **400** 175–8

[120] Wang Y, Zhang L, Liang C, Wang G and Peng X 2002 Catalytic growth and photoluminescence properties of semiconductor single-crystal ZnS nanowires *Chemical Physics Letters* **357** 314–8

[121] Liang Y, Xu H and Hark S K 2010 Orientation and Structure Controllable Epitaxial Growth of ZnS Nanowire Arrays on GaAs Substrates *J. Phys. Chem. C* **114** 8343–7

[122] Liang Y, Liang H, Xiao X and Hark S 2012 The epitaxial growth of ZnS nanowire arrays and their applications in UV-light detection *J. Mater. Chem.* **22** 1199–205

[123] Li Q and Wang C 2003 Fabrication of wurtzite ZnS nanobelts via simple thermal evaporation *Appl. Phys. Lett.* **83** 359–61

[124] Jiang Y, Meng X-M, Liu J, Hong Z-R, Lee C-S and Lee S-T 2003 ZnS Nanowires with Wurtzite Polytype Modulated Structure *Advanced Materials* **15** 1195–8

[125] Wang M, Fei G T, Zhu X G, Wu B, Kong M G and Zhang L D 2009 Density-Controlled Homoepitaxial Growth of ZnS Nanowire Arrays *J. Phys. Chem. C* **113** 4335–9

[126] Xiong Q, Chen G, Acord J D, Liu X, Zengel J J, Gutierrez H R, Redwing J M, Lew Yan Voon L C, Lassen B and Eklund P C 2004 Optical Properties of Rectangular Cross-sectional ZnS Nanowires *Nano Lett.* **4** 1663–8

[127] Cheng B C and Wang Z G 2005 Synthesis and Optical Properties of Europium-Doped ZnS: Long-Lasting Phosphorescence from Aligned Nanowires *Adv. Funct. Mater.* **15** 1883–90

[128] Hao Y, Meng G, Wang Z L, Ye C and Zhang L 2006 Periodically Twinned Nanowires and Polytypic Nanobelts of ZnS: The Role of Mass Diffusion in Vapor−Liquid−Solid Growth *Nano Lett.* **6** 1650–5

[129] Fang, Bando Y, Ye, Shen and Golberg D 2007 Shape- and Size-controlled Growth of ZnS Nanostructures *J. Phys. Chem. C* **111** 8469–74

[130] Dai J, Song X, Zheng H and Wu C 2016 Excitonic photoluminescence and photoresponse of ZnS nanowires *Materials Chemistry and Physics* **174** 204–8

[131] Kim J H, Kim J G, Song J, Bae T-S, Kim K-H, Lee Y-S, Pang Y, Oh K H and Chung H-S 2018 Investigation of the growth and in situ heating transmission electron microscopy analysis of Ag2S-catalyzed ZnS nanowires *Applied Surface Science* **436** 556–61

[132] Sue Y-S, Pan K-Y and Wei D-H 2019 Optoelectronic and photocatalytic properties of zinc sulfide nanowires synthesized by vapor-liquid-solid process *Applied Surface Science* **471** 435–44

[133] Huang X, Wang Z-J, Weinberg G, Meng X-M and Willinger M-G 2015 In Situ Scanning Electron Microscopy Observation of Growth Kinetics and Catalyst Splitting in Vapor-Liquid-Solid Growth of Nanowires *Adv. Funct. Mater.* **25** 5979–87

[134] Rehman S, Shehzad M A, Hafeez M and Bhatti A S 2014 Essential role of catalysts (Mn, Au, and Sn) in the vapor liquid solid growth kinematics of ZnS nanowires *Journal of Applied Physics* **115** 024312

[135] Lu H-Y, Chu S-Y and Chang C-C 2005 Synthesis and optical properties of well-aligned ZnS nanowires on Si substrate *Journal of Crystal Growth* **280** 173–8

[136] Fang X, Zhai T, Gautam U K, Li L, Wu L, Bando Y and Golberg D 2011 ZnS nanostructures: From synthesis to applications *Progress in Materials Science* **56** 175–287

[137] Premkumar S, Nataraj D, Bharathi G, Ramya S and Thangadurai T D 2019 Highly Responsive Ultraviolet Sensor Based on ZnS Quantum Dot Solid with Enhanced Photocurrent *Scientific Reports* **9** 18704

[138] Wang Z, Daemen L L, Zhao Y, Zha C S, Downs R T, Wang X, Wang Z L and Hemley R J 2005 Morphology-tuned wurtzite-type ZnS nanobelts *Nature Mater* **4** 922–7

[139] Karazhanov S Zh, Ravindran P, Kjekshus A, Fjellvåg H, Grossner U and Svensson B G 2006 Coulomb correlation effects in zinc monochalcogenides *Journal of Applied Physics* **100** 043709

[140] Yeh C-Y, Wei S-H and Zunger A 1994 Relationships between the band gaps of the zinc-blende and wurtzite modifications of semiconductors *Phys. Rev. B* **50** 2715–8

[141] Karazhanov S Zh, Ravindran P, Kjekshus A, Fjellvåg H and Svensson B G 2007 Electronic structure and optical properties of Zn X (X = O , S, Se, Te): A density functional study *Phys. Rev. B* **75** 155104

[142] Akiyama T, Sano K, Nakamura K and Ito T 2007 An Empirical Interatomic Potential Approach to Structural Stability of ZnS and ZnSe Nanowires *Jpn. J. Appl. Phys.* **46** 1783–7

[143] Akizuki M 1981 Investigation of phase transition of natural ZnS minerals by high resolution electron microscopy *American Mineralogist* **66** 1006–12

[144] Thelander C, Caroff P, Plissard S, Dey A W and Dick K A 2011 Effects of Crystal Phase Mixing on the Electrical Properties of InAs Nanowires *Nano Lett.* **11** 2424–9

[145] Belabbes A, Panse C, Furthmüller J and Bechstedt F 2012 Electronic bands of III-V semiconductor polytypes and their alignment *Phys. Rev. B* **86** 075208

[146] Spirkoska D, Arbiol J, Gustafsson A, Conesa-Boj S, Glas F, Zardo I, Heigoldt M, Gass M H, Bleloch A L, Estrade S, Kaniber M, Rossler J, Peiro F, Morante J R, Abstreiter G, Samuelson L and Fontcuberta i Morral A 2009 Structural and optical properties of high quality zinc-blende/wurtzite GaAs nanowire heterostructures *Phys. Rev. B* **80** 245325

[147] Assali S, Zardo I, Plissard S, Kriegner D, Verheijen M A, Bauer G, Meijerink A, Belabbes A, Bechstedt F, Haverkort J E M and Bakkers E P A M 2013 Direct Band Gap Wurtzite Gallium Phosphide Nanowires *Nano Lett.* **13** 1559–63

[148] Harmand J-C, Patriarche G, Glas F, Panciera F, Florea I, Maurice J-L, Travers L and Ollivier Y 2018 Atomic Step Flow on a Nanofacet *Phys. Rev. Lett.* **121** 166101

[149] Panciera F, Baraissov Z, Patriarche G, Dubrovskii V G, Glas F, Travers L, Mirsaidov U and Harmand J-C 2020 Phase Selection in Self-catalyzed GaAs Nanowires *Nano Lett.* **20** 1669–75

[150] Zamani M, Tütüncüoglu G, Martí-Sánchez S, Francaviglia L, Güniat L, Ghisalberti L, Potts H, Friedl M, Markov E, Kim W, Leran J-B, Dubrovskii V G, Arbiol J and Fontcuberta i Morral A 2018 Optimizing the yield of A-polar GaAs nanowires to achieve defect-free zinc blende structure and enhanced optical functionality *Nanoscale* **10** 17080–91

[151] Yuan X, Caroff P, Wong-Leung J, Fu L, Tan H H and Jagadish C 2015 Tunable Polarity in a III-V Nanowire by Droplet Wetting and Surface Energy Engineering *Adv. Mater.* **27** 6096–103

[152] Dhanaraj G, Byrappa K, Prasad V and Dudley M 2010 *Springer Handbook of Crystal Growth* (Berlin, Heidelberg: Springer Berlin Heidelberg)

[153] Harmand J-C, Patriarche G, Glas F, Panciera F, Florea I, Maurice J-L, Travers L and Ollivier Y 2018 Atomic Step Flow on a Nanofacet *Phys. Rev. Lett.* **121** 166101

[154] Markov I V 2003 *Crystal Growth for Beginners* (WORLD SCIENTIFIC)

[155] Elliott R J 1961 Phenomenological Discussion of Magnetic Ordering in the Heavy Rare-Earth Metals *Phys. Rev.* **124** 346–53

[156] Fisher M E and Selke W 1980 Infinitely Many Commensurate Phases in a Simple Ising Model *Phys. Rev. Lett.* **44** 1502–5

[157] Cheng C, Needs R J and Heine V 1988 Inter-layer interactions and the origin of SiC polytypes *Journal of Physics C: Solid State Physics* **21** 1049–63

[158] Engel G E and Needs R J 1990 Total energy calculations on zinc sulphide polytypes *Journal of Physics: Condensed Matter* **2** 367–76

[159] Priante G, Harmand J-C, Patriarche G and Glas F 2014 Random stacking sequences in III-V nanowires are correlated *Phys. Rev. B* **89** 241301

[160] Johansson J, Zanolli Z and Dick K A 2016 Polytype Attainability in III–V Semiconductor Nanowires *Crystal Growth & Design* **16** 371–9

[161] Johansson J, Bolinsson J, Ek M, Caroff P and Dick K A 2012 Combinatorial Approaches to Understanding Polytypism in III–V Nanowires *ACS Nano* **6** 6142–9

[162] Glas F, Harmand J-C and Patriarche G 2007 Why Does Wurtzite Form in Nanowires of III-V Zinc Blende Semiconductors? *Phys. Rev. Lett.* **99** 146101

[163] Joyce H J, Wong-Leung J, Gao Q, Tan H H and Jagadish C 2010 Phase Perfection in Zinc Blende and Wurtzite III−V Nanowires Using Basic Growth Parameters *Nano Lett.* **10** 908–15

[164] Johansson J, Karlsson L S, Dick K A, Bolinsson J, Wacaser B A, Deppert K and Samuelson L 2009 Effects of Supersaturation on the Crystal Structure of Gold Seeded III−V Nanowires *Crystal Growth & Design* **9** 766–73

[165] Oliveira J B, Morbec J M and Miwa R H 2017 Mechanical and electronic properties of SiC nanowires: An *ab initio* study *Journal of Applied Physics* **121** 104302

[166] Wei G, Qin W, Wang G, Sun J, Lin J, Kim R, Zhang D and Zheng K 2008 The synthesis and ultraviolet photoluminescence of 6H–SiC nanowires by microwave method *J. Phys. D: Appl. Phys.* **41** 235102

[167] Guo Y, Wang Q, Kawazoe Y and Jena P 2015 A New Silicon Phase with Direct Band Gap and Novel Optoelectronic Properties *Sci Rep* **5** 14342

[168] Boutaiba F, Belabbes A, Ferhat M and Bechstedt F 2014 Polytypism in ZnS, ZnSe, and ZnTe: First-principles study *Phys. Rev. B* **89** 245308

[169] Yang F H 2014 Modern metal-organic chemical vapor deposition (MOCVD) reactors and growing nitride-based materials *Nitride Semiconductor Light-Emitting Diodes (LEDs)* (Elsevier) pp 27–65

[170] Thiandoume C, Sallet V, Triboulet R and Gorochov O 2009 Decomposition kinetics of tertiarybutanol and diethylzinc used as precursor sources for the growth of ZnO *Journal of Crystal Growth* **311** 1411–5

[171] Thiandoume C 1997 PhD Thesis (Sénégal: University Cheikh Anta Diop of Dakar)

[172] Williams D B and Carter C B 2009 *Transmission Electron Microscopy* (Boston, MA: Springer US)

[173] Gilliland G D 1997 Photoluminescence spectroscopy of crystalline semiconductors *Materials Science and Engineering: R: Reports* **18** 99–399

[174] Spindler C, Galvani T, Wirtz L, Rey G and Siebentritt S 2019 Excitation-intensity dependence of shallow and deep-level photoluminescence transitions in semiconductors *Journal of Applied Physics* **126** 175703

[175] Schue L, Loiseau A and Barjon J 2017 *Optical and structural properties of sp^2 hybridized boron nitride : from bulk to monolayer crystals, Propriétés optiques et structurales du nitrure de bore en hybridation sp^2 : des cristaux massifs aux feuillets atomiques* (Université Paris Saclay (COmUE))

[176] Khanlary M R, alijarahi S and Reyhani A 2018 Growth temperature dependence of VLS-grown ultra-long ZnS nanowires prepared by CVD method *J Theor Appl Phys* **12** 121–6

[177] Stringfellow G B 1999 Preface to the Second Edition *Organometallic Vapor-Phase Epitaxy (Second Edition)* ed G B Stringfellow (San Diego: Academic Press) pp xvii–xviii

[178] Granqvist C G and Buhrman R A 1976 Size distributions for supported metal catalysts: Coalescence growth versus ostwald ripening *Journal of Catalysis* **42** 477–9

[179] Xu H, Guo Y, Sun W, Liao Z, Burgess T, Lu H, Gao Q, Tan H H, Jagadish C and Zou J 2012 Quantitative study of GaAs nanowires catalyzed by Au film of different thicknesses *Nanoscale Research Letters* **7** 589

[180] Gomes U P, Ercolani D, Zannier V, Beltram F and Sorba L 2015 Controlling the diameter distribution and density of InAs nanowires grown by Au-assisted methods *Semiconductor Science and Technology* **30** 115012

[181] Harmand J C, Patriarche G, Péré-Laperne N, Mérat-Combes M-N, Travers L and Glas F 2005 Analysis of vapor-liquid-solid mechanism in Au-assisted GaAs nanowire growth *Applied Physics Letters* **87** 203101

[182] Han N, Wang F, Hou J J, Yip S, Lin H, Fang M, Xiu F, Shi X, Hung T and Ho J C 2012 Manipulated Growth of GaAs Nanowires: Controllable Crystal Quality and Growth Orientations via a Supersaturation-Controlled Engineering Process *Crystal Growth & Design* **12** 6243–9

[183] Dayeh S A, Yu E T and Wang D 2007 III−V Nanowire Growth Mechanism: V/III Ratio and Temperature Effects *Nano Lett.* **7** 2486–90

[184] Bellet-Amalric E, Elouneg-Jamroz M, Bougerol C, Den Hertog M, Genuist Y, Bounouar S, Poizat J P, Kheng K, André R and Tatarenko S 2010 Epitaxial growth of ZnSe and ZnSe/CdSe nanowires on ZnSe *Phys. Status Solidi (c)* **7** 1526–9

[185] Zhang X, Zou J, Paladugu M, Guo Y, Wang Y, Kim Y, Joyce H J, Gao Q, Tan H H and Jagadish C 2009 Evolution of Epitaxial InAs Nanowires on GaAs (111)B *Small* **5** 366–9

[186] Takeuchi S, Suzuki K, Maeda K and Iwanaga H 1985 Stacking-fault energy of II–VI compounds *Philosophical Magazine A* **50** 171–8

[187] Guo Y, Wang Q, Kawazoe Y and Jena P 2015 A New Silicon Phase with Direct Band Gap and Novel Optoelectronic Properties *Scientific Reports* **5** 14342

[188] Fissel A, Kaiser U, Schröter B, Richter W and Bechstedt F 2001 MBE growth and properties of SiC multi-quantum well structures *Applied Surface Science* **184** 37–42

[189] Xue M, Li M, Huang Y, Chen R, Li Y, Wang J, Xing Y, Chen J, Yan H, Xu H and Chen J 2020 Observation and Ultrafast Dynamics of Inter-Sub-Band Transition in InAs Twinning Superlattice Nanowires *Advanced Materials* **32** 2004120

[190] Zagorac D, Schön J C, Zagorac J and Jansen M 2015 Theoretical investigations of novel zinc oxide polytypes and in-depth study of their electronic properties *RSC Advances* **5** 25929–35

[191] Glas F 2008 A simple calculation of energy changes upon stacking fault formation or local crystalline phase transition in semiconductors *Journal of Applied Physics* **104** 093520

[192] Boutaiba F, Belabbes A, Ferhat M and Bechstedt F 2014 Polytypism in ZnS, ZnSe, and ZnTe: First-principles study *Phys. Rev. B* **89** 245308

[193] Zagorac D, Zagorac J, Schön J C, Stojanović N and Matović B 2018 ZnO/ZnS (hetero)structures: ıt ab initio investigations of polytypic behavior of mixed ZnO and ZnS compounds *Acta Crystallographica Section B* **74** 628–42

[194] Thombare S V, Marshall A F and McIntyre P C 2012 Size effects in vapor-solid-solid Ge nanowire growth with a Ni-based catalyst *Journal of Applied Physics* **112** 054325

[195] Zannier V, Grillo V and Rubini S 2014 Diameter-dependent morphology of vapour–solid–solid grown ZnSe nanowires *J. Phys. D: Appl. Phys.* **47** 394005

[196] Fang X, Bando Y, Liao M, Gautam U K, Zhi C, Dierre B, Liu B, Zhai T, Sekiguchi T, Koide Y and Golberg D 2009 UV Photodetectors: Single-Crystalline ZnS Nanobelts as Ultraviolet-Light Sensors (Adv. Mater. 20/2009) *Adv. Mater.* **21** NA-NA

[197] Jiang Y, Meng X-M, Liu J, Hong Z-R, Lee C-S and Lee S-T 2003 ZnS Nanowires with Wurtzite Polytype Modulated Structure *Advanced Materials* **15** 1195–8

[198] Liang Y, Xu H and Hark S K 2010 Orientation and Structure Controllable Epitaxial Growth of ZnS Nanowire Arrays on GaAs Substrates *J. Phys. Chem. C* **114** 8343–7

[199] Geng B Y, Liu X W, Du Q B, Wei X W and Zhang L D 2006 Structure and optical properties of periodically twinned ZnS nanowires *Appl. Phys. Lett.* **88** 163104

[200] Biswas S and Kar S 2008 Fabrication of ZnS nanoparticles and nanorods with cubic and hexagonal crystal structures: a simple solvothermal approach *Nanotechnology* **19** 045710

[201] Rothman A, Forsht T, Danieli Y, Popovitz-Biro R, Rechav K, Houben L and Joselevich E 2018 Guided Growth of Horizontal ZnS Nanowires on Flat and Faceted Sapphire Surfaces *J. Phys. Chem. C* **122** 12413–20

[202] Liang Y, Liang H, Xiao X and Hark S 2012 The epitaxial growth of ZnS nanowire arrays and their applications in UV-light detection *J. Mater. Chem.* **22** 1199–205

[203] Ortiz A L, Sánchez-Bajo F, Cumbrera F L and Guiberteau F 2013 The prolific polytypism of silicon carbide *Journal of Applied Crystallography* **46** 242–7

[204] Gibbon D L 1971 Electron diffraction effects in silicon carbide. I. Pure polytypes. II. whiskers *Journal of Applied Crystallography* **4** 95–103

[205] FRONDEL C and PALACHE C 1948 Three New Polymorphs of Zinc Sulfide *Science* **107** 602–602

[206] Wang Y, Yang Z, Wu X, Han N, Liu H, Wang S, Li J, Tse W, Yip S, Chen Y and Ho J C 2016 Growth and Photovoltaic Properties of High-Quality GaAs Nanowires Prepared by the Two-Source CVD Method *Nanoscale Research Letters* **11** 191

[207] Han N, Wang Y, Yang Z, Yip S, Wang Z, Li D, Hung T F, Wang F, Chen Y and Ho J C 2017 Controllable III–V nanowire growth via catalyst epitaxy *J. Mater. Chem. C* **5** 4393–9

[208] Johansson J, Bolinsson J, Ek M, Caroff P and Dick K A 2012 Combinatorial Approaches to Understanding Polytypism in III–V Nanowires *ACS Nano* **6** 6142–9

[209] Sourribes M J L, Isakov I, Panfilova M, Liu H and Warburton P A 2014 Mobility Enhancement by Sb-mediated Minimisation of Stacking Fault Density in InAs Nanowires Grown on Silicon *Nano Lett.* **14** 1643–50

[210] Kim Y, Im H S, Park K, Kim J, Ahn J-P, Yoo S J, Kim J-G and Park J 2017 Bent Polytypic ZnSe and CdSe Nanowires Probed by Photoluminescence *Small* **13** 1603695

[211] Isik Goktas N, Sokolovskii A, Dubrovskii V G and LaPierre R R 2020 Formation Mechanism of Twinning Superlattices in Doped GaAs Nanowires *Nano Lett.* **20** 3344–51

[212] Yu H, Wang Q, Yang L, Dai B, Zhu J and Han J 2019 Ultraviolet–visible light photoluminescence induced by stacking faults in 3C–SiC nanowires *Nanotechnology* **30** 235601

[213] Dubrovskii V G, Sibirev N V, Harmand J C and Glas F 2008 Growth kinetics and crystal structure of semiconductor nanowires *Phys. Rev. B* **78** 235301

[214] Johansson J, Zanolli Z and Dick K A 2016 Polytype Attainability in III–V Semiconductor Nanowires *Crystal Growth & Design* **16** 371–9

[215] Bellet-Amalric E, Elouneg-Jamroz M, Rueda-Fonseca P, Bounouar S, Hertog M D, Bougerol C, André R, Genuist Y, Poizat J P, Kheng K, Cibert J and Tatarenko S 2013 Growth of II–VI ZnSe/CdSe nanowires for quantum dot luminescence *Journal of Crystal Growth* **378** 233–7

[216] Sun Q, Pan D, Li M, Zhao J, Chen P, Lu W and Zou J 2020 In situ TEM observation of the vapor–solid–solid growth of <00$\bar{1}$> InAs nanowires *Nanoscale* **12** 11711–7

[217] Rueda-Fonseca P, Orrù M, Bellet-Amalric E, Robin E, Den Hertog M, Genuist Y, André R, Tatarenko S and Cibert J 2016 Diffusion-driven growth of nanowires by low-temperature molecular beam epitaxy *Journal of Applied Physics* **119** 164303

[218] Simon H, Krekeler T, Schaan G and Mader W 2013 Metal-Seeded Growth Mechanism of ZnO Nanowires *Crystal Growth & Design* **13** 572–80

[219] Okamoto H and Massalski T B 1985 The Au-S (Gold-Sulfur) system *Bulletin of Alloy Phase Diagrams* **6** 518–9

[220] Ishikawa K, Isonaga T, Wakita S and Suzuki Y 1995 Structure and electrical properties of Au2S *Solid State Ionics* **79** 60–6

[221] Okamoto H and Massalski T B 1989 The Au-Zn (Gold-Zinc) system *Bulletin of Alloy Phase Diagrams* **10** 59–69

[222] Cui H, Lü Y Y, Yang G W, Chen Y M and Wang C X 2015 Step-Flow Kinetics Model for the Vapor–Solid–Solid Si Nanowires Growth *Nano Letters* **15** 3640–5

[223] Maliakkal C B, Jacobsson D, Tornberg M, Persson A R, Johansson J, Wallenberg R and Dick K A 2019 In situ analysis of catalyst composition during gold catalyzed GaAs nanowire growth *Nat Commun* **10** 4577

[224] Arbiol J, Kalache B, Cabarrocas P R i, Morante J R and Morral A F i 2007 Influence of Cu as a catalyst on the properties of silicon nanowires synthesized by the vapour–solid–solid mechanism *Nanotechnology* **18** 305606

[225] Tuan H-Y, Lee D C, Hanrath T and Korgel B A 2005 Germanium Nanowire Synthesis: An Example of Solid-Phase Seeded Growth with Nickel Nanocrystals *Chem. Mater.* **17** 5705–11

[226] Dubrovskii V G, Cirlin G E, Sibirev N V, Jabeen F, Harmand J C and Werner P 2011 New Mode of Vapor−Liquid−Solid Nanowire Growth *Nano Lett.* **11** 1247–53

[227] Johansson J, Karlsson L S, Dick K A, Bolinsson J, Wacaser B A, Deppert K and Samuelson L 2009 Effects of Supersaturation on the Crystal Structure of Gold Seeded III−V Nanowires *Crystal Growth & Design* **9** 766–73

[228] Panciera F, Baraissov Z, Patriarche G, Dubrovskii V G, Glas F, Travers L, Mirsaidov U and Harmand J-C 2020 Phase Selection in Self-catalyzed GaAs Nanowires *Nano Lett.* **20** 1669–75

[229] de la Mata M, Magen C, Gazquez J, Utama M I B, Heiss M, Lopatin S, Furtmayr F, Fernández-Rojas C J, Peng B, Morante J R, Rurali R, Eickhoff M, Fontcuberta i Morral A, Xiong Q and Arbiol J 2012 Polarity Assignment in ZnTe, GaAs, ZnO, and GaN-AlN Nanowires from Direct Dumbbell Analysis *Nano Lett.* **12** 2579–86

[230] Ross F M, Tersoff J and Reuter M C 2005 Sawtooth Faceting in Silicon Nanowires *Phys. Rev. Lett.* **95** 146104

[231] Moll N, Kley A, Pehlke E and Scheffler M 1996 GaAs equilibrium crystal shape from first principles *Phys. Rev. B* **54** 8844–55

[232] Pankoke V, Kratzer P and Sakong S 2011 Calculation of the diameter-dependent polytypism in GaAs nanowires from an atomic motif expansion of the formation energy *Phys. Rev. B* **84** 075455

[233] Zangwill A 1988 *Physics at Surfaces* (Cambridge University Press)

[234] Panse C, Kriegner D and Bechstedt F 2011 Polytypism of GaAs, InP, InAs, and InSb: An *ab initio* study *Phys. Rev. B* **84** 075217

[235] Yuan X, Caroff P, Wong-Leung J, Fu L, Tan H H and Jagadish C 2015 Tunable Polarity in a III-V Nanowire by Droplet Wetting and Surface Energy Engineering *Adv. Mater.* **27** 6096–103

[236] Hamad S, Cristol S and Catlow C R A 2002 Surface Structures and Crystal Morphology of ZnS: Computational Study *J. Phys. Chem. B* **106** 11002–8

[237] Joyce H J, Wong-Leung J, Gao Q, Tan H H and Jagadish C 2010 Phase Perfection in Zinc Blende and Wurtzite III−V Nanowires Using Basic Growth Parameters *Nano Lett.* **10** 908–15

[238] Glas F, Harmand J-C and Patriarche G 2007 Why Does Wurtzite Form in Nanowires of III-V Zinc Blende Semiconductors? *Phys. Rev. Lett.* **99** 146101

[239] Jaffal A, Redjem W, Regreny P, Nguyen H S, Cueff S, Letartre X, Patriarche G, Rousseau E, Cassabois G, Gendry M and Chauvin N 2019 InAs quantum dot in a needlelike tapered InP nanowire: a telecom band single photon source monolithically grown on silicon *Nanoscale* **11** 21847–55

[240] Xiong Q, Wang J and Eklund P C 2006 Coherent Twinning Phenomena: Towards Twinning Superlattices in III−V Semiconducting Nanowires *Nano Lett.* **6** 2736–42

[241] Burgess T, Breuer S, Caroff P, Wong-Leung J, Gao Q, Hoe Tan H and Jagadish C 2013 Twinning Superlattice Formation in GaAs Nanowires *ACS Nano* **7** 8105–14

[242] Wang D-H, Xu D, Wang Q, Hao Y-J, Jin G-Q, Guo X-Y and Tu K N 2008 Periodically twinned SiC nanowires *Nanotechnology* **19** 215602

[243] Algra R E, Verheijen M A, Feiner L-F, Immink G G W, Enckevort W J P van, Vlieg E and Bakkers E P A M 2011 The Role of Surface Energies and Chemical Potential during Nanowire Growth *Nano Lett.* **11** 1259–64

[244] Wallentin J, Ek M, Wallenberg L R, Samuelson L, Deppert K and Borgström M T 2010 Changes in Contact Angle of Seed Particle Correlated with Increased Zincblende Formation in Doped InP Nanowires *Nano Lett.* **10** 4807–12

[245] Grap T, Rieger T, Blömers C, Schäpers T, Grützmacher D and Lepsa M I 2013 Self-catalyzed VLS grown InAs nanowires with twinning superlattices *Nanotechnology* **24** 335601

[246] Kim H S, Myung Y, Cho Y J, Jang D M, Jung C S, Park J and Ahn J-P 2010 Three-Dimensional Structure of Twinned and Zigzagged One-Dimensional Nanostructures Using Electron Tomography *Nano Lett.* **10** 1682–91

[247] Johansson J, Karlsson L S, Patrik T. Svensson C, Mårtensson T, Wacaser B A, Deppert K, Samuelson L and Seifert W 2006 Structural properties of 〈111〉B -oriented III–V nanowires *Nature Mater* **5** 574–80

[248] De Luca M, Fasolato C, Verheijen M A, Ren Y, Swinkels M Y, Kölling S, Bakkers E P A M, Rurali R, Cartoixà X and Zardo I 2019 Phonon Engineering in Twinning Superlattice Nanowires *Nano Lett.* **19** 4702–11

[249] Wang Y Q, Philipose U, Xu T, Ruda H E and Kavanagh K L 2007 Twinning modulation in ZnSe nanowires *Semicond. Sci. Technol.* **22** 175–8

[250] Meng Q, Jiang C and Mao S X 2008 Temperature-dependent growth of zinc-blende-structured ZnTe nanostructures *Journal of Crystal Growth* **310** 4481–6

[251] Kim S, Na S, Jeon H, Kim S, Lee B, Yang J, Kim H and Lee H-J 2013 Effects of Sn doping on the growth morphology and electrical properties of ZnO nanowires *Nanotechnology* **24** 065703

[252] Ikonić Z, Srivastava G P and Inkson J C 1993 Electronic properties of twin boundaries and twinning superlattices in diamond-type and zinc-blende-type semiconductors *Phys. Rev. B* **48** 17181–93

[253] Tadic M and Ikonic Z 1999 The multiband effective-mass model of the electronic structure and intersubband absorption in p-type-doped twinning superlattices *J. Phys.: Condens. Matter* **11** 6891–909

[254] Dowdy R, Mohseni P, Fortuna S A, Wen J and Li X 2012 Twinning superlattice in VLS grown planar GaAs nanowires induced by impurity doping *IEEE Photonics Conference 2012* 2012 IEEE Photonics Conference (IPC) (Burlingame, CA, USA: IEEE) pp 693–4

[255] Akiyama T, Yamashita T, Nakamura K and Ito T 2010 Band Alignment Tuning in Twin-Plane Superlattices of Semiconductor Nanowires *Nano Lett.* **10** 4614–8

[256] Tsuzuki H, Cesar D F, Rebello de Sousa Dias M, Castelano L K, Lopez-Richard V, Rino J P and Marques G E 2011 Tailoring Electronic Transparency of Twin-Plane 1D Superlattices *ACS Nano* **5** 5519–25

[257] Liu Z, Papadimitriou I, Castillo-Rodríguez M, Wang C, Esteban-Manzanares G, Yuan X, Tan H H, Molina-Aldareguía J M and Llorca J 2019 Mechanical Behavior of InP Twinning Superlattice Nanowires *Nano Lett.* **19** 4490–7

[258] Wang J, Sansoz F, Huang J, Liu Y, Sun S, Zhang Z and Mao S X 2013 Near-ideal theoretical strength in gold nanowires containing angstrom scale twins *Nat Commun* **4** 1742

[259] Sallet V, Lusson A, Rommeluere M and Gorochov O 2000 MOCVD growth and characterization of ZnS and Zn1−xMgxS alloys *Journal of Crystal Growth* **220** 209–15

[260] Thiandoume C, Ka O, Lusson A, Cohen C, Bouanani A, Rommeluere M, Tromson-Carli A and Gorochov O 1998 MOVPE growth of ZnSxSe1−x/GaAs(1 0 0) using

ditertiarybutylselenium, tertiarybutylmercaptan and dimethylzinc triethylamine as precursors *Journal of Crystal Growth* **184–185** 149–52

[261] Wojnar P, Szymura M, Zaleszczyk W, Kłopotowski Ł, Janik E, Wiater M, Baczewski L T, Kret S, Karczewski G, Kossut J and Wojtowicz T 2013 Activation of an intense near band edge emission from ZnTe/ZnMgTe core/shell nanowires grown on silicon *Nanotechnology* **24** 365201

[262] Van de Walle C G and Neugebauer J 2003 Universal alignment of hydrogen levels in semiconductors, insulators and solutions *Nature* **423** 626–8